Garcia Bedregal, Alejandro Pablo (2007) The Formation and Evolution of S0 Galaxies. PhD thesis, University of Nottingham.

The Formation and Evolution of S0 Galaxies

Alejandro P. García Bedregal

The University of Nottingham

Thesis submitted to the University of Nottingham
for the degree of Doctor of Philosophy

January 2007

A mi Abu y Tata, Angelines y Guillermo

Abstract

This thesis studies the origin of local S0 galaxies and their possible links to other morphological types, particularly during their evolution. To address these issues, two different – and complementary – approaches have been adopted: a detailed study of the stellar populations of S0s in the Fornax Cluster and a study of the Tully–Fisher Relation of local S0s in different environments.

The data utilised for the study of Fornax S0s includes new long-slit spectroscopy for a sample of 9 S0 galaxies obtained using the FORS2 spectrograph at the 8.2m ESO VLT. From these data, several kinematic parameters have been extracted as a function of position along the major axes of these galaxies. These parameters are the mean velocity, velocity dispersion and higher-moment h_3 and h_4 coefficients. Comparison with published kinematics indicates that earlier data are often limited by their lower signal-to-noise ratio and relatively poor spectral resolution. The greater depth and higher resolution of the new data mean that we reach well beyond the bulges of these systems, probing their disk kinematics in some detail for the first time. Qualitative inspection of the results for individual galaxies shows that some of them are not entirely simple systems, perhaps indicating a turbulent past. Nonetheless, circular velocities are reliably derived for seven rotationally-supported systems of this sample.

The analysis of the central absorption line indices of these 9 galaxies indicates that they correlate with central velocity dispersions (σ_0) in a way similar to what previous studies found for ellipticals. However, the stellar population properties of Fornax S0s indicates that the observed trends seem to be produced by relative differences in age and α-element abundances, contrary to what is found in ellipticals where the overall metallicities are the main drivers of the correlations. It was found that the observed scatter in the line indices versus σ_0 relations can be partially explained by the rotationally-supported nature of many of these systems. The tighter correlations found between line indices and maximum rotational velocity support this statement. It was also confirmed that the dynamical mass is the driving physical property of all these correlations and in our Fornax S0s it has to be estimated assuming rotational support.

In this thesis, a study of the local B- and K_s-band Tully–Fisher Relation (TFR) in S0 galaxies is also presented. Our new high-quality spectral data set from the Fornax Cluster and kinematical data from the literature was combined with homogeneous photometry from the RC3 and 2MASS catalogues to construct the largest sample of S0 galaxies ever used in a study of the TFR. Independent of environment, S0 galaxies are found to lie systematically below the TFR for nearby spirals in both

the optical and infrared bands. This offset can be crudely interpreted as arising from the luminosity evolution of spiral galaxies that have faded since ceasing star formation.

However, a large scatter is also found in the S0 TFR. Most of this scatter seems to be intrinsic, not due to the observational uncertainties. The presence of such a large scatter means that the population of S0 galaxies cannot have formed exclusively by the above simple fading mechanism after all transforming at a single epoch.

To better understand the complexity of the transformation mechanism, a search for correlations was carried out between the offset from the TFR and other properties of the galaxies such as their structural properties, central velocity dispersions and ages (as estimated from absorption line indices). For the Fornax Cluster data, the offset from the TFR correlates with the estimated age of the stars in the centre of individual galaxies, in the sense and of the magnitude expected if S0 galaxies had passively faded since being converted from spirals. This correlation could imply that part of the scatter in the S0 TFR arises from the different times at which galaxies began their transformation.

Published work

Much of the work in this thesis has been previously presented in two papers:

1.- Bedregal A.G., Aragón-Salamanca A., Merrifield M.R. & Milvang-Jensen B., 2006, "S0 galaxies in Fornax: data and kinematics", MNRAS, 371, 1912

2.- Bedregal A.G., Aragón-Salamanca A. & Merrifield M.R., 2006, "The Tully-Fisher relation for S0 galaxies", MNRAS, 373, 1125,

   while the rest will be presented in a following paper:

3.- Bedregal A.G., Aragón-Salamanca A., Merrifield M.R. & Cardiel N., 2007, "S0 galaxies in Fornax: Stellar populations at large galactocentric distances", in preparation.

Paper I contains much of the work detailed in Chapter 2. Paper II describes the work presented in Chapter 4. The contents of Chapter 3 will be presented in Paper III. The work presented in this thesis was performed by the author, with advice from the paper coauthors listed above. Where the material presented is taken from literature, this is mentioned explicitly in the relevant chapter.

Finally, other work performed during the PhD which *is not* included in this thesis has being publish in two other papers:

4.- Aragón-Salamanca A., Bedregal A.G. & Merrifield M.R., 2006, "Measuring the fading of S0 galaxies using globular clusters", A&A, 458, 101

5.- Barr J.M., Bedregal A.G., Aragón-Salamanca A., Merrifield M.R. & Bamford S.P., 2007, "The Formation of S0 galaxies: evidence from globular clusters", submitted to A&A

Acknowledgements

My foremost thanks go to my family in South America for their constant support and encouragement not only during these years but also throughout my entire education. Thank you for being supportive when I had to take difficult decisions; thank you for "being with me" despite half the World was between us, no matter the (literally) years we could not see each other. Thank you for being my family.

I also want to thank my friends, spread around the World as a result of my nomadic life, for their support, jokes, promises (threats) of visiting and everything. I am specially grateful with those from Chile, Perú and China, for their periodic, long and expensive phone calls.

Thank you to Alfonso, my supervisor, for his encouragement, ideas, time, dedication and effort on making of me a more "positive" researcher. Thank you also to Mike, my co-supervisor, for being there when most required, for being always available for a quick talk about my stuff and for dealing with some issues concerning my subsistence in Nottingham.

Thanks a lot to the Astronomy & Particle Theory Group in general, staff and students, for creating such a nice atmosphere which made my stay in Nottingham a much enjoyable experience. Thank you for being so nice and kind to me, for offering your help when Alfonso was sick. A special mention for the "Mediterranean People" (Nacho, Fayna, Riccardo, Lorena, +Dolf), for the music, food, movies and common things to complain about. Dolf, nice office and house mate, thank you for all the "decent" chocolate you provide us (seriously, God bless you, Dolf... sorry, Riccardo, for the blasphemy). I am grateful with Dr. O. Nakamura, Dr. S. Bamford, Dr. M. Mouhcine, Dr. N. Cardiel, Dr. J. Falcón-Barroso, Dr. I. Trujillo, Dr. D. Michielsen and Mr. R. Brunino, for their help, suggestions and interesting discussion during different periods of my PhD.

My studies were funded by the University of Nottingham, for which I am grateful. The School of Physics & Astronomy gave me financial support during my studies and writing-up period for which I am deeply grateful too. I have benefited from the attendance of numerous conferences and summer schools thanks to funding from the University and the MAGPOP European Research Network.

The work in this thesis was based on observations made with ESO telescopes at Paranal Observatory under programme ID 070.A-0332. This work makes also use of data products from the Two Micron All Sky Survey, which is a joint project of the University of Massachusetts and the Infrared Processing and Analysis Center/California Institute of Technology, funded by the National Aeronautics and Space Administration and the National Science Foundation.

Contents

List of Figures

List of Tables

Chapter 1

Introduction

From an astronomical point of view, galaxies are considered as fundamental building blocks of the Universe. They are gravitationally-linked groups of stars and gas, with total masses typically ranging between 10^7–10^{13} M$_\odot$ and sizes between tenths to hundreds of kpc (Carroll & Ostlie 1996). Galaxies exhibit a wide variety of shapes, being usually classified according to their morphologies. Edwin Hubble (1926) proposed that galaxies be grouped into three main categories, based on their overall appearance. This morphological classification scheme, known as the Hubble Sequence (arranged in the form of a "tuning fork" diagram, Figure 1.1) divides galaxies into ellipticals (E), spirals and irregulars (Irr). The spirals are further subdivided into two parallel sequences: the normal spirals (S) and the barred spirals (SB). A transitional class of objects between ellipticals and spirals can be either S0 or SB0, depending on whether they are normal or barred, respectively. Originally, Hubble interpreted (incorrectly) his diagram as an evolutionary sequence for galaxies, refering to galaxies towards the left of the diagram (E) as *early-type* and those towards the right (S and SB) as *late-type*. This terminology is widely spread today, with S0s and Es usually studied as one class of objects under the label of *early-type galaxies*.

1.1 Galaxy Morphology and Evolution

One of the key areas of research in extragalactic astronomy is the study of the formation and evolution of galaxies in different environments, from the low-density field to rich clusters. In this context, the morphology of galaxies may reflect the governing physical processes involved in their evolutionary history, although our understanding of such mechanisms and their relative importance in each environment is still rather poor. That is why the origin of S0 galaxies, given their location between ellipticals and spirals in the Hubble Diagram, has become an important focus of debate for many years. One fundamental – and sometimes controversial – issue is whether the formation of these galaxies is more closely linked to that of ellipticals or to that of spirals. For example, the presence of stellar disks in S0s points towards a close relation to spirals. However similarities exist between ellipticals and S0s in their colours, stellar populations, gas content and location on the fundamental
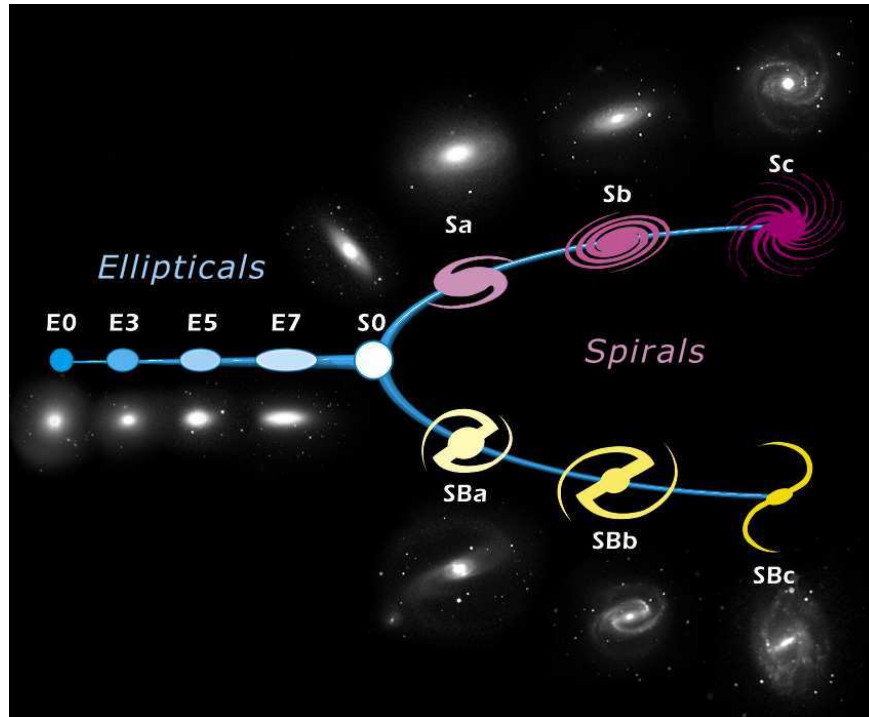
Figure 1.1. Hubble Diagram of morphological classification of galaxies.

plane. Therefore the debate as to whether S0s are more closely related to spirals or ellipticals remains open.

1.1.1 Observational evidence

To study galaxy evolution, galaxy clusters provide a useful "laboratory" to study the physical phenomena involved in this process. Although only a small fraction of galaxies are located in rich clusters, such environments are sites where both fast and slow galaxy evolution takes place. Therefore, they can potentially provide important clues on a variety of astrophysical phenomena, not only restricted to clusters, but important for the overall galaxy population.

A first important observation comes from the evolution with redshift of the Morphology–Density relation in clusters of galaxies (Dressler 1980; Dressler et al. 1997; Figure 1.2). Local clusters are mainly dominated by passively-evolving ellipticals and S0s, while at intermediate redshifts the relative number of spirals is much larger. In particular, these studies show that the relative fraction of S0 galaxies increased from $z \sim 0.5$ to the present in a similar proportion to the decrease in spirals while the fraction of ellipticals do not present large variations during this period. An evolutionary connection between S0s and spirals has thus been proposed, at least in cluster environments. More recent works seem to support such ideas (e.g. Fasano et al. 2000; Desai 2004; Postman et al. 2005), although alternative views do exist (Andreon 1998).
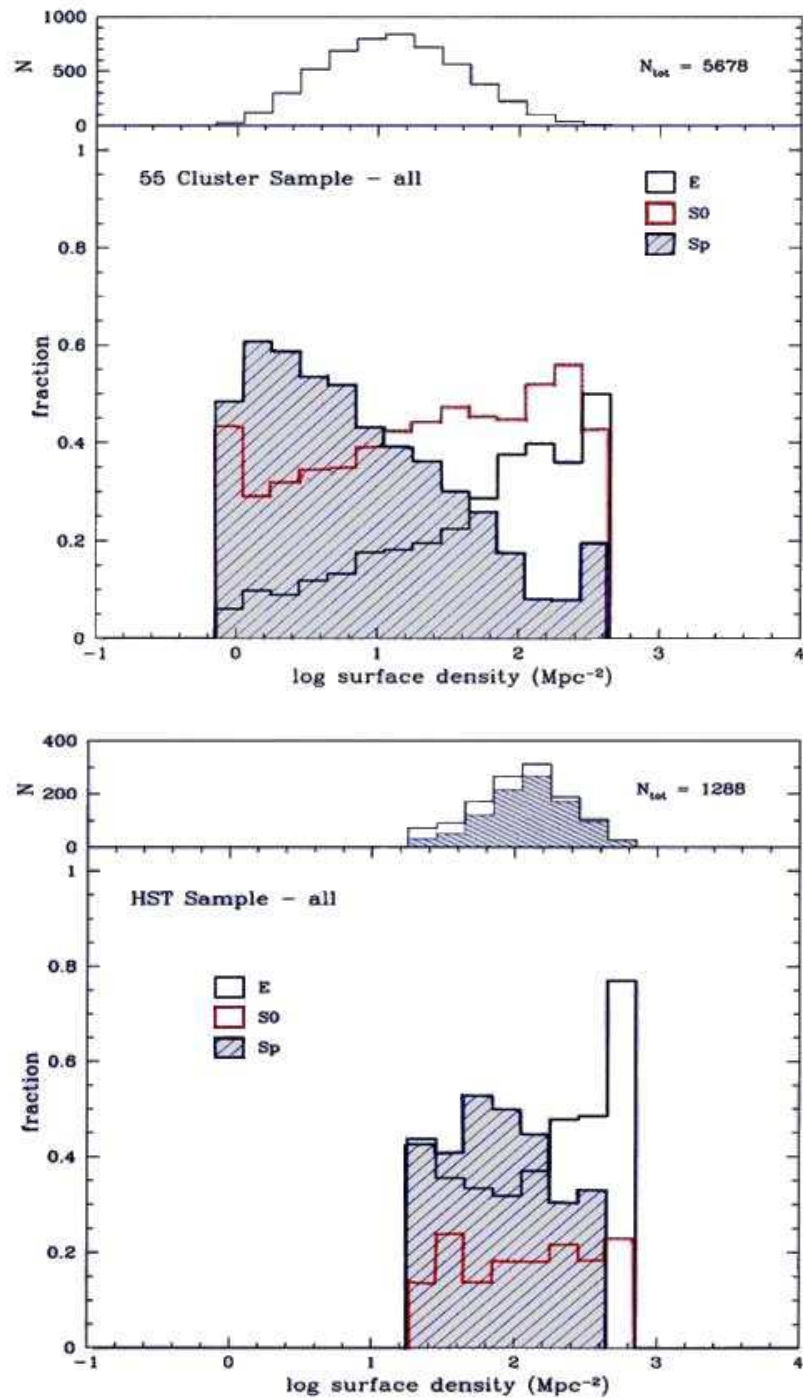
Figure 1.2. Morphology-Density Relations. Top: galaxies from 55 local clusters (Dressler 1980). Bottom: galaxies from 10 clusters at intermediate redshift, $0.36 \leq z \leq 0.57$ (Dressler et al. 1997).

The structure formation scenario from ΛCDM models predicts the infall of many field galaxies to clusters since $z \lesssim 1$ (De Lucia et al. 2004). This comes accompanied by observational evidence that the properties of disk galaxies are different at high redshift than locally. There is a significant fraction of blue galaxies at high redshift (Butcher & Oemler 1978), found to be star-forming (Dressler & Gunn 1982, 1992) and usually with spiral morphology (Couch et al. 1998; Postman et al. 2005), which contrast with the dominant S0 population found in the core of local clusters. This evidence suggests that starforming spirals are transformed into passive S0s by the cluster environment. Additional evidence for this picture comes from the presence of two conspicuous type of galaxies in clusters. The first are "Passive Spirals", usually found in the outer parts of clusters and not in the field, with spiral morphology but no signs of recent star formation. Their presence suggest that some interaction with the intra-cluster medium (ICM) has truncated their star formation (Goto et al. 2003). The second are so-called "E+A Galaxies". The relevant ones for this discussion are those with disky isophotes which usually populate clusters at intermediate redshift. These galaxies have an E+A (also known as k+a) spectra with features of both an old (several Gyr; K stars which characterise Es' stellar populations) and a young ($\leq$ 1 Gyr, A stars) stellar population, but no signs of on-going star formation (Dressler & Gunn 1983; Dressler et al. 1999). These kind of spectra have been interpreted as indicative of a recent starburst before the truncation of the star formation (Poggianti et al. 1999). These two type of galaxies may be considered as intermediate steps in the evolution of spirals to S0s in clusters.

1.1.2 Possible mechanisms of morphological transformation

The presence of S0s in both cluster and field environments raises the real possibility that multiple evolutionary paths exist for the formation of these systems. Indeed, a variety of mechanisms have been proposed that can, in principle, alter a cluster galaxy's morphology in this direction.

Gunn & Gott (1972) proposed the *Ram-pressure Gas Stripping* scenario as a possible path that could transform spirals to S0s in clusters. When a spiral galaxy passes from the field to the cluster environment, the pressure due to the hot ICM could remove the cold gas from the disk producing a fast truncation of the star formation (Abadi et al. 1999; Quilis et al. 2000). Galaxies with clear signs of undergoing ram-pressure striping have been observed in the Coma (Gavazzi 1989; Bravo-Alfaro et al. 2001; Vollmer et al. 2001), Virgo (Kenney & Koopmann 1999; Vollmer et al. 1999, 2000, 2004; Vollmer 2003; Kenney et al. 2004; Yoshida et al. 2004; Veilleux et al. 1999; Oosterloo & van Gorkom 2005) and Abell 1367 clusters (Dickey & Gavazzi 1991; Gavazzi et al. 1995, 2001). A variation of this scenario considers that the gas could merely be removed from the galaxy halo in the so-called *Starvation* or *Strangulation* model (Larson, Tinsley & Caldwell 1980; Bekki et al. 2002). The disk gas consumed in star formation is usually replenished by infall from the reservoir of the halo gas. This alternative leads to a gradual decrease in the star formation as the amount of available gas in the disk diminishes. Before the truncation of the star

formation the gas compression in the disk can facilitate the collapse of molecular clouds, thereby increasing the star formation rate (Bekki & Couch 2003). The duration of this star burst is self-limiting in the sense that it causes an increase in the rate of disk gas consumption, reducing the time taken for star formation to cease.

Other possible mechanism in clusters is *Galaxy Harassment*, proposed by Moore, Lake & Katz (1998). They propose that the evolution of cluster galaxies is governed by the combined effect of multiple high speed galaxy-galaxy close encounters. The multiple encounters heat the stellar component increasing the galaxies' velocity dispersion and decreasing their angular momentum, meanwhile the gas sinks towards the central regions producing a starburst. The enhanced central star formation is predicted by Fujita (1998) models given the higher probability of close cloud-cloud encounters. During this process, a galaxy may lose an important fraction of its original disk stellar population. This mechanism would be more effective in low-mass/low-surface brightness galaxies than in massive objects with strong disks and deeper potential wells (Moore et al. 1999). Late-type spirals (Sc) have been proposed as candidates to be strongly affected by this process during their infall in clusters (Kuntschner 2000).

Unequal-mass Galaxy Mergers (Mihos & Hernquist 1994; Bekki 1998) may cause the eventual truncation of star formation by first inducing a starburst. The enhancement of the star formation rate would quickly diminish the amount of gas available for further formation of stars, eventually stopping the overall process. From simulations, Bekki (1998) found that unequal mergers with mass ratio $\sim$ 3:1 produce S0 morphologies, while minor mergers ($\geq$ 10:1) have a smaller effect on the larger galaxy. However, repeated minor mergers could also lead to an S0 appearance. On the other hand, equal-mass mergers would generally destroy any disk component, resulting in elliptical morphologies. It is usually considered very difficult to create (or re-create) disks in cluster conditions given the lack of cold gas from which a disk might form and the hostile environment itself. The fact that counter-rotating co-spatial stellar disks in S0s are not so frequent ($\leq$ 5% of the cases; Kuijken, Fisher & Merrifield 1996) is consistent with this statement.

The interaction between the individual galaxies and the overall cluster potential (*Galaxy-Cluster Interactions*) has been proposed as an effective mechanism for the evolution of massive cluster galaxies (Merritt 1984; Miller 1986; Byrd & Valtonen 1990). It may produce gas inflow, bar formation, nuclear and perhaps disk star formation. The total amount of gas in galaxies would decrease but mainly through consumption in star formation events and not by direct removal by the interaction (Boselli & Gavazzi 2006). While in the static case this is judged to only be important in the cluster core (Henriksen & Byrd 1996), the existence of substructure and in particular cluster-group and cluster-cluster mergers, may result in a time-varying tidal field with more significant effects (Bekki 1999; Gnedin 2003a,b). Direct observations seem to support some of these scenarios. Owen et al. (2005) and Ferrari et al. (2005) suggest that tidal interactions due to cluster-cluster mergers are the most likely explanation for the enhanced star formation in Abell 2125 and Abell 3921, respectively.

In summary, a number of plausible mechanisms have been proposed which could explain the transformation of spirals to S0s in the cluster environment. However, it is still unclear whether some of these processes would work in practice, and, if more than one, their relative importance in different environments.

1.2 Evidence of sub-populations of S0 galaxies

Given the variety of mechanisms which could alter the galaxy appearance, it would be possible for them to produce distinctive types of remnants. Their morphology may be characterised not only by how each particular process works but also by the galaxy type over which they act more efficiently.

Van den Bergh (1990), analysing the Revised Shapley–Ames Catalog of Bright Galaxies (Sandage & Tammann 1987), found that the frequency distribution of the luminosity of S0s is not intermediate between E and Sa galaxies. This discontinuity could imply the existence of sub-populations amongst the S0s: bright S0s, the "real″ intermediate class between E and Sa galaxies; and faint S0s, many of which could be miss-classified as faint Es if viewed close to face-on. The works of Nieto et al. (1991) and Jorgensen & Franx (1994) support this hypothesis, pointing out the similarity between disky [and thus faint (Kissler-Patig 1997)] E and S0 galaxies, based on their isophotal central shapes. Also, Graham et al. (1998), in a study of the extended stellar kinematics of elliptical galaxies in the Fornax Cluster, found that five of the galaxies are in fact rotationally supported systems, suggesting that they could be misclassified S0 galaxies.

Studies of the stellar populations in cluster galaxies (Kuntschner 2000; Smail et al. 2001) also support the idea of a dichotomy between low- and high-luminosity S0s: bright S0s are old and seem to coeval with E galaxies, while faint members present younger central ages, indicating more recent star formation episodes. Furthermore, Poggianti et al. (2001) examined the star formation history of early-type galaxies in the Coma Cluster, and found that $\sim 40\%$ of the S0 population seemed to have experienced a star formation event during the last few billion years, a phenomenon which is absent in their sample of elliptical galaxies. Thus, it has been proposed that faint S0s could be the descendants of the post-starburst galaxies found in intermediate redshift clusters. The work of Mehlert et al. (2000, 2003) in early type galaxies in the same cluster confirms the dichotomy found by Poggianti et al. between old and young lenticulars; however, the high α-element ratios found in the latter seems to argue against the occurrence of recent star formation: the authors suggest that the strong Balmer line indices measured in apparently "young″ S0s could actually be produced by unusually blue horizontal branches rather than by young stellar populations. Clearly, more work remains to be done in the study of stellar populations to interpret the physical significance of the two apparently-distinct types of S0.

1.3 Scaling Relations and S0 galaxies

One approach to understand the origins of S0 galaxies lies in their scaling relations. As for other lines of research, S0s have been usually studied together with ellipticals as one class of object. Some of the most important results, relevant to the present study, are summarised below.

The *Color-Magnitude relation* (CMR; Faber 1973) showed that more luminous galaxies are redder, with E and S0 galaxies following the same correlation in the local universe (Visvanathan & Sandage 1977). Typically, this correlation has been interpreted as a mass-metallicity relation, in the sense that more massive galaxies host more metal-rich stellar populations. The fact that the intensity of certain metallic lines increases with velocity dispersion re-enforces this interpretation (Terlevich et al. 1981; Bender et al. 1993; Colless et al. 1999). Different studies in local samples of cluster galaxies have confirmed the universal properties of the CMR, including their slope, zero-point and intrinsic scatter (e.g. Bower et al. 1992; van Dokkum et al. 1998; Hogg et al. 2004; López-Cruz et al. 2004; Bell et al. 2004; Bernardi et al. 2005; McIntosh et al. 2005). The CMR evolves back in time according to passive evolution models (Ellis et al. 1997; Stanford et al. 1998; van Dokkum et al. 2000, 2001; Blakeslee et al. 2003; Holden et al. 2004; De Lucia et al. 2004). At higher redshifts it is found that the CMR is already in place at $z \sim 1.3$ (e.g. Stanford et al. 1997; Mullis et al. 2005) showing a whole picture where E and S0 galaxies passively coevolve (at least) since then. However, recent results using ACS-HST seem to point in another direction. Mei et al. (2006a,b) by studing two clusters at $z \sim 1.1$ found that S0s present a larger scatter in their CMR than Es, while in one cluster the former are systematically bluer than the latter. These observations suggest that S0s are still forming at $z \sim 1$ and have formed later than Es, whose CMR is consistent with passive evolution at those redshifts. These results seem more consistent with the evolution of the morphology-density relation described in the previous section. Certainly, only more extended studies using high quality data will confirm if the observed differences in the CMR of Es and S0s are common in high-z clusters.

One of the most important examples of scaling relations is the one relating effective radius (R_e), surface brightness (I_e) and velocity dispersion (σ) in early-type galaxies, known as *The Fundamental Plane* (FP; Dressler et al. 1987; Djorgovski & Davis 1987). Although the physics behind it is not totally understood, the FP seems to imply a dependence between the dynamical mass-to-light ratio (M/L) on structural parameters (e.g. Jorgensen et al. 1996). The observed relations and modest scatter of the FP ($\sim 0.1 \, \mathrm{dex}$) do not seem to be strongly different for local E and S0 galaxies (Jorgensen et al. 1996; Bernardi et al. 2003; Cappellari et al. 2006). At higher redshifts there is no compelling evidence of differences in the FP of E and S0 galaxies apart of a zero-point evolution consistent with passive fading (Jorgensen et al. 1999; Kelson et al. 2000). However, some studies have found a marginally larger luminosity evolution with respect to the local FP for S0s than for ellipticals (Fritz et al. 2005) and larger scatter for the former than for the latter (Barr et al. 2006).

One of the most widely studied scaling relations in early-type galaxies is the Mg_2–σ *relation* (e.g., Burstein et al. 1988; Guzmán et al. 1992; Bender et al. 1993, 1998; Jorgensen et al. 1996; Colless et al. 1999; Jorgensen 1999; Kuntschner 2000; Mehlert et al. 2003; Sánchez-Blázquez et al. 2006) which is usually interpreted as a correlation between mass and metallicity. Only in recent studies in the Fornax (Kuntschner 2000) and Coma (Mehlert et al. 2003) Clusters some differences have appeared between the trends observed in E and S0's for different line indices. Luminous S0s seem to follow the relations for normal ellipticals, while the fainter ones have stronger Hβ absorption with larger dispersions with respect to the E's relations. It is not totally clear which properties of the faint S0's stellar populations are behind these differences.

1.3.1 The Tully-Fisher Relation and S0 Galaxies

Given the importance of the *Tully-Fisher Relation* (TFR; Tully & Fisher 1977) for this thesis, a more detailed description is presented here for this scaling relation.

The Tully–Fisher relation is one of the most important physically-motivated correlations found in spiral galaxies. The correspondence between luminosity and maximum rotational velocity (V_{MAX}) is usually interpreted as a product of the close relation between the stellar and total masses of galaxies or, in other words, as the presence of a relatively constant M/L in the local spiral galaxy population (e.g. Gavazzi 1993; Zwaan et al. 1995). Such a general property in spirals puts strong constraints on galaxy formation scenarios (e.g. Mao et al. 1998; van den Bosch 2000) and cosmological models (e.g. Giovanelli et al. 1997; Sakai et al. 2000). Also, the low scatter in the TFR (only ~ 0.35 mag in the I-band, according to Giovanelli et al. 1997; Sakai et al. 2000; Tully & Pierce 2000 and Verheijen 2001) permits us to use this tool as a good distance estimator (e.g. Yasuda et al. 1997).

Attempts to ascertain whether S0 galaxies follow a similar TFR have two main motivations. First, if there is a TFR for S0s, it would prove useful for estimating distances in the nearby universe, particularly in clusters where S0s are very prevalent (Dressler 1980). Second, and more related to the present study, a possible scenario where S0 galaxies are the descendants of evolved spirals at higher redshifts (Dressler 1980; Dressler et al. 1997) could leave traces of this evolution in the observed TFR of S0s. Different mechanisms have been proposed as the channels for such evolution (see section 1.1.2). If this picture is correct, it would be expected that S0s retain some memory of their past as spirals, in particular through their TFR, and perhaps even some clues as to which of the channels they evolved down.

Only a few studies of the TFR for S0 galaxies can be found in the literature. The first effort, made by Dressler & Sandage (1983), found no evidence for the existence of a TFR for S0 galaxies. However, the limited spatial extent of their rotation curves, the inhomogeneous photographic photometry employed and the large uncertainties in the distances to their sample made it almost certain that any correlation between luminosity and rotational velocity would be lost in the observational uncertainties.

Fifteen years later, Neistein et al. (1999) explored the existence of a TFR for S0s in the I-band, using a sample of 18 local S0s from the field. Although some

evidence for a TFR was uncovered in this study, they also found a large scatter of 0.7 magnitudes in the relation, suggesting the presence of more heterogeneous evolutionary histories for these galaxies when compared to spirals. Also, a systematic shift 0.5 magnitudes was found between their galaxies and the relation for local spirals.

In two papers, Hinz et al. (2001, 2003), explored the I- and H-band TFRs for 22 S0s in the Coma Cluster and 8 S0s in the Virgo Cluster. By using cluster data, they avoided some of the errors that arise from the uncertainty in absolute distances. The analysis of I-band data from the Coma Cluster revealed very similar results to the study by Neistein et al. (1999), implying that the larger scatter found by the latter could not be attributed to distance errors or the heterogeneous nature of the data. In the H-band, an even larger scatter of 1.3 magnitudes was found, but with a smaller offset from the corresponding spiral galaxy TFR of only 0.2 magnitudes. Interestingly, there was no evidence for any systematic difference between the results for the Virgo and Coma Clusters, despite their differences in richness and populations, implying that these factors could not be responsible for the scatter in the TFR. Given the large scatter and small shift in the H-band TFR for S0s compared to spirals, it was concluded that these galaxies' properties are not consistent with what would be expected for spiral galaxies whose star formation had been truncated; instead they suggested that other mechanisms such as minor mergers are responsible for the S0s' TFR.

By contrast, Mathieu, Merrifield & Kuijken (2002) found in their detailed dynamical modeling of six disk-dominated field S0s that these galaxies obey a tight I-band TFR with a scatter of only 0.3 magnitudes, but offset from the spiral galaxy TFR by a massive 1.8 magnitudes. The authors therefore concluded that these objects were consistent with being generated by passively fading spirals that had simply stopped producing stars. This result does not appear to be consistent with the previous studies, although it should be borne in mind that the galaxies in this study were selected to be disk-dominated, so they morphologically resemble spiral galaxies more than those in the other works. In addition, their field locations means that they are less likely to have had their evolution complicated by mergers. It is therefore possible that these S0s really are just passively-fading spirals where those in clusters have led more complicated lives.

As can be seen, there is no general consensus as to either the scatter or the shift in the TFR for S0 galaxies when compared to spirals, and so no agreement as to their interpretation. Much of the difficulty arises from the heterogeneous nature of the data that have been used in these studies. In some cases, the data come from objects in a range of ill-defined differing environments, while in others the issues are more to do with the varying quality of the observations.

1.4 Other studies on S0 galaxies

The formation of S0 galaxies has also been the subject of numerical simulations. The work of Shioya et al. (2004) on "red Hδ-strong" galaxies suggests two different evolutionary paths for S0s, each one able to match different spectral features in

different galaxies: a "truncation" scenario, in which the star formation is stopped and followed by passive evolution, and a "starburst" one, in which a relatively recent and short star formation event precedes the cessation of star formation. On the other hand, Christlein & Zabludoff (2004) found that simulations based on a fading stellar population could not match the observed luminosity distribution of galaxies with the larger bulge-to-total-light ratios (B/T) typically observed in S0s. Although ram-pressure gas stripping in disks has been observed as described in the previous section, this study points out that the disk fading by itself cannot reconcile the observed B/T distributions of spirals and S0s. They therefore advocated a "bulge enhancement" model, where disk fading is accompanied by an increase in the luminosity of the bulge; this model seems to match the observations over a wide range of B/T. In this context, it is interesting that Moss & Whittle (2000) found spiral galaxies in clusters have more central star formation than their field counterparts.

The extended stellar kinematics of S0 galaxies have been studied mostly in conjunction with those of ellipticals, and often as one single class of objects. For instance, D'Onofrio et al. (1995) studied a sample of 15 early-type galaxies in the Fornax Cluster, and did not find major differences between Es and S0s other than stronger rotational support and higher projected ellipticities for the latter. In a sample of 35 E and S0 galaxies in the Coma cluster, Mehlert et al. (2000, 2003) found that elliptical galaxies have, on average, slightly higher velocity dispersions than S0s, as is also apparent from the velocity dispersion profiles presented in D'Onofrio et al. (1995). Although these differences could be real, they may also at least in part arise from the selection effects that render S0s more reliably identified when close to edge-on.

With current techniques using integral-field units and high quality spectra, it is possible to examine stellar-kinematic substructure in search of further clues as to how these systems form. The work by Emsellem et al. (2004), for example, revealed that kinematically-decoupled components, bars and misalignments between photometric and kinematic axes seems to be present in both Es and S0s. There are also instances of even more extreme kinematic substructure such as counter-rotating co-spatial stellar disks in S0s (Rubin, Graham & Kenney 1992), but, as mentioned before, these seem to be very rare (Kuijken, Fisher & Merrifield 1996). This rarity is something of a surprise, as counter-rotating gas is relatively common in S0s (Bertola, Buson & Zeilinger 1992), which led to the suggestion that it might be quite common for S0s to be enhanced by the kind of minor mergers likely responsible for this phenomenon. These observations can only be reconciled if there is some mechanism for inhibiting star formation in such counter-rotating material, but the situation is clearly quite complex.

In summary, the above paragraphs illustrate the wide range of techniques that have been applied to trying to understand the nature of S0s, and the sometimes inconsistent results that have emerged. There are certainly indications of a dichotomy between faint and bright S0s, but it is still unclear which observables best characterise this distinction, and how those observables might translate into differences in the evolutionary history of the two types. Many of the inconsistencies, however,

might be apparent only. Some of the results summarised here are based on low quality data (e.g., photographic plates) and biased towards very bright objects. To this we should add the rather complicated task of morphological classification itself, particularly difficult in "transitional objects" like S0s, which could bias results and conclusions towards particular formation histories.

However, as discused above, some recent works based on high-quality data from HST and 8-metre-class telescopes seem to draw a new picture, revealing richer, more complex scenarios while undermining some strong preconceptions about how galaxies form, evolve and reach their current appearance.

1.5   Outline of this thesis

The thesis is organised as follows.

- ○ Chapter 2 describes the long-slit spectroscopy dataset of S0 galaxies in the Fornax Cluster, including the sample selection, the observations and the data reduction. Also, the extraction of the kinematic parameters along the radius is included in this chapter.

- ○ Chapter 3 presents a study of the central stellar populations of Fornax S0s. It includes the applied procedure followed to measure absorption line indices, the corrections, the age and metallicity estimation and a study of several Index–σ relations and other scaling relations.

- ○ Chapter 4 presents a study of the local Tully–Fisher relation of S0 galaxies in different environments using both the B- and K_s- bands.

- ○ Chapter 5 summarises the results and the conclusions and outlines a number of future projects that build on the work presented in this thesis.

- ○ Appendix A presents plots of four kinematic parameters along the semimajor axis calculated in Chapter 2 for our sample of Fornax S0s.

- ○ Appendix B includes tables with structural parameters, line index measurements, ages, metallicities and other relevant parameters of the different galaxy samples used in Chapters 3 and 4.

Chapter 2

Fornax Data and Kinematics

The study presented in this thesis is mainly based on a long-slit spectroscopy dataset from a sample of S0 galaxies. These data have been entirely reduced and analysed by the author and the basic steps of the procedure are described in this chapter.

The sample was selected from galaxies in the Fornax Cluster classified as S0s by Kuntschner (2000). Nine of the total 11 objects classified as S0 were observed. These objects span a wide range of luminosities ($-22.3 < M_{\mathrm{B}} < -17.3$) and are sufficiently inclined to measure rotations along their major axes. The basic properties of the resulting sample are presented in Table 2.1.

The necessary observations were made in service mode between 2002 October 2 and 2003 February 24 at the 8.2m Antu/VLT using the FORS2 instrument in long-slit spectroscopy mode; exposure times and dates are provided in Table 2.1. Spectrophotometric standard stars were observed each night, as well as stars with a range of spectral classes to act as velocity templates in the kinematic analysis; these objects are listed in Table 2.2. During the observations, the seeing varied from 0.75 to $1.48''$ FWHM, which is more than adequate for the study of these large objects.

The detector in FORS2 comprises two 2k×4k MIT CCDs, with a pixel size of $15 \times 15 \mu\mathrm{m}^2$ (chip 1, master and chip 2, slave). The standard resolution collimator and the unbinned readout mode were used, yielding a scale of $0.125''$/pixel. The spectrograph slit was set to $0.5''$ wide and covered $6.8'$ in length. The GRIS1400V + 18 grism was used, providing a dispersion of $0.318\,\text{Å}$/pixel and covering the $4560\,\text{Å} \leq \lambda \leq 5860\,\text{Å}$ wavelength range. This set-up provided a spectral resolution, as measured from the FWHM of the arc lines, of ≈ 4 pixels (or $1.12\,\text{Å}$), which translates into a velocity resolution of $73.3\,\mathrm{km\,s^{-1}}$ FWHM (or $31.0\,\mathrm{km\,s^{-1}}$ in terms of the velocity dispersion). The CCD was read out at $200\,\mathrm{kHz}$, which is twice the normal speed used for spectroscopy. The high readout speed was the only one available for unbinned readout of the CCD.

2.1   Data Reduction

The reduction of long-slit spectroscopy required a number of steps, and each one requires a careful consideration and adaptation to the particular properties of the dataset. The overall procedure is rather standardised; however it is important to present here some details in order to appreciate the characteristics of the data. In

Table 2.1. Sample of S0 galaxies in Fornax.

Name	RA	DEC	B_T^*	D^* [']	Exp.Time [sec]	P.A. [^{o}]	Seeing ["]	Date dd/mm/yy
NGC 1316	03 22 41	−37 12 30	9.4	11.0	3×1200	50.2^a	1.27	13/10/02
NGC 1380	03 36 27	−34 58 34	10.9	4.8	2×1200	3.9^b	1.41	24/02/03
NGC 1381	03 36 31	−35 17 43	12.4	2.7	2×1600	-41.7^c	1.48	24/02/03
IC 1963	03 35 30	−34 26 51	12.9	2.6	2×1600	82.6^d	1.20	31/01/03
NGC 1375	03 35 16	−35 15 56	13.2	2.2	2×1800	89.7^d	1.19	28/12/02
NGC 1380A	03 36 47	−34 44 23	13.3	2.4	2×1700	-3.5^b	0.93	28/12/02
ESO 358-G006	03 27 18	−34 31 35	13.9	1.2	2×2400	1.5^a	1.05	14/10/02
ESO 358-G059	03 45 03	−35 58 22	14.0	1.0	1×2550	-23.7^c	1.14	08/02/03
ESO 359-G002	03 50 36	−35 54 34	14.2	1.3	1×2250	47.2^a	0.75	26/11/02

* Apparent total B-band magnitude (B_T) and diameter (D) from RC3, de Vaucouleurs et al. (1991). Slit orientation: (^{a}) NE-SW; (^{b}) N-S; (^{c}) NW-SE; (^{d}) E-W.

the following paragraphs the data reduction is summarised, stressing those aspects of the process particular to the dataset. The reduction was entirely carried out using `IRAF` tasks (Tody 1986, 1993). The different procedures were applied separately for each chip unless the text indicates explicitly the opposite. Error images ($1\,\sigma$) were prepared for all the science/stellar-calibration exposures using the standard CCD noise model (photon noise + readout noise) and were processed in parallel to the main spectra. Other methods to obtain error images (i.e. direct estimations from the data) were not attempted, given the small number of exposures of the same source and the consequent low pixel-to-pixel statistics.

2.1.1 Preparing Bias subtraction

Bias or zero images allow measurement of the zero noise level of the CCD. For each night of observation, between 5 to 15 good bias images were combined in order to create a masterbias by taking a 3-sigma clipped mean of the images using the `IRAF` task *zerocombine*. In this way, the few pixels affected by cosmic rays (mainly during the reset and readout of the detector) can be effectively removed from the mean.

2.1.2 Bad Pixels Masks

We can usually find dead columns or bad pixels in CCDs which do not respond linearly to incoming radiation. They can cause problems during calibration and analysis by hindering software processes and not allowing correct flux estimates to be made for the pixels that they affect. In order to remove such pixels, an interpolation of their values was applied by using a bad pixel mask. For each observing run, bad pixels have been detected by dividing two sets of screen flat-field images of different exposure times (5 images in each subset with a mean of 5000 and 20000 counts, respectively). After bias subtraction, the masks have been created using the `IRAF` task *ccdmask*.

2.1.3 Removing Cosmic Rays

The following procedure was carried out to remove cosmic ray events in the data. First, preliminary detections of cosmic rays were made by using the task *cosmicrays*. This task identifies the brightest pixel within an specified detection window (typically 7×7 pixel^2). The mean flux in the surrounding pixels with the second brightest pixel excluded (which may also be a cosmic ray event) is computed and the candidate pixel must exceed this mean by an amount specified by a certain threshold. In a second step, after local background subtraction a new mean flux is calculated and the ratio (as a percent) between this mean and the candidate pixel must be typically smaller than 10% in order to label the pixel as a cosmic ray event. Since only the locally strongest pixel is considered a cosmic ray, multiple detection passes (usually 5) are needed to detect cosmic ray events with multiple neighbouring pixels. These detections were overplotted into the original image, checked by eye and corrected in order to identify (1) all the pixels corresponding to each individual cosmic ray event (7 pixels on average) and (2) false detections such as spectral lines and the peaks of the galaxies' profiles. Finally, cosmic ray masks were created to interpolate the values of affected pixels (tasks *badpiximage* and *fixpix* respectively).

2.1.4 Instrumental Distortion correction

In practice it is often found that CCD spectra are not precisely aligned with the CCD pixels and are curved on the detector as the result of camera optics, instrumental distortions, or CCD flatness issues. As a result, this distortion has the effect of misaligning the dispersion axis with respect to the CCD rows. Because such misalignment could also vary along the spatial direction, a 2-dimensional correction was necessary. This cannot be achieved by simply tracing the central peak of a galaxy's profile and transforming the spectra by the inverse of that function. At this stage, we use the calibration data from another program in which FORS2 was used, kindly provided by Dr. Steven Bamford. These particular data have mainly the same instrumental settings as ours but uses the MXU (multiobject) mode instead of the long-slit mode of our dataset. The multiobject mode made possible to study (and eventually, correct) the distortions caused by the instrumental optics along the spatial direction of the chips. Raw calibration data were used from this program in order to perform a data reduction process consistent with ours (bias subtraction, removal of cosmic rays and bad pixel interpolation). The distortions were mapped by measuring the positions along the edges of slit apertures in the flat images. This was done on images of the aperture edges, created by taking the gradient of the flat images in the spatial direction (columns). The flat image was shifted one pixel down and subtracted from the unshifted version: the lower edges appear as positive features and the upper edges as negative features in the resulting image. Absolute pixel values were taken and both chips were considered separately in all these processes. In Figure 2.1 a section of this image clearly shows the effect of the distortion after expanding the vertical scale.

The magnitude of the distortions were not considerable ($\approx$ 6 to 7 pixels in spatial direction in the extreme edges of the CCDs). A characteristic U-shape distortion was
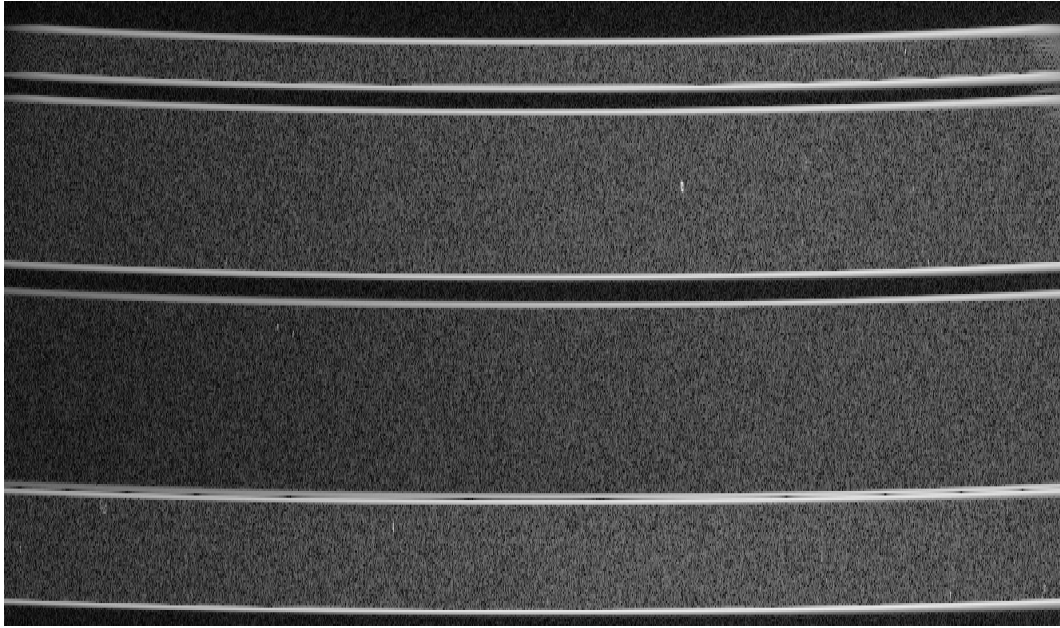
Figure 2.1. Section of chip 1 from a flat-field edge image in MXU mode. Vertical axis has been expanded by a factor of four to better show the geometric distortion caused by the instrument's optical system. Bright features correspond to high gradients in the flat-field image, marking the edges of the different apertures. The apertures themselves appear slightly lighter than the gaps between them, because of their higher level, and hence larger absolute variations due to Poisson noise in the flat.

present in the upper edge of chip 1, decreasing its curvature towards the centre of the field and becoming upsidedown-U-shaped in the lower edge of chip 2. The aperture edges were traced along the dispersion direction and 2-dimensional functions were fitted. The `IRAF` tasks *identify*, *reidentify* and *fitcords* (typically used for wavelength calibration) were used at this stage. Typically, polynomials of order 3 (in both axis) gave an appropriate description of the distortions. The corrected images present small residuals of ≤ 0.2 pixels measured at the luminosity peak of the galaxies, usually located in the lower part of chip 1. The spectra of NGC 1316 made possible to test the quality of the correction in the upper part of chip 1, given the position of its centre in that region of the CCD. The correction was very good, presenting similar residuals to the other cases. Finally, all science and calibration images were corrected by the derived functions by using the task *transform*.

2.1.5 Preparing Flat Fields

In a CCD, each pixel has a slightly different gain or quantum efficiency value when compared with its neighbours. In order to flatten the relative response for each pixel to the incoming radiation, a normalised master flat image was used (one per night) to perform this calibration. After careful examination of each individual flat image, bias subtraction, bad pixel interpolation and geometrical distortion correction, a total of 4 to 5 flat field images were combined in a masterflat using the task *flatcombine* with the *reject* option set to *crreject* in order to optimise the removal of cosmic rays events. The large-scale, wavelength dependent structure observed in the masterflats

was also removed; it seems to be characteristic to the flat-field and it was not found in all the stellar or galaxies' spectra. The different temperatures between the lamp and the observed astronomical sources could be a reason for this difference. A careful normalisation was applied by fitting a 15-piece cubic spline function along the dispersion direction (`IRAF` task *response*). Extreme care was taken in fitting only the large-scale features of the flats in order not to introduce artificial features in the science data. The resulting fits produced excellent results along the spatial direction of the CCDs (columns) and the resulting normalised masterflats were confidently applied.

At this stage, the previous corrections were applied to each exposure of the scientific data by using the task *ccdproc*: the masterbias was subtracted, bad pixels and cosmic rays were interpolated using masks, geometrical distortion corrections were applied and finally, the images were divided by the (corrected) masterflat.

2.1.6 Combining different exposures

When more than one exposure was obtained for a galaxy (see Table 2.1), the individual spectral images of each chip were combined to maximise the signal-to-noise ratio. Before combining them, the position of each galaxy's spectrum and the locations and widths of several sky lines were checked and compared between the different exposures. For all our sample, the match between them was found to be excellent within a small fraction of a pixel (~ 0.6 pixel on average), so no further alignment was necessary prior to combination.

Then, chips 1 and 2 were combined in a single spectrum. According to the FORS2 manual, a gap of $480\,\mu m$ (or 32 pixels) separates both chips in the spatial direction, while a 2 pixel shift is present in the dispersion direction. From the lower edge of chip 1 and the upper edge of chip 2, about 10 additional pixels were trimmed in order to avoid edge effects (such as ripples) along the spatial direction of the combined spectra. Special attention was put on checking the common zero-count level for both chips, given that the sky must be subtracted in the following steps (see Sec. 2.1.8). To estimate the appropriate relative number of counts in both sides of the gap, 4 bands 200 pixels wide (dispersion direction) and 10 pixels long (spatial direction) were selected on both sides of the gap and put along the wavelength direction, having pairs of bands at the same wavelength range in both sides of the gap. The mean pixel values within each band was compared to its pair equivalent and no strong variations were found along the dispersion axis in terms of relative difference in count level. The gaps were located far from the luminosity peaks of the galaxies, where count levels range between 5 and 20 depending on the observed object. In consequence, pairs of bands did not present strong variations on their relative count numbers, usually ranging between 1 and 5 counts. Having these values, they were compared to equivalent twin-mirror-bands results, symmetrically located in the other spatial side of the spectra (chip 1) using the luminosity peak of the galaxies' profile as point of symmetry. The agreement between both sides was excellent in all cases. Only in few cases an adjustment of chip 2 with respect to chip 1 was applied, by adding or subtracting 3 or 4 counts from chip 2. In any case,
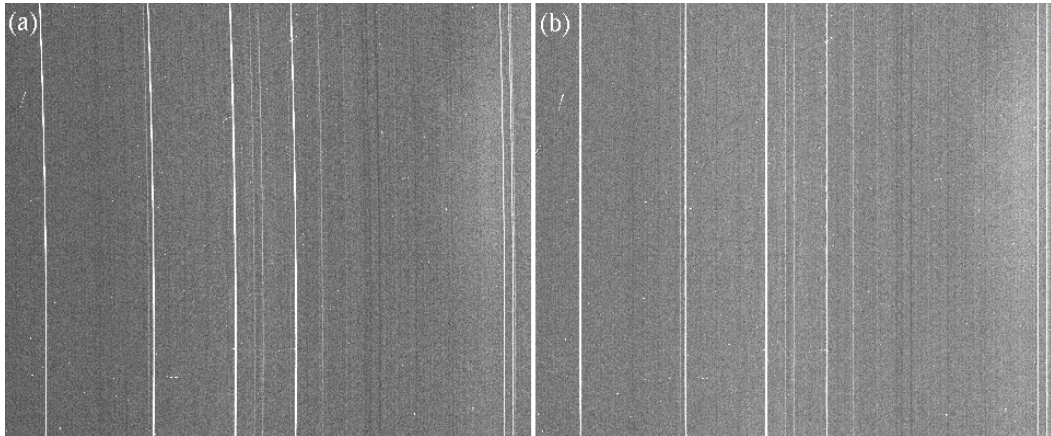
Figure 2.2. Section of He-Ne lamp spectrum before (a) and after (b) wavelength correction.

the corrections were small enough to be confident on the sky level of the combined spectra. From the combined image, some columns and rows were trimmed: along the lateral edges and bottom of chip 2, to compensate the horizontal shift (2 pixels) between the chips and to remove rows with no spectrum, respectively. From this point, we work with one 2-dimensional spectrum for each galaxy.

2.1.7   Wavelength calibration

To put the spectra on a wavelength scale, previously reduced He–Ne lamp spectra were used. The lamp's prototype spectrum and exact wavelengths of the spectral features are provided in the FORS2 manual. Using the task *identify* a few of the lamp spectral lines were identified along the central row, providing a few points for the dispersion solution function. The remaining spectral features were automatically identified by iteration, changing the fitting polynomials and its orders and minimising systematic residuals of the fit. Using the solution for the central row as a guide, the task *reidentify* found the same features along the spatial direction, fitting new dispersion functions or determining zero-point shifts. The task *fitcoords* fits a 2-dimensional function from pixel coordinates to wavelength. In general, Chebychev polynomials of orders 4 and 2 (in dispersion and spatial directions, respectively) provide a good fit. As a test, the solution was applied to the lamp spectra and an example is presented in Figure 2.2. Given the excellent quality of the results, the science and stellar-calibration data was transformed with the same solutions using the task *transform*. The original dispersion of the spectra was $0.318\,\text{Å}/\text{pixel}$ and it was imposed during the wavelength calibration process. Flux conservation and linear interpolations were also applied during the transformation. The residuals of the wavelength fits were typically $0.1\text{–}0.2\,\text{Å}$.

2.1.8   Sky subtraction

The sky background was subtracted using the `IRAF` task *background*. Two regions free of signal from the astronomical source were selected, typically 100 pixels wide in the spatial direction and close to the edges of the image. The sky level was removed
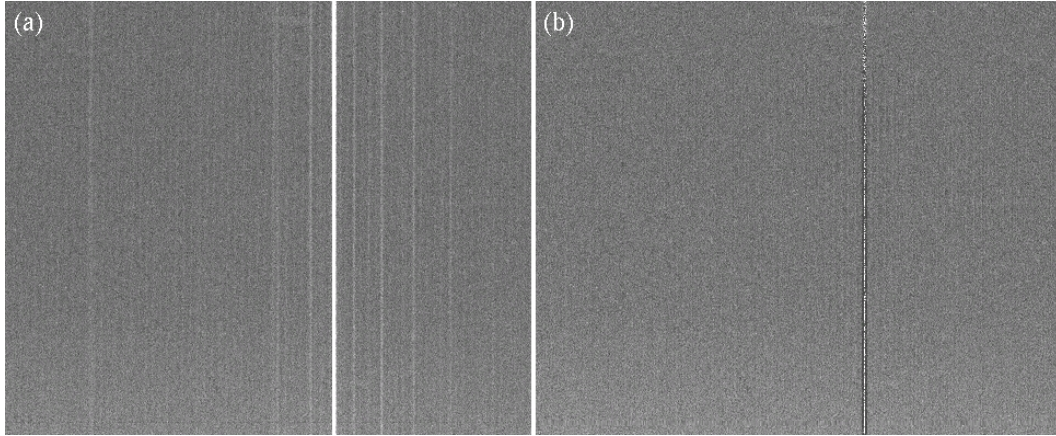
Figure 2.3. Section of galaxy spectrum before (a) and after (b) sky subtraction. Some structure is seen for the strong sky-line ([O$_I$] at 5577 Å) because its profile is undersampled by the pixel scale.

by fitting a first order function to each spatial column defined in the sky-bands, interpolating and subtracting the fits from the data. In the case of NGC 1316, the largest and brightest galaxy, two sky region in chip 2 were used because the galaxy centre was placed close the upper edge of chip 1 to maximise the spatial coverage. An example of the result is presented in Figure 2.3. The extraction of strong sky-lines produce higher noise levels, given the undersampling of the sky-line profile by the pixel scale. In any case, these regions are not considered for any further calculation of kinematics/line indices (see section 2.2 and Chapter 3).

2.1.9 "Hum″ removal

A periodic, square wave noise pattern or 'hum' was present along the dispersion direction in all the spectra. The amplitude of this hum varied from 3 to 6 counts, and its frequency, 0.077 cycles/pixel, was reasonably constant, with some deviations mainly due to previous data processing. Because this pattern could partially mask the spectral features at low S/N (affecting the kinematics and line indices), it should be removed or at least decreased. The signal presents a shift in the dispersion direction along the CCD which explains why the pattern could not be eliminated during the sky subtraction. Given this shift and variations in amplitude, there is not a reliable subtraction method applicable in pixel space (i.e. fitting the pattern). Finally, it was decided to use a Fourier technique (Brown 2001) developed for the B-side of HST spectrograph, STIS, which suffers from the same problem. Dr. Paul Barrett (STIS Team) provided constant support and suggestions during the process. Ideally, one would apply this technique to the raw data frames, but the low level of the signal implies that it could only be reliably identified and removed after sky subtraction. The specially developed package of `IRAF` routines *STSDAS/fourier* was used and the process is summarised below:

- The Fourier Transformation (FT) of the 2-dimensional spectra was computed using the task *forward*, producing two images: the real and imaginary part of the FT. These two images were in frequency space instead of pixel space.
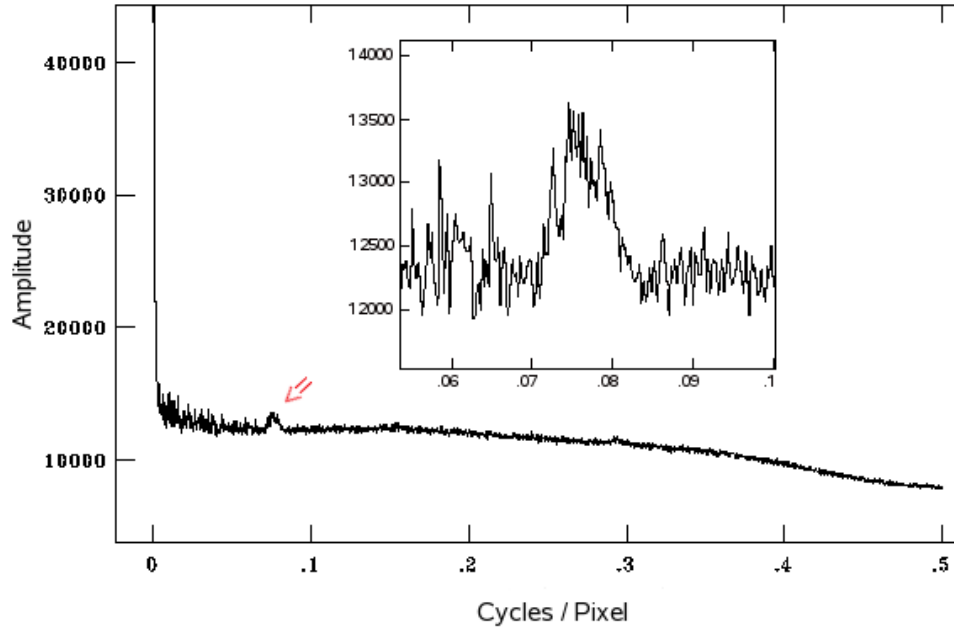
Figure 2.4. Example of *amplitude* image. 1-D cut showing a zoomed-in section truncated at 0.5 cycles/pixel (complete image is symmetric between 0 and 1 cycles/pixel). Frequencies affected by hum are pointed with red arrow and zoomed-in in internal panel.

- Using *topolar* those images were transformed into *amplitude* and *phase* images. In Figure 2.4 a cut along the frequency axis for an *amplitude* image is presented. The small lateral peaks in amplitude corresponding to the frequencies of the hum are clearly identifiable.

- Because of the previous data reduction processing the frequencies affected range between 0.072 and 0.085 cycles/pixel. The amplitude of the frequencies affected was diminished by using a smoothed box-shape function in the affected regions of the *amplitude* image.

- Finally, the spectra were transformed back to pixel space using the tasks *frompolar* and *inverse*. In Figure 2.5 we can see a section of a 2-dimensional spectrum, before and after the correction. The amplitude of the hum clearly decreases. No signs of ringing effects were observed in any galaxy spectrum after the correction.

For this procedure, it was not recommended to use any *windowing* technique[1] because the resulting decrement in amplitudes made it very difficult to identify the affected frequencies in the *amplitude* image. Inspection of the resulting cleaned images and tests during the extraction of the kinematics showed that this processing had no adverse impact on our ability to remove this source of systematic noise.

---

[1]Modulating pixel values in such a way that they fall smoothly to zero at the edges of the image; i.e. convolving the data with a 2-dimensional gaussian.
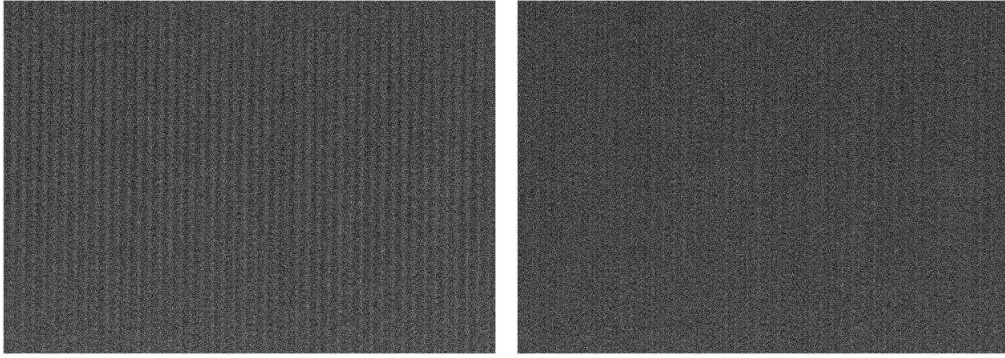
Figure 2.5.   Right: section of 2D spectrum of NGC 1380; Left: same section after decreasing the amplitude of the hum.

2.1.10   Binning the spectra

The calibrated 2-dimensional galaxy spectra were binned along the spatial direction so as to generate 1-dimensional spectral bins at different radii with comparable signal-to-noise (S/N) ratios. To calculate the S/N, the so-called "CCD Equation" was used, for which the general form is

$$\frac{S}{N} = \frac{N_*}{\sqrt{N_* + n_{pix}(N_S + N_R^2)}},\tag{2.1}$$

where N_* is the total number of photons collected from the object of interest, n_{pix} is the number of pixels under consideration for the S/N calculation, N_S is the total number of photons per pixels from the background or sky and N_R is the total number of electrons per pixel resulting from the read noise.

Adjacent galaxy spectra were co-added to a desired S/N, starting from the row corresponding to the luminosity-profile peak of the galaxy. The S/N applied was 53 per Å (or 30 per pixel). When the outer parts of the CCD were reached and no more bins with that S/N could be built, the S/N was reduced to 30 per Å and the binning restarted from the first row of the last bin. In the same way the S/N was subsequently reduced to 15 and 10 and farther bins were calculated. The assigned radial distance for each bin was defined by the pixel where the total number of counts is split in half. An illustrative diagram of the binning process is presented in Figure 2.6.

2.1.11   Atmospheric Extinction correction and Flux calibration

To correct for the effect of atmospheric extinction, the `IRAF` task *setairmass* was used to define the effective airmass for each spectrum. Then, the extinction correction was applied by using an appropriate atmospheric extinction table (wavelength versus extinction in magnitudes per airmass, see ESO website) and the task *calibrate*. The spectra were subsequently flux calibrated using the set of spectrophotometric standard stars listed in Table 2.2, which allowed the transformation of the observed counts into relative spectral fluxes as a function of wavelength. The sensitivity functions as derived from the different stars varied by typically $\sim 1\%$, reaching
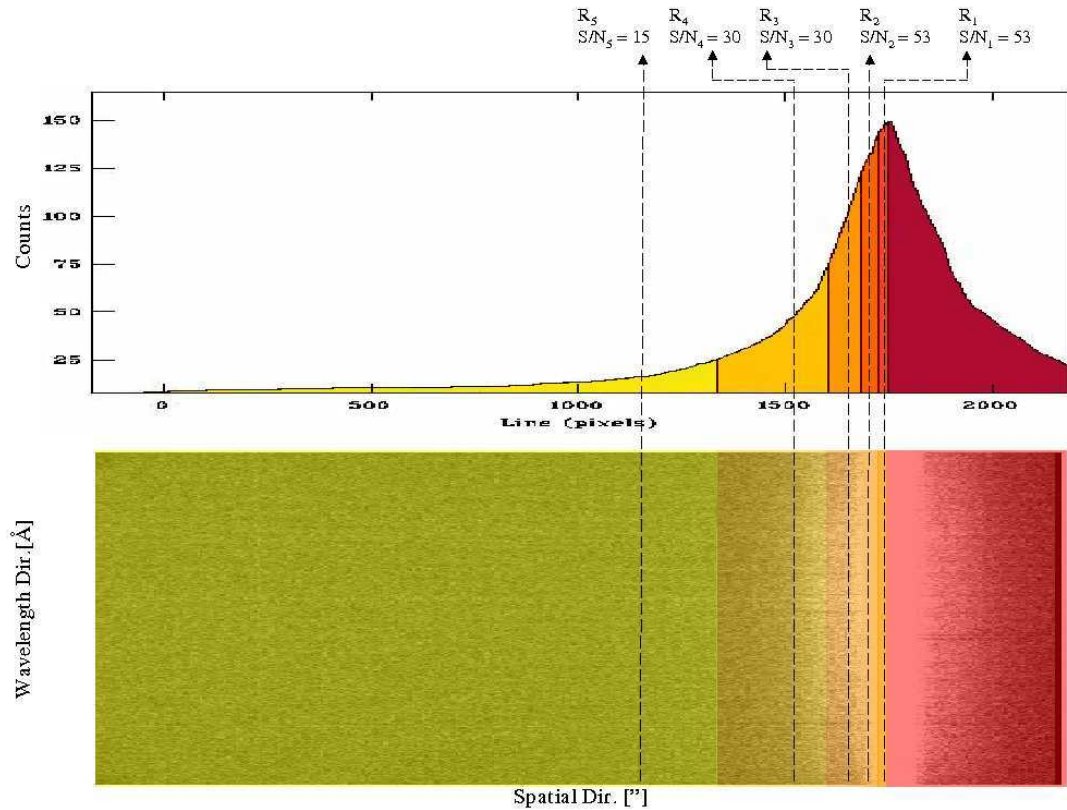
Figure 2.6. Diagram of binning process along radius. Top: luminosity profile of a galaxy along the slit. Bottom: the corresponding 2-dimensional spectrum. The left-hand side of the profile is binned using different S/N ratios (decreasing as radius increases). Some illustrative bins are shaded in colours from yellow to orange. Dashed arrows mark the assigned radius for each bin.

$\sim 3\%$ towards the edges of the wavelength range. In consequence, a single sensitivity function was created from all of them. All spectra of galaxies and template stars (see Table 2.2) were divided by their exposure times, and finally transformed using the sensitivity curve. The tasks *standard*, *sensfunc* and *calibrate* were used in this part of the reduction. Examples of central galaxy's spectra are presented in Figures 2.7 and 2.8.

2.2   Extraction of the kinematics

In the present study, the kinematic properties of the galaxies were derived using the Penalised Pixel Fitting method (pPXF, Cappellari & Emsellem 2004), which is a parametric technique based on maximum penalised likelihood. Since the resulting kinematic parameters are so central to this work, the workings of this method as they apply to the current dataset are described, as well as the test undertaken to check the reliability of the resulting parameters. All data were re-binned to a logarithmic wavelength scale in the dispersion direction to enable the kinematic measurements.

The parametric method used by pPXF models the line-of-sight velocity distribution (LOSVD) as a Gaussian plus a series of Gauss-Hermite polynomials. The

Table 2.2. Spectrophotometric (S) and Template (T) Stars.

Name	T/S	Spectral Class
BD-01-0306	T	G1 V
HD1461	T	G0 IV
HD7565	T	K2 III-IV
HD16784	T	G0 V
HD18234	T	K0
HD19170	T	K2
HD21197	T	K5 V
HD23261	T	G5
HD36395	T	M1.5 V
HD61606	T	K2 V
LTT1020	S	–
LTT1788	S	–
LTT3218	S	–
HZ4	S	–
GD71	S	–
Feige67	S	–

fits return the mean line-of-sight velocity, V_{LOS}, and the velocity dispersion, σ, from the Gaussian, together with the h_3 and h_4 coefficients from the polynomials. These two coefficients are related, respectively, to the skewness and the kurtosis of the LOSVD, which are higher moments associated with the asymmetric and symmetric departures of the LOSVD from a Gaussian.

This software works in pixel space, finding the combination of template spectra which, when convolved with an appropriate LOSVD, best reproduces the galaxy spectrum in each bin. A subroutine of the program fits the continuum, using Legendre polynomials of order 4 (in this case), and divides the spectra by the fit to remove any possible low-frequency mismatches between the galaxy spectra and the model. The method carries out a pixel-by-pixel minimisation of the residuals (quantified by χ^2), adding an adjustable penalty term to the χ^2 to bias the resulting LOSVD towards a Gaussian shape when the higher moments h_3 and h_4 are unconstrained by the data. Thus, a deviation D of the LOSVD from a Gaussian shape will be accepted as an improvement of the fit only if it is able to decrease the residuals by an amount

$$\chi_p^2 = \chi^2(1 + \lambda^2 \cdot D^2). \tag{2.2}$$

The λ parameter defines the threshold between a deviation considered as an improvement of the pure Gaussian fit, and one considered as due to noise, and thus rejected. As Cappellari & Emsellem (2004) suggest, the value of λ has to be determined for each particular dataset because the ability of the software to find the correct LOSVD parameters (especially the higher moments) will depend critically on the S/N of the data and other properties of the particular spectra such as the spectral range covered. To estimate the optimum parameter for this study, Monte-Carlo simulations were performed in which the template spectra were convolved with a LOSVD whose shape was specified by model parameters V_{in}, $h_{3\mathrm{in}}$ and $h_{4\mathrm{in}}$, and whose width was
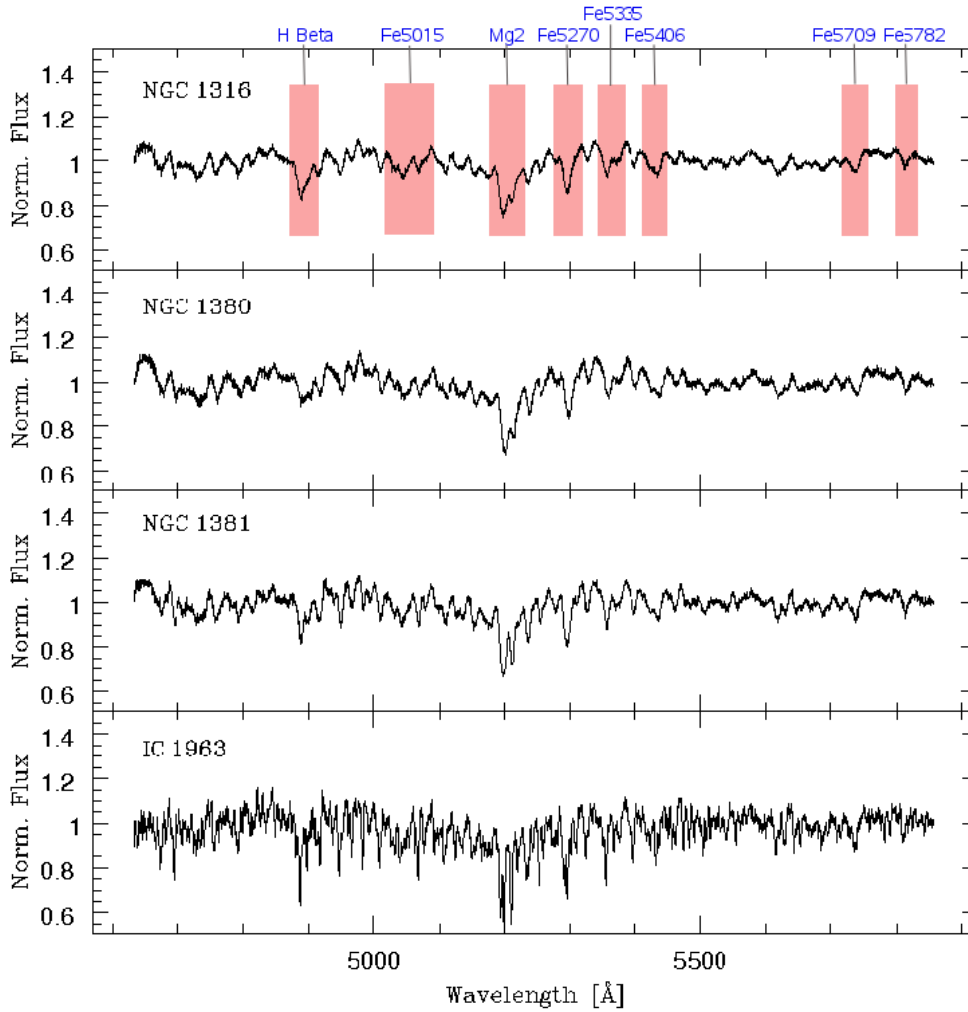
Figure 2.7. Normalised central spectrum of NGC 1316, NGC 1380, NGC 1381 and IC 1963. Characteristic spectral features are highlighted in red, labeled with Lick spectral indices.

allowed to vary such that $0 < \sigma_{in} < 250\,\mathrm{km\,s^{-1}}$. These spectra, degraded to the S/N of the various 1-dimensional galaxy spectra, were then passed through the pPXF software to recover estimates for the parameters, V_{out}, σ_{out}, h_{3out} and h_{4out}. An example of one such run is presented in Figure 2.9. After extensive testing using a variety of input parameters and S/N, $\lambda = 0.3$ was found to provided an optimum value for the spectra in the current dataset, yielding values that minimised both errors and bias in the results.

Having derived the optimum λ, the kinematic parameters were extracted from the galaxies' spectra. Three spectral regions were excluded from the minimisation process: ~ 30 pixels around $5577\,\text{Å}$ corresponding to residuals of a strong sky-line, and two wavelength bands including the Hβ and $[\mathrm{O_{III}}]_{\lambda5007,\lambda4959}$ typical spectral ranges. If weak nebular emission is present, these features cannot be properly modeled with the template stars' spectra.

As it is apparent from Figure 2.9, even at this fairly modest value for the λ parameter, a degree of bias appears in the answers at low dispersion, particularly
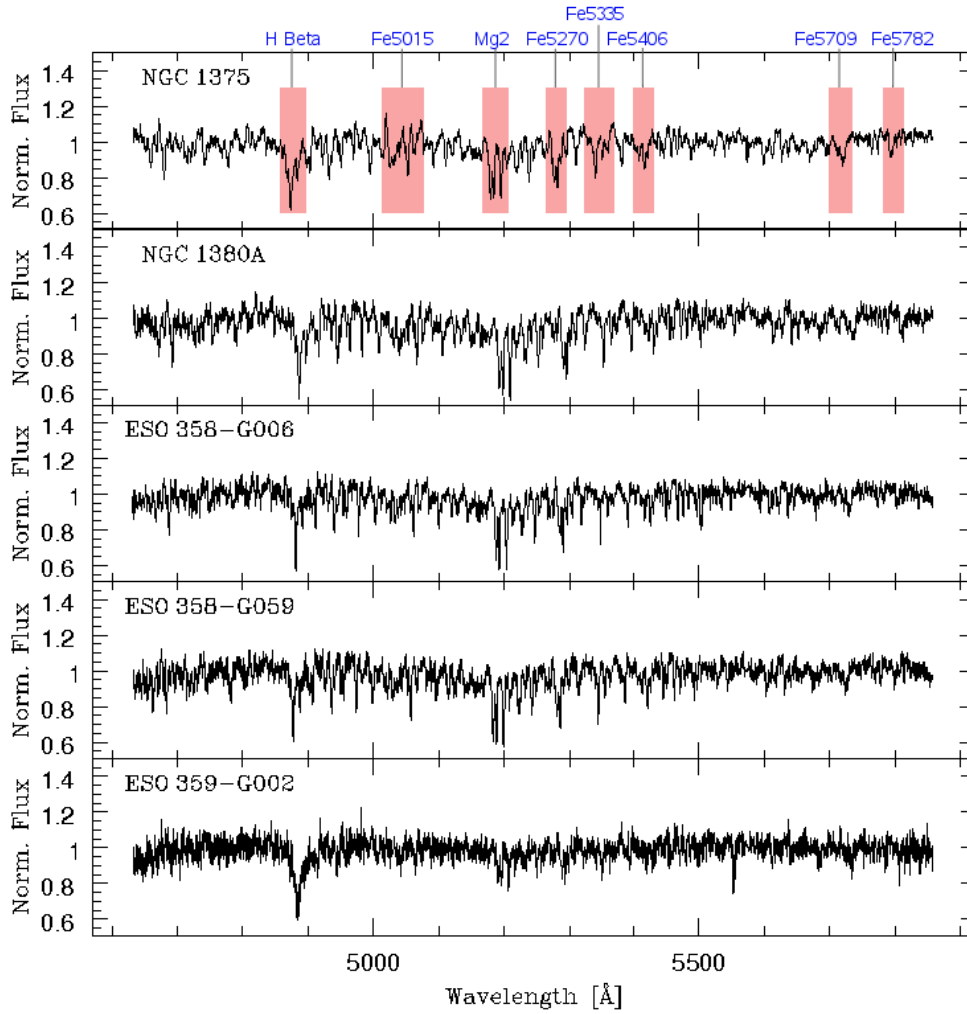
Figure 2.8. Normalised central spectrum of NGC 1375, NGC 1380A, ESO 358-G006, ESO 358-G059 and ESO 359-G002. Characteristic spectral features are highlighted in red, labeled with Lick spectral indices.

in the derived values of σ and h_4. This kind of bias, particularly prevalent in such even moments, is a well-known phenomenon (e.g. Cappellari & Emsellem 2004). Clearly, it is necessary to understand and possibly to correct for this effect before interpreting the calculated parameters.

2.2.1 Bias study in pPXF Kinematics

The results obtained with pPXF software (V_{LOS}, σ, h_3 and h_4) were subject to a bias study and correction (when necessary) in order to obtain accurate measurements of the kinematic parameters. The ideal approach to this problem is to study the variations of each individual parameter with respect of the other 3 via Monte-Carlo simulations (MCS), creating a covariance matrix for each different S/N of the data. However, in practice, it would be a very time consuming procedure (because of the number of MCS needed) and also impractical, considering what is already known
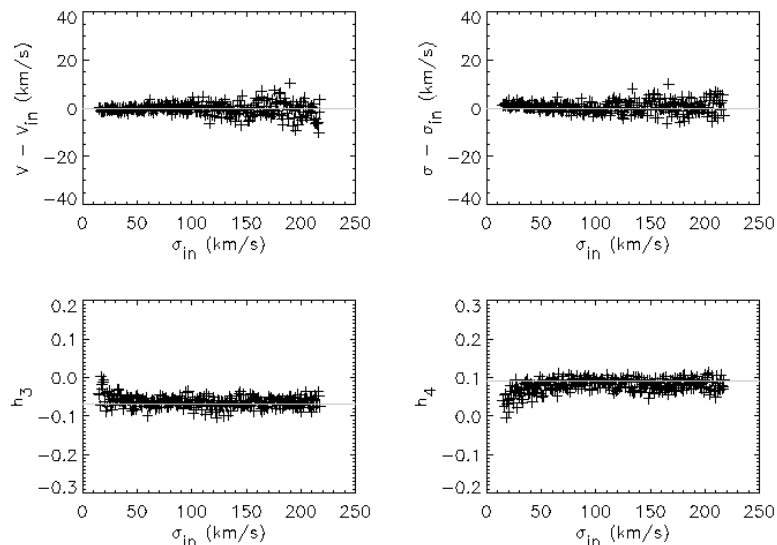
Figure 2.9. Sample 1000 pPXF simulations carried out in order to find the optimum value of the λ parameter for this dataset. In this particular case, the simulated spectra have S/N = 53 and λ has been set to 0.3. The model LOSVD has $V_{\text{in}} = 0$, $h_{3\text{in}} = -0.07$, $h_{4\text{in}} = 0.09$ and the derived values of V_{out}, $h_{3\text{out}}$ and $h_{4\text{out}}$ are shown for different values of σ_{in}.

about the covariance of these 4 parameters. As is pointed out in Cappellari & Emsellem (2004), the strongest anti-correlation between parameters (at low S/N) takes place in the pairs V_{LOS}-h_3 and σ-h_4. In datasets which cannot constrain properly the parameters, the first pair can describe the asymmetric deviations from a Gaussian distribution (with values of h_3 different from 0 or shifting the velocity peak of the distribution), while the second pair can describe the symmetric deviations from gaussianity (with values of h_4 different from 0 or increasing-decreasing σ). Using low S/N data, the situation is more delicate for the pair σ-h_4, mainly because the physical moments μ_k (μ_3 and μ_4 are related to the Gauss-Hermite coefficients h_3 and h_4) are proportional to $(V_i - \langle V \rangle)^k$, where $\langle V \rangle$ is the mean velocity of the distribution (Binney & Merrifield 1998). Such a dependence implies that high moments, like the one described by h_4, will depend strongly on the values far from the centre of the distribution (the wings), where a poor S/N hardly describes it with accuracy. Considering this dependence on "the wings", parameters like h_4 will also be more sensitive to errors in the subtraction of the continuum. The whole picture shows us that we could expect a bias in the values of σ and, mainly, in h_4, if our data is too noisy.

The present bias analysis is focused in the pair σ-h_4 only. Because of the much greater dependence of this pair on the S/N, it is better to be sure that velocity dispersions, σ, are accurate, in order to be used in the analysis of the kinematics and line index calculations. The objective is to estimate an error associated to the bias for both parameters and also, if necessary, to correct such values between certain margins of confidence. The errors associated to this procedure will take into account the uncertainties produced by the anti-correlations between σ-h_4 and the

remaining two moments, $V_{\rm LOS}$ and h_3. The correlation of σ and h_4 with the odd moments is expected to be much less important.

The Models

First, MCS were run, creating models which will be compared to the kinematical parameters extracted from real data (using pPXF). The starting point is the MCS code which comes with the pPXF package. Basically, this code produces artificial data using the template stars and adding the required noise (in our case, to reach S/N= 10, 15, 30 and 53 per Å). An example is presented in Figure 2.9. The user specifies a LOSVD, via the parameters $V_{\rm LOS}$, h_3 and h_4 (hereafter, $V_{\rm in}$, $h_{3\rm in}$, $h_{4\rm in}$). Because we are interested in studying σ-h_4 only, we set $V_{\rm in} = h_{3\rm in} = 0$. Some tests using non-zero values of $V_{\rm in}$ and $h_{3\rm in}$ were run, and no major differences were found in the results of this procedure. On the other hand, for each S/N, values of $h_{4\rm in}$ between -0.25 and 0.30 were chosen in steps of 0.05, giving a total of 12 runs of the simulation for each S/N. The code convolves the spectra with the LOSVD, using different values of σ ($\sigma_{\rm in}$, running 200 iterations with $\sigma_{\rm in}$ values between 20 and $260\,\mathrm{km\,s^{-1}}$) and then it recovers the kinematic parameters using the normal pPXF routine (the output parameters are $V_{\rm out}$, $\sigma_{\rm out}$, $h_{3\rm out}$, $h_{4\rm out}$). In this way, we can check how good the extraction of the kinematics is, for a certain S/N, as a function of σ. As an example, in Figure 2.10 the plots $\sigma_{\rm in}$ vs $\sigma_{\rm out}$ and $h_{4\rm out}$ vs $\sigma_{\rm in}$ are presented for a run using S/N=10 and $h_{4\rm in} = 0.30$. A total of 12 plots like these (using different $h_{4\rm in}$) were created for S/N=10, as well as for the other S/N of 15, 30 and 53. In Figure 2.11 (*a* and *b*) the corresponding 12 fits are presented in the case of S/N=10. For each S/N, the polynomials obtained in the fits define our models and, in the next step, real data values are going to be compared with these results.

Calculation of the biases

At this stage, the bias in the kinematical parameters extracted with pPXF from real data (for us, $\sigma_{\rm ppxf}$ and $h_{4\rm ppxf}$) were studied and some corrections were applied. The correction process (in this example using S/N=10) includes the following steps for each galaxy bin:

- The value of $\sigma_{\rm ppxf}$, which is a particular $\sigma_{\rm out}$ from pPXF, was used as input for the equations plotted in Figure 2.11(*a*). It means that for each $\sigma_{\rm ppxf}$ we obtain 12 possible values of the "real" $\sigma_{\rm in}$ (hereafter, $\sigma_{\rm inFit}$).

- Having the 12 $\sigma_{\rm inFit}$, we use the equations plotted in Figure 2.11(*b*) in order to associate each $\sigma_{\rm inFit\it{i}}$ with 12 possible values of $h_{4\rm out}$ (hereafter, $h_{4\rm outFit}$).

- Remembering that each of the curves in Figure 2.11(*b*) comes from an original input value of $h_{4\rm in}$ equal to -0.25, -0.20,..., 0.30, we can plot for each $\sigma_{\rm inFit\it{i}}$ 12 points in the plane $h_{4\rm in}$ vs $h_{4\rm outFit}$. These 12 sets of 12 points each were fitted using a polynomial of order 3. As an example, we present in Figure 2.12(*a*) the 12 fits together for a S/N=10.
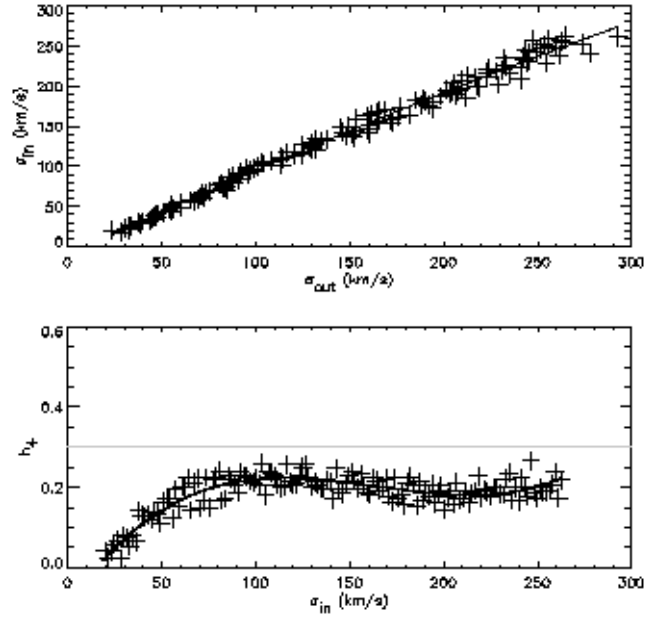
Figure 2.10. Example of one simulation, using $h_{4in} = 0.3$ and S/N=10. Top: σ_{in} vs σ_{out}; continuous line corresponds to best-fit polynomial of order 2. Bottom: h_{4out} vs σ_{in}; straight line is the original h_{4in} value; continuous curve is the best fit, using polynomial of order 3.
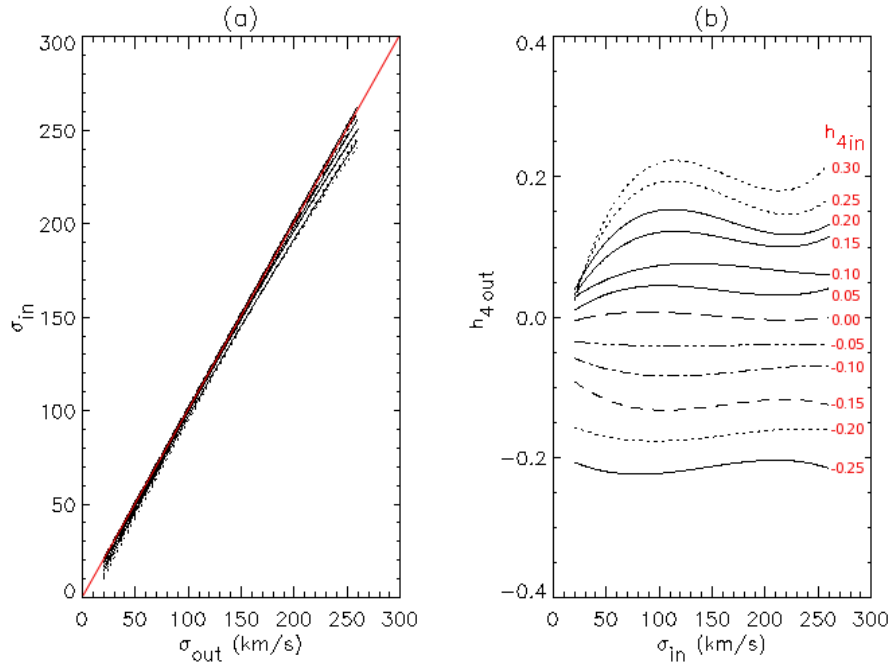
Figure 2.11. All simulations (fittings) for S/N=10 using 12 different values of h_{4in} (a): σ_{in} vs σ_{out}.(b): h_{4out} vs σ_{in}.
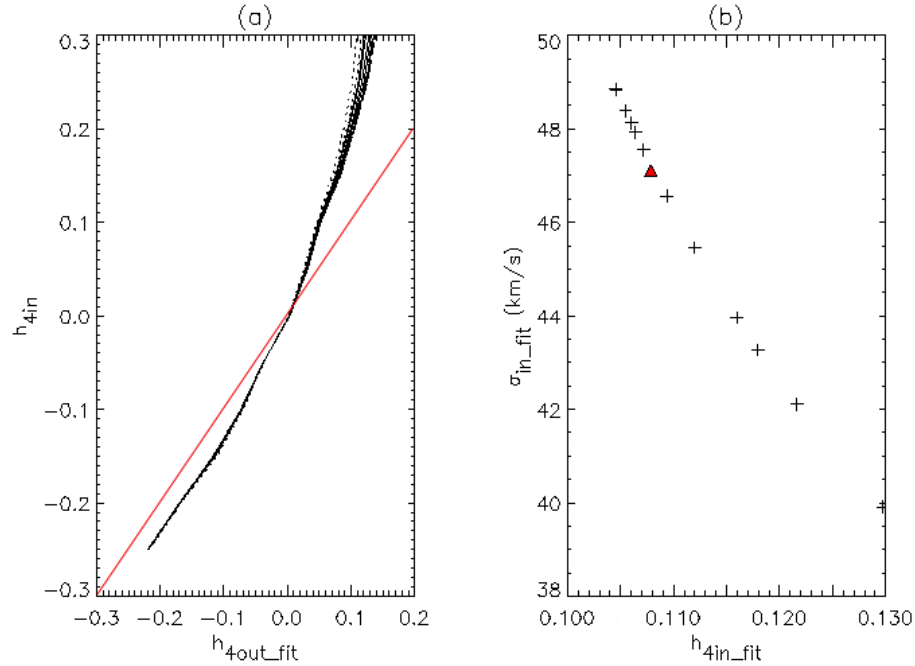
Figure 2.12. (*a*): $h_{4\text{in}}$ vs $h_{4\text{outfit}}$ of our models, using data bin with S/N=10. Twelve curves are overplotted, corresponding to each σ_{infit} value. (*b*): Final σ vs h_4 possible values for this bin. Crosses are the individual values, triangle is the weighted mean value.

- Having the fits in Figure 2.12(*a*), we assume that they are a good representation of the "real" σ_{in} relation between $h_{4\text{in}}$ vs $h_{4\text{out}}$, which is reasonable considering how good the fits are in figures like 2.12.

- Now, we use $h_{4\text{ppxf}}$ (from real spectrum) as an input for the fits in Figure 2.12(*a*). Because we have 12 functions we will have 12 possible values of $h_{4\text{in}}$ (hereafter $h_{4\text{inFit}}$), each one related to one specific value of σ_{inFit}.

- In this way, we can plot Figure 2.12(*b*), which shows a range of "real" σ_{in} pairs of parameters (σ_{inFit}, $h_{4\text{inFit}}$) from the source (crosses in figure) associated to the measured ones (σ_{ppxf}, $h_{4\text{ppxf}}$).

- Finally, histograms for σ_{inFit} and $h_{4\text{inFit}}$ were created in order to weight each data-point and calculate a weighted average of these parameters, obtaining a σ_{ppxfCorr} and a $h_{4\text{ppxfCorr}}$ (triangle in Figure 2.12(*b*)). One sigma errors were estimated from these values assuming that our sample of points in Figure 2.12(*b*)) is a good representation of all the distribution.

The conclusion from this study is that the bias in σ is small and well-defined at a maximum level of ± 2–$3\,\text{km}\,\text{s}^{-1}$; the results were corrected for this bias, but it makes no substantial difference. The case for h_4 is a little more disturbing, as this parameter, particularly in galaxies with low values of σ, can suffer significant bias, amounting to offsets as high as 0.4 in the most extreme cases. The uncertain nature of this bias means that h_4 was not corrected for it explicitly in our final derived value, and we would caution against interpreting the h_4 values as too precise,

particularly from spectra where S/N is low and where σ is small. Nonetheless, this study does demonstrate that the principal parameters of interest, V_{LOS} and σ, are robustly extracted from spectra of the quality that we present here, irrespective of the detailed shape of the LOSVD as specified by h_3 and h_4.

2.2.2 Errors in the Kinematics

To estimate the errors on the derived parameters for each 1-dimensional galaxy spectrum, further series of MCS were run. Each such spectrum was modeled using the corresponding best combination of template stars, broadened by the best-fit LOSVD, and degraded to the S/N of the galaxy data. These model spectra were then passed through the pPXF software to measure the distribution of the derived parameters, and hence a measure of the uncertainty in a single spectrum. The dispersion in the parameters derived in each Monte Carlo simulation is quoted as the error bar on the corresponding parameter derived for the real galaxy spectrum. The uncertainties from the bias study were also considered for σ, but it made no substantial difference.

Before presenting the final dataset of kinematic parameters versus distance along the major axes for these S0 galaxies, the only remaining issue is to define the zero-points of velocity and position for each galaxy. The velocity zero-point was simply set to the median value of V_{LOS} determined along the slit for each galaxy. For the spatial zero-point – the galaxy's centre – the simplest definition would just be the point along the slit that admitted the greatest amount of light. However, this definition could well pick up on an off-centre localised feature that would then distort the over-all kinematic structure of each galaxy that is the primary goal of this study. Instead, the adopted spatial origin was the position along the slit that renders the plot of V_{LOS} versus radius as close to anti-symmetric as possible. The only case where this method was not applied was NGC 1316; the large size of this system meant that the slit was primarily placed to cover only one side of the galaxy, so it was not possible to subtract the median velocity along the slit nor match up the two sides of the rotation curve to find the kinematic centre. For this galaxy, the point along the slit with the largest value of σ was chosen to define the spatial location of the galaxy's centre, and then used the value of V_{LOS} at this point to specify the galaxy's systemic velocity.

2.3 Results and comparisons with literature

The values for the kinematic parameters V_{LOS}, σ, h_3 and h_4 versus radius, as derived using the analysis set out in Section 2.2, are presented in Appendix A.

A number of these galaxies have been studied previously with lower quality spectra or less sophisticated spectral analyses, so as well as presenting the results some comparisons were made to these published data. The most extensive study for comparison is that of D'Onofrio et al. (1995), who obtained major-axis kinematics (V_{LOS} and σ) for six galaxies in common with the current sample. One complication in comparing their data with the new observations is that they presented the kinemat-
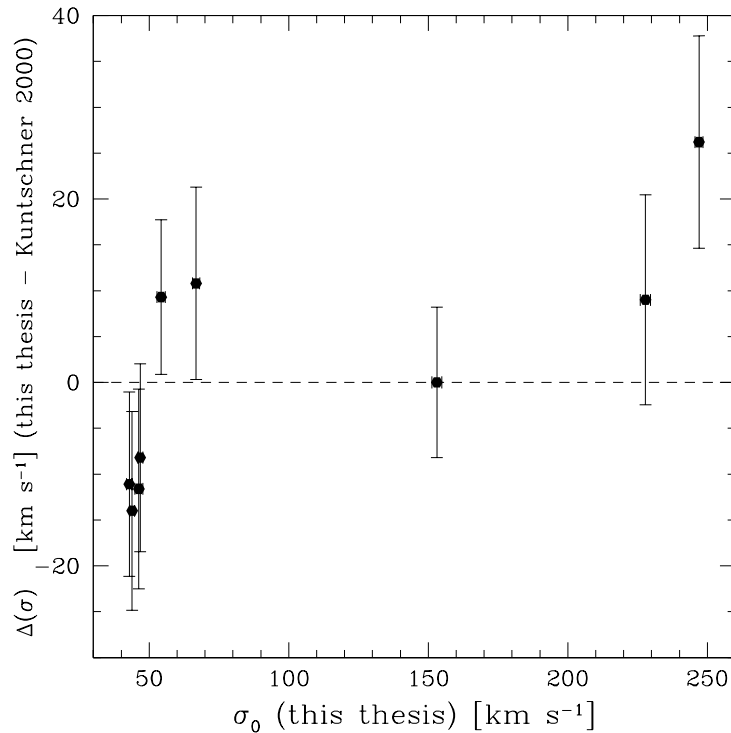
Figure 2.13. Comparison of our central velocity dispersions (σ_0) with Kuntschner (2000).

ics folded about the centre of each galaxy, leading to an ambiguity in the actual spatial location of each measurement. Therefore it was not possible to match up individual features that occur on one side of a galaxy, but one can use these data to examine the overall profile. The other limitation of their data was its relatively low spectral resolution ($\sim 60\,\mathrm{km\,s^{-1}}$ in velocity dispersion), which, as we will see, introduces a significant bias into the kinematics. Further long-slit data for single galaxies in the current sample can be found in Graham et al. (1998) and Longhetti et al. (1998), so these data were also included in the comparison. There are also a number of measurements of the central velocity dispersion that provide a single comparison point. Kuntschner (2000) obtained central dispersions for all the galaxies in this sample, although he warns that the relatively low spectral resolution of his data, corresponding to a velocity dispersion of $\sim 50\,\mathrm{km\,s^{-1}}$, mean that the measurements should only provide a rough guide for the fainter galaxies. Further measurements can be found in the compilation of Bernardi et al. (2002), although the variety of sources from which these data were drawn mean that their reliability is less assured than in the other measurements.

As a first comparison with literature, Figure 2.13 confronts the central velocity dispersions from Kuntschner (2000; σ_{K00}) with the measurements based on our new data (σ_0). σ_0 corresponds to the mean, S/N-weighted, velocity dispersion for all the bins within $1/8$ of the effective radius of the bulge (R_e, see Table 2.3). In general, there is good agreement between the two datasets, with differences being consistent with zero within $\sim$ 1-sigma uncertainties. The observed discrepancies

might be partially attributed to the different apertures used by Kuntschner (constant effective aperture off $2.''3 \times 3.''85$) in comparison to ours ($0.''5 \times R_{\mathrm{e}}/8''$) and, as we already mention, Kuntschner data may suffer of some resolution issues at low velocity dispersion. These two effects are not quantified in the error bars.

2.3.1 Results for individual galaxies

In the following paragraphs brief descriptions of the observed kinematics are given for each individual galaxy. These results are also compared to previous studies from literature.
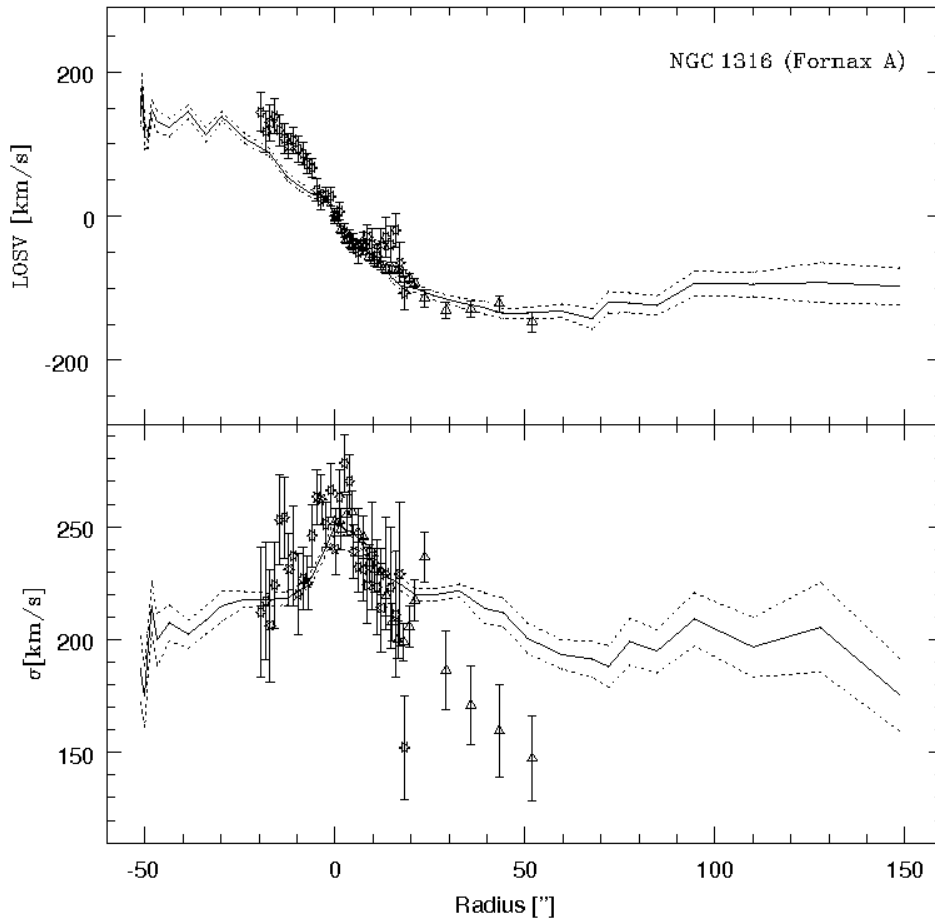
Figure 2.14. Comparison between the new results for mean velocity, V_{LOS}, and velocity dispersion, σ, and kinematics from the literature for NGC 1316. The new results are shown as a continuous line with 1σ errors as short dashed lines. The D'Onofrio et al. (1995) data are shown as triangles, the Longhetti et al. (1998) data are shown as stars, and the Graham et al. (1998) data are shown as squares. Horizontal dashed lines in the velocity dispersion plots indicate the resolution limit of the archival data.

NGC 1316 (FORNAX A)

For this well-known merger remnant, Figure 2.14 reveals good agreement with the published results within a central raduis of ~ 20 arcsec. At larger radii, however, the new results are in conflict with D'Onofrio et al. (1995) and Longhetti et al. (1998) data, indicating a rather higher dispersion than in the previous measurements. The lowest S/N of the older observations may explain the difference. The more extended velocity dispersion profile from the new data for the first time reveals a seemingly-distinct feature of enhanced dispersion within the central 15 arcsec. In this galaxy, as might be expected in a merger, random motions dominate out to large radii in the new data, bringing into question whether this galaxy should really be classified as an S0 system.
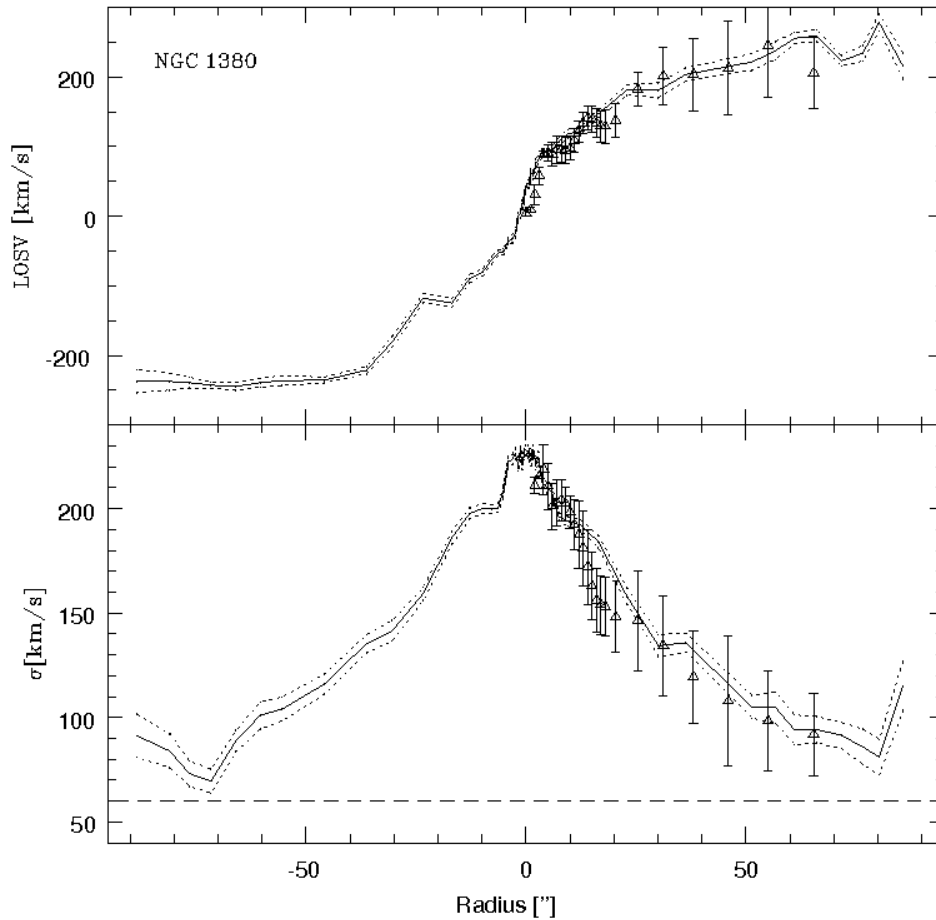
Figure 2.15. Comparison between the new results for mean velocity, V_{LOS}, and velocity dispersion, σ, and kinematics from the literature for NGC 1380.

NGC 1380

Figure 2.15 shows that the new data agree extremely well with the previous observations, but with much improved error bounds. The new data with their smaller errors and unfolded presentation give some indication of localised substructure that differs between the two sides of the galaxy. An enhancement in velocity dispersion within the central ~ 7 arcsec, first suggested by D'Onofrio et al. (1995), is strongly confirmed with the new data. It is also notable from Figure A.2 that this region also shows structure in the h_3 skewness measure, indicative of a distinct kinematic component. Interestingly, this feature coincides with photometric evidence for a distinct component which comprises a strong variation in isophotal ellipticity and position angle (Caon et al. 1994).
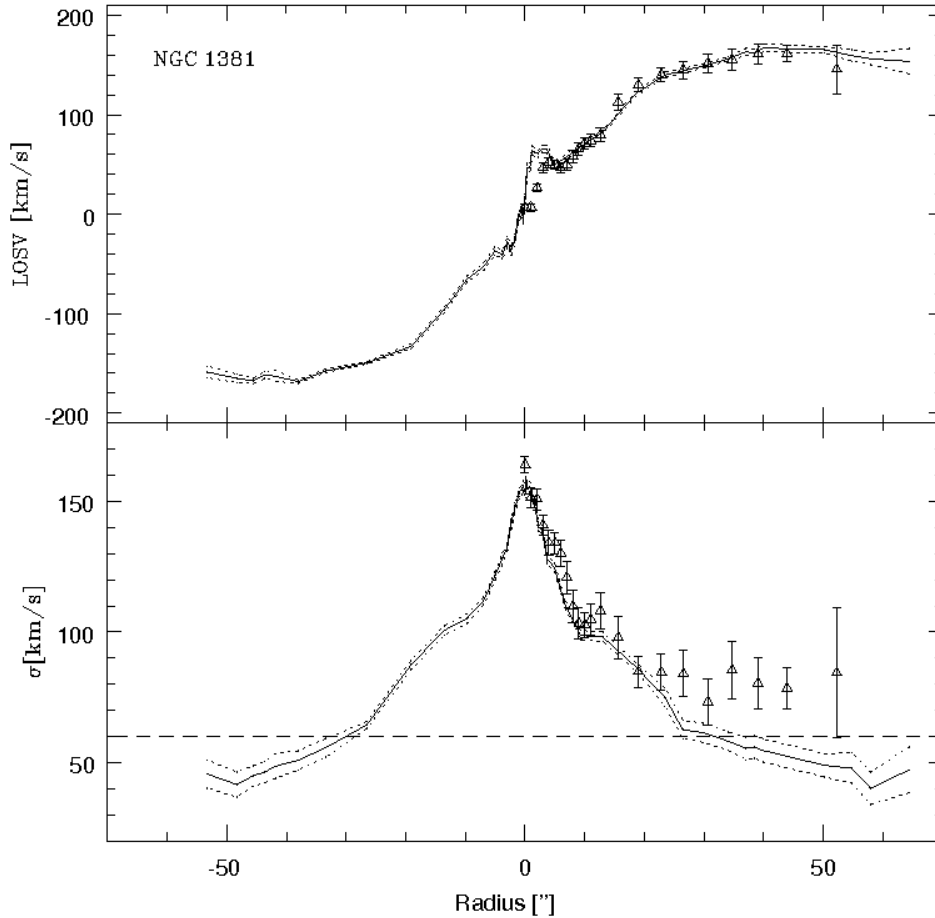
Figure 2.16. Comparison between the new results for mean velocity, V_{LOS}, and velocity dispersion, σ, and kinematics from the literature for NGC 1381.

NGC 1381

Figure 2.16 reveals a distinctive feature in this galaxy's rotational motion which was not apparent in the previous data. There is a correspondingly very strong signal in the h_3 profile shown in Figure A.3. Such kinematic features are characteristic of a bar viewed edge-on (Bureau & Athanassoula 2005), so we would seem to have identified this edge-on galaxy, previously designated as unbarred, as a barred system. The new velocity dispersion profile diverges at large radii from the D'Onofrio et al. (1995) data, but this would seem to be because the latter has been artificially enhanced in regions where the dispersion approaches the resolution limit of the older data.
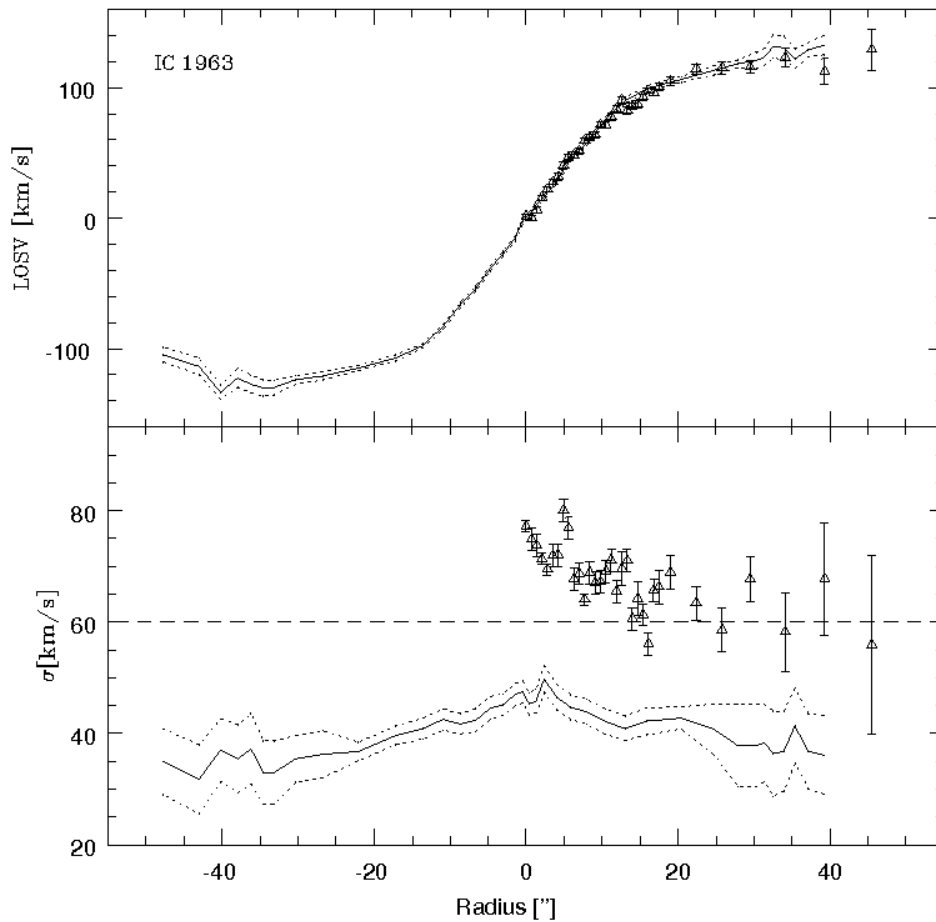
Figure 2.17. Comparison between the new results for mean velocity, V_{LOS}, and velocity dispersion, σ, and kinematics from the literature for IC 1963.

IC 1963

Figure 2.17 shows very good agreement between new measurements of mean streaming velocity and those in D'Onofrio et al. (1995) for this rather nondescript S0 system. The velocity dispersion measurements do not agree at all well, but once again this conflict can be attributed to the inadequate spectral resolution of the older data.
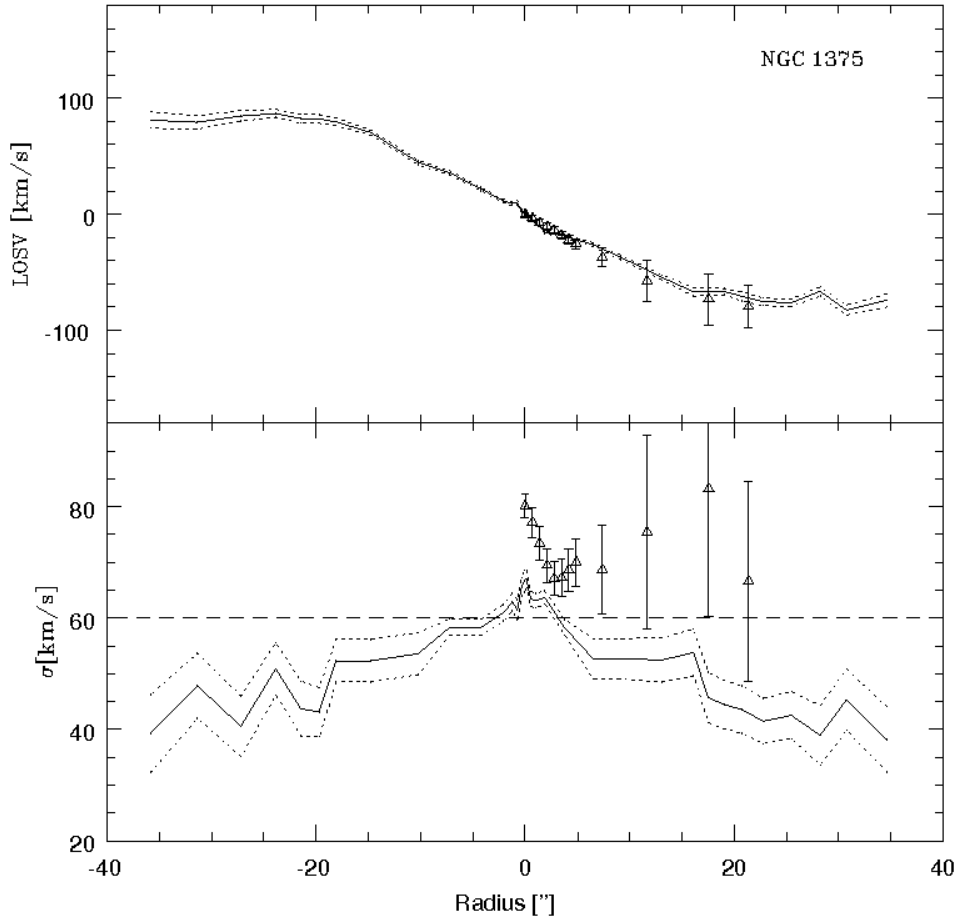
Figure 2.18. Comparison between the new results for mean velocity, V_{LOS}, and velocity dispersion, σ, and kinematics from the literature for NGC 1375.

NGC 1375

Once again, Figure 2.18 shows that the measured rotational motion for this galaxy agrees well with previous data, while the disagreement with earlier velocity dispersion data seems to arise from the limited spectral resolution of the older data. Support for this interpretation of the inconsistency comes from Kuntschner's (2000) value for the central dispersion of $56 \pm 10 \, \text{km s}^{-1}$, in agreement with the new data. A further issue with the earlier analysis is revealed by Figure A.5, as the structure in h_3 and h_4 at small radii would indicate that there is more information in these dynamics than would be revealed by the earlier Gaussian fit. Once again, this structure indicates the presence of a distinct kinematic component such as a bar. Photometric support for this conclusion comes from the work by Lorenz et al. (1993), who found that NGC 1375 possesses a complex structure characterised by boxy isophotes within a radius of 15 arcsec; such boxy isophotes are often associated with the kinematic signature of an edge-on bar (Kuijken & Merrifield 1995).
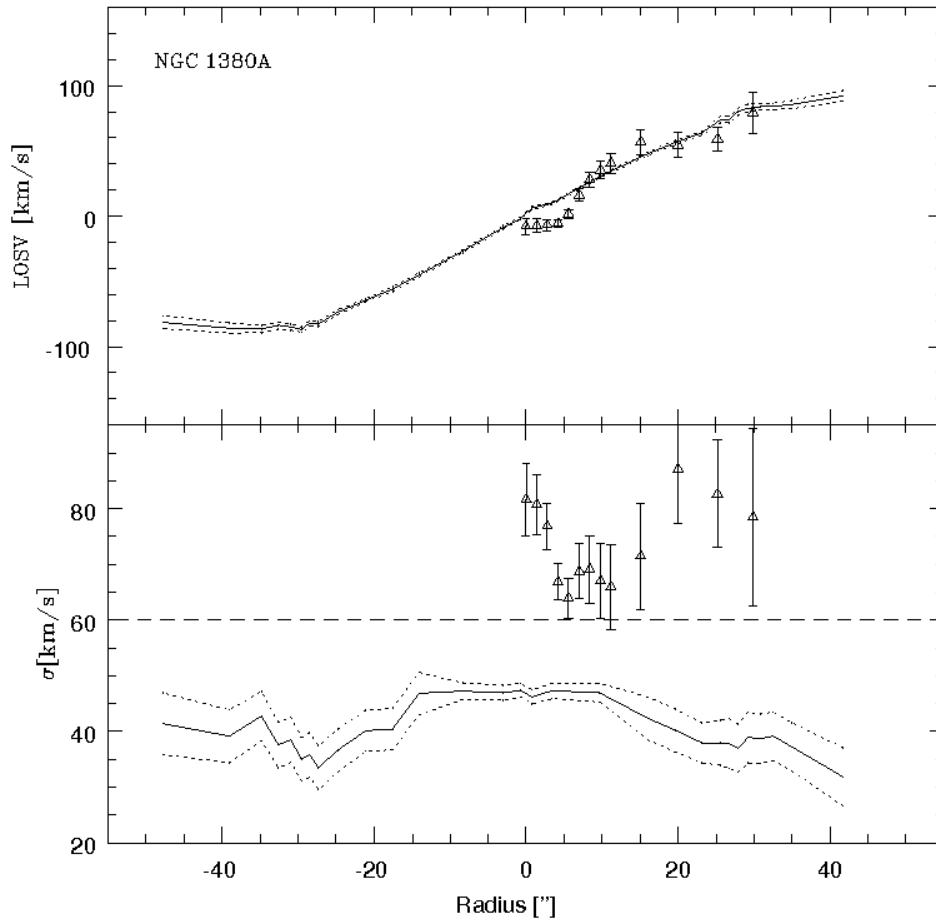
Figure 2.19. Comparison between the new results for mean velocity, V_{LOS}, and velocity dispersion, σ, and kinematics from the literature for NGC 1380A.

NGC 1380A

The well-constrained measurements of rotational motion for this galaxy are fairly featureless, and, as Figure 2.19 shows, do not reproduce the rather strange profile found by D'Onofrio et al. (1995). The similar absence of peculiarities in the h_3 and h_4 profiles shown in Figure A.6 suggest that the velocity structure in this galaxy is quite simple, so the smooth mean velocity curve is not unexpected. Once again, the new measurements of velocity dispersion lie systematically well below those in D'Onofrio et al. (1995), presumably due to the spectral resolution of the latter; Kuntschner's (2000) published central dispersion of $55 \pm 9\,\mathrm{km\,s^{-1}}$ fits rather better with the new measurements, but may also be running into resolution issues.
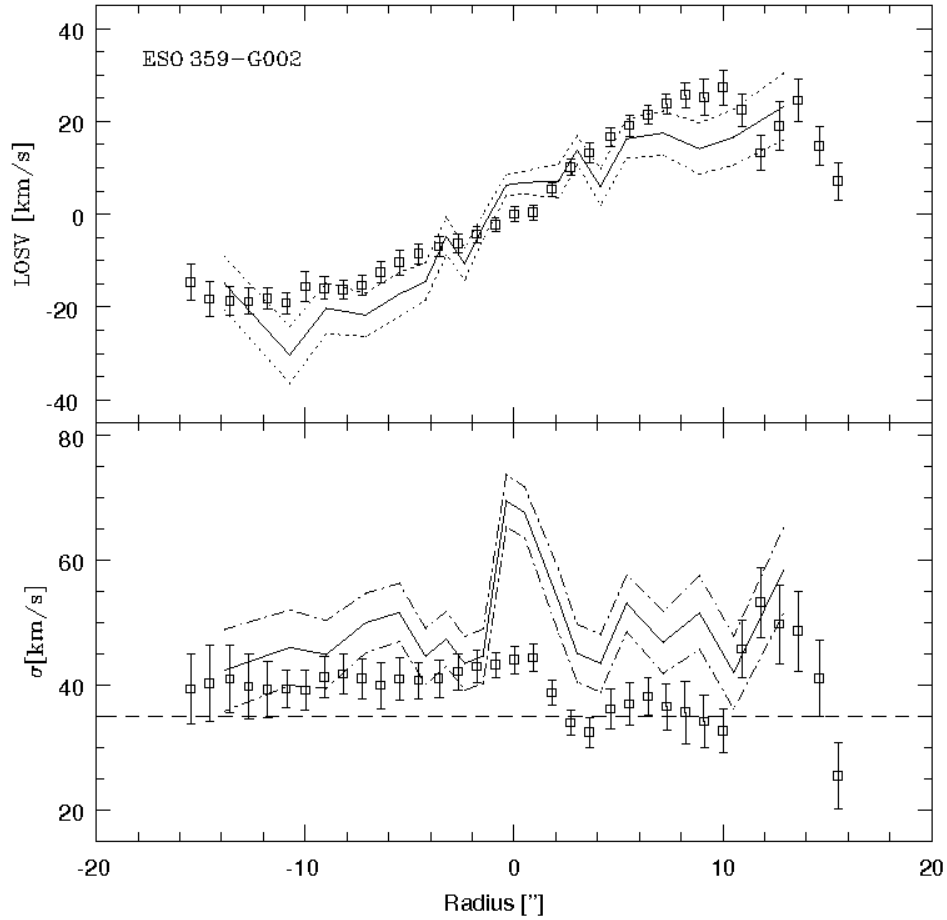
Figure 2.20. Comparison between the new results for mean velocity, V_{LOS}, and velocity dispersion, σ, and kinematics from the literature for ESO 359-G002.

ESO 359-G002

As Figure 2.20 shows, this fainter lenticular galaxy has a slowly rising mean velocity curve, in good agreement with the previous data from Graham et al. (1998) and despite being below the estimated spectral resolution. The previous velocity dispersion measurements are in reasonable agreement with the new data, but seem to lie systematically lower. In particular, the sharp central peak in velocity dispersion, which is accompanied by a similar structure in h_4 (see Figure A.7), was not seen in the earlier data. In this case both, the velocity curve and the dispersion profile should be viewed with some caution.

ESO 358-G006

There are no previous studies of the extended kinematics for this faint galaxy. Figure A.8 reveals generic featureless rotational motions that rise to a plateau at large radii, and a rather strange velocity dispersion profile with a slight central depression and a hint of a rising profile at large radii. The existing values for the central velocity dispersion of $58 \pm 8\,\mathrm{km\,s^{-1}}$ from Kuntschner (2000) and $46 \pm 3\,\mathrm{km\,s^{-1}}$ (Bernadi et al. 2002) are in accord with the new dispersion measurements.

ESO 358-G059

The extended kinematics of this faint galaxy have not previously been studied. Figure A.9 shows the rather strange kinematics for this system. It has a relatively well-behaved mean velocity profile that rises to an amplitude of $\sim 50\,\mathrm{km\,s^{-1}}$ at $\sim 5\,\mathrm{arcsec}$, then declines slightly. The dispersion profile is remarkably flat in the region where the rotation increases, then starts to rise when the rotational velocities decline. The published values for the central velocity dispersion, $54 \pm 9\mathrm{km\,s^{-1}}$ (Kuntschner 2000) and $46 \pm 3\,\mathrm{km\,s^{-1}}$ (Bernadi et al. 2002), are in reasonable agreement with the new data. One possible explanation for the enhanced dispersion and depressed rotation at larger radii would be the presence of a counter-rotating stellar disk (Rubin et al. 1992), but for such a faint galaxy the data clearly do not have sufficient quality to test this hypothesis rigorously.

2.4 Circular velocity calculation

In order to go beyond the kinematic measurements of section 2.2 to place these observations in their astrophysical context, it is necessary to translate them into the related intrinsic dynamical properties of the galaxies. In particular, since we ultimately want to explore the Tully–Fisher relation for these galaxies, it is necessary to derive the circular (or maximum) velocity as a function of radius, $V_{\mathrm{MAX}}(R)$. Although this quantity is clearly connected to the observed mean velocity profile, $V_{\mathrm{LOS}}(R)$, the transformation from one to the other is not trivial, so the procedure adopted is described in some detail.

The first ingredient we need is the inclination, i, of the galaxy to the line of sight, in order to determine the fraction of rotational motion that will have been projected into the observed line-of-sight mean velocity. In principle, the inclination can be estimated by simply measuring the flattening of isophotes at large radii, but this approach is not advisable as it uses only the lowest S/N photometry. Instead, a full two-dimensional fit to images of the galaxies was carried out using the GIM2D software (Simard et al. 2002). The software was applied to the publicly-available 2MASS K_{s}-band images of the objects in our sample (Jarrett et al. 2003). The uniform quality of these data means that we can study all of the galaxies in a consistent manner, and the use of infrared light means that we are tracing the bulk of the population in these systems, avoiding any problems that might arise from localised star formation or dust obscuration. In addition to obtaining a best estimate for the galaxies' inclinations, this analysis also returns estimates for the

parameters of a bulge-plus-disk model, including a bulge effective radius, R_{e}, and a disk scalelength, R_{exp}. As we will see below, these photometric parameters are also useful in determining the properties of the rotation curve, so their values are presented in Table 2.3. The K_{s}-band images of the galaxies, the GIM2D models and the residuals are presented in Figure 2.21 and 2.22.

To convert line-of-sight velocities into rotational motions, the same approach used in previous studies of long-slit kinematics for S0s was followed here (i.e. Neistein et al. 1999, hereafter N99). First of all, allowance has to be made for the extra degree of "roundness" contributed by the fact that the disks of S0s are not infinitely thin; as in N99, it was assumed that all galaxies would have an edge-on axis ratio $q_0 = 0.22$ (de Vaucouleurs et al. 1991), although this assumption turns out not to be critical to the results.

The second major effect that must be corrected for is that arising from projection along the line-of-sight. Although stars close to the minimum radius along a line through a highly-inclined disk will have most of their rotational velocity projected along the line of sight, those further from the centre of the galaxy will have most of their motion transverse to the line of sight, so their measured component of velocity will be small. A diagram of the problem and definitions for the geometric variables are shown in Figure 2.23. This tail of low-velocity stars means that the measured line-of-sight mean velocity will lie systematically below the rotational velocity of the stars by a factor g(R',z',i) of the form

$$g(R', z', i) = \frac{\int_0^\infty \nu(r', z') \cos(\phi) dS'}{\int_0^\infty \nu(r', z') dS'} \qquad (2.3)$$

by assuming a flat rotation curve as described in Merrett et al. (2004). In this simple model, ν is a density profile describing a double exponential disk of the form

$$\nu(r', z') = \nu_0 \exp\left(-r' - \frac{z' R_{\mathrm{exp}}}{z_{\mathrm{exp}}}\right), \qquad (2.4)$$

where z_{exp} is the disk scale height ($0.2\, R_{\mathrm{exp}}$) and the primed quantities have been defined in units of the disk scale length, R_{exp}, i.e. $R' = \frac{R}{R_{\mathrm{exp}}}$, $r' = \frac{r}{R_{\mathrm{exp}}}$, $z' = \frac{z}{R_{\mathrm{exp}}}$ and $S' = \frac{S}{R_{\mathrm{exp}}}$. This technique can only be reliably applied in regions where the disk dominates the light. So the photometric parameters derived above were used to ascertain the minimum radius, R_{LIM}, at which this correction can be made, corresponding to the radius where the Sérsic profile of the bulge and the exponential of the disk cross. The values for R_{LIM} are given in Table 2.3. If R_{LIM} did not lie within the radius inside we have data, then no correction was applied. Where it could be applied, this correction amounted to $\sim 20\%$. Although it is clearly significant, it is still sufficiently small that its exact value is not critical. At this stage, the azimuthal velocity, V_ϕ, was calculated as

$$V_\phi(R) = \frac{V_{\mathrm{LOS}}}{g(R', z', i)} \cdot \sqrt{\frac{1 - q_0^2}{2e - e^2}}, \qquad (2.5)$$

where e is the ellipticity derived from the inclination angle i.
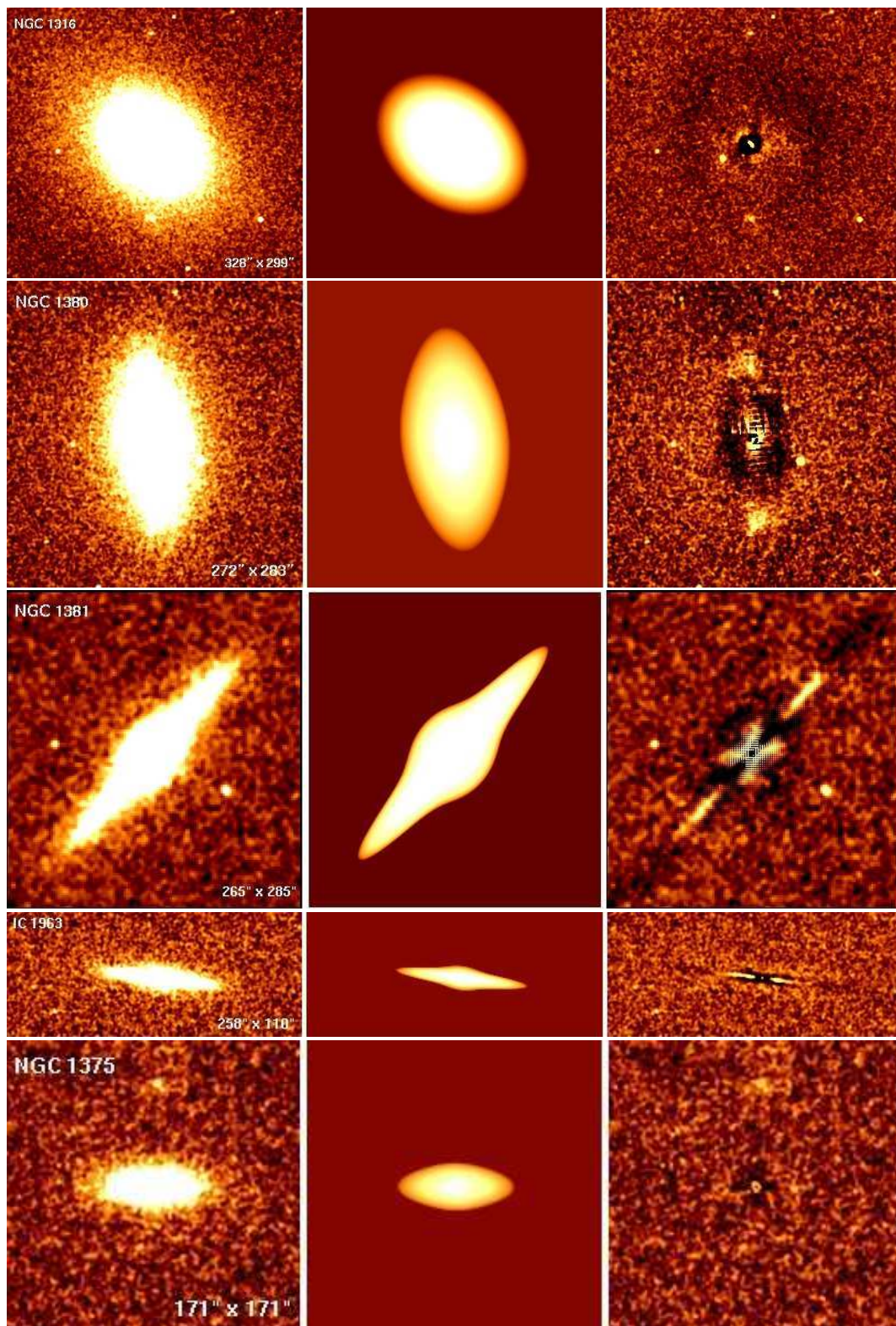
Figure 2.21. K_s-band images of S0s in Fornax (left). Image size in arcseconds indicated in lower right corner. Bulge + Disk model using GIM2D software (middle). Image − Model residuals (right).
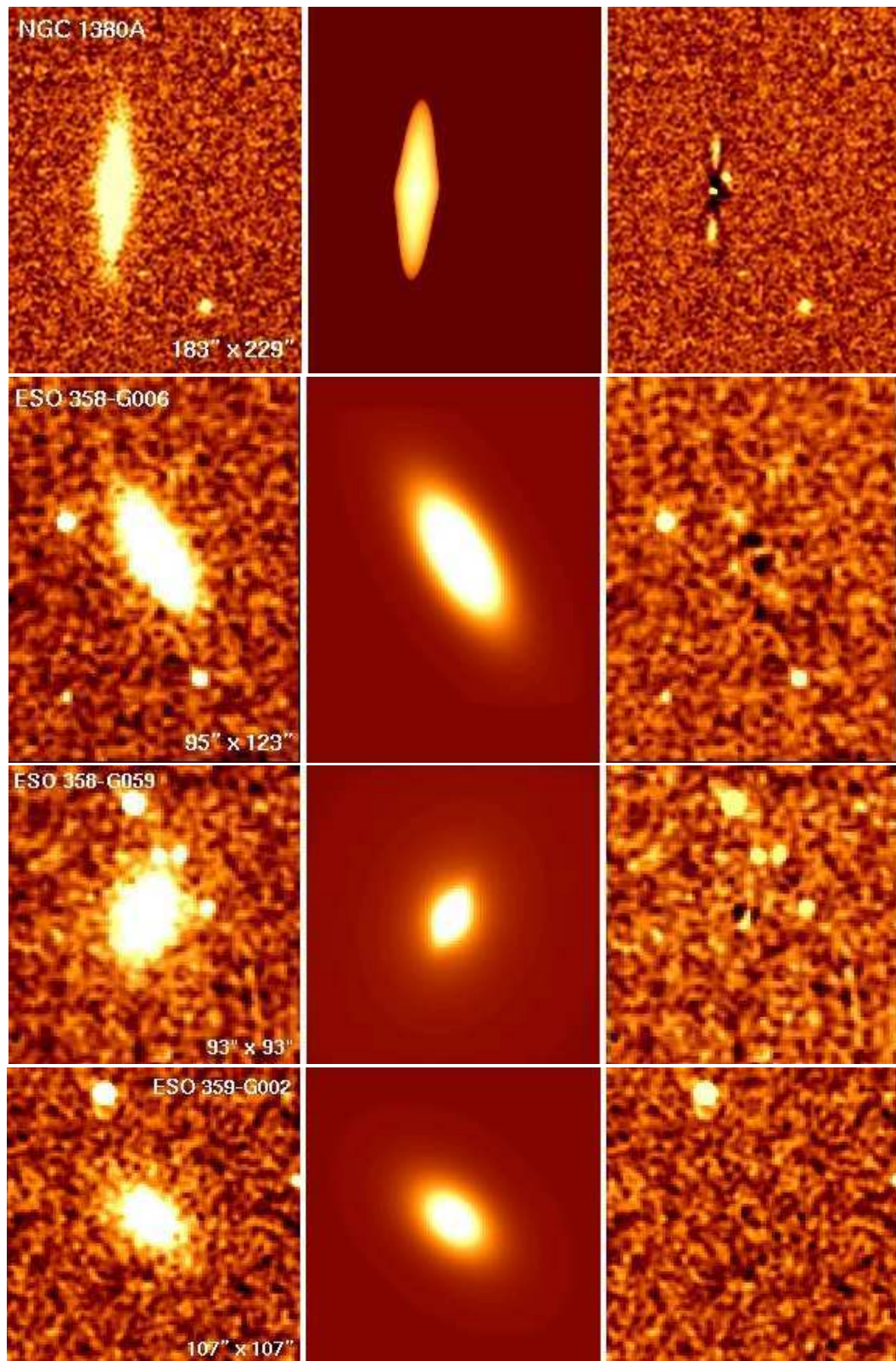
Figure 2.22. K_s-band images of S0s in Fornax (left). Image size in arcseconds indicated in lower right corner. Bulge + Disk model using GIM2D software (middle). Image − Model residuals (right).

Table 2.3. Structural and other important parameters of S0 galaxies in the Fornax Cluster.

Name	i [^{o}]	B/T	$R_{\rm e}$ ["]	$R_{\rm exp}$ ["]	Sérsic n	$R_{\rm LIM}$ ["]	$R_{\rm out}$ ["] $\{[R_e]\}$	$V_{\rm MAX}$ [km s^{-1}]	$M_{\rm B}$
(1)	(2)	(3)	(4)	(5)	(6)	(7)	(8)	(9)	(10)
NGC 1316	43.2 $^{43.8}_{42.4}$	0.58 $^{0.62}_{0.47}$	36.0 $^{41.7}_{24.8}$	49.4 $^{52.7}_{47.2}$	2.9 $^{3.2}_{2.3}$	–	148.5 {4.1}	–	−22.3 (0.1)
NGC 1380	66.9 $^{67.5}_{66.5}$	0.58 $^{0.59}_{0.57}$	17.6 $^{18.0}_{17.3}$	36.3 $^{37.3}_{35.9}$	3.3 $^{3.4}_{3.3}$	35.7	88.6 {5.0}	309.6 (26.6)	−20.6 (0.1)
NGC 1381	82.5 $^{82.9}_{82.2}$	0.57 $^{0.58}_{0.55}$	7.4 $^{7.7}_{7.3}$	20.8 $^{21.6}_{20.3}$	3.1 $^{3.2}_{3.0}$	35.2	64.2 {8.7}	278.8 (32.4)	−19.0 (0.1)
IC 1963	84.6 $^{84.7}_{84.3}$	0.39 $^{0.42}_{0.36}$	22.6 $^{24.9}_{21.2}$	15.8 $^{16.1}_{15.5}$	3.6 $^{3.7}_{3.5}$	5.5	47.8 {2.1}	164.7 (16.8)	−18.5 (0.1)
NGC 1375	67.5 $^{68.3}_{66.3}$	0.19 $^{0.21}_{0.17}$	3.2 $^{3.4}_{2.9}$	14.8 $^{15.2}_{14.0}$	2.2 $^{2.3}_{2.1}$	10.7	35.9 {11.2}	113.4 (19.6)	−18.2 (0.2)
NGC 1380A	78.1 $^{78.8}_{77.4}$	0.18 $^{0.24}_{0.14}$	10.9 $^{14.5}_{8.1}$	19.8 $^{20.4}_{19.2}$	3.7 $^{3.8}_{3.6}$	5.5	47.9 {4.4}	119.7 (3.0)	−18.1 (0.2)
ESO 358-G006	65.9 $^{67.2}_{64.8}$	0.02 $^{0.04}_{0.01}$	1.5 $^{2.9}_{0.2}$	9.2 $^{9.6}_{8.8}$	3.0 $^{3.3}_{2.7}$	0.00627	29.4 {19.6}	155.8: (26.0)	−17.5 (0.2)
ESO 358-G059	61.9 $^{63.9}_{59.8}$	0.72 $^{0.76}_{0.65}$	16.2 $^{18.4}_{14.7}$	2.3 $^{2.5}_{2.2}$	2.0 $^{2.2}_{1.6}$	–	14.2 {0.9}	108.5: (53.8)	−17.4 (0.2)
ESO 359-G002	49.4 $^{51.7}_{47.2}$	0.07 $^{0.14}_{0.03}$	6.0 $^{10.2}_{4.9}$	7.8 $^{8.2}_{7.4}$	3.1 $^{3.4}_{2.9}$	0.4	13.9 {2.3}	–	−17.3 (0.2)

Note: For all pertinent calculations, $H_0 = 70\,{\rm km\,s^{-1}\,Mpc^{-1}}$. From (2) to (6), 99% confidence intervals are presented; from (9) to (10), $1\,\sigma$ errors between "()". Col (2), inclination angle with respect to the line-of-sight; col (3), bulge to total fraction; col (4), effective radius of the bulge; col (5), exponential disk scale length; col (6), Sérsic index; col (7), minimum radius where the "projected velocities correction" is applied; col (8), distance of the outermost bin in arc-seconds and in units of the effective radius; col (9), maximum circular velocity, values followed by ' : ' should be taken as an upper limit only; col (10), absolute magnitude in B-band, assuming a distance modulus of 31.35 for the cluster, according to Madore et al. (1999).
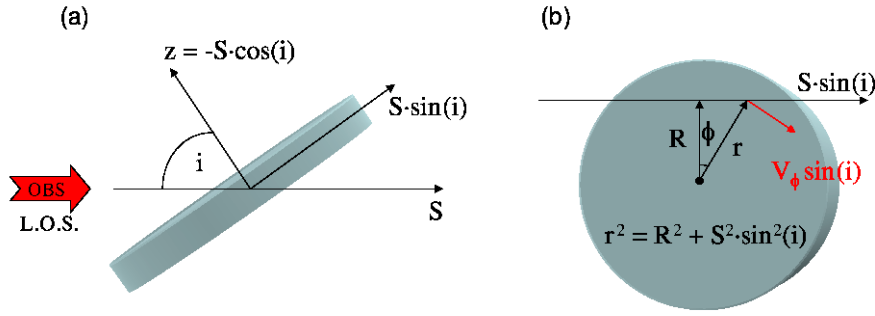
Figure 2.23. Model for line-of-sight integration through the disk, shown with the disk (a) edge-on, (b) face-on.

The last correction that must be applied is the difference between mean streaming velocity, V_ϕ, and circular rotation speed that arises because the stars have a random component to their motions as well as a rotational motion. This "asymmetric drift" can be corrected using the appropriate Jeans equation (Binney & Tremaine 1987) by which

$$V_{\mathrm{MAX}}^2 = V_\phi^2 + \sigma_{\mathrm{fit}}^2 \left(2\frac{R}{R_{\mathrm{exp}}} - 1 \right), \tag{2.6}$$

where σ_{fit} is the velocity dispersion at radius R determined from a fit to the velocity dispersion profile using a low-order polynomial (see Appendix A).

Strictly speaking, this low-order correction is only valid for rather cold disks with $V_\phi \gg \sigma_{\mathrm{fit}}$. Some experimenting with simulated data revealed that the corrections remained fairly reliable for any galaxy with $V_\phi/\sigma_{\mathrm{fit}} \geq 2$, but that artifacts from the correction would begin to appear in the rotation curve below this limit. This requirement was met for five of the sample galaxies, but for two (ESO 358-G006 and ESO 358-G059), the limit was relaxed to $V_\phi/\sigma_{\mathrm{fit}} > 1$. In these cases, the asymmetric drift correction of equation 2.6 tends to be large, so the resulting rotation velocities should be taken as an upper limit. In two cases (NGC 1316 and ESO 359-G002), random motions dominate at all radii, so this correction cannot even be attempted. In consequence, these two galaxies have to be excluded from subsequent analysis.

After carrying out the above procedures, the measured mean line-of-sight velocity data points have been converted into discrete estimates of the local circular speed at the corresponding radii. These estimates have two limitations: first, each point will have a significant error bar from all the propagated uncertainties; and second, the data will lie over only a limited range in radii since the rotation velocities cannot be determined in this way at small radii where random motions dominate, and the galaxies become too faint at large radii to have their kinematics measured. We therefore cannot simply read off dynamical parameters such as the maximum velocity, V_{MAX}, from these data. Instead, we effectively interpolate and extrapolate the limited data by modelling the contributions to the rotation curve by disk and bulge. Using the photometric parameters derived above, the disk component of the rotation curve was modeled using the formula for a pure exponential,

$$V_{\mathrm{MAX}}^2(R) = 4\pi G \Sigma_0 R_{\mathrm{exp}} y^2 [I_0(y)K_0(y) - I_1(y)K_1(y)], \tag{2.7}$$
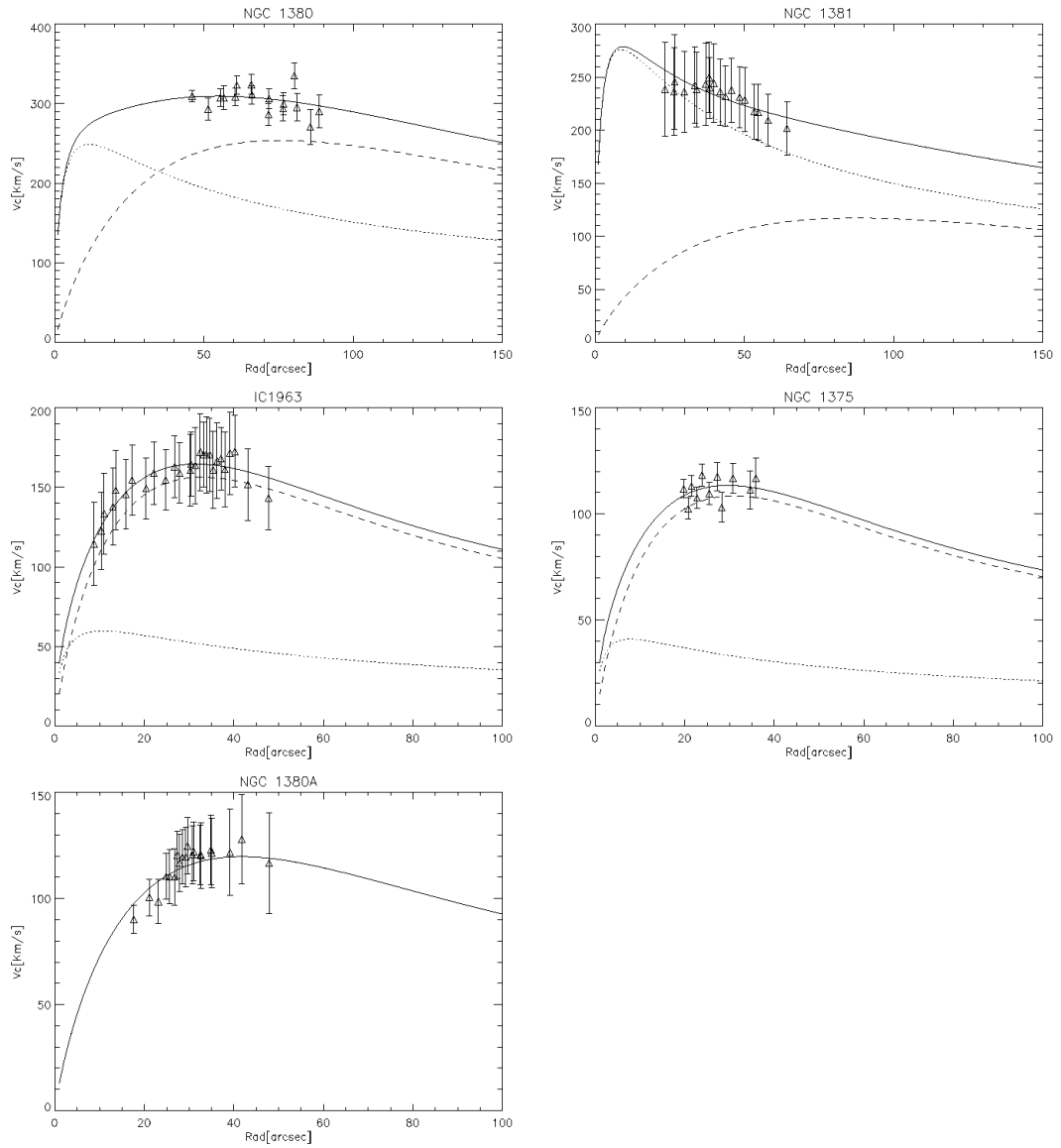
Figure 2.24. Derived circular velocity (V_C in here) as a function of radius and the corresponding best-fit models for Fornax Cluster S0 galaxies. The dotted line shows the bulge contribution, the dashed line shows the disk contribution, and the solid line shows the quadrature-summed total. For NGC 1380A a pure disk model gives the best fit.

where G is the gravitational constant, Σ_0 is the central surface density, I_0, K_0, I_1 and K_1 are modified Bessel functions, and $y = R/R_{\mathrm{exp}}$ (Freeman 1970). For the bulge, the rotation curve of Hernquist (1990) was used,

$$V_{\mathrm{MAX}}^2(R) = \frac{GM_{\mathrm{bulge}}}{R} \frac{R^2}{(R + a)^2}, \qquad (2.8)$$

where M_{bulge} is the mass of this component, and the scalelength a can be approximately related to R_{e} by $a/R_{\mathrm{e}} = 1.82$. The normalisations of these two components (effectively, the mass-to-light ratios of the photometric components) were then varied such that their quadrature sum produced the best fit to the circular speed data over the range that it is available. The result of this process is presented in Figure 2.24; this procedure was not attempted for the two galaxies in which the circular velocities are less certain because the asymmetric drift corrections were large.

These fits were used to read off quantities of interest. For example, for a Tully–Fisher analysis, the maximum rotation velocity V_{MAX} is needed. The resulting values are presented in Table 2.3; for the two galaxies for which the complete fit was not carried out, the maximum circular speed was simply quoted as derived from the data. Note that although V_{MAX} was generally derived from the fitting procedure, it is apparent from Figure 2.24 that the values returned do not differ greatly from the measured rotation speeds. This similarity arises because the new VLT observations go deep enough to enable us, for the first time, to measure velocities in the flat part of the rotation curve. By reaching these radii, we enter a regime in which the maximum velocity is reasonably tightly constrained irrespective of the details of the model fit.

Chapter 3

The Stellar Populations of S0 galaxies in the Fornax Cluster

In this chapter a study of the central stellar populations of 9 S0 galaxies in the Fornax Cluster is presented. The analysis is based on different Lick/IDS indices calculated from the spectra. Using Bruzual & Charlot (2003) simple stellar population models (hereafter BC03), the well known age-metallicity degeneracy was broken, allowing not only the inclusion of these two parameters in the present study, but also providing an estimate of the relative α-element abundances between these galaxies. The choice of BC03 instead of other alternatives, like the models of Thomas, Maraston & Bender (2003, hereafter TMB03), was made based on the higher resolution of the stellar libraries of the former (3 Å, Le Borgne et al. 2003), which permitted the study of the spectral features of these galaxies in greater detail. For the study of the main stellar population properties, however, a BC03 model with Lick resolution had to be used (resolution from FWHM ~ 11 Å around 4000 Å to ~ 8.5 Å around 5000 Å) given the higher reliability of these models when individual ages and metallicities are estimated.

3.1 The Data: Line Index Measurement

In this section, the main steps followed to calculate Lick/IDS line-strength indices (Burstein et al. 1984, 1986; Worthey et al. 1994; Worthey & Ottaviani 1997) using long-slit spectra are described. This will allow us to study scaling relations such as the one between Mg_2 and central velocity dispersion (e.g. Burstein et al. 1988; Guzmán et al. 1992; Bender, Burstein & Faber 1993) and to compare the results to predictions from simple stellar population models (SSP) of BC03.

The basic data reduction and extraction of the kinematics are described in Chapter 2. The only change introduced at this level is a new criterion for the binning process, following the precepts of Cardiel et al. (1998). The aim of this procedure is to estimate the minimum signal-to-noise (S/N) required for the new bins in order to obtain reasonably small uncertainties in $H\beta$ ($\delta(H\beta)$ between 0.04 and 0.3) and so, in the relative ages. An estimate of the minimum $\delta(H\beta)$ was made for each galaxy by using different $H\beta$-versus-metallic-index diagrams and BC03 model grids; depending on the position of the galaxies' data points on the grids, a given uncertainty in the

Table 3.1. Lick indices used in this study. The final column indicates the resolution at which each index was measured when Lick resolution was adopted.

Index	Blue Band [Å]		Central Band [Å]		Red Band [Å]		Lick Resol. [km s^{-1}]
Hβ	4827.875	4847.875	4847.875	4876.625	4876.625	4891.625	225
Fe5015	4946.500	4977.750	4977.750	5054.000	5054.000	5065.250	200
Mg$_1$	4895.125	4957.625	5069.125	5134.125	5301.125	5366.125	200
Mg$_2$	4895.125	4957.625	5154.125	5196.625	5301.125	5366.125	200
Mgb	5142.625	5161.375	5160.125	5192.625	5191.375	5206.375	200
Fe5270	5233.150	5248.150	5245.650	5285.650	5285.650	5318.150	200
Fe5335	5304.625	5315.875	5312.125	5352.125	5353.375	5363.375	200
Fe5406	5376.250	5387.500	5387.500	5415.000	5415.000	5425.000	200
Fe5709	5672.875	5696.625	5696.625	5720.375	5722.875	5736.625	200
Fe5782	5765.375	5775.375	5776.625	5796.625	5797.875	5811.625	200

indices will translate into a corresponding error in age. In the majority of cases, an uncertainty no larger than 4 Gyr was allowed for the outermost bins. Then, the following expression of Cardiel et al. was used to obtain the S/N required for a given uncertainty $\delta(\mathrm{H}\beta)$:

$$\mathrm{S/N}[\text{Å}] = \frac{7.301 - 0.2539 \cdot \mathrm{H}\beta}{\delta(\mathrm{H}\beta)} \qquad (3.1)$$

The S/N per Å of the new bins are 100, 50 and a minimum of $\sim$ 30 (this last one, varying from galaxy to galaxy), decreasing as the radius increases. As a result of the new binning, the data cover median radii $\sim$ 2 bulge R_e for this sample of S0s.

3.1.1 Transformation to the Stellar Library Resolution

The Lick/IDS indices studied are listed in Table 3.1. To be able to compare the results to SSP models, the indices must be measured at the same spectral resolution as the model's stellar libraries. The width of the observed spectral lines are a convolution between the instrumental width and the velocity dispersion of the stars projected along the line-of-sight. Therefore, to transform the galaxies' spectra to the required resolution, they were convolved with a Gaussian of dispersion, σ, equal to

$$\sigma = \sqrt{\sigma_{\mathrm{lib}}^2 - \sigma_{\mathrm{inst}}^2 - \sigma_{\mathrm{gal}}^2}, \qquad (3.2)$$

where σ_{lib} is the resolution from the stellar library, σ_{inst} is the instrumental widening ($\sim$ 30 km s^{-1}, see Chapter 2) and σ_{gal} is the velocity dispersion of the galaxy at the corresponding radius, already calculated in previous steps.

Once the spectra were widened, line-strength indices were measured in the central regions of the galaxies (within $R_\mathrm{e}/8$ of the bulge, see Chapter 2) using the software INDEXF of Dr. Nicolás Cardiel[1]. Following the Lick/IDS index definition, the program calculates a *pseudocontinuum* (a local continuum level) for each spectral feature defined by the means within two pseudocontinuum bands ("Blue″ and

---

[1]http://www.ucm.es/info/Astrof/software/indexf/indexf.html
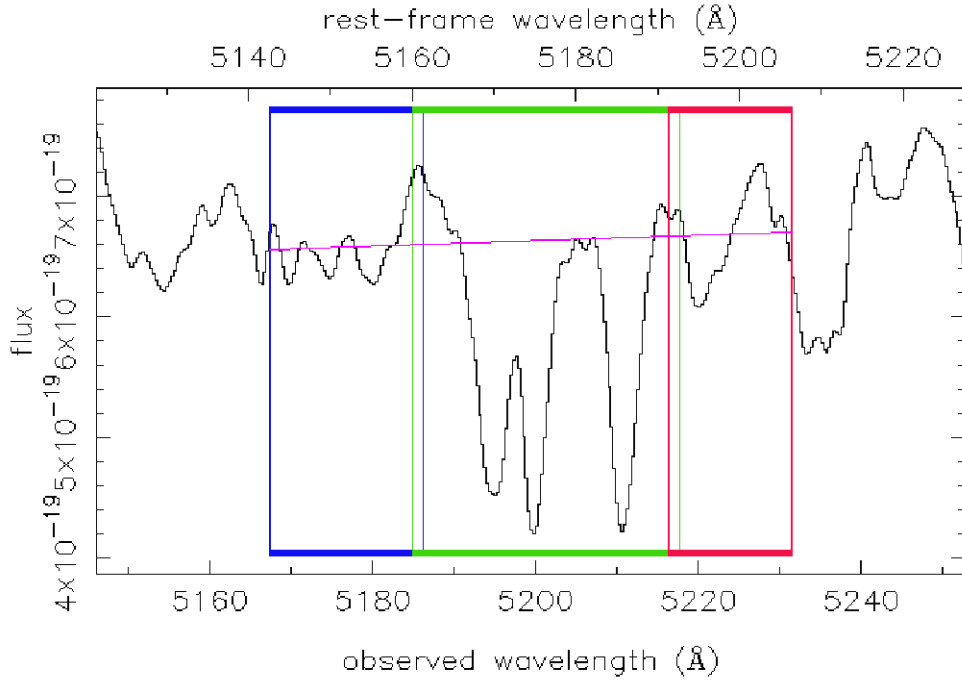
Figure 3.1. Line index measurement using `INDEXF`. Blue and red bands represent the pseudocontinuum bands, which define a local continuum level represented as a purple line. The spectral feature (in this case, corresponding to the Magnesium Triplet) is measured within the central green band.

"Red″ in Table 3.1), located one at each side of the spectral feature. An example of the line index measurement for the magnesium triplet is presented in Figure 3.1. Then, the line index is measured with respect of the pseudocontinuum by integrating within the feature band ("Central″ in Table 3.1)

$$\text{Index} = \int_{\lambda_{c1}}^{\lambda_{c2}} \left(1 - \frac{S_\lambda}{C_\lambda}\right) d\lambda, \tag{3.3}$$

where λ_{c1} and λ_{c2} are the initial and final wavelengths of the central band, S_λ is the flux of the spectrum at a certain λ and C_λ is the corresponding pseudocontinuum flux. This program also estimates the uncertainties resulting from the propagation of random errors, local continuum level and from the effect of uncertainties on radial velocity by performing Monte-Carlo simulations.

As mentioned at the beginning of this chapter, BC03 models at both Lick and 3 Å resolution were used in this study. In consequence, all indices were measured at both resolutions by applying the previously described procedures. Further comparisons between the two index sets are presented in the following sections.

For NGC 1316, NGC 1380 and NGC 1381, the velocity dispersions within their central regions are higher than the 3 Å stellar library's resolution. Therefore, the procedure described above cannot be applied and the indices must be corrected after they have been measured. In these cases, we proceed as follows: for each galaxy,

the best stellar-template combination for the affected bins were used as models of the non-convolved galaxy spectra (apart from the instrumental widening). Using equation 3.2, these spectra were widened to the stellar library resolution and then, in steps of $20\,\mathrm{km\,s^{-1}}$, convolved with Gaussians of dispersions σ_{gal} between 0 and $400\,\mathrm{km\,s^{-1}}$. The next step consisted of measuring all line indices in each spectrum and calculate a correction factor for each index, $\mathrm{C}(\sigma)_{\mathrm{Index}}$, of the form

$$\mathrm{C}(\sigma)_{\mathrm{Index}} = \mathrm{Index}(0)/\mathrm{Index}(\sigma). \tag{3.4}$$

$\mathrm{Index}(0)$ is the index measured from the best stellar-template combination degraded at the stellar library resolution, and $\mathrm{Index}(\sigma)$ is the index measured from the same spectrum but widened by $\sigma\,\mathrm{km\,s^{-1}}$. Therefore, the corrected index is given by

$$\mathrm{Index}(0) = \mathrm{C}(\sigma)_{\mathrm{Index}} \cdot \mathrm{Index}(\sigma). \tag{3.5}$$

Notice, however, that for the molecular indices Mg_1 and Mg_2, measured in magnitudes, the correction applied was of the form

$$\mathrm{C}(\sigma) = \mathrm{Index}(0) - \mathrm{Index}(\sigma). \tag{3.6}$$

The correction factors for the individual bins turned out to be similar within each galaxy. Therefore, it was decided to apply a unique set of correction factors for each S0 by taking the average of the individual bins' corrections and fitting the results with polynomials of order 3. The final polynomials used to correct the line indices of these galaxies to a $3\,\text{Å}$ resolution are presented in Table 3.2. For NGC 1316 and 1380, analogous corrections were applied when Lick resolution was used. The corresponding polynomials used to correct these indices to Lick resolution are presented in Table 3.3.

The corrections were applied along the radius, R, to all spectral bins for which the velocity dispersion was higher than the stellar library's resolution ($\sigma_{\mathrm{gal}}^2(R) + \sigma_{\mathrm{inst}}^2 \geq \sigma_{\mathrm{lib}}^2$). For NGC 1380 and NGC 1381 the different corrections ranged between 2–10% of the value of the measured indices, while for NGC 1316 they were slightly larger, typically between 10–20% of the original measurements. For each galaxy, an estimate of the uncertainty in these corrections was attempted by measuring the deviations of all the coefficients $\mathrm{C}(\sigma)_{\mathrm{Index}}$ from each bin at a velocity dispersion of $400\,\mathrm{km\,s^{-1}}$. The resulting errors translate into uncertainties of the order of $0.001\,\text{Å}$ for the different indices, negligible compared to other sources of error from the data reduction/kinematics extraction processes. Therefore they were neglected for future analysis.

3.1.2 Emission Correction

For a long time early-type galaxies were considered as gas/dust free objects. However, subsequent work on large samples of ellipticals has revealed that about 50% of these objects show weak nebular emission lines in their optical spectra (Caldwell et al. 1984; Phillips et al. 1986; Goudfrooij et al. 1994). Measurements of different nebular lines indicates the presence of 10^3–$10^5\,\mathrm{M_\odot}$ of ionised gas in the central

Table 3.2. Polynomials used to correct central line indices of NGC 1316, NGC 1380 and NGC 1381 to 3 Å resolution.

Name	Const.	Coeff. of σ	Coeff. of σ^2	Coeff. of σ^3
NGC 1316				
Hβ	1.0712	-0.0016	$7.4469\ 10^{-6}$	$-9.7647\ 10^{-9}$
Fe5015	0.9736	$-4.1914\ 10^{-5}$	$5.5492\ 10^{-6}$	$-6.3904\ 10^{-9}$
Mg$_1$	0.0015	$-3.6088\ 10^{-5}$	$1.7343\ 10^{-7}$	$-1.8005\ 10^{-10}$
Mg$_2$	-0.0005	$4.3450\ 10^{-6}$	$-9.5869\ 10^{-10}$	$4.3056\ 10^{-11}$
Mgb	0.9809	0.0005	$1.2787\ 10^{-6}$	$1.3268\ 10^{-9}$
Fe5270	0.9328	0.0011	$3.7107\ 10^{-7}$	$6.0995\ 10^{-10}$
Fe5335	1.0216	-0.0011	$1.0620\ 10^{-5}$	$-5.3157\ 10^{-9}$
Fe5406	0.9625	0.0007	$1.7911\ 10^{-6}$	$6.7305\ 10^{-9}$
Fe5709	0.9428	0.0011	$-3.3989\ 10^{-6}$	$8.8090\ 10^{-9}$
Fe5782	0.9027	0.0011	$3.7207\ 10^{-6}$	$4.8544\ 10^{-9}$
NGC 1380				
Hβ	0.9813	0.0003	$-4.7346\ 10^{-7}$	$-2.5894\ 10^{-10}$
Fe5015	0.9516	0.0004	$3.8813\ 10^{-6}$	$-4.0271\ 10^{-9}$
Mg$_1$	-0.0009	$8.7309\ 10^{-6}$	$7.5170\ 10^{-8}$	$-8.5862\ 10^{-11}$
Mg$_2$	-0.0028	$4.5967\ 10^{-5}$	$-7.9677\ 10^{-8}$	$7.1194\ 10^{-11}$
Mgb	1.0571	-0.0012	$5.7886\ 10^{-6}$	$-3.8354\ 10^{-9}$
Fe5270	0.9807	$-3.1446\ 10^{-5}$	$4.8870\ 10^{-6}$	$-4.6176\ 10^{-9}$
Fe5335	0.9719	$6.1938\ 10^{-5}$	$5.6647\ 10^{-6}$	$4.1535\ 10^{-10}$
Fe5406	1.0125	-0.0006	$6.4806\ 10^{-6}$	$1.4419\ 10^{-9}$
Fe5709	0.9530	0.0007	$-7.6132\ 10^{-7}$	$5.0166\ 10^{-9}$
Fe5782	0.9426	0.0008	$1.0811\ 10^{-6}$	$8.9001\ 10^{-9}$
NGC 1381				
Hβ	1.0359	-0.0007	$1.8405\ 10^{-6}$	$-7.2808\ 10^{-10}$
Fe5015	0.9973	-0.0005	$6.6197\ 10^{-6}$	$-7.5246\ 10^{-9}$
Mg$_1$	0.0009	$-2.4671\ 10^{-5}$	$1.3804\ 10^{-7}$	$-1.3489\ 10^{-10}$
Mg$_2$	-0.0007	$8.2230\ 10^{-6}$	$9.4177\ 10^{-9}$	$3.5917\ 10^{-12}$
Mgb	1.0142	-0.0004	$3.4221\ 10^{-6}$	$-1.1281\ 10^{-9}$
Fe5270	0.9743	0.0002	$3.7933\ 10^{-6}$	$-3.4406\ 10^{-9}$
Fe5335	1.0135	-0.0006	$7.6551\ 10^{-6}$	$-1.4202\ 10^{-9}$
Fe5406	1.0086	-0.0005	$5.1088\ 10^{-6}$	$2.7895\ 10^{-9}$
Fe5709	0.9263	0.0012	$-3.0779\ 10^{-6}$	$7.5129\ 10^{-9}$
Fe5782	1.0004	-0.0005	$7.2717\ 10^{-6}$	$1.2275\ 10^{-9}$

Table 3.3. Polynomials used to correct central line indices of NGC 1316 and NGC 1380 to Lick resolution.

Name	Const.	Coeff. of σ	Coeff. of σ^2	Coeff. of σ^3
NGC 1316				
Hβ	1.0006	$5.3666 \ 10^{-5}$	$1.3659 \ 10^{-6}$	$9.5717 \ 10^{-10}$
Fe5015	1.0004	$1.2300 \ 10^{-3}$	$2.6953 \ 10^{-7}$	$5.2095 \ 10^{-10}$
Mg$_1$	$-2.5719 \ 10^{-5}$	$1.1023 \ 10^{-5}$	$4.1369 \ 10^{-8}$	$-7.1004 \ 10^{-9}$
Mg$_2$	$8.9892 \ 10^{-5}$	$4.6711 \ 10^{-6}$	$4.2295 \ 10^{-8}$	$1.3146 \ 10^{-10}$
Mgb	0.9978	$9.8458 \ 10^{-4}$	$1.8889 \ 10^{-6}$	$-4.2710 \ 10^{-10}$
Fe5270	0.9981	$1.2363 \ 10^{-3}$	$-6.3519 \ 10^{-7}$	$3.8867 \ 10^{-9}$
Fe5335	0.9984	$1.9167 \ 10^{-3}$	$5.6863 \ 10^{-6}$	$-1.0333 \ 10^{-9}$
Fe5406	0.9997	0.0015	$6.2923 \ 10^{-6}$	$-5.3199 \ 10^{-10}$
Fe5709	1.0006	0.0005	$2.5124 \ 10^{-6}$	$3.9764 \ 10^{-9}$
Fe5782	0.9989	0.0023	$3.6037 \ 10^{-6}$	$8.7130 \ 10^{-9}$
NGC 1380				
Hβ	1.0015	$-1.3234 \ 10^{-4}$	$1.1722 \ 10^{-6}$	$9.9105 \ 10^{-10}$
Fe5015	1.0004	$1.3389 \ 10^{-3}$	$5.1020 \ 10^{-7}$	$-6.2380 \ 10^{-11}$
Mg$_1$	$-1.4897 \ 10^{-5}$	$3.0197 \ 10^{-5}$	$5.9841 \ 10^{-9}$	$-4.1630 \ 10^{-11}$
Mg$_2$	0.0001	$1.6290 \ 10^{-5}$	$-8.6877 \ 10^{-9}$	$8.5451 \ 10^{-11}$
Mgb	0.9975	$7.7187 \ 10^{-4}$	$2.1790 \ 10^{-6}$	$-6.6265 \ 10^{-10}$
Fe5270	0.9974	$1.4207 \ 10^{-3}$	$-5.5325 \ 10^{-7}$	$3.3666 \ 10^{-9}$
Fe5335	0.9976	$2.0785 \ 10^{-3}$	$4.3729 \ 10^{-6}$	$8.8428 \ 10^{-10}$
Fe5406	0.9994	0.0018	$6.9471 \ 10^{-6}$	$-6.7793 \ 10^{-10}$
Fe5709	1.0004	0.0008	$2.3100 \ 10^{-6}$	$4.3474 \ 10^{-9}$
Fe5782	0.9993	0.0019	$5.3759 \ 10^{-6}$	$6.9817 \ 10^{-9}$

regions of these galaxies. Despite the small amount of gas, some absorption line features can be affected by these emissions.

Weak traces of nebular emission ($[O_{III}]_{\lambda5007}$ rest frame) were found in the spectra, which affects the measurement of the indices Fe5015 (within its central band) and Mgb (within one of the pseudocontinuum bands). To correct these indices of emission, the best stellar-template combination was compared to the galaxy spectrum and the spectral feature of $[O_{III}]_{\lambda5007}$ was replaced by the corresponding section of the best stellar-template combination before the indices were calculated. No other signatures of emission, such as $[O_{III}]_{\lambda4959}$ or $[Ni]_{\lambda5200}$, were found which could affect the measurements of other metallic indices. An example spectrum with weak nebular emission in $[O_{III}]_{\lambda5007}$ is presented in Figure 3.2.

It was also found that the index Hβ has traces of contamination from emission. The correction of this index is of particular importance in this study given that it is the main age indicator. The presence of emission in Hβ decreases the magnitude of the measured index and the inferred age becomes older (Hβ decreases with the age of the stellar population). González (1993), studying a sample of bright elliptical galaxies found an empirical correlation between the EW$[O_{III}]_{\lambda5007}$ and the EW of Hβ in emission. For his brightest galaxies he found that $\frac{H\beta_{emission}}{EW[O_{III}]_{\lambda5007}} \sim 0.7$. However, Trager et al. (2000) found in a sample of 27 elliptical galaxies that this relation has variations between 0.33 and 1.25, and that the mean value is 0.6 instead of 0.7.
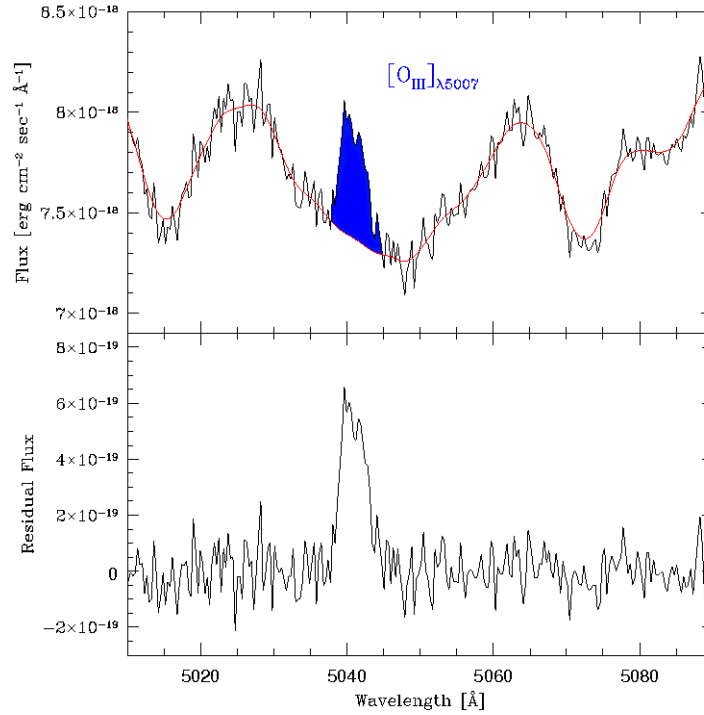
Figure 3.2. Top: $[O_{III}]_{\lambda 5007}$ nebular emission in an S0 galaxy spectrum; red line represents the best combination of stellar templates that reproduce the galaxy's spectrum. Bottom: residuals between the galaxy's spectrum and best stellar template; the equivalent width of $[O_{III}]_{\lambda 5007}$ was measured from these residual spectra.

Accordingly, it was decided to apply the following (additive) emission correction for the index $H\beta$:

$$\Delta(H\beta) = 0.6 \cdot EW[O_{III}]_{\lambda 5007}, \tag{3.7}$$

where $EW[O_{III}]_{\lambda 5007}$ was measured from the residual spectra obtained by subtracting the best combinations of stellar templates from the galaxy spectra (Figure 3.2, bottom). The variations found by Trager et al. (2000) in the ratio $H\beta/[O_{III}]_{\lambda 5007}$ are translated into uncertainties in the determination of the age of the order of 3%, negligible compared to other sources of error for this index. For our S0 galaxies, the corrections applied to $H\beta$ were not usually larger than 10% of the original measurements.

In this work, two combined indices were also used, $\langle Fe \rangle$ (Gorgas, Efstathiou & Aragón-Salamanca 1990) defined as

$$\langle Fe \rangle = \frac{Fe5270 + Fe5335}{2}, \tag{3.8}$$

and $[MgFe]'$ (González 1993; Thomas, Maraston & Bender 2003) defined as

$$[MgFe]' = \sqrt{Mgb \cdot (0.72 \times Fe5270 + 0.28 \times Fe5335)}. \tag{3.9}$$

$[MgFe]'$ will be particularly important for the analysis of stellar population pa-

rameters, like age and metallicity, given its almost null dependency on α-element abundance (Thomas, Maraston & Bender 2003).

All measured and corrected central indices for the Fornax sample are presented in Tables B.2 (at 3 Å resolution) and B.3 (at Lick resolution) in the Appendix.

Finally, note that in different parts of this work the atomic indices are sometimes expressed in magnitudes (following Colless et al. 1999) according to the expression

$$\text{Index}^* = -2.5 \cdot \log\Big(1 - \frac{\text{Index}}{\Delta\lambda}\Big), \tag{3.10}$$

were Index* represents the index in magnitudes, Index is the index expressed in Å, and $\Delta\lambda$ is the central bandwidth in Å, listed in Table 3.1. In the particular case of $\langle\text{Fe}\rangle$, the index in magnitudes was calculated using

$$\langle\text{Fe}\rangle^* = -2.5 \cdot \log \frac{1}{2}\Big(1 - \frac{\text{Fe5270}}{\Delta\lambda_{\text{Fe5270}}} - \frac{\text{Fe5335}}{\Delta\lambda_{\text{Fe5335}}}\Big), \tag{3.11}$$

while [MgFe]$'$ was always expressed in Å.

3.2 Comparison between indices at different resolutions

In this section, comparisons between line indices measured at different resolutions are made in order to understand in a qualitative way the possible effects on the ages and metallicities when inferred from degraded spectra. In Figure 3.3, measurements of all central indices at 3 Å and Lick resolution are compared for the whole galaxy sample.

All forthcoming comparisons are made in relation to the 3 Å indices and the estimated stellar population parameters derived with such data. The Hβ index suffers little degradation, where only the galaxy NGC 1375, with the strongest Hβ-absorption, may suffer from a small relative decrement of its luminosity-weighted age estimate. Also all Mg indices suffer very little change, while the Fe indices present larger variations in the low-resolution measurements. In general, Fe indices present systematic shifts with respect to the 1:1 lines with slightly larger differences for galaxies with strong spectral features. The dependence on index intensity may introduce some differences in the relative metallicities derived using Fe features by diminishing this parameter in galaxies with strong Fe lines. However, the relative differences in shifts among the galaxies are not strong enough to make this an important effect. The relative index variations between galaxies can be easily appreciated in Figure 3.4, where the indices at 3 Å resolution are plotted versus the fractional change when they are measured at Lick resolution.

The Fe features vary, on average, by -15%, while the Hβ and the Mg indices variations are usually less than -10%. Concerning the estimate of the [Mg/Fe] relative abundances, the fact that the Mg indices present little variation in comparison to the Fe indices will certainly introduce changes for each individual galaxy if the abundances are measured as the differences between metallicities (e.g. [Fe/H]$_{\text{Mgb}}$ − [Fe/H]$_{\langle\text{Fe}\rangle}$). However, the similar variations in the Fe indices experienced by all the galaxies will result in the *relative* [Mg/Fe] abundances between them being mostly
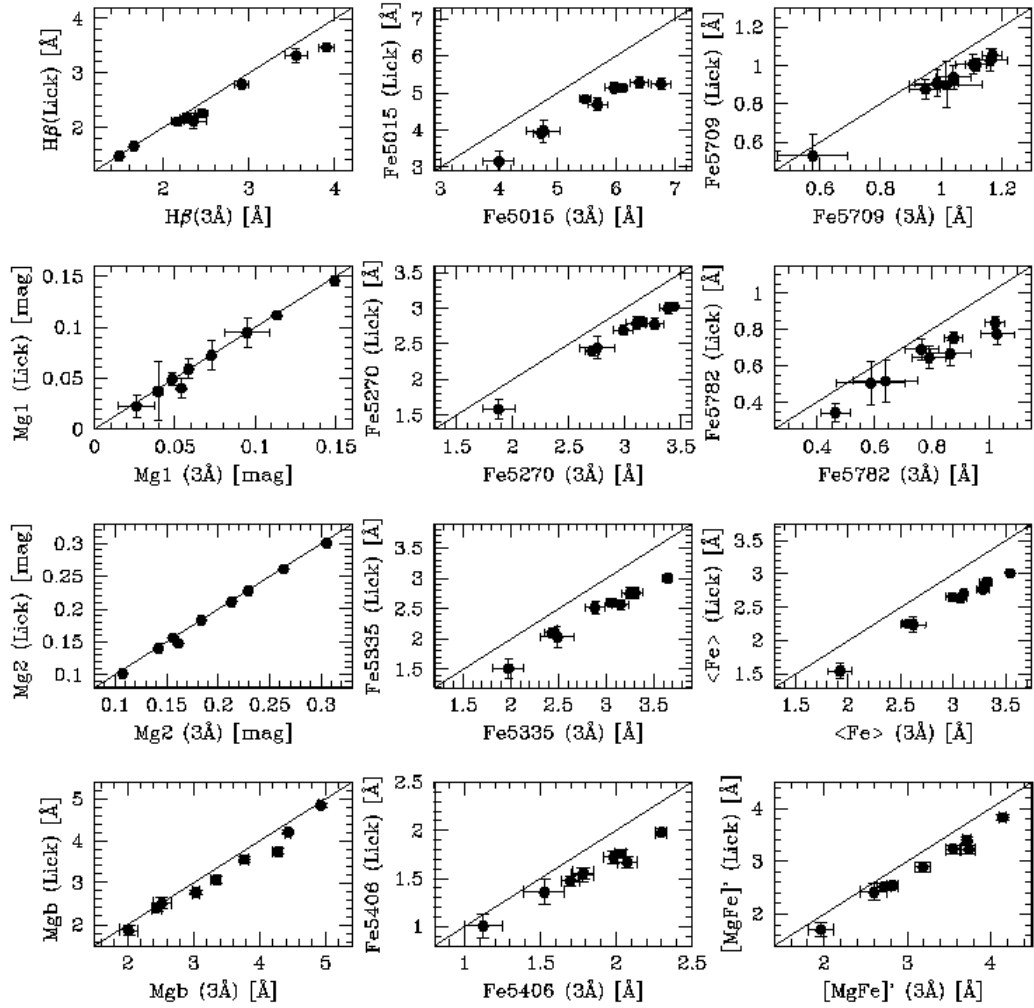
Figure 3.3. Comparison of the central line indices measured at 3 Å and Lick resolutions.
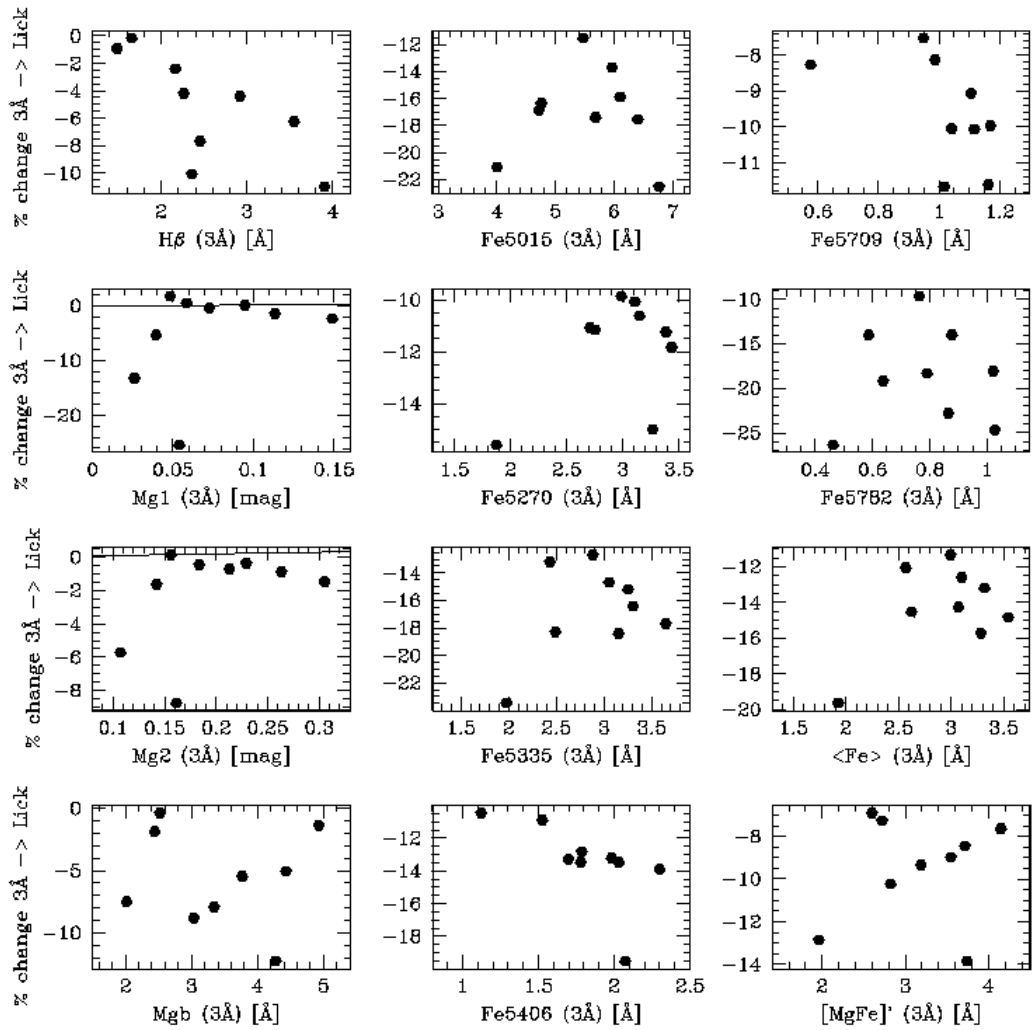
Figure 3.4. Central line indices at 3 Å resolution versus fractional change (%) when measured at the Lick resolution.

unaffected. In any case, the index ratio Mgb/$\langle$Fe$\rangle$ provides an alternative model-independent tracer of the α-element abundances previously applied by other authors (see TMB03).

In summary, in this section comparisons between line indices measured at 3 Å and Lick resolution have been made in order to find possible systematic differences which could affect our conclusions when one set or the other is used. Negligible variations are found in the Hβ and Mg indices. A somewhat larger change is detected in the Fe features, but we conclude that such effects will not introduce important *relative* changes in the ages, metallicities and [Mg/Fe] abundances between the galaxies.

3.3 The Models: consistency with the data

Before showing the main results, in this section some consistency checks between the BC03 models and the data are presented. These tests give an idea of how well the models describe the data and, in consequence, how the model results should be interpreted. For a stellar population study, it is important to check if there are significant differences in the relative spectrophotometric calibrations of the data and the stellar libraries used by the models. If differences are found, the results must be interpreted accordingly. Although ages and metallicities were estimated using Lick resolution data and models, some qualitative comparisons were also made with the higher resolution data. Therefore, the consistency tests were performed for both the 3 Å and Lick resolution BC03 models and data sets.

3.3.1 3 Å resolution models and data

When using the 3 Å resolution STELIB library, it is expected to find little differences with the data because both of them were flux calibrated by using spectrophotometric standard stars.

The tests consist of creating index–index plots which are almost degenerate in age and metallicity. In this way, the model grids describe narrow bands in the index–index space, regions which should trace the galaxies' data if the models describe accurately the properties of these objects and if there are no problems with the relative flux calibrations.

In Figure 3.5, different Mg indices are plotted against each other. The folded grids represent BC03 3 Å resolution models, and the line indices measured within $R_{\rm e}/8$ are plotted for the complete S0 sample. The match between data and models is very good, with a hint of a small systematic deviation for galaxies with intense Mg indices (NGC 1316, 1380 and 1381). A similar plot is presented in Figure 3.6 for six Fe indices. In these cases, the scatter from the models is larger than for the Mg indices, but the models seem to trace the mean trends in the data. For the three plots with Fe5015, however, there seems to be some systematic deviation between the data and model grids. Because the central bandpass of Fe5015 was corrected from [O$_{\rm III}$]$_{\lambda 5007}$ emission, this particular index must be used with caution.

In summary, no important mismatches were found between indices and model predictions at 3 Å resolution, suggesting that the relative flux calibrations are con-
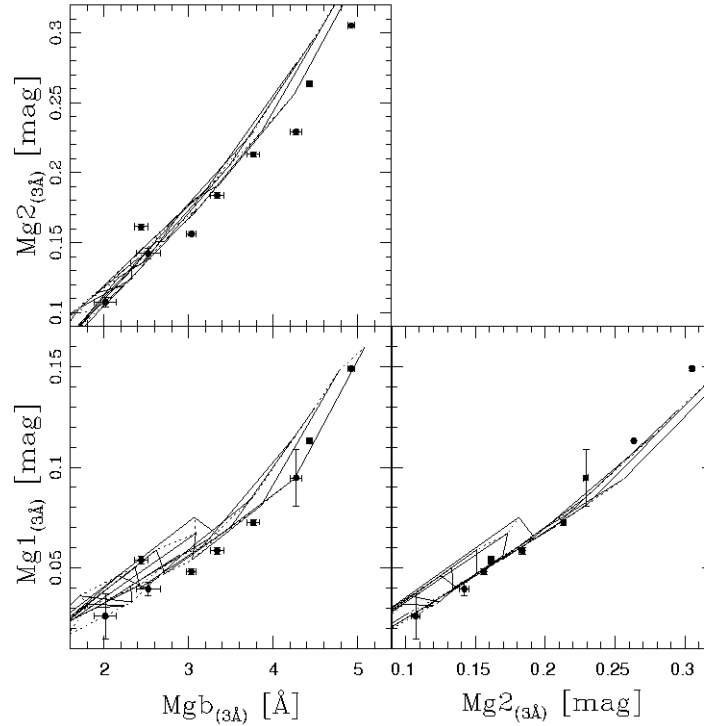
Figure 3.5. Consistency test using Mg indices and BC03 models at 3 Å resolution. Folded grids are BC03 models and datapoints correspond to central indices (within $R_{\rm e}/8$) of S0 galaxies in Fornax Cluster.

sistent with each other. By assuming solar abundances, BC03 models are able to consistently reproduce the observations for the majority of our galaxies. Therefore, in the following sections these models can be confidently used to make qualitative comparisons with our data set.

3.3.2 Lick resolution models and data

In comparison to the previous case, models based on Lick/IDS libraries (e.g. some of the models published by BC03, TMB03) could be more problematic. This is because the Lick libraries are not calibrated in flux, but flux-normalised by using a tungsten lamp. Therefore, in this system the measured indices are usually corrected by additive factors calculated from observations of stars from the Lick library with the same instrumental configuration and photometric conditions as the data. We lack such data in the current study, so any potential difference between data and models cannot be corrected, but has to be taken into consideration in the interpretation of the resulting ages and metallicities. The test described in the previous section were also applied to the Lick resolution data and models and the results are presented in Figures 3.7 and 3.8.

Figure 3.8 shows Fe indices in good agreement with model predictions. The scatter found in the previous section and a hint of a systematic deviation in panels involving Fe5015 are also present here, which reenforce the idea that the Fe5015

Figure 3.6. Consistency test using Fe indices and BC03 models at 3 Å resolution. Folded grids are BC03 models and datapoints correspond to central indices (within $R_e/8$) of S0 galaxies in Fornax Cluster.

index must be used with caution. Stronger deviations between models and data are evident for the Mg indices in comparison to the tests at 3 Å resolution. These deviations are particularly strong in the plots with Mgb, while Mg$_2$ versus Mg$_1$ are in better agreement with the models, confirming the fact that these two indices are almost spectrophotometric (Worthey et al. 1994). In his study of early type galaxies in Fornax, Kuntschner (2000, hereafter K00) found in similar tests comparable discrepancies between the Mg indices and other Lick-based models (Worthey et. al 1994 and Vazdekis et al. 1996), pointing out that these differences are inherent to the Lick/IDS system. So, any model based on the Lick libraries or their fitting functions is likely to show the same offsets. The fact that similar deviations in the Mg features and none in Fe were found here and in K00 (who used spectrophotometrically-corrected data to the Lick system) makes us suspect that the observed mismatches between the BC03 models and our data are mainly driven by the effect described in K00 and not by the absence of a spectrophotometric correction to our indices. In any case, it was preferred to take a conservative approach and interpret model results (ages, metallicities) as *relative* and not as *absolute* values.
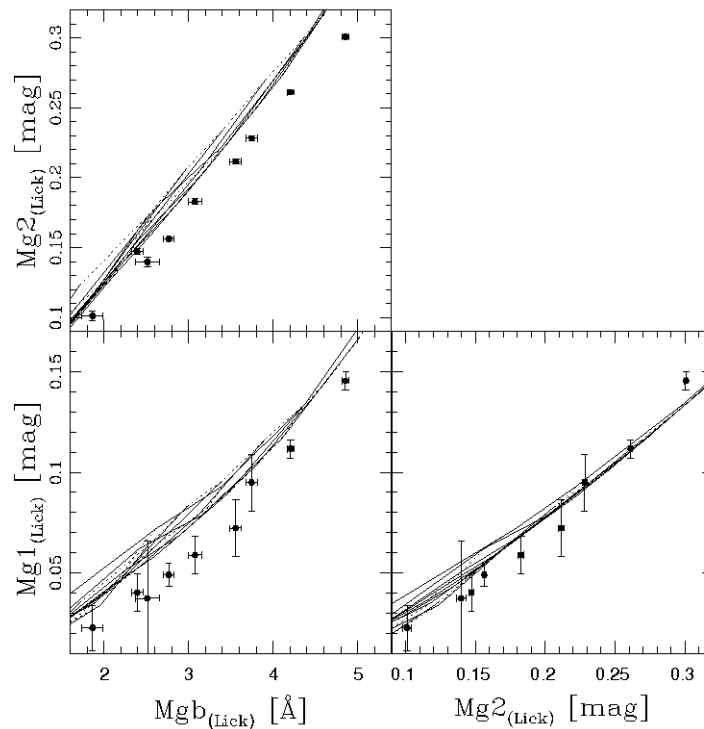
Figure 3.7. Consistency test using Mg indices and BC03 models at the Lick resolution. Folded grids are BC03 models and datapoints correspond to central indices (within $R_e/8$) of S0 galaxies in the Fornax Cluster.

3.4 Results and Discussion

In this section, the main results of the central stellar populations study are presented. As mentioned earlier, K00 studied the central stellar populations of all ellipticals and S0s in the Fornax Cluster by using lower quality optical spectra than the one presented in this thesis. Therefore, his study will be a constant reference in the forthcoming pages. From this point on, the BC03 models at $3\,\text{Å}$ resolution were always preferred for qualitative comparisons between the data and model grids. Only for the explicit calculation of ages, metallicities and [Mg/Fe] abundances the models and data at the Lick resolution were applied. Unless explicitly mentioned, the $3\,\text{Å}$ resolution data and models should be assumed.

Many previous works on stellar populations of early-type galaxies have concentrated on the relations between velocity dispersion and Mg indices (e.g. Terlevich et al. 1981; Gorgas et al. 1990; Guzmán et al. 1992; Bender et al. 1993; Jorgensen et al. 1996; Bender et al. 1998; Bernardi et al. 1998; Colless et al. 1999; Jorgensen 1999; K00; Poggianti et al. 2001; Mehlert et al. 2003; Thomas et al. 2004), which are usually interpreted as correlations between mass and metallicity. In this work, the relations between 10 line indices and the central velocity dispersion, σ_0, are studied in order to unmask the driving variables behind the observed slopes and scatter. In Figure 3.9, the relations between line indices (in magnitudes, equation 3.10) and
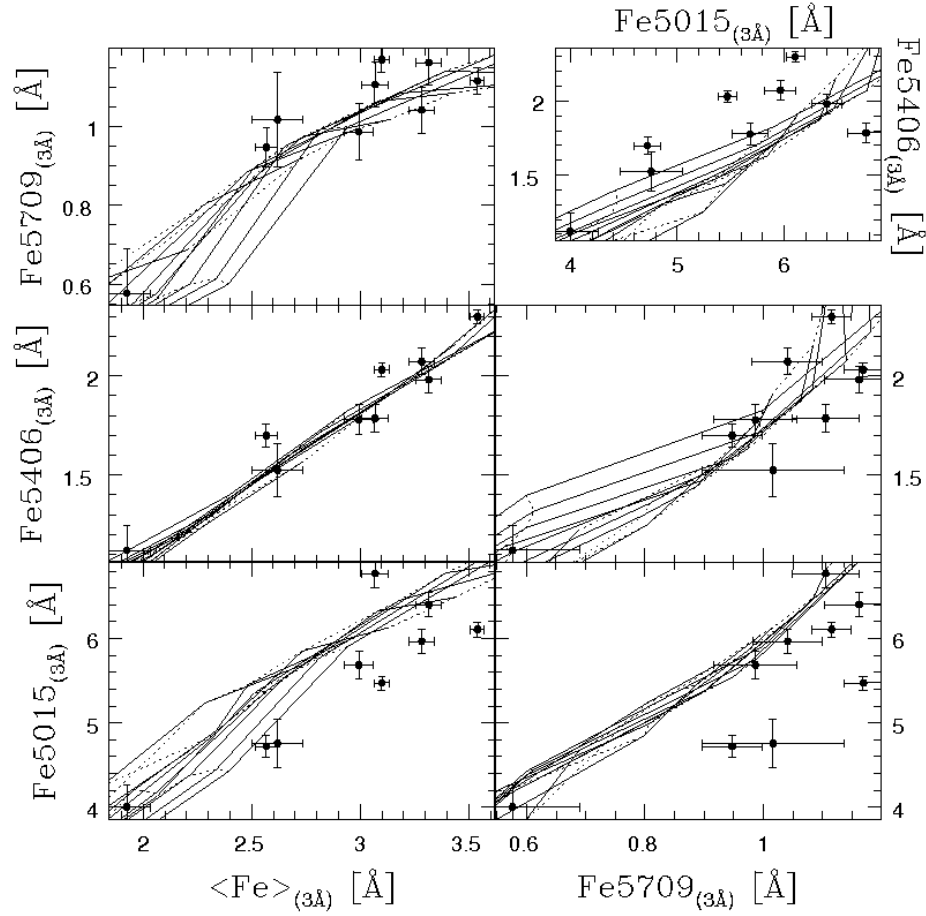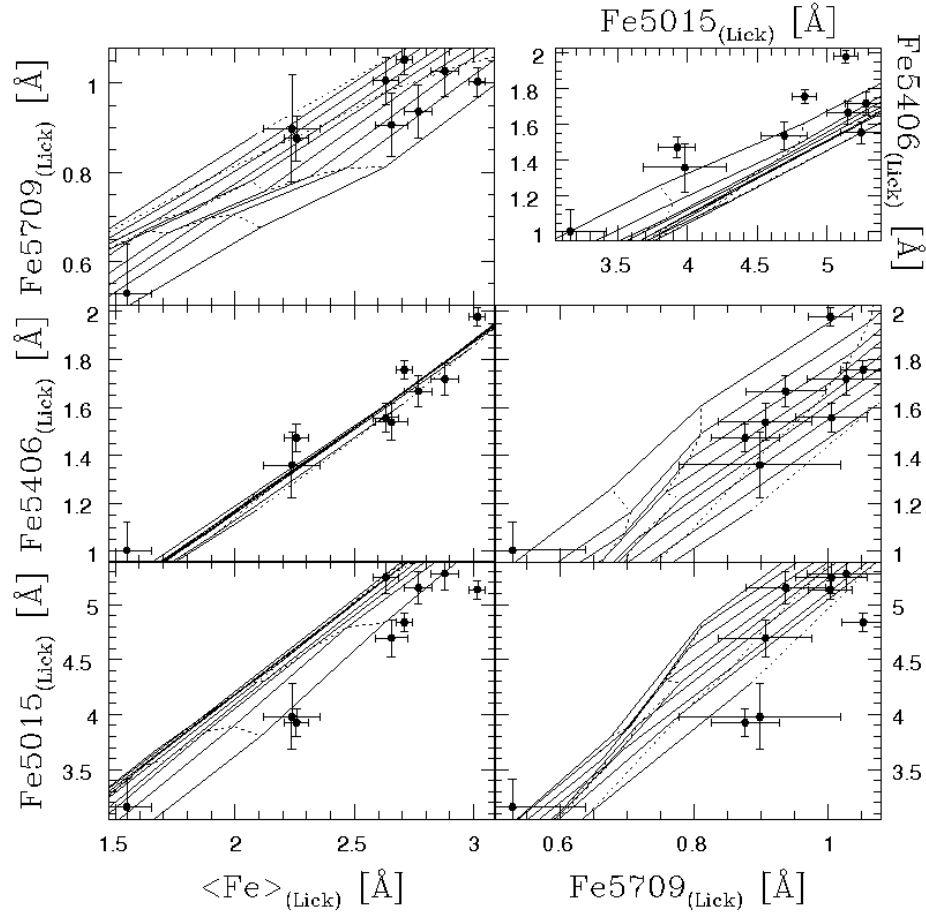
Figure 3.8. Consistency test using Fe indices and BC03 models at the Lick resolution. Folded grids are BC03 models and datapoints correspond to central indices (within $R_e/8$) of S0 galaxies in the Fornax Cluster.

$\log(\sigma_0)$ are presented for our sample of 9 S0s.

Rather than forming continuous trends, Figure 3.9 shows the three bright galaxies (NGC 1316, 1380 and 1381) and the rest of faint S0s in two separate clumps, each one in opposite extremes of the σ_0 range. However, because the sample was selected only according to morphological classification at optical wavelengths (see K00), there is no obvious selection bias against galaxies of intermediate σ_0 values. Therefore, this sample will be considered to describe the two extremes of continously-populated Index*–$\log(\sigma_0)$ relations.

The plots in Figure 3.9 confirm some of the results of K00. First, faint S0s have a large scatter with respect to the main relations, while the bright galaxies NGC 1380 and NGC 1381 closely follow the relations for ellipticals estimated by K00 (red dashed lines in Figure 3.9). Also, the merger remnant NGC 1316 (triangle in Figure 3.9) departs significantly from the Mg_1– and Mg_2–$\log(\sigma_0)$ relations (at more than 4-sigma level in both indices) towards low Mg absorption at a given σ_0, while closely following the remaining Fe–$\log(\sigma_0)$ relations. These facts, and the comparatively-high Hβ absorption in the Hβ–$\log(\sigma_0)$ diagram have been interpreted by K00 as the
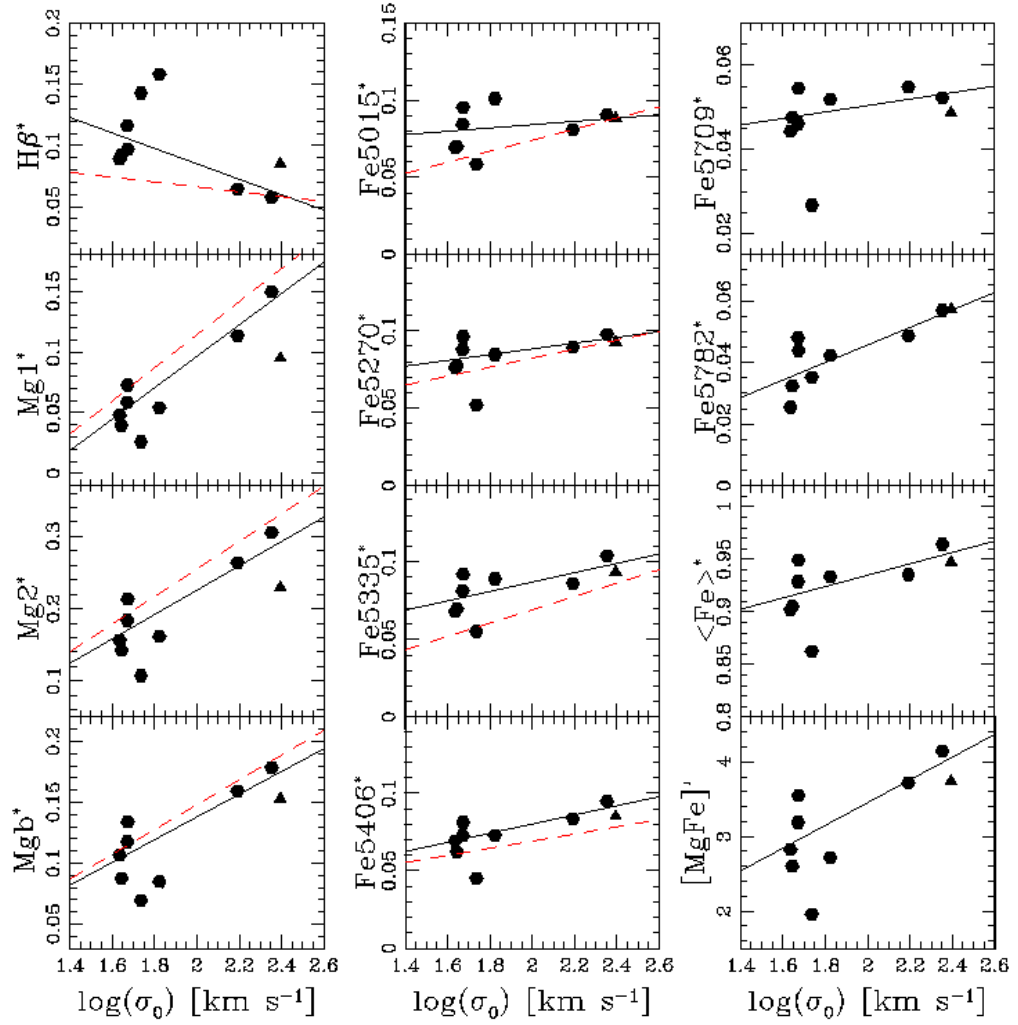
Figure 3.9. Central line indices (in magnitudes) versus $\log(\sigma_0)$. Continuous lines are the best fits to the datapoints; red dashed lines represent the best fits to normal ellipticals in Fornax from Kuntschner (2000).

Table 3.4. Parameters of the linear fits Index* = $a + b \cdot \log(\sigma_0)$ of the S0 galaxies in Fornax. σ_{std} is the standard deviation about the fit.

Index	$b \pm \delta(b)$	$a \pm \delta(a)$	σ_{std}
Hβ^*	-0.0633 ± 0.0031	0.2114 ± 0.0066	0.0360
Fe5015*	0.0107 ± 0.0021	0.0625 ± 0.0045	0.0219
Mg$_1^*$	0.1290 ± 0.0016	-0.1618 ± 0.0034	0.0229
Mg$_2^*$	0.1683 ± 0.0018	-0.1111 ± 0.0038	0.0462
Mgb^*	0.0932 ± 0.0027	-0.0486 ± 0.0056	0.0258
Fe5270*	0.0185 ± 0.0022	0.0509 ± 0.0045	0.0161
Fe5335*	0.0303 ± 0.0025	0.0262 ± 0.0052	0.0135
Fe5406*	0.0293 ± 0.0027	0.0214 ± 0.0056	0.0112
Fe5709*	0.0077 ± 0.0025	0.0349 ± 0.0053	0.0125
Fe5782*	0.0284 ± 0.0032	-0.0113 ± 0.0068	0.0071
$\langle$Fe$\rangle^*$	0.0538 ± 0.0037	0.8272 ± 0.0077	0.0310
[MgFe]$'$	1.5212 ± 0.0801	0.4087 ± 0.1661	0.5311

signature of the presence of a younger stellar population in this galaxy, probably formed during the merger. Finally, the slopes of the Mg–$\log(\sigma_0)$ trends are steeper than the ones for the Fe lines (see fit equations in Table 3.4), as K00 found for his fits to normal ellipticals.

3.4.1 The Slopes of the Index*–$\log(\sigma_0)$ relations

To study which parameters are driving the observed slopes in the Index*–$\log(\sigma_0)$ relations, the models of BC03 were used to parametrise the individual indices as a function of metallicity ([Fe/H]) and $\log$(age). Because our galaxies cover a wide range in ages and [Fe/H], we use models with ages from 1.0 to 12.6 Gyr and metallicities from -0.64 to 0.55 dex. The resulting parametrisations are presented in Table 3.5. The last two columns give the required dependence of $\log(\sigma_0)$ on metallicity and age respectively, if that is the *only* driving variable for the observed slopes in the Index*–$\log(\sigma_0)$ relations. Interestingly, these parametrisations show that the Mg–$\log(\sigma_0)$ relations depend as strongly on age as on metallicity. On the other hand, the slopes of the Fe indices versus $\log(\sigma_0)$ relations can be reproduced with weaker dependencies on metallicity than on age, but the differences between both dependencies are not very large. Naively, a much lower dependence on metallicity relative to the one on age would be expected for these metallicity tracers. Only the behaviour of the Hβ^*–$\log(\sigma_0)$ relation matches the expectations, presenting a slope much easier to reproduce by an age dependence than by a metallicity one.

It is also interesting to notice that not all the [Fe/H]-sensitive indices have the same dependence on [Fe/H]; the three Mg indices (Mg$_1$, Mg$_2$ and Mgb) required a stronger [Fe/H] dependence than the Fe indices in order to explain their slopes in the Index*–$\log(\sigma_0)$ diagrams. This would not be expected if metallicity is the only parameter varying with $\log(\sigma_0)$.

Therefore, these results suggest that age could be an important driver of the observed correlations while the role of metallicity is more uncertain. Also a third variable, such as the relative Mg abundances, may affect the relations by producing

Table 3.5. Parametrisation of the line indices using BC03 models: Index$^* = a + b \cdot [\text{Fe/H}] + c \cdot \log(\text{age[yr]})$. Last two columns: dependence of $\log(\sigma_0)$ on metallicity (age) if this is the only driving variable for the observed slopes in the Index*–$\log(\sigma_0)$ relations.

Index	a	$b \pm \delta(b)$	$c \pm \delta(c)$	$\frac{\partial[\text{Fe/H}]}{\partial\sigma_0}$	$\frac{\partial(\log(\text{age}))}{\partial\sigma_0}$
Hβ^*	0.7778	-0.0157 ± 0.0014	-0.0712 ± 0.0020	4.029	0.888
Fe5015*	-0.0854	0.0323 ± 0.0007	0.0177 ± 0.0011	0.330	0.601
Mg$_1^*$	-0.4602	0.0502 ± 0.0023	0.0547 ± 0.0032	2.568	2.357
Mg$_2^*$	-0.8310	0.1075 ± 0.0031	0.1053 ± 0.0044	1.564	1.597
Mgb^*	-0.4431	0.0521 ± 0.0014	0.0572 ± 0.0019	1.790	1.629
Fe5270*	-0.1509	0.0366 ± 0.0005	0.0244 ± 0.0007	0.505	0.757
Fe5335*	-0.1665	0.0388 ± 0.0006	0.0256 ± 0.0008	0.779	1.180
Fe5406*	-0.2017	0.0419 ± 0.0006	0.0284 ± 0.0008	0.699	1.029
Fe5709*	-0.0511	0.0199 ± 0.0007	0.0098 ± 0.0009	0.386	0.781
Fe5782*	-0.0856	0.0293 ± 0.0006	0.0137 ± 0.0009	0.968	2.074

relative differences between indices, each one with different sensitivities to changes in the chemical composition of these systems (Vazdekis et al. 2001; Sánchez-Blázquez et al. 2006).

A closer comparison between the data and the BC03 models could shed more light on the origin of the observed correlations. Individual ages and [Fe/H] were calculated by plotting different [Fe/H]-sensitive indices versus Hβ; data and models at the Lick resolution were used in this step. The details of the procedure applied here are described in Cardiel et al. (2003). Briefly, the ages and metallicities were logarithmically-interpolated from the model grid values by fitting the four closest cells to a datapoint with quadratic polynomials. The procedure also considers the effect of covariance when estimating the uncertainties for both parameters. In this way the age-[Fe/H] degeneracy is broken and luminosity-weighted estimates of both parameters were obtained. As an example, in Figure 3.10 four of these plots are presented for our central index values, also including the different BC03 model grids labeled in terms of age and [Fe/H]. Central line indices and the corresponding ages and metallicities are presented in Table B.4 for all the Fornax sample.

In Figure 3.11, $\log(\sigma_0)$ is plotted against age and [Fe/H] using different [Fe/H] sensitive indices. The continuous lines represent the best linear fits whose slopes are presented in Table 3.6. It is surprising that no obvious trends are observed in any of the [Fe/H]–$\log(\sigma_0)$ plots, considering that the Index–$\log(\sigma_0)$ relations are usually attributed, at least for ellipticals, to a chemical composition change with galaxy mass. The slope for the [Fe/H]–$\log(\sigma_0)$ relation using Mgb seems to be an artifact of the linear fit instead of pointing to a real correlation. Comparing the slopes for metallicity presented in Table 3.6 with the required metallicity dependences for each Index*–$\log(\sigma_0)$ relation in Table 3.5 it is clear that [Fe/H] cannot be the main driver of any of the Index* correlations with $\log(\sigma_0)$. The plots against age present stronger trends in the same direction as the Index*–$\log(\sigma_0)$ diagrams: the three high-σ_0 galaxies seem to be, on average, older than the rest of the sample. This result holds for all the age estimations, including the one using [MgFe]' which is unsensitive to α-element relative abundance variations. Comparing the slopes of
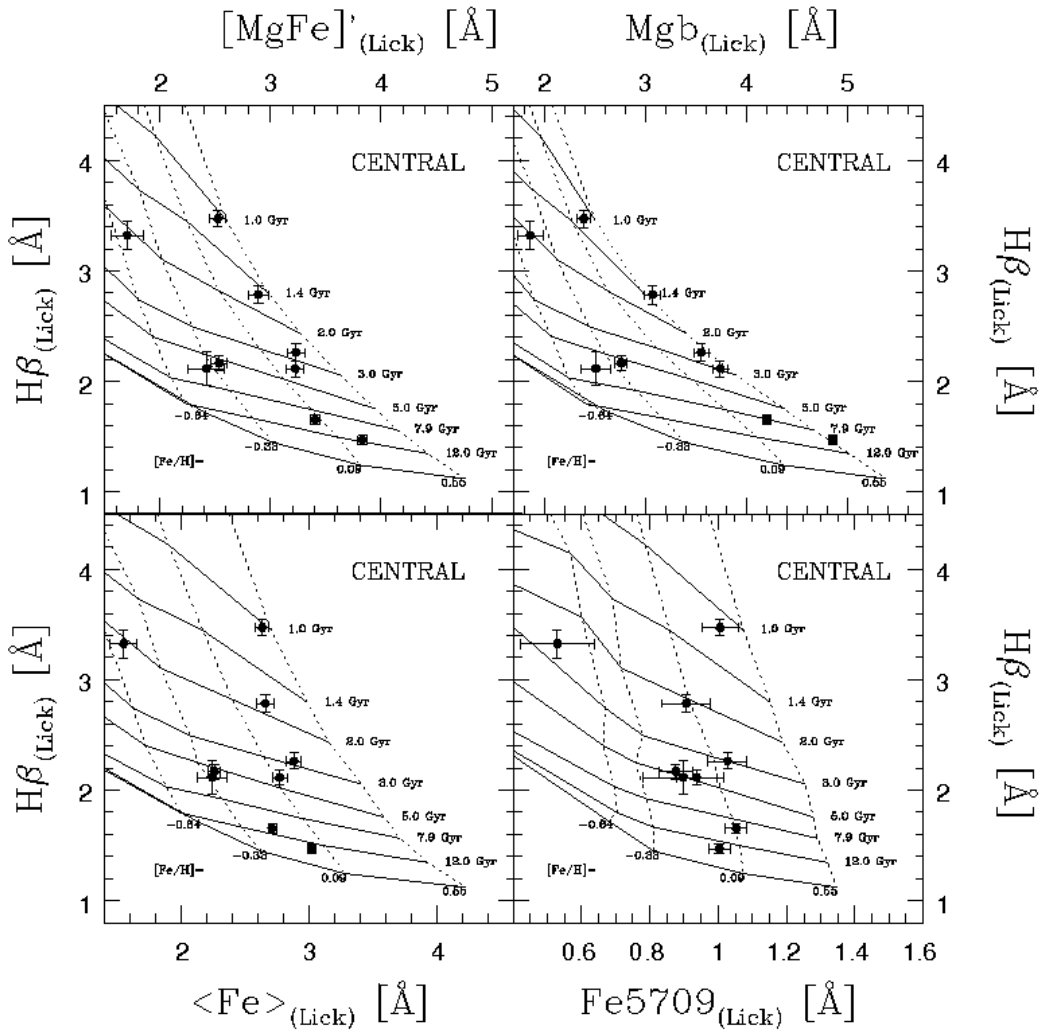
Figure 3.10. Central metallic indices versus Hβ for S0s in Fornax Cluster. The grids represent BC03 models labeled in terms of age and [Fe/H].

Table 3.6. Slopes from linear parametrization of log(age) or [Fe/H] versus $\log(\sigma_0)$ for S0 galaxies in Fornax (Figure 3.11) using different line indices as metallicity tracers.

Parameter	Slope	Parameter	Slope
$\log(\text{age})_{[\text{MgFe}]'}$	0.946 ± 0.079	$[\text{Fe/H}]_{[\text{MgFe}]'}$	0.208 ± 0.090
$\log(\text{age})_{\langle\text{Fe}\rangle}$	0.994 ± 0.075	$[\text{Fe/H}]_{\langle\text{Fe}\rangle}$	-0.189 ± 0.057
$\log(\text{age})_{\text{Mgb}}$	0.803 ± 0.080	$[\text{Fe/H}]_{\text{Mgb}}$	0.806 ± 0.106
$\log(\text{age})_{\text{Fe5709}}$	1.033 ± 0.074	$[\text{Fe/H}]_{\text{Fe5709}}$	-0.189 ± 0.113

these relations with the required age dependences for the observed Index*–$\log(\sigma_0)$ trends, we found that the Hβ* and almost all the Fe trends can be explained by an age effect. However, differences in relative age do not seem to explain the steeper slopes found for the Mg indices in comparison to Fe, reinforcing the idea that α-element relative abundances are playing an important role too.

The fact that NGC 1316 seems to depart from the main Mg relations while closely following the Fe trends may be explained by the effect of age. This merger remnant has a low luminosity-weighted age compared to the other bright S0s, closely resembling the mean for the fainter galaxies. Such a young population could reduce the intensity of some metallic features by increasing the overall continuum level. This effect would be particularly important for strong metallic features, like the Mg triplet (indices Mgb and Mg$_2$) and for the molecular indices Mg$_1$ and Mg$_2$ whose pseudocontinuum level is strongly dependent on large-scale changes in the continuum. The weaker Fe features in this spectral range could be less influenced by this effect, explaining why NGC 1316 appears in good agreement with the mean Fe relations.

At the beginning of this section, the possibility of a Mg (or α-element) abundance dependence of the Index*–$\log(\sigma_0)$ relations was pointed out, being re-enforced by the results presented above. This alternative was further explored by plotting Mg- versus Fe-sensitive indices and comparing the data to the solar-abundance predictions of the models (see Worthey, Faber & Gonzalez 1992). In Figure 3.12, twelve panels plotting central Mg versus Fe indices are presented, together with BC03 model grids. What is clear from almost all these panels is that the three brightest (high-σ_0) galaxies of our sample (open symbols in Figure 3.12) are not properly described by models which assume solar abundance ratios, presenting stronger Mg indices for a given Fe index than the model predictions. Between these three galaxies, the effect seems to be stronger for NGC 1380 and 1381, while NGC 1316 (the merger remnant) is usually closer to the solar-model grids. In similar plots, K00 found that only the nucleus of NGC 1380 presented this behaviour, suggesting that this galaxy is Mg overabundant compared to Fe.

An estimate of the relative Mg overabundances was calculated by comparing the relative metallicities derived from Fe- and Mg-sensitive indices and the same age indicator (Hβ in our case). In the top panel of Figure 3.13, $\log(\sigma_0)$ is plotted against the difference of the metallicities calculated by using Mgb and $\langle$Fe$\rangle$ as metallicity indicators. Data and models at the Lick resolution were used to estimate these metallicities. It is apparent from this plot that bright S0s are, on average, Mg
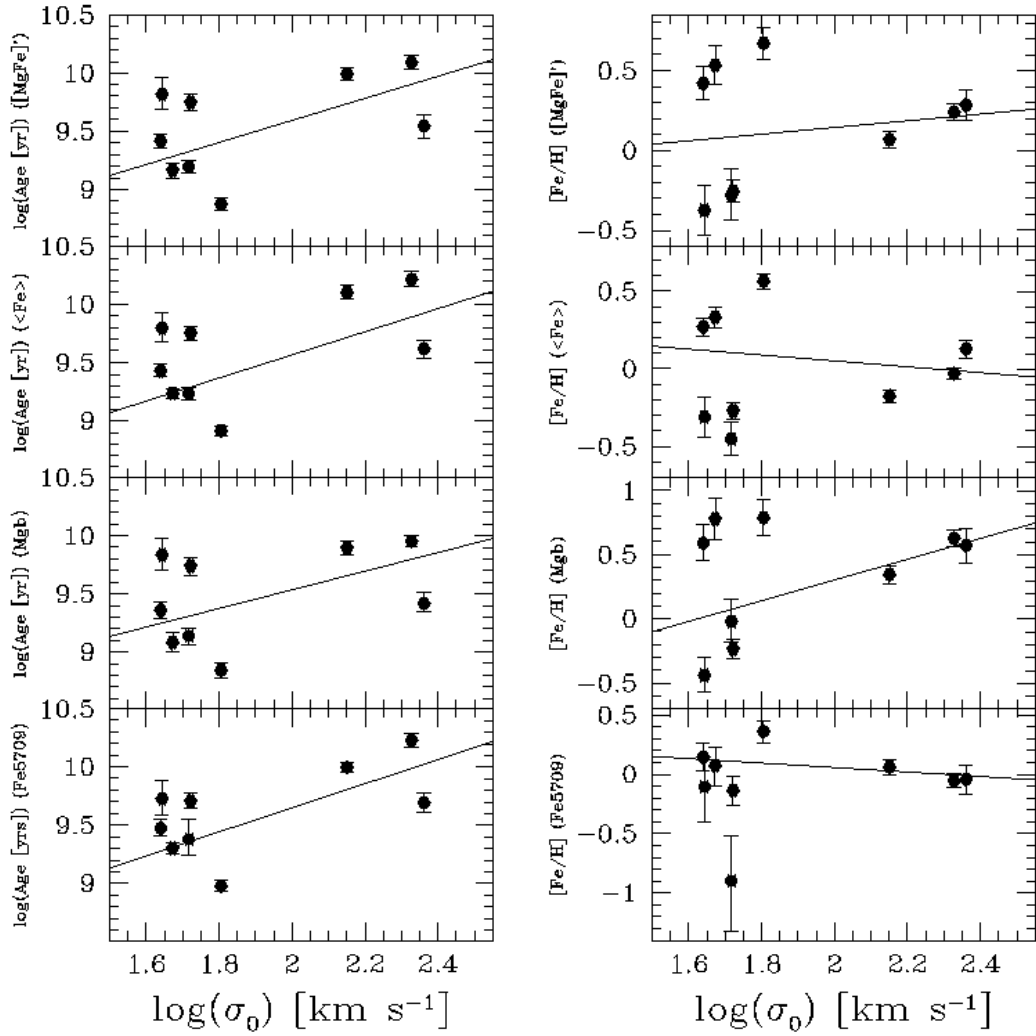
Figure 3.11. Central Ages and metallicities versus $\log(\sigma_0)$ for Fornax S0s. Lines represent the best linear fits to the data.
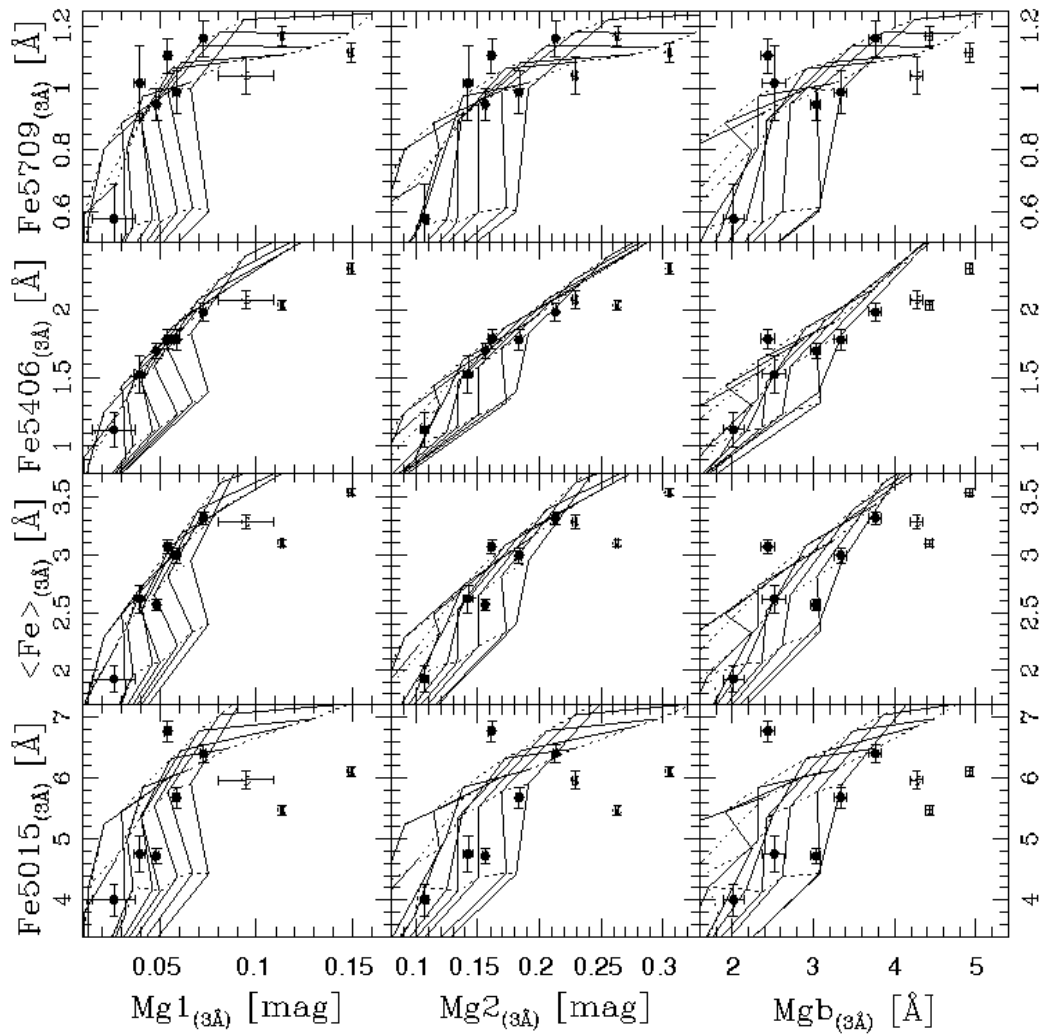
Figure 3.12. Central Mg versus Fe indices for Fornax S0s. Grids correspond to BC03 models at 3 Å resolution.
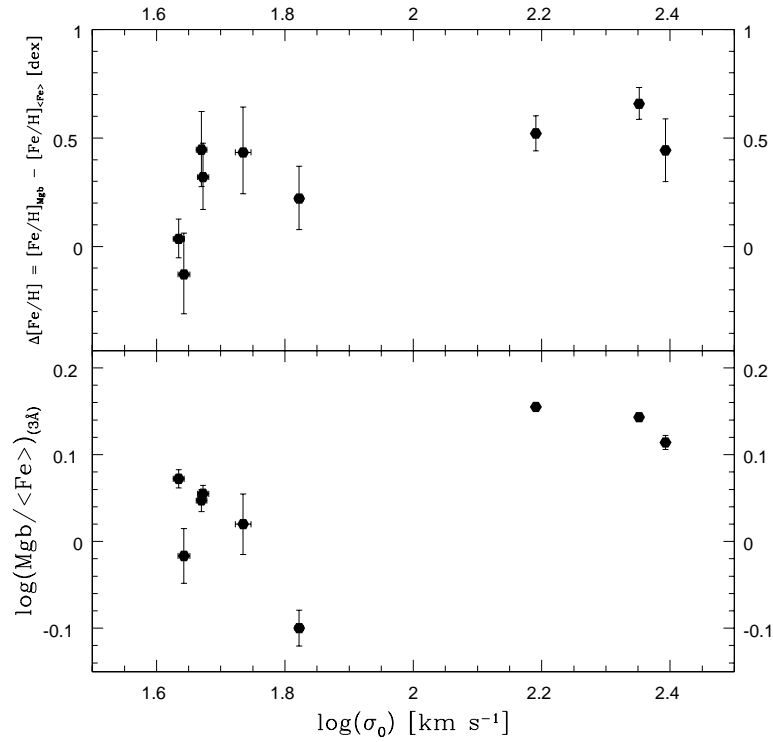
Figure 3.13. Mg/Fe relative abundance tracers versus $\log(\sigma_0)$ for Fornax S0s.

overabundant with respect to fainter galaxies; however the uncertainties coming from the models make this difference only marginally significant. The bottom panel of Figure 3.13 shows the index quotient $\mathrm{Mg}b/\langle \mathrm{Fe}\rangle$ versus the velocity dispersion. The ratio of these two indices has been used by TMB03 to calibrate the $[\alpha/\mathrm{Fe}]$ abundance ratio of their models, so it provides a good estimate of the relative behaviour of the Mg overabundance and, equally important, a model-independent test. With much reduced errors, it is clear that bright S0s have larger $\mathrm{Mg}b/\langle \mathrm{Fe}\rangle$ ratios than fainter objects. This model-independent test can explain why the slopes of the Index*– $\log(\sigma_0)$ correlations are steeper for the Mg indices than for the Fe ones, confirming the previous results of this section. The overall results also imply the existence of a correlation between age and $\mathrm{Mg}b/\langle \mathrm{Fe}\rangle$ (or $[\alpha/\mathrm{Fe}]$; see Figure 3.19, bottom panel in second column), in agreement to the previous findings of Fisher, Franx & Illingworth (1995) and Thomas, Maraston & Bender (2002) in elliptical galaxies.

Different authors have tried to explain the observed [Mg/Fe] overabundances in the context of galaxy formation and evolution. All these scenarios are based on nucleosynthesis models which predict that SNe Type II explosions mainly eject α-elements, like Mg, while Type Ia SNe are the main sources of enrichment of the ISM with Fe. Possible explanations include variations in the initial mass function (e.g. Schmidt 1963; Worthey et al. 1992; Vazdekis et al. 1999; Nagashima et al. 2005), selective loss of metals (Worthey et al. 1992), different time scales of star formation and different star formation histories. The last two have been very popular in the last few years in order to explain the observed overabundances in bright

ellipticals (e.g. Mehlert et al. 2003, Sánchez-Blázquez et al. 2006). In this scenario, early-type galaxies are believed to be remnants of gaseous mergers. This process produces a starburst where part of the gas is consumed and the remainder is ejected via stellar winds (for low mass remnants) or heated by different mechanisms (e.g. AGN, SNe, thermal conduction) in more massive systems, stopping further star formation. According to hierarchical merging, the starburst is more intense in the central regions of the remnant given the stronger potential well in the centre and subsequent dissipation of the gas towards it. The merger process implies a faster build-up of the system total mass, having shorter star formation timescales than systems grown by secular or more gentle processes. A short burst of star formation would not give enough time to incorporate the gas enriched with Fe from SNe Type Ia to the formation of further generations of stars, while SNe Type II would succeed in incorporation α-elements (like Mg) given their much earlier occurrence (in less than $1\,\mathrm{Gyr}$). In consequence, a relative [Mg/Fe] overabundance will be observed in these systems (understood as an *underabundance* of Fe) with respect to galaxies with younger luminosity-weighted ages and more extended star formation histories.

This scenario is in agreement with the results found here for our bright S0s, and is not surprising for NGC 1316, a well known merger remnant. However, whether this picture can be applied to the entire NGC 1380 and NGC 1381 galaxies or only to their nuclei, is something that cannot be tested with central line indices alone.

3.4.2 The Residuals of the Index*–log(σ_0) relations

Previous studies have looked for correlations between the Index*–log(σ_0) residuals (ΔIndex*) and different parameters that characterise the galaxies' structure or their stellar populations. Some of these efforts point out the existence of a dependence between ΔIndex* and the relative ages of elliptical galaxies (Schweizer et al. 1990; González & Gorgas 1996; Worthey & Collobert 2003) by comparing the residuals to the index Hβ.

Figure 3.14 shows these relations for our sample of S0 galaxies. A clear trend is observed only for the ΔHβ versus Hβ relation, which may be produced by correlated errors. Hints of trends are seen for the Mg indices but they do not seem to be statistically significant, while residuals from the Fe relations are clearly uncorrelated with Hβ.

The residuals were also compared to other parameters. In Figure 3.15, ΔIndex* is plotted against a measure of the rotational support of these galaxies, $V_{\mathrm{MAX}}/\sigma_{\langle \mathrm{R_e} \rangle}$, where V_{MAX} is the maximum rotational velocity (Chapter 2) and $\sigma_{\langle \mathrm{R_e} \rangle}$ is the mean velocity dispersion within $1\,R_{\mathrm{e}}$ of the bulge. Because NGC 1316 and ESO 359-G002 are not rotationally-supported systems, a proper V_{MAX} could not be estimated for these galaxies so their deprojected azimuthal velocities, V_{ϕ}, were used as lower limits. Hints of very weak trends are observed in Figure 3.15 for the panels corresponding to Hβ and the Mg indices, which are strongly dependent on the two pressure-supported galaxies for which V_{MAX} is more uncertain. However, because the Index*–log(σ_0) relations of these four indices present the largest scatter (see Table 3.4) it was decided to go one step further and explore the Index*–log(V_{MAX}) diagrams.
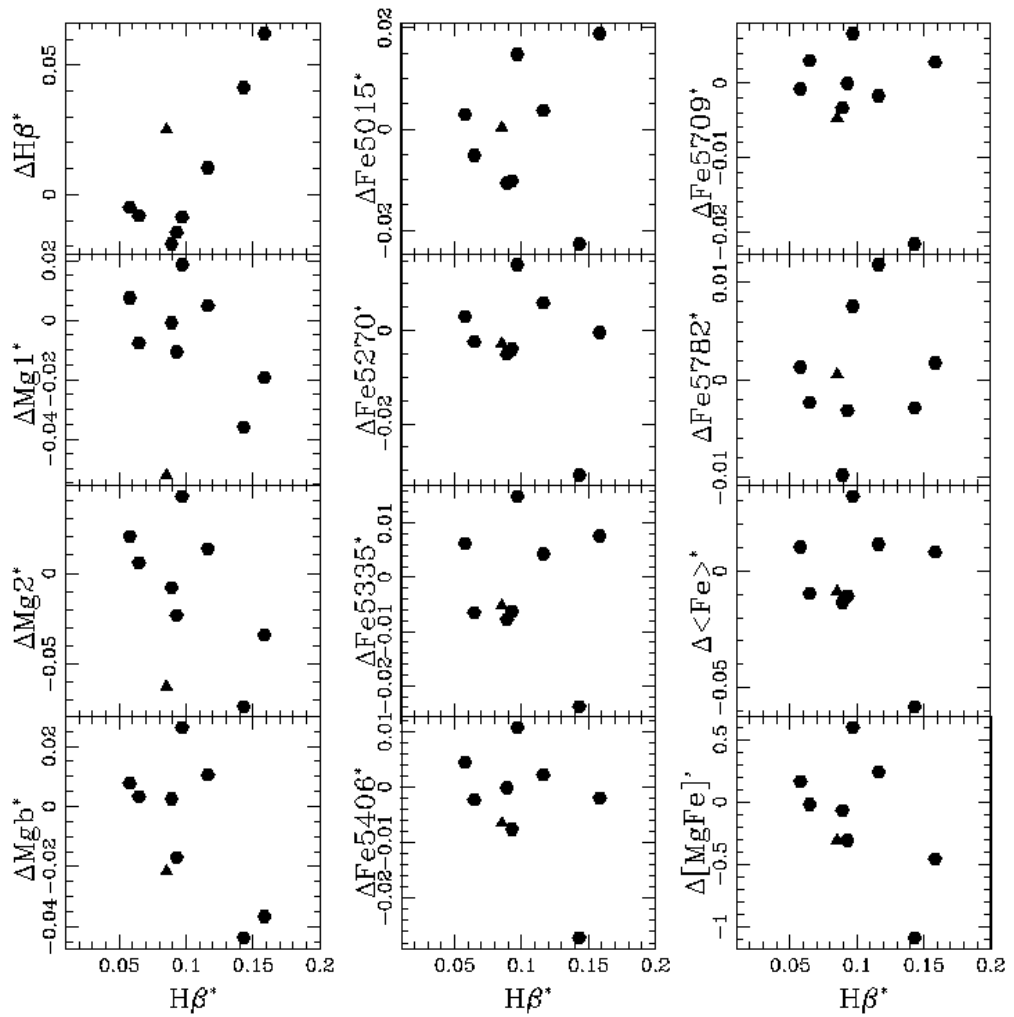
Figure 3.14. Residuals of the central Index*–log(σ_0) relations versus Hβ.
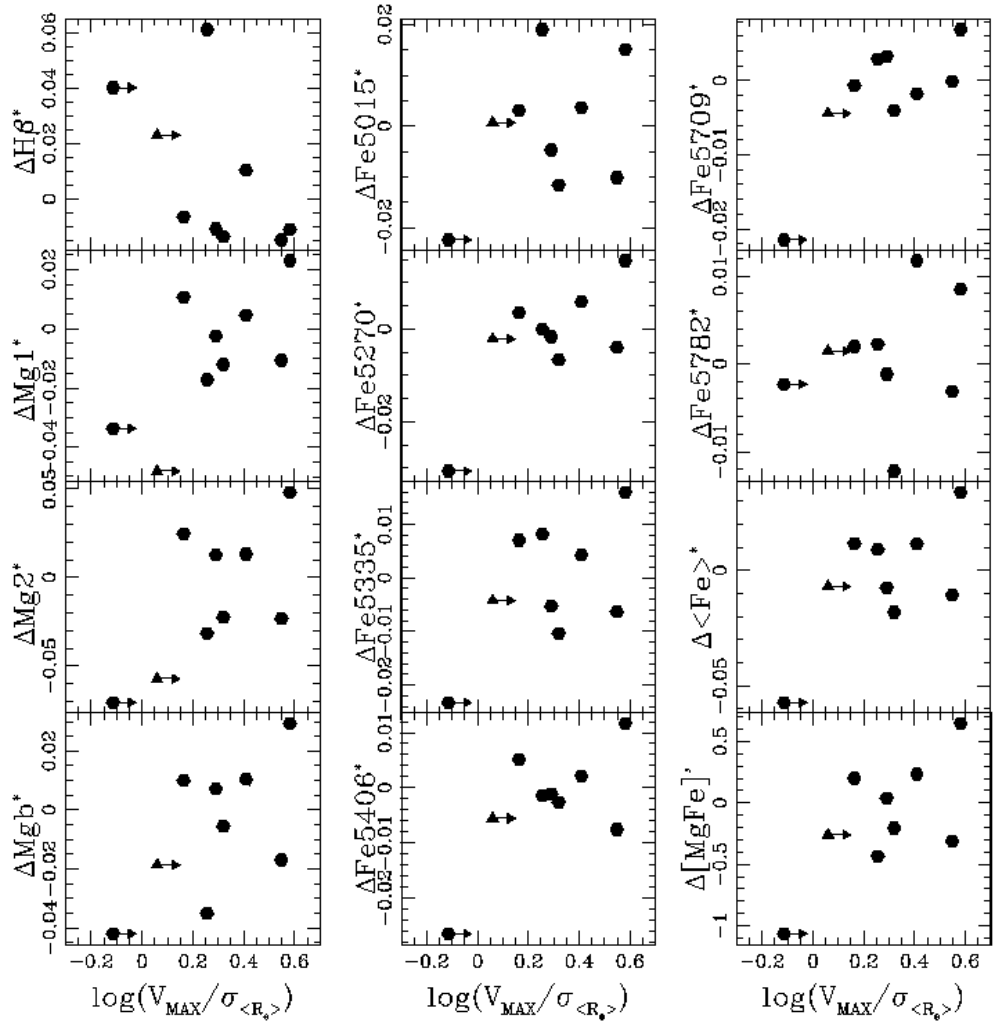
Figure 3.15. Residuals of the central Index*–$\log(\sigma_0)$ relations versus rotational support parameter, $V_{\text{MAX}}/\sigma_{\langle R_e \rangle}$. The triangle represents NGC 1316, a merger remnant. For the two galaxies with arrows, the deprojected azimuthal velocity, V_ϕ, was used instead of V_{MAX} as a lower limit.

Table 3.7. Parameters of linear fits Index* = $a + b \cdot \log(V_{MAX})$ of S0 galaxies in Fornax. σ_{std} is the standard deviation about the fit.

Index	$b \pm \delta(b)$	$a \pm \delta(a)$	σ_{std}
Hβ^*	-0.1099 ± 0.0046	0.3354 ± 0.0108	0.0214
Fe5015*	0.0197 ± 0.0030	0.0389 ± 0.0071	0.0143
Mg$_1^*$	0.2015 ± 0.0026	-0.3665 ± 0.0062	0.0233
Mg$_2^*$	0.2593 ± 0.0026	-0.3633 ± 0.0061	0.0355
Mgb^*	0.1446 ± 0.0038	-0.1906 ± 0.0089	0.0194
Fe5270*	0.0358 ± 0.0031	0.0062 ± 0.0073	0.0070
Fe5335*	0.0462 ± 0.0036	-0.0181 ± 0.0083	0.0094
Fe5406*	0.0475 ± 0.0038	-0.0279 ± 0.0090	0.0057
Fe5709*	0.0185 ± 0.0037	0.0080 ± 0.0086	0.0050
Fe5782*	0.0377 ± 0.0047	-0.0399 ± 0.0109	0.0098
$\langle Fe \rangle^*$	0.0895 ± 0.0053	0.7313 ± 0.0122	0.0166
[MgFe]$'$	2.5019 ± 0.1147	-2.2356 ± 0.2655	0.2802

Figure 3.16 shows the different line indices versus V_{MAX}, where clear trends appear in all the panels. Linear (least-squares) fits to the data were performed and presented as straight lines in each panel. The galaxy with the lowest velocity, ESO 359-G002, was excluded from the fitting process because the slope and zero-points would be strongly affected by an object with uncertain V_{MAX}.

In Table 3.7 the linear fit coefficients and standard deviations, σ_{std}, are presented. It is interesting to notice that for almost all the indices, σ_{std} is smaller than its counterpart from the Index*–$\log(\sigma_0)$ fits (see Table 3.4). If we assume that mass is the fundamental physical parameter governing the properties of these galaxies, the improvement in the fits may be interpreted in the sense that V_{MAX} is a better estimator of the total dynamical mass than σ_0, which is not totally surprising after highlighting in Chapter 2 the predominant rotational nature of these systems. As a test, the mass of these galaxies was parametrised as a function of the velocity dispersion and of V_{MAX} in order to compare how central indices correlate with both possible descriptions. If the galaxies are supported by rotation, we can write

$$M \propto V_{MAX}^2 \cdot R_d, \qquad (3.12)$$

where M is the total dynamical mass and the disk scale-length, R_d, was used to characterise the radius of the galaxies because it reaches the regions where the rotation curves become flat. If the galaxies are mainly supported by velocity dispersion, a similar expression can be obtained,

$$M \propto \langle \sigma^2 \rangle_{R_e} \cdot R_e, \qquad (3.13)$$

where R_e is the effective radius of the bulge and $\langle \sigma^2 \rangle_{R_e}$ is $\langle \sigma^2 \rangle$ inside R_e. It is important to point out that the results found within R_e hold for larger radii such as the half-light radius found in section 4.1. However, it was decided to present the results for R_e because this parameter is better constrained by the `GIM2D` models.

In Figures 3.17 and 3.18, central line indices are plotted versus $R_e \cdot \langle \sigma^2 \rangle_{R_e}$ and
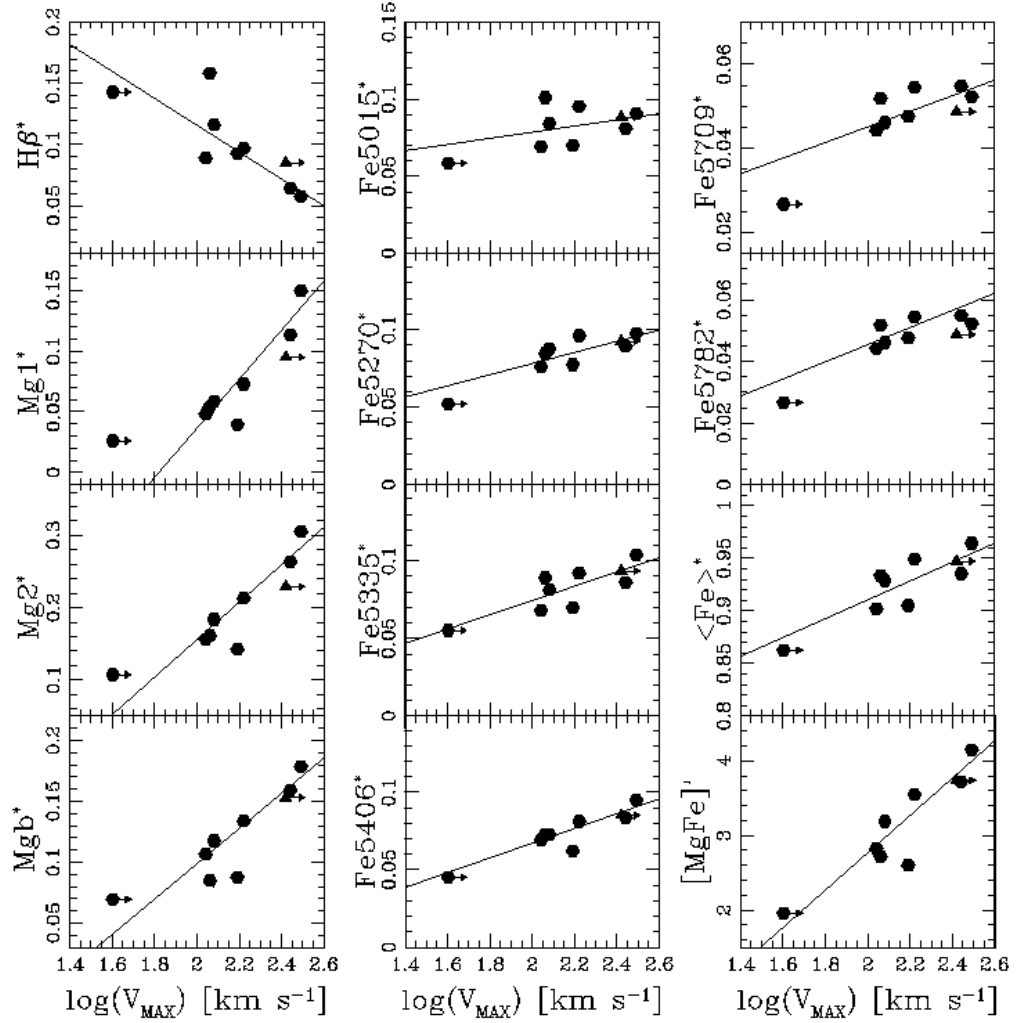
Figure 3.16. Central line indices (in magnitudes) versus $\log(V_{\mathrm{MAX}})$. Solid lines are the best fits to the datapoints, excluding ESO 359-G002. The triangle represents NGC 1316, a merger remnant. For the two galaxies with arrows, the deprojected azimuthal velocity, V_{ϕ}, was used instead of V_{MAX} as a lower limit.

Table 3.8. Spearman and Student-t tests for central stellar population parameters versus dynamical mass of S0 galaxies in Fornax (Figure 3.19). In parenthesis, probability of rejecting the null hypothesis of no correlation.

Dyn. Mass vs.	Spearman Test Coeff.	Student-t test Coeff.
$\log(\text{age})_{[\text{MgFe}]'}$	0.4167 ($< 90\%$)	1.2127 (85–90%)
$[\text{Fe/H}]_{[\text{MgFe}]'}$	0.2833 ($< 90\%$)	0.7817 (75–80%)
$\text{Mg}b/\langle\text{Fe}\rangle$	0.6833 (95–97.5%)	2.4762 (97.5–99%)

$R_\text{d} \cdot V_\text{MAX}^2$, respectively. Clearly, both parameters, σ and V_MAX, are tracing, to some extent, the mass of these systems. However, an important difference arises between pressure- and rotation-supported galaxies (open and filled dots, respectively): when the mass is estimated using σ, it is underestimated in rotationally supported systems with respect to pressure-supported ones, as is evident from the offset between open and filled dots in Figure 3.17. On the other hand, Figure 3.18 shows that if we estimate the mass using V_MAX, all the galaxies follow a common sequence. In this plot, lower limits for the two pressure-supported S0s (using V_ϕ) are indicated as open dots with arrows. For these two galaxies, masses were also estimated from their measured σ's by assuming a simple isothermal sphere in hydrostatic equilibrium and presented as open stars in Figure 3.18. The much tighter trends observed in this plot are consistent with our hypothesis that V_MAX is a much better tracer of the dynamical mass of these systems than σ.

Finally, in the first column of Figure 3.19, the derived physical parameters of the central stellar populations are plotted against the total dynamical mass as estimated by using V_MAX (or the isothermal sphere assumption for pressure-supported systems). No strong correlations are obvious from these plots. However Spearman rank and Student-t correlation tests (Table 3.8) indicate that the relation between α-elements overabundance and dynamical mass is significant at a 95–99 % confidence level. One possibility is that the uncertainties in the models are washing-out the real trends with age and metallicity. An alternative explanation is that the tight correlations observed between the line indices and galaxy mass are not governed by the variation of one of these stellar population parameters alone, but by a combination of them in some correlated way.

In summary, after applying different tests, the Index*–$\log(\sigma_0)$ relations for our S0s in the Fornax Cluster do not seem to be driven by metallicity as is usually assumed for ellipticals. Instead, stronger dependences on age and [Mg/Fe] overabundance are apparent, where the central regions of our bright galaxies seem to be formed in shorter timescales compared to fainter objects with more extended (and recent) star formation histories. Clearly, dynamical mass is the governing physical property in these correlations, and in S0s mass has to be estimated assuming rotational support. The scatter of the Index*–$\log(\sigma_0)$ relations is partially explained by the need to consider rotational support. The existence of tighter trends between Index* and $\log(V_\text{MAX})$ confirms this statement.
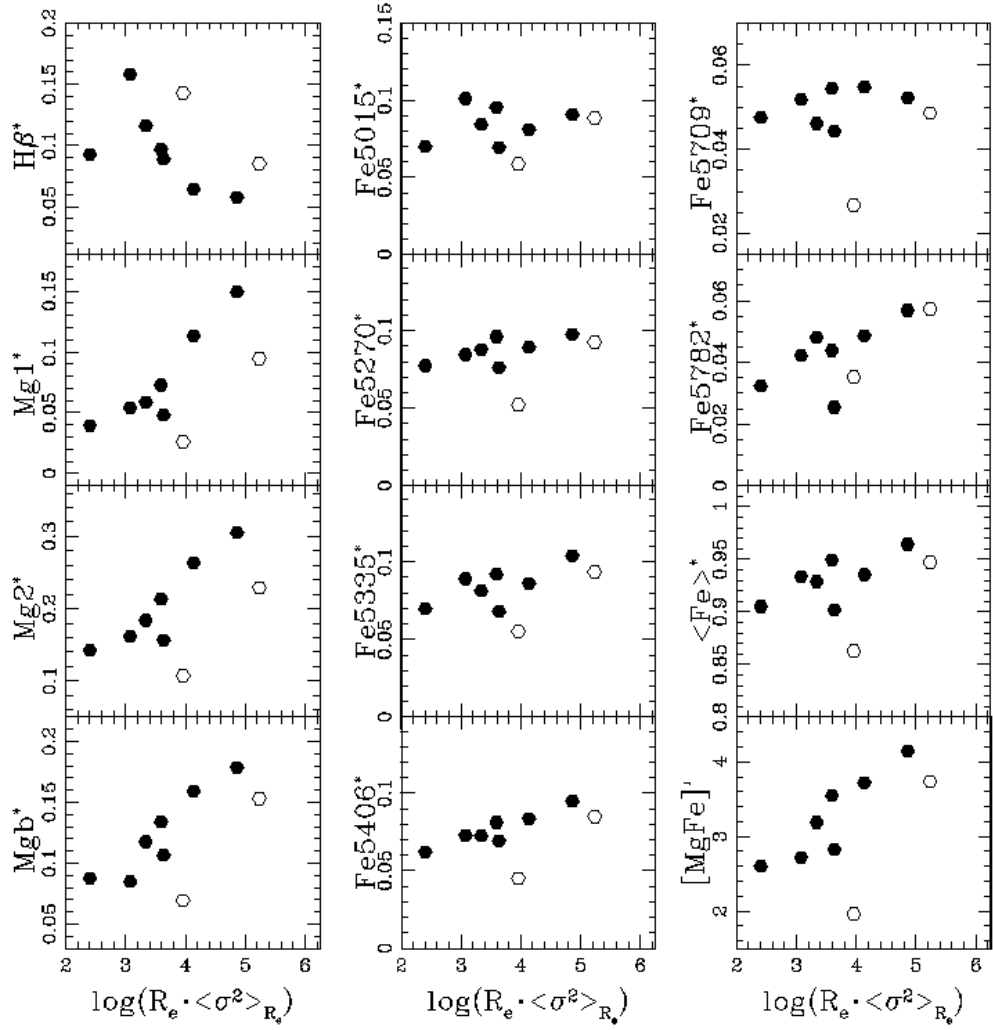
Figure 3.17. Central line indices versus $\log(R_e \cdot \sigma^2_{(R_e)})$, proportional to the total dynamical mass for pressure-supported galaxies. Open symbols represent NGC 1316 and ESO 359-G002, two pressure supported galaxies.
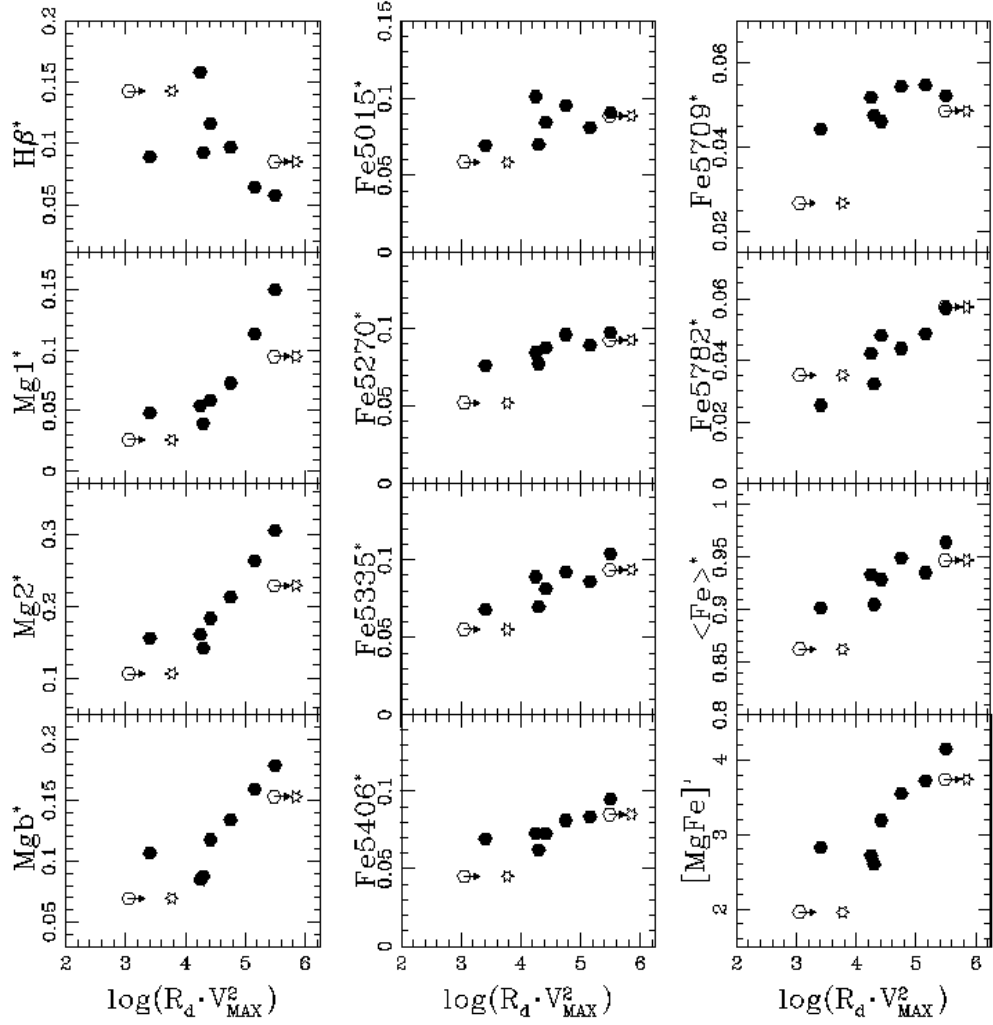
Figure 3.18. Central line indices versus $\log(R_d \cdot V^2_{\mathrm{MAX}})$, proportional to the total dynamical mass for rotationally-supported galaxies. Open symbols with arrows represent NGC 1316 and ESO 359-G002, two pressure supported galaxies. For these two objects the deprojected azimuthal velocity, V_ϕ, was used as a lower limit instead of V_{MAX}. Open stars correspond to the dynamical mass of these two galaxies estimated from σ by assuming an isothermal sphere in hydrostatic equilibrium.
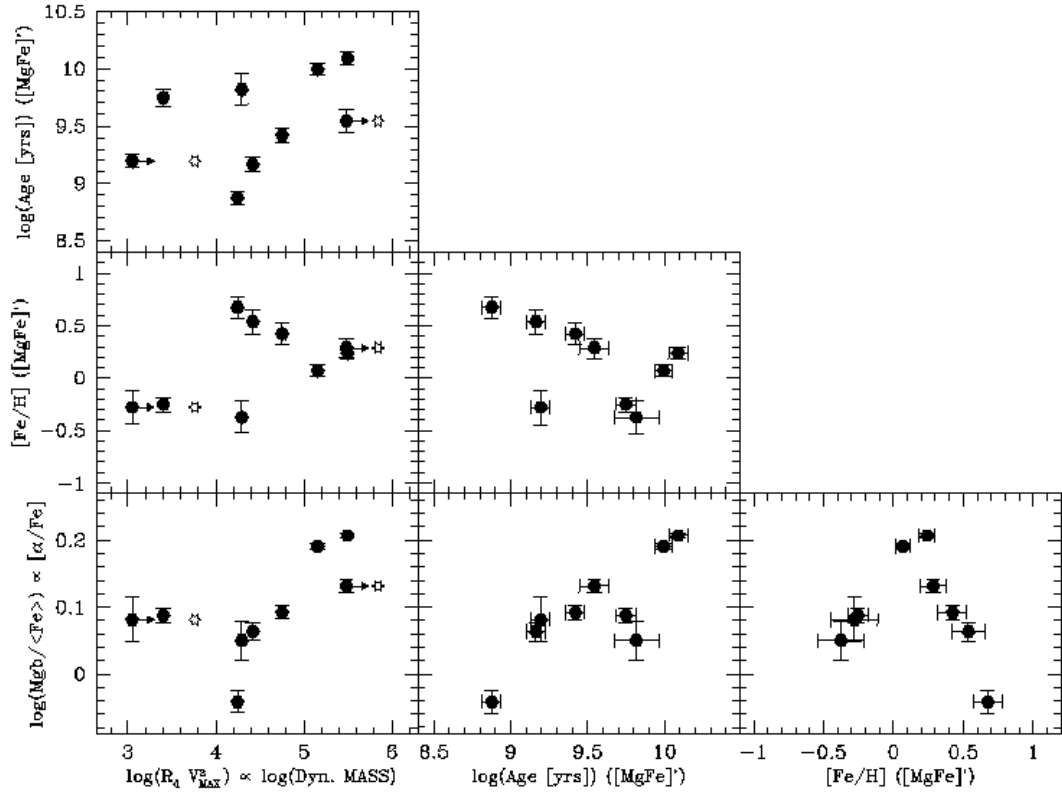
Figure 3.19.   Central ages, metallicities, Mgb/$\langle$Fe$\rangle$ ($\propto$ α-elements overabundance) and dynamical mass (as estimated from V_{MAX}) versus each other. The same symbols are used as in Figure 3.18.

These results support the idea of different star formation histories for the central regions of bright and faint S0 galaxies. Other authors have reached similar conclusions by studying early-type systems in the Coma Cluster (Poggianti et al. 2001; Mehlert et al. 2003).

Here we found that faint S0s are potential candidates for being spiral descendants who lost (or exhausted) their gas and suffered a final central gasp of star formation during cluster infall, while bright systems seems to be closer to normal ellipticals. However, are the nuclei characterising the entire galaxies? Have the outermost regions another story to tell? These questions lie beyond the scope of this thesis, but will be addressed in the future, when a stellar population study at larger galactocentric distances will give us new clues about the detailed star formation history of S0s in Fornax Cluster.

Chapter 4

The Tully-Fisher Relation of local S0 galaxies

In this chapter a study of the local B- and K_s-band Tully–Fisher Relation (TFR) between absolute magnitude and maximum circular speed in S0 galaxies is presented. To make this study, a combination of kinematic data was used, including the new high-quality spectral data set from the Fornax Cluster, with homogeneous photometry from the RC3 and 2MASS catalogues, to construct the largest sample of S0 galaxies ever used in a study of the TFR.

4.1 The Data

4.1.1 Kinematics

To build the TFR of local S0 galaxies, the data on their kinematics were collated from four previous studies. These works are: Neistein et al. (1999), hereafter N99; Hinz et al. (2001, 2003), hereafter H01 and H03, respectively; and Mathieu, Merrifield & Kuijken (2002), hereafter M02. From the sample of N99, the galaxy NGC 4649 was excluded as it has a low degree of rotational support and it presents evidence of interaction with a neighbouring system. From H01, the Sab spiral galaxy IC 4088 was also excluded. To these data, the observations obtained using the VLT of S0 galaxies in the Fornax Cluster were added (Chapter 2); of the galaxies observed in this cluster, seven are rotationally supported systems, so are suitable for this study. This combined dataset provides 60 S0 galaxies with measured kinematics, the largest sample yet used in a study of the S0 TFR. The collated kinematic data values for the maximum rotation speed, V_MAX (for all the sample), and the central velocity dispersion, σ_0 (for 51 galaxies of the sample), are listed in Table B.1.

4.1.2 Photometry

In the present study, K_s-band photometry from the Two Micron All Sky Survey (2MASS, Jarrett et al. 2003) and B-band photometry from the Third Reference Catalogue of Bright Galaxies (RC3, de Vaucouleurs et al. 1991) were adopted. Of the complete sample of 60 galaxies, photometry in K_s-band is available for all objects, while 54 galaxies have photometry in B-band.

In order to convert these data to absolute magnitudes, distances to all objects in the sample are required. A distance modulus of 31.35 for members of the Fornax Cluster was adopted (Madore et al. 1999). For the Virgo and Coma clusters, redshifts from Ebeling et al. (1998) and Struble & Rood (1999) were used respectively. They were corrected for the effect of the local velocity field (Virgo + Local infall) by using Mould et al. (2000) models, leading to recessional velocities of $1224\,\mathrm{km\,s^{-1}}$ for Virgo and $7269\,\mathrm{km\,s^{-1}}$ for Coma. For the field galaxies from N99, the distance moduli of Tonry et al. (2001) were used. Finally, for the M02 sample, redshifts from the NASA/IPAC Extragalactic Database were used where available. For two of their galaxies (NGC 1611 and NGC 2612), an estimate of the distance was calculated by those authors by using the systemic velocity derived from their spectra. A Hubble constant of $70\,\mathrm{km\,s^{-1}\,Mpc^{-1}}$ was adopted in converting redshifts into distances. Galactic extinction corrections were calculated using the Schlegel, Finkeiner & Davis (1998) reddening curve description, $A_b^\lambda = R_\lambda E(B-V)$, where R_λ=4.32 and 0.37 for $\lambda = B$ and K_s, respectively. In the B-band, the k-corrections from Poggianti et al. (1997) were applied; no correction was adopted for the K_s-band, as it is negligible. No internal extinction correction was applied to the apparent magnitudes; there is no definitive study on the internal extinction of S0 galaxies, but the apparent lack of dust in these systems suggests that such a correction would be very small. The resulting absolute magnitudes in K_s-bands are listed in Table B.1.

In addition to the absolute magnitudes, structural parameters were derived from the spatially-extended photometry available for these galaxies. The data used were the publicly-available "postage stamp" images in the K_s-band from 2MASS. The procedure followed was analogous to the one described in section 2.4: bulge+disk models were fitted directly to these images using GIM2D (Simard et al. 2002), with a Sérsic law adopted for the bulge distribution, and an exponential for the disk. In this way, the values for the bulge effective radius, R_e, its Sérsic index, n, the disk scalelength, R_exp, the half-light radius, R_half, the bulge-to-total fraction, B/T, and the galaxy inclination, i, were calculated. In a few cases, the derived bulge scale length was found to be smaller than the seeing (~ 2.5 arcsec). In those cases, the structural parameters are not well constrained by the observations, so the values were excluded. The structural parameters derived for the remaining 48 galaxies are listed in Table B.1 in the Appendix.

4.1.3   Line indices and ages

For part of this analysis, some Lick indices calculated in Chapter 3 for the Fornax sample will be needed. The indices Hβ, Mgb, $\langle$Fe$\rangle$ and [MgFe]$'$ were measured within $R_\mathrm{e}/8$ ("Central" values), and, for the aims of section 4.2.3, between 0.75 and 1.25 R_e ("1 R_e''" values) and between 1.5 and 2.5 R_e ("2 R_e''" values). The resulting values measured at Lick resolution are presented in Tables B.3 ("Central"), B.5 ("1 R_e''") and B.6 ("2 R_e''" values). Luminosity-weighted ages and metallicities were derived as described in Chapter 3 by using simple single-age stellar population models of BC03. The resulting ages and metallicities (Lick resolution) are also included in Tables B.4, B.5 and B.6 for the "Central", "1 R_e''" and "2 R_e''" measurements respectively.

Central line indices for a handful of other objects in the sample can be found in the literature (Fisher et al. 1996; Terlevich et al. 2002; Denicolo et al. 2004) mainly corresponding to field S0s from the N99 subsample. Unfortunately, these datasets mainly include the brightest objects of the sample, so it is difficult to make meaningful comparisons with the fainter galaxies from Fornax. Also, differences between the two samples could arise because of the superior quality of Fornax data, an effect which is difficult to quantify. In consequence, the analysis of the line indices, and ages presented in section 4.2.3 was focused on the data from the Fornax Cluster only.

4.2 Results and Discussion

The basic result of this analysis is presented in the Tully–Fisher plots of rotation velocity versus absolute magnitude shown in Figure 4.1 and 4.2 (for the B- and K_s-band respectively). In these plots, the solid line represents the TFR of spirals in local clusters found by Tully & Pierce (2000, hereafter TP00), shifted by -0.207 magnitudes in order to be consistent with the adopted Hubble constant of $H_0 = 70\,\mathrm{km\,s^{-1}\,Mpc^{-1}}$. The long-dashed line in the B-band represents the TFR of cluster spirals by Sakai et al. (2000, hereafter Sak00). The difference between these lines gives an indication of the remaining systematic uncertainty in the spiral galaxy TFR with which we seek to compare the S0s.

4.2.1 Shift between the spiral and S0 TFRs

The first point that is immediately clear from Figure 4.1 and 4.2 is that whichever spiral galaxy TFR is adopted, the S0s lie systematically below it. It is also interesting to note that this result holds true for the S0 data from all environments, from the poorest field objects to fairly rich clusters, so it is clearly a very general phenomenon. Therefore in the following sections, the possible origins of such an offset will be explored.

Observational results

One problem in trying to quantify the offset in the TFR is that the incompleteness in magnitude of the data presented in Figure 4.1 and 4.2 will bias a conventional fit. Therefore the approach of Willick (1994) was adopted, which involves fitting the inverse function,

$$\log(\mathrm{V_{MAX}}) = a + bM_\lambda, \qquad \text{where } \lambda = B \text{ or } K_\mathrm{s}, \tag{4.1}$$

to minimise this source of bias. The slope b was fixed to match the slope for the spiral galaxy TFR, and a is varied to find the least-squares fit between this function and the data, with each point i weighted by

$$w_i = \frac{1}{\sigma_i^2}, \tag{4.2}$$
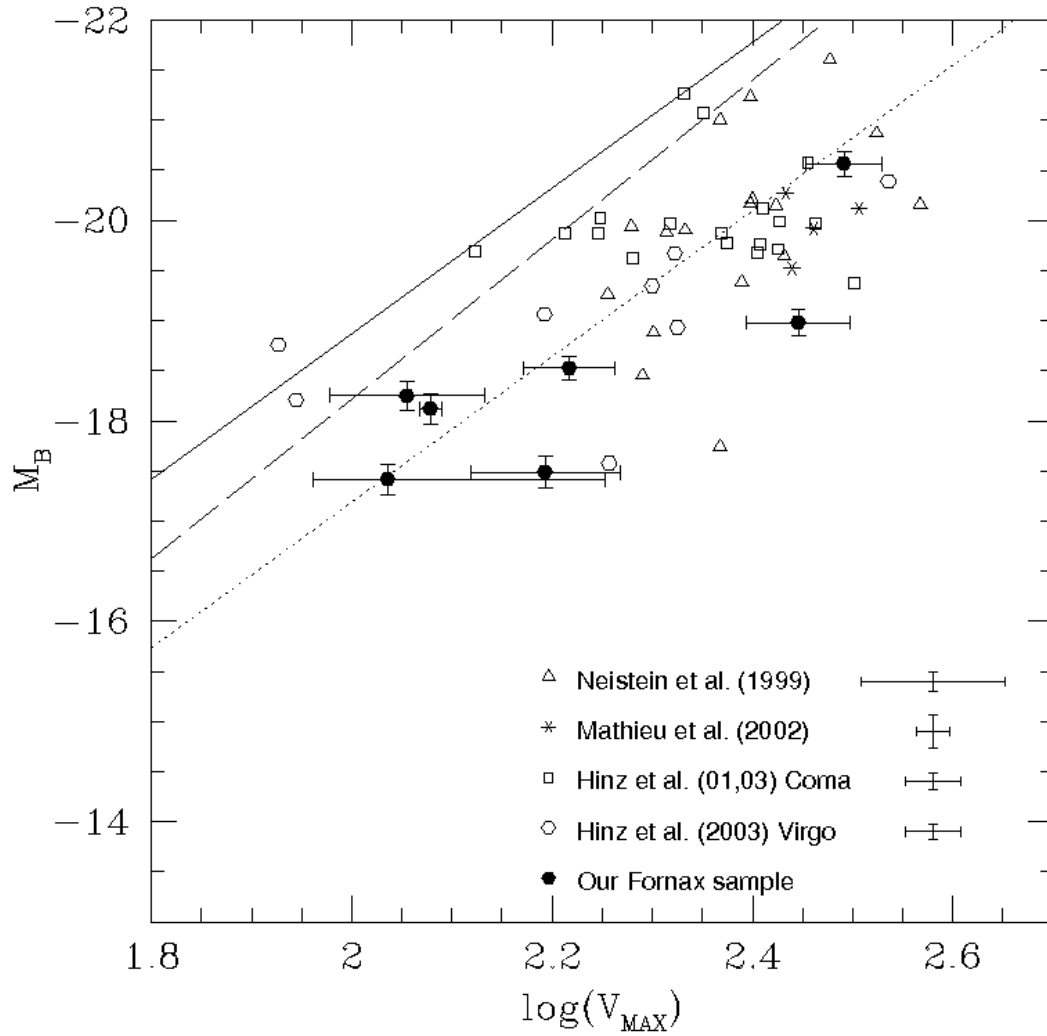
Figure 4.1. *B*-band Tully–Fisher relation of S0 galaxies. Solid line represents the TFR of spiral galaxies from Tully & Pierce (2000); dashed line represents the spiral TFR by Sakai et al. (2000); dotted line is the best fit to the S0 data-points using the slope from Tully & Pierce (2000). The error bars in the right bottom corner correspond to the median value for each subsample, while for the Fornax Cluster data the errors are plotted for each data-point.
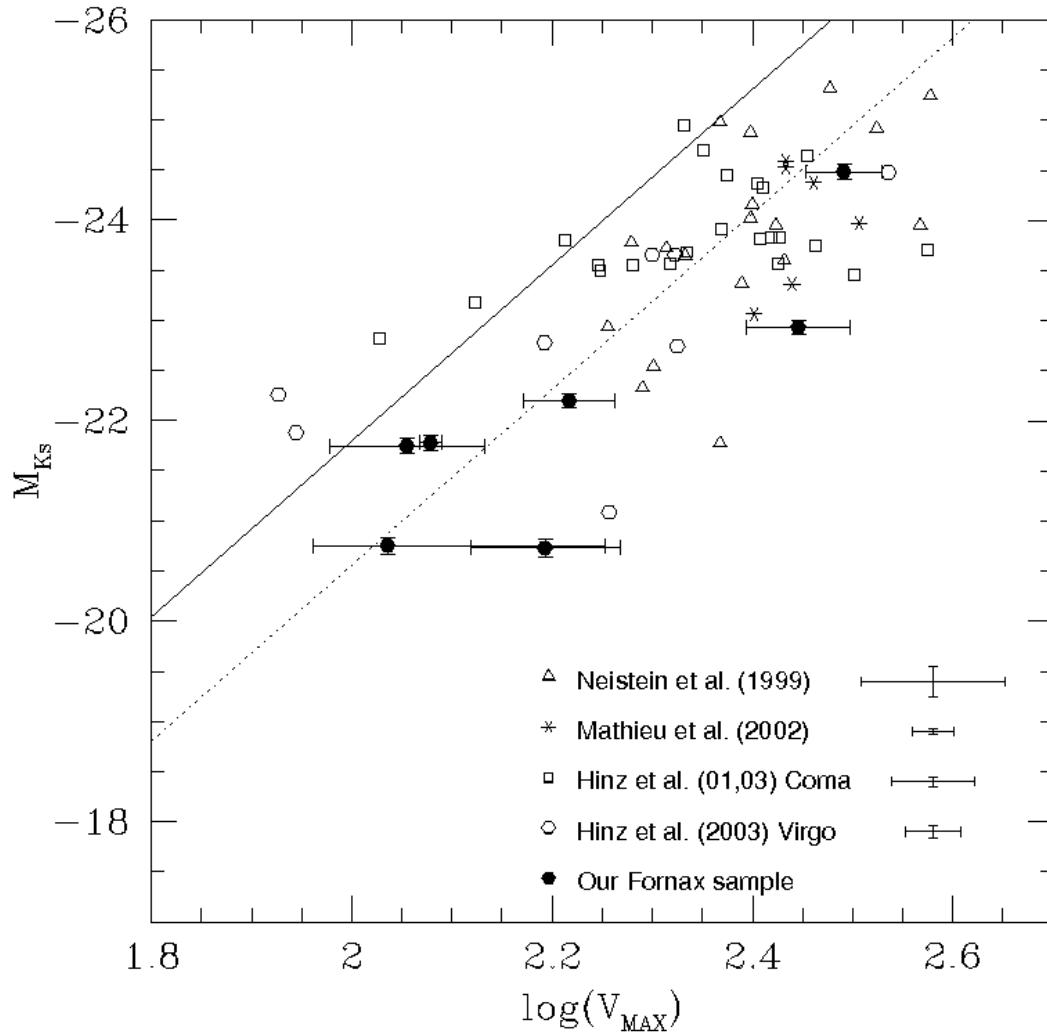
Figure 4.2. K_s-band Tully–Fisher relation of S0 galaxies. Solid line represents the TFR of spiral galaxies from Tully & Pierce (2000); dotted line is the best fit to the S0 data-points using the slope from Tully & Pierce (2000).The error bars in the right bottom corner correspond to the median value for each subsample, while for the Fornax Cluster data the errors are plotted for each data-point.

where

$$\sigma_i^2 = \sigma_{\log(V_{\text{MAX}}),i}^2 + b^2 \sigma_{M_\lambda,i}^2 + \sigma_{\text{int}}^2, \tag{4.3}$$

to account for the uncertainty in the measured maximum velocity, $\sigma_{\log(V_{\text{MAX}}),i}$, and that in the absolute magnitude, $\sigma_{M_\lambda,i}$. The quantity σ_{int} was set to quantify the intrinsic scatter in the relation such that the reduced χ^2 of the fit comes out at unity; this procedure is discussed in more detail in section 4.2.2.

Setting b equal to the inverse of the spiral TFR slope determined by TP00, the zero-point parameter a can be determined and hence the offset in magnitudes from the TP00 TFR relations in the B- and K_{s}-band. The resulting best-fit lines are shown dotted in Figure 4.1 and 4.2. The offsets from the TP00 relations are

$$\Delta M_{\text{B,TP00}} = -1.7 \pm 0.4 \tag{4.4}$$

and

$$\Delta M_{\text{K}_{\text{s}},\text{TP00}} = -1.2 \pm 0.4, \tag{4.5}$$

where the quoted error includes the uncertainty in zero point of both the S0 and spiral TFRs. To test the robustness of this result against the uncertainty in the spiral TFR, the analysis was repeated using the Sak00 B-band relation to fix the slope and measure the offset from their relation. This analysis resulted in an offset of

$$\Delta M_{\text{B,Sak00}} = -1.3 \pm 0.1, \tag{4.6}$$

within the errors of the previous analysis but somewhat smaller. Sak00 did not publish a K_{s}-band TFR, but the parallel nature of the Sak00 and TP00 TFRs in Figure 4.1 suggest that most of the difference might arise from a zero-point shift due to a different distance-scale calibration. Therefore, and just for illustrative purposes, it might be possible to extrapolate from the Sak00 B-band results on the assumption that $\Delta M_{\text{B,TP00}} - \Delta M_{\text{K}_{\text{s}},\text{TP00}} \approx \Delta M_{\text{B,Sak00}} - \Delta M_{\text{K}_{\text{s}},\text{Sak00}}$, to infer a corresponding K_{s}-band offset of

$$\Delta M_{\text{K}_{\text{s}},\text{Sak00}} = -0.8 \pm 0.4. \tag{4.7}$$

These new estimates for the offset between spiral and S0 TFRs tend to lie toward the upper end of earlier estimates, mainly because of the more recent refinements in the calibration to the spiral galaxy TFR that have been included in this analysis. However, even neglecting these systematic changes, the values obtained here lie within the range of offsets in the TFR suggested by previous studies, implying that this quantity can be fairly reliably determined, particularly with the larger and more homogeneous data set presented here.

Interpretation

A natural interpretation of the offset between the S0 and spiral TFRs is that it represents a simple fading as a spiral galaxy's star formation is truncated when it mutates into an S0. One complication in attempting to quantify this scenario is that one needs to know what luminosity the spiral galaxy started at in this evolution. However, observations out to redshifts beyond unity seem to show that there has
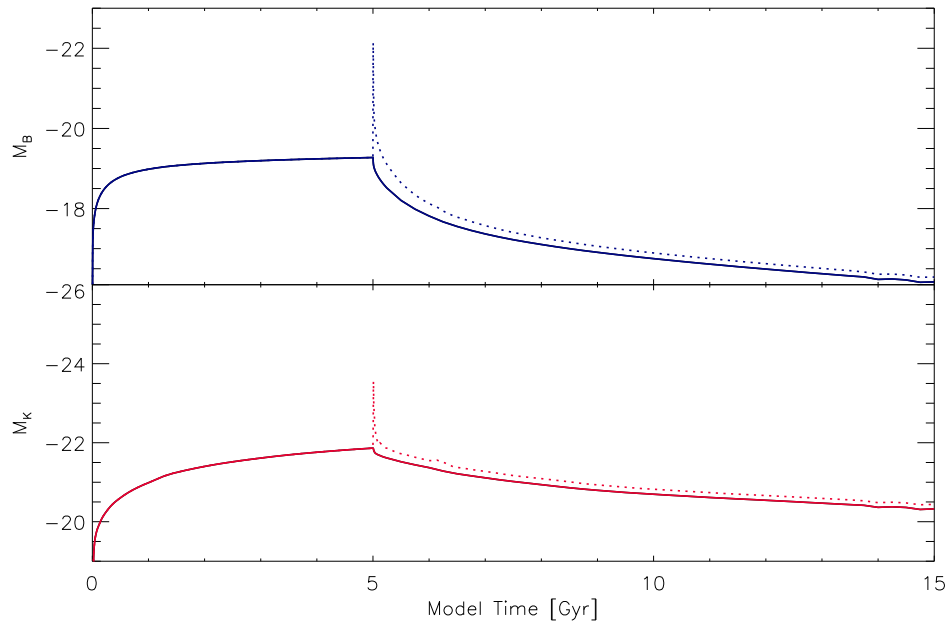
Figure 4.3. Magnitudes versus time from BC03 synthesis models. Constant star formation rate of $1\,\mathrm{M}_\odot\,\mathrm{yr}^{-1}$ for $5\,\mathrm{Gyr}$, then truncated (continuous lines) or final starburst of 10% the total stellar mass (dotted lines).

been essentially no (or little) evolution in the slope and zero-point of the spiral galaxy TFR in infrared wavebands over this period (Conselice et al. 2005; Flores et al. 2006; Weiner et al. 2006). The situation in the visual regime is more uncertain with no general agreement in terms of the amount of fading and slope evolution in the B-band TFR (Rix et al. 1997; Vogt et al. 1997; Böhm et al. 2004; Bamford et al. 2006; Weiner et al. 2006). The lack of evolution (at least in the infrared) means that the starting point for fading spirals is the same spiral galaxy TFR that we see today, and the offset between the nearby galaxy spiral and S0 TFRs does provide a measure of the degree to which the S0 galaxies must have faded if this picture is correct.

To see if this scenario is plausible and to quantify the timescales involved, the BC03 synthesis models were used to calculate the fading of a stellar population that started with a constant star formation rate of $1\,\mathrm{M}_\odot\mathrm{yr}^{-1}$ for $5\,\mathrm{Gyr}$, then stopped. Plots of the evolution of magnitudes versus time for this model are shown in Figure 4.3 (continuous lines). The stellar population was assumed to have solar metallicity and the initial mass function of Chabrier (2003).

By matching the decrease in luminosity to the observed shifts between spiral and S0 TFRs, it can be estimated how long ago (on average) the truncation in star formation must have occurred to be consistent with the observations. Using the TP00 offsets in the B- and K_s-bands given in equations 4.4 and 4.5, the resulting times since truncation are

$$\tau_{\mathrm{B,TP00}}^{\mathrm{trunc}} = 1.5^{+1.2}_{-0.7}\,\mathrm{Gyr} \qquad (4.8)$$

and

$$\tau_{\mathrm{K_s,TP00}}^{\mathrm{trunc}} = 5.5_{-3.1}^{+\infty} \, \mathrm{Gyr},\tag{4.9}$$

respectively. These values are somewhat inconsistent with each other, but this may just reflect the calibration of the spiral TFR in TP00. If instead the values infered from the Sak00 calibration are used (equations 4.6 and 4.7), more consistent timescales since truncation are obtained of

$$\tau_{\mathrm{B,Sak00}}^{\mathrm{trunc}} = 0.66_{-0.30}^{+0.63} \, \mathrm{Gyr}\tag{4.10}$$

and

$$\tau_{\mathrm{K_s,Sak00}}^{\mathrm{trunc}} = 1.1_{-1.0}^{+1.6} \, \mathrm{Gyr}.\tag{4.11}$$

The shorter timescale simply reflects the smaller offset in the TFR that the Sak00 calibration implies, but it should be kept in mind the additional uncertainty of not really having a K_s-band TFR from Sak00. This timescale is, if anything, worryingly short: it would be quite a coincidence if we are living at an epoch so close to the point at which all these galaxies transformed from spirals into S0s. There is also evidence that many of these galaxies have large luminosity-weighted ages (Terlevich & Forbes 2002; Denicoló et al. 2005). In any case, it is important to emphasize that this age is an average value, and since there is a considerable range in offsets, there is also a range in age.

One possible resolution is that the star formation history in transforming a spiral into an S0 might be somewhat more complex. Indeed, Poggianti et al. (1999) have suggested that cluster galaxies with k+a/a+k spectra observed at intermediate redshifts are the best candidates for S0 progenitors because of their spectro-photometric characteristics and the predominance of disk-dominated morphologies. Since such spectra are usually identified with post-starburst galaxies, it would seem that spiral galaxies may undergo a "last gasp" burst of star formation when they start their transitions into S0s. To investigate this possibility, a burst of star formation was added, amounting to 10% of the total stellar mass, to the above truncated star formation model. The magnitude evolution versus time is represented as dotted lines in Figure 4.3. Repeating the comparison between the luminosity of this model as predicted by the BC03 population synthesis code and the observed offsets in the TFR resulted in estimates for the time since the burst and truncation of

$$\tau_{\mathrm{B,TP00}}^{\mathrm{burst}} = 2.0_{-0.8}^{+1.3} \, \mathrm{Gyr},\tag{4.12}$$

$$\tau_{\mathrm{K_s,TP00}}^{\mathrm{burst}} = 7.0_{-3.7}^{+\infty} \, \mathrm{Gyr}\tag{4.13}$$

using the TP00 calibration, and

$$\tau_{\mathrm{B,Sak00}}^{\mathrm{burst}} = 1.1_{-0.4}^{+0.7} \, \mathrm{Gyr},\tag{4.14}$$

$$\tau_{\mathrm{K_s,Sak00}}^{\mathrm{burst}} = 1.7_{-1.1}^{+1.9} \, \mathrm{Gyr}\tag{4.15}$$

using the Sak00 values. As might be expected, the inclusion of a starburst increases the age of the stellar population compared to those found in the truncation model. These values are therefore a little more comfortable in terms of the timescales in-

volved, but still showing important differences between mean age values when TP00 is used.

It is interesting to notice, however, that if we consider that the zero-point of the spiral B-band TFR has evolved with time, we obtain much more consistent timescales for B and $K_{\rm s}$. Although still controversial, some authors have found a systematic brightening of $\sim 1\,{\rm mag}$ between the low and high redshift TFRs in the B-band (Bamford et al. 2006; Weiner et al. 2006). To crudely consider this possibility, an additional shift of $1\,{\rm mag}$ was added to equation 4.1 (in B-band) without any further changes in the slopes. The resulting timescales using the new B-band shift are

$$\tau_{\rm B,TP00}^{\rm trunc} = 6.5\,{\rm Gyr} \tag{4.16}$$

$$\tau_{\rm B,TP00}^{\rm burst} = 7.5\,{\rm Gyr}, \tag{4.17}$$

using the TP00 calibration, which are in nice agreement with the results in the infrared presented in equations 4.9 and 4.13, respectively. So better consistency is reached between optical and near infrared derived ages if we allow for the parent populations to have been brighter in the past as some evidence suggests.

However, there is a limit to how far it is worth pursuing these simple models, as it is extremely unlikely that all S0 galaxies will have undergone the same star formation history. Indeed, the large scatter apparent in the points in Figure 4.1 and 4.2 indicates a relatively heterogeneous history for these systems: the average evolution may be as described above, but each galaxy has its own story to tell. Therefore the scatter in the S0 TFR is now looked in more detail, in an attempt to quantify it and explore its origins.

4.2.2 The Scatter in TFR of S0 galaxies

Observational results

As outlined in the previous section, the intrinsic scatter in the TFR was estimated, $\sigma_{\rm int}$, during the fitting process by varying its value in the weights of equation 4.2 until the reduced χ^2 of the fit,

$$\chi_r^2 = \frac{1}{n-1} \sum_i \left(\frac{\log(V_{{\rm MAX},i}) - a - bM_{\lambda,i}}{\sigma_i} \right)^2, \tag{4.18}$$

was equal to unity. The inverse slope of the TFR, b, was set to the value appropriate to either the TP00 or the Sak00 spiral TFR (the values are so similar that it made no substantial difference to the measured scatter), while the zero-point a was allowed to vary. The presence of variables in both numerator and denominator of equation 4.18 mean that the fit is no longer linear, but it was found that it could be robustly performed by a simple iterative procedure in which at the jth iteration the estimate for $\sigma_{\rm int}$ was updated such that

$$\sigma_{{\rm int},j}^2 = \sigma_{{\rm int},j-1}^2 \times \chi_r^{2\alpha}. \tag{4.19}$$

By setting the convergence parameter α to 2/3, the iterative solution was well be-haved and converged in no more than 15 iterations. For comparison, a weighted total scatter using the formula

$$\sigma_{\text{tot}}^2 = \frac{\sum_i w_i (\log(V_{\text{MAX},i}) - a - bM_{\lambda,i})^2}{\sum_i w_i}. \tag{4.20}$$

was also calculated. For the B-band TFR of S0s (using TP00 slope), the results were

$$\begin{aligned} \sigma_{\text{tot,B}} &= 0.88 \pm 0.06 \text{ mag} \\ \sigma_{\text{int,B}} &= 0.78 \pm 0.06 \text{ mag,} \end{aligned} \tag{4.21}$$

while for K_{s}-band data (using TP00 slope) it was found that

$$\begin{aligned} \sigma_{\text{tot,K}_{\text{s}}} &= 0.98 \pm 0.06 \text{ mag} \\ \sigma_{\text{int,K}_{\text{s}}} &= 0.87 \pm 0.06 \text{ mag.} \end{aligned} \tag{4.22}$$

These values imply that $\approx 90\%$ of the observed scatter in Figure 4.1 and 4.2 cannot be explained by the known observational uncertainties in M_λ and $\log(V_{\text{MAX}})$. These results seem to be bracketed by previous estimates: H03 report a scatter in the H-band TFR of 1.18 magnitudes in the Coma Cluster and 1.33 in the Virgo Cluster, whereas previous I-band estimates of scatter have been lower at 0.68 magnitudes (N99) and 0.82 magnitudes (H03). However, these previous studies are not directly comparable to the current estimates, because of their different wavebands and be-cause they did not use the more robust inverse-fitting approach adopted here. In addition, it is not entirely clear whether the previous estimates have been corrected for measurement error, particularly in the uncertain measurement of $\log(V_{\text{MAX}})$.

Interpretation

Perhaps the simplest possible explanation for the large value σ_{int} is that the errors in the observed quantities plotted in Figure 4.1 and 4.2 have been underestimated, and have been erroneously attributed to the intrinsic scatter. Therefore this section begins by considering possible additional sources of uncertainty in the data.

The adopted fluxes for the sample galaxies, particularly the infrared 2MASS data, form a uniformly-measured reliable set, so it is unlikely that much of the scat-ter in the TFR could arise from errors in these data. However, their transformation into absolute magnitudes could introduce some uncertainty. For example, no correc-tion was applied to the magnitudes due to the internal extinction of these systems. Although such corrections are believed to be small in the relatively dust-free en-vironment of an S0, they might still be non-negligible. However, if such an effect were distorting the results, it could be expected to have a much stronger effect in the B-band than in the K_{s}-band; the very similar values for σ_{int} derived in both bands imply that extinction is not a significant issue. Similarly, it is possible that unaccounted errors in the adopted distances to the sample galaxies could contribute to the scatter in absolute magnitudes. However, although such an error could offset all the points derived from S0s in a single cluster, it would not increase their scatter. The lack of offsets between the Virgo, Coma and Fornax Cluster data and their

similar large scatters in Figure 4.1 and 4.2 imply that such errors are not significant.

The measurement of $\log(V_{MAX})$, as set on in Chapter 2, is more challenging. The measured Doppler shift in the stellar component is only indirectly related to this quantity. First, a correction must be applied for inclination. However, it is in the nature of identifying S0 galaxies that only those relatively close to edge-on are classified as such (Jorgensen & Franx 1994): as Table B.1 confirms, the vast majority of galaxies in the sample are at inclinations close to 90 degrees, so the corrections are relatively small. Second, the stars in S0s do not follow perfectly circular orbits, so the measured rotation velocity will differ from the circular (maximum) speed by the "asymmetric drift". For the Virgo, Coma and Fornax Cluster data, the approach of N99 that uses the measured random velocities to correct for the asymmetric drift was adopted; although this relatively simple correction may contain systematic uncertainties, it is unlikely to increase the scatter significantly. It is also notable that the new Fornax Cluster kinematic data used here reach to larger radii than the earlier samples. Since the size of the asymmetric drift correction decreases with radius, it would be expected that any scatter induced by it is smaller for these larger-radii data, but no differences are discernible. Finally, it is noted that M02 used a more sophisticated dynamical modelling technique that removed the need for any asymmetric drift correction. Although they claimed a resulting decrease in the scatter in the TFR, the better photometry presented here suggests that this is only marginally the case. Irrespective of the way that $\log(V_{MAX})$ is derived, there seems to be a sizeable residual scatter in the TFR.

Therefore now possible astrophysical origins for the scatter in the TFR are considered. In this context, it is notable that the scatter derived here, although much larger than that seen in the TFR of nearby spirals (~ 0.4 magnitudes; TP00, Sak00, Verheijen 2001), is similar to the scatter observed in the TFR of galaxies at higher redshift. Bamford et al. (2006) obtained similar values for σ_{int} for their sample of high-redshift spirals in the B-band, while Conselice et al. (2005) found a similar scatter in their K-band TFR of spirals at redshifts between 0.2 and 1.2. This larger scatter in the spiral TFR at higher redshift has been attributed to variations in the star formation rate in these systems due to more frequent interactions with other galaxies, gas clouds and cluster environment, as well as the less relaxed dynamical state of these systems (e.g. Shi et al. 2006; Flores et al. 2006). It is therefore possible that the scatter in the S0 TFR was in some sense imprinted into these systems while they were still "normal" spiral galaxies at higher redshift, and that scatter has remained frozen into their TFR as they have evolved more gently to the present day. Alternatively, the scatter could be a signature of the transformation process itself. For example, if the transition from spiral to S0 began over a range of times, then different galaxies will have faded by different amounts, leading to the observed scatter in the relation. As we have seen in section 4.2.1, the mean TFR will shift downward by more than a magnitude on billion-year timescales, so a spread in start times could explain the ultimate scatter. As a further complication, subsequent minor mergers might induce extra late bursts of star formation, or they could kill off the galaxy's star formation a little sooner, further scattering the relation. In order to try to distinguish between these possibilities, the offset of individual S0s from the
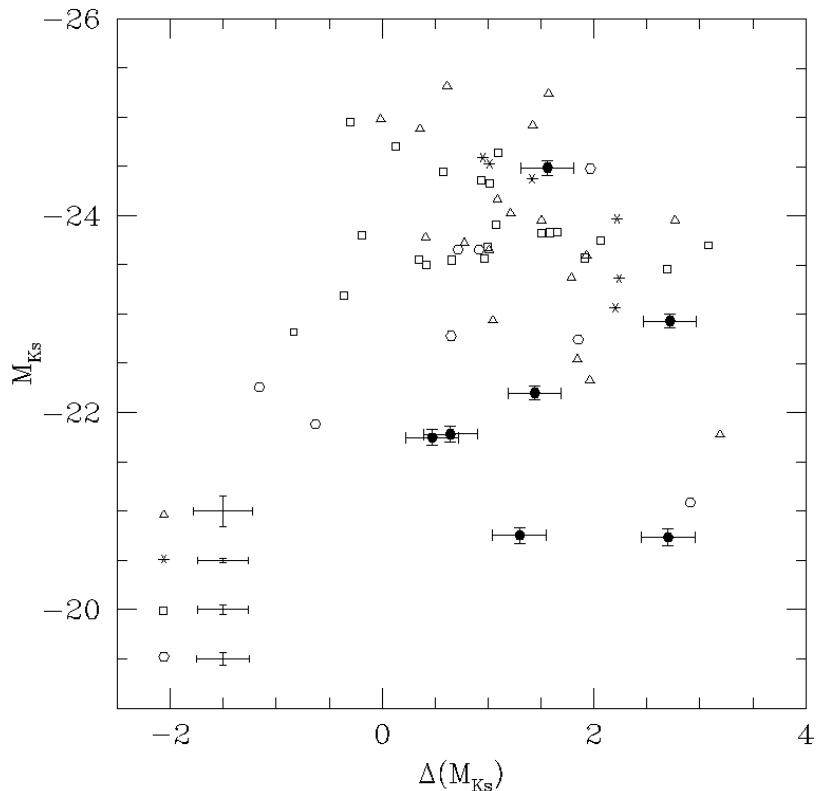
Figure 4.4. Plot of infrared absolute magnitude, M_{K_s}, against offset from the TFR, ΔM_{K_s}. In the lower left corner, the median uncertainties for the N99, M02, H01 and H03 subsamples are shown, while errors for the individual Fornax Cluster data are presented.

spiral galaxy TFR were investigated to see whether they correlate with any of their other astrophysical properties.

4.2.3 Correlations with other parameters

Structural parameters [1]

In searching for correlations between the offset from the infrared TFR, ΔM_{K_s}, and other structural parameters, one concern is that the offset may not be the driving variable. In particular, residual bias in the fitting of the TFR to Figure 4.1 and 4.2 could induce a correlation between ΔM_{K_s} and the absolute magnitude of the galaxies, M_{K_s}. Since it is well know that other properties such as galaxies' sizes correlate with their magnitudes, then such a bias in the TFR fit would also induce correlations with ΔM_{K_s}. In practice, Figure 4.4 shows that there is only the slightest hint of an anti-correlation between the derived values ΔM_{K_s} and M_{K_s}, so this potential source of bias has clearly been dealt with reasonably effectively.

Figures 4.5–4.10 show the correlations between the various structural properties

---

[1]Here we discuss the results for the K_s-band data, since the structural parameters were calculated from the same photometry and the infrared dataset is somewhat more uniform and reliable. However, similar results are found if the analysis is performed using the optical B-band data.
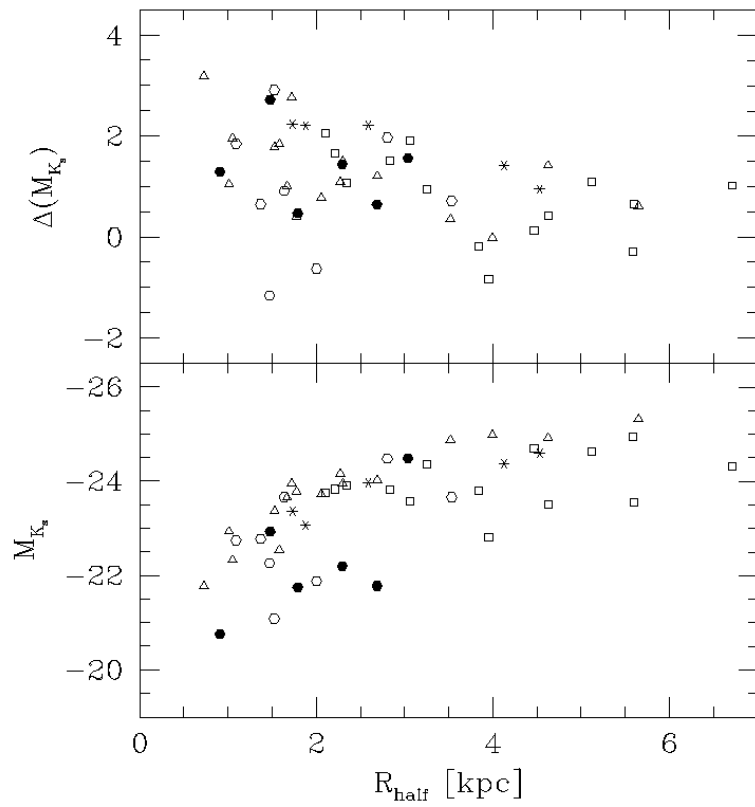
Figure 4.5. M_{K_s} and ΔM_{K_s} versus half-light radius.

Figure 4.6. M_{K_s} and ΔM_{K_s} versus disk scalelength.

Figure 4.7. M_{K_s} and ΔM_{K_s} versus bulge effective radius.

Figure 4.8. M_{K_s} and ΔM_{K_s} versus Sérsic Index of the bulge.

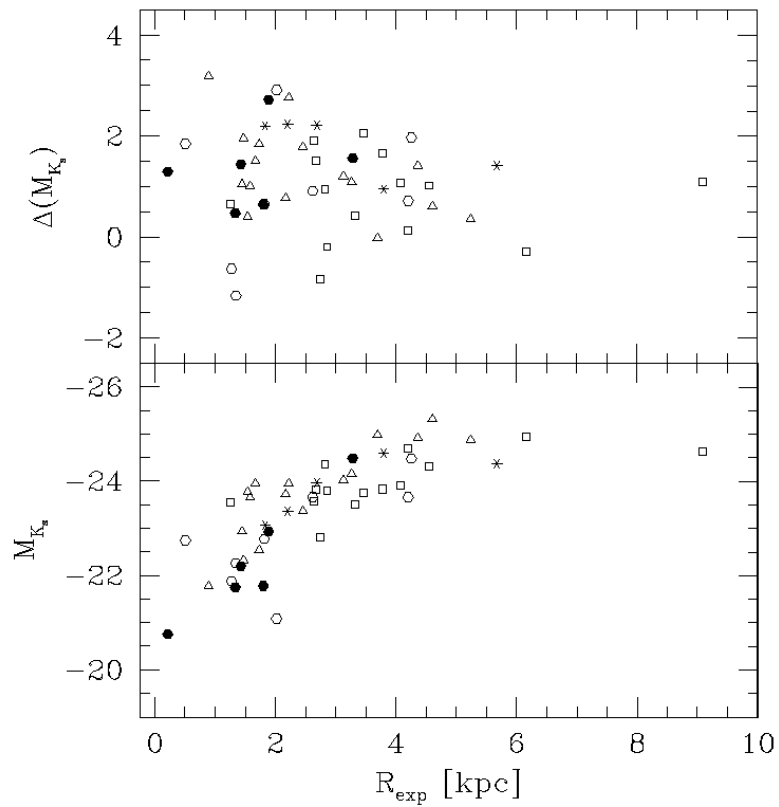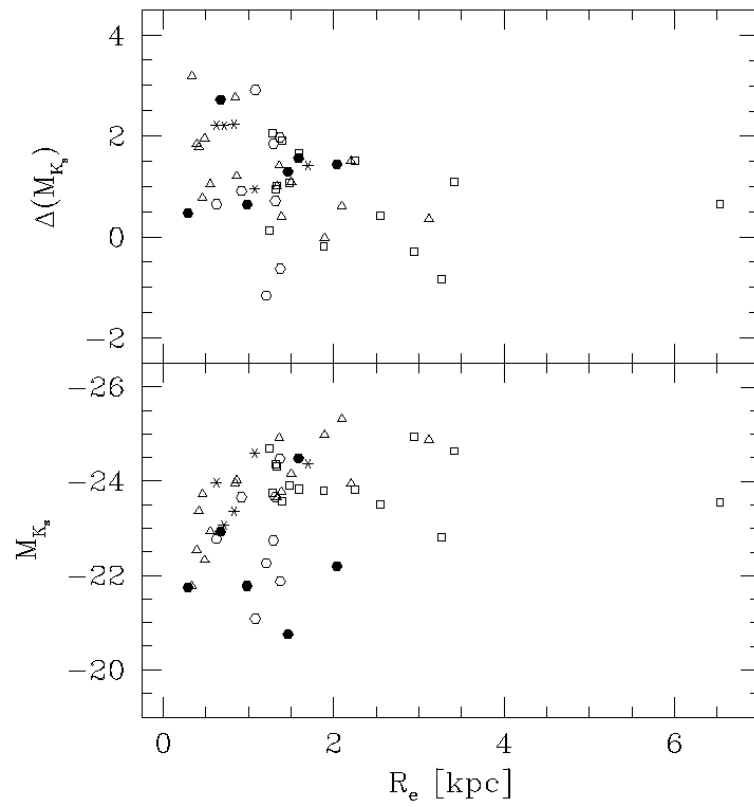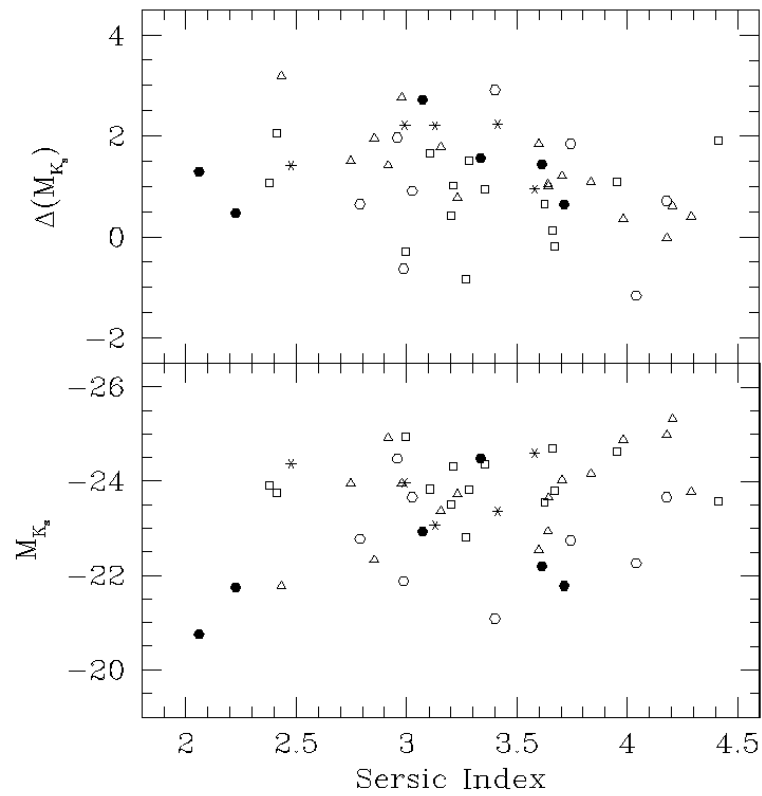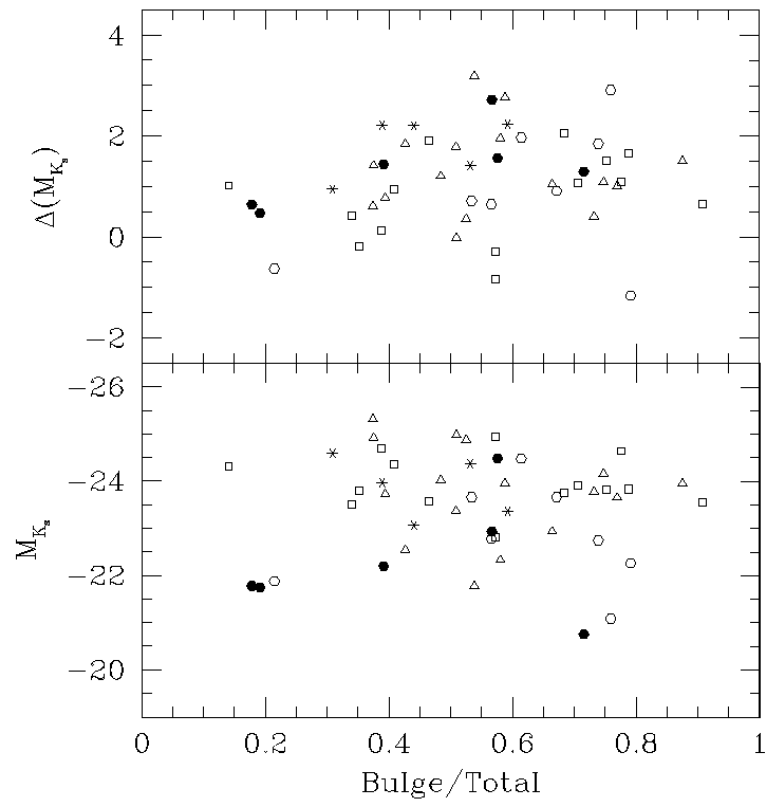**Figure 4.9.** M_{K_s} and ΔM_{K_s} versus bulge-to-total luminosity ratio.
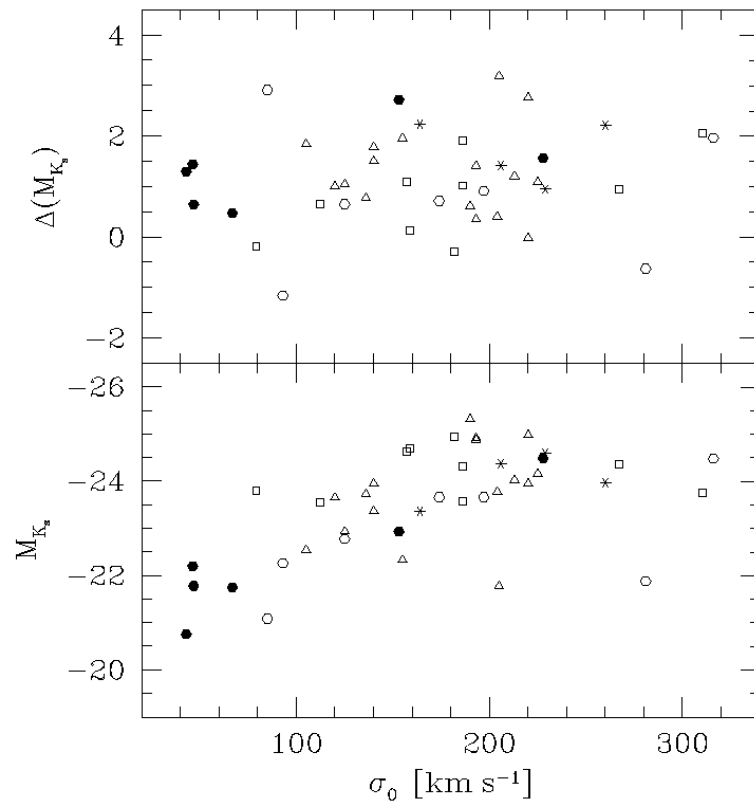
Figure 4.10. M_{K_s} and ΔM_{K_s} versus central velocity dispersion.

of the S0 galaxies (as presented in Table B.1 in the appendices), and their absolute magnitudes and offset from the spiral galaxy TFR in the K_s-band. The symbols used in these figures are the same as in Figure 4.1 and 4.2. Some of the resulting correlations are fairly trivial. For example, the absolute magnitude correlates quite well with the size of the galaxy, as characterised by its half-light radius (see Figure 4.5). It is, however, interesting to note that this correlation is mainly driven by the size of the disks in these systems (see Figure 4.6), and is almost uncorrelated with the photometric properties of the bulge (see Figures 4.7 and 4.8). Similarly, as Figure 4.9 shows, the magnitudes do not seem to be systematically affected by how much of the total luminosity is in the bulge or disk components. It is notable that cluster galaxies are mainly responsible of the scatter in Figures 4.5 and 4.7, while field S0s tend to follow tighter trends in both diagrams. However, such a difference between cluster and field galaxies could be related to different selection criteria, so any further interpretation would be excessive.

The lack of correlation with bulge photometric properties make it intriguing that the absolute magnitude does correlate with the central velocity dispersion, which is primarily a property of the galaxy's bulge (see Figure 4.10). Presumably, this correlation is a manifestation of the well-known conspiracy by which rotation curves remain fairly flat across regions dominated by the bulge, disk or halo: this conspiracy means that the bulge dispersion will be tightly related to the rotation speed in the disk, and, as we have seen above, disk properties do correlate with total luminosity (Whitmore et al. 1979; Ferrarese 2002; Baes et al. 2003; Pizzella et al. 2005; Courteau, McDonald & Widrow 2006). This effect can be clearly appreciated in Figure 4.11.

In the attempt to understand the origins of the offset (scatter) from the spiral galaxy TFR, it is the correlation of parameters with this offset, $\Delta M_{\mathrm{K_s}}$, that is of more immediate interest. For most plots, however, there are no significant correlations to be seen; where there is some hint of a correlation, it goes in the opposite sense to that seen with $M_{\mathrm{K_s}}$, suggesting that it may well be the kind of artifact discussed at the beginning of this section. Therefore, seems unlikely that these structural parameters have much bearing on the scatter in the TFR.

Spectral parameters

A hint as to the origins of the scatter in the TFR can be found by considering line index measurements and the inferred luminosity-weighted ages from stellar populations synthesis models. For the reasons outlined in section 4.1.3, the analysis is focused on the Fornax sample only.

Giving the homogeneity of the Fornax dataset and the use of luminosity-weighted parameters derived at optical wavelengths, it was decided to use the offset from the B-band TFR, ΔM_B, together with $\Delta M_{\mathrm{K_s}}$, in the rest of the analysis. Despite the fact that uncertainties in RC3 B-band photometry are larger than in the 2MASS K_s-band counterpart, the total errors in $\Delta M_{\mathrm{B,K_s}}$ are dominated by the uncertainties of the TFR from spirals. Also, the B-band data is more sensitive to recent changes in the star formation history than the infrared band, being a good complement for
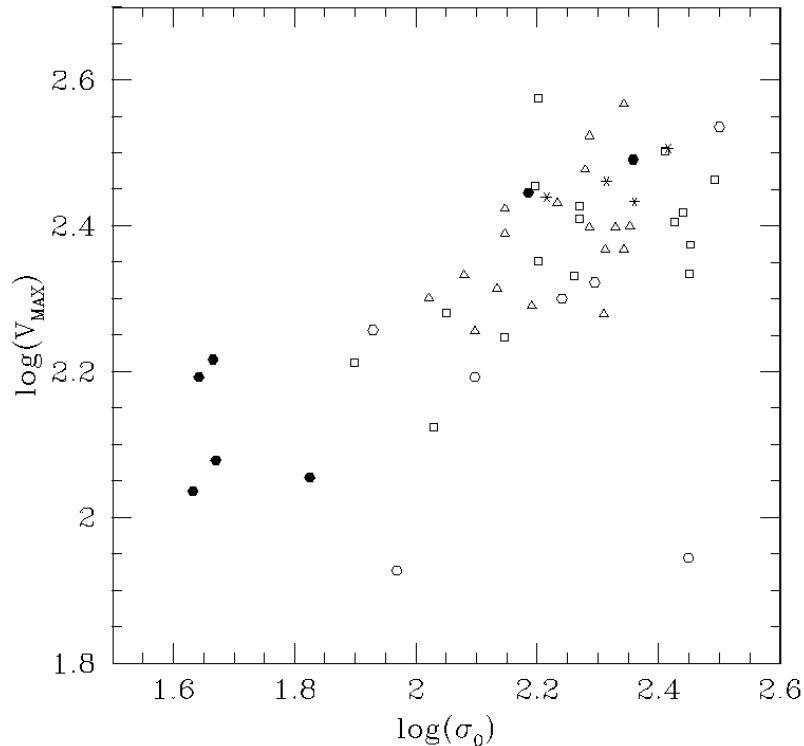
Figure 4.11. Maximum rotational velocity, V_{MAX}, versus central velocity dispersion, σ_0.

this kind of study. However, similar results are found when using B- or K_s-band data.

Figure 4.12 shows $\Delta M_{\mathrm{B,K_s}}$ plotted against different central indices (Hβ, Mgb) and the combined indices $\langle \mathrm{Fe} \rangle$ and $[\mathrm{MgFe}]'$. The only indication of a trend with the offset from the TFR comes from the Hβ index, where $\Delta M_{\mathrm{B,K_s}}$ seem to get weaker as Hβ increases, and stronger as Hβ decreases. This correlation is interesting since it is in the sense expected if the degree of fading of S0s is driven by the timescale since the last significant star formation.

This possibility can be examined more quantitatively if the ages derived from these spectral indices in Chapter 3 are used (see also section 4.1.3). To ascertain whether the resulting ages have been significantly influenced by enhancement of α-elements via the well-known age-metallicity degeneracy, the estimates derived using Mgb, $\langle \mathrm{Fe} \rangle$ and $[\mathrm{MgFe}]'$ parameters were considered separately as the metallicity-sensitive index; the results are shown in Figures 4.13 and 4.14. The first column of these figures confirms the trend indicated by the central line indices alone: the fading of the Fornax Cluster S0s seems to be accompanied by an ageing of their stellar population. Suggestively, the size of the effect is about the amplitude expected for a passively fading stellar population as it was seen in section 4.2.1. For illustration, the predictions from these models are overplotted in all the pertinent panels of Figures 4.13 and 4.14. The second and third columns of these figures present
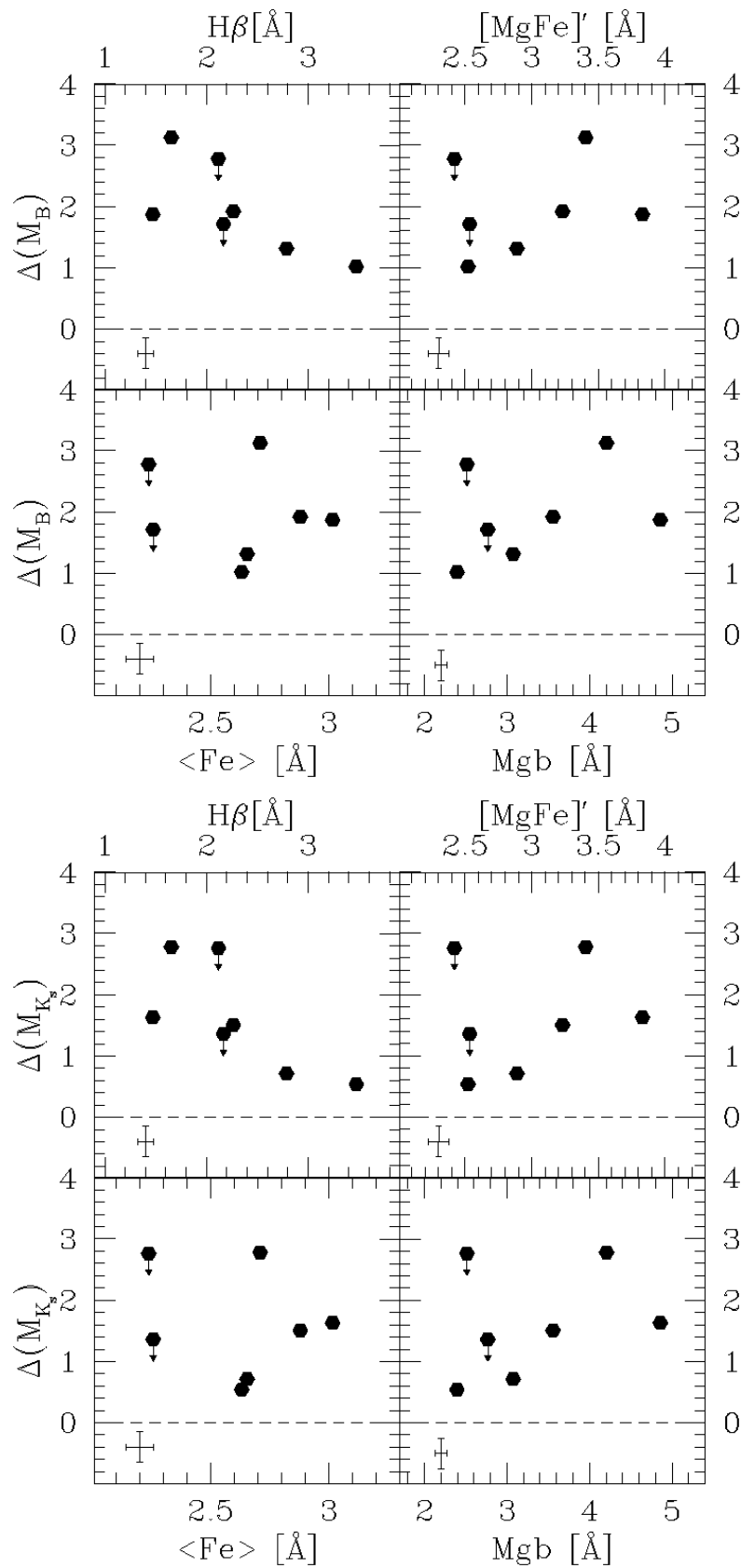
Figure 4.12. $\Delta M_{B,K_s}$ versus Hβ, $\langle$Fe$\rangle$, [MgFe]$'$ and Mgb central line indices for Fornax data. The error bar in the lower left corner of each panel shows the median error. Dots with arrows indicate upper limits in $\Delta M_{B,K_s}$.
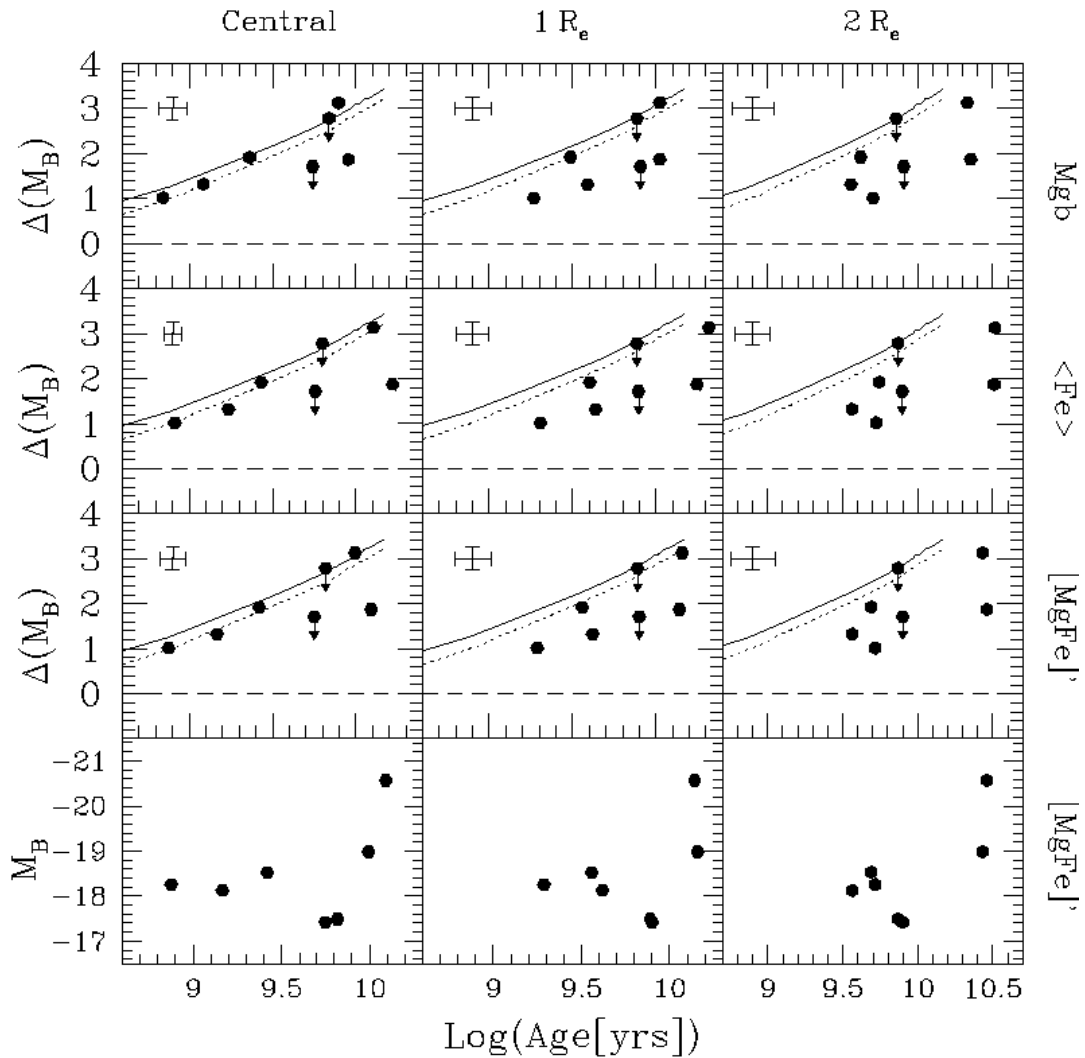
Figure 4.13. ΔM_B and M_B versus ages in the center, at $1\,R_e$ and at $2\,R_e$ of the bulge, using different metallicity indicators (Mgb, $\langle$Fe$\rangle$ and [MgFe]$'$). BC03 predictions of fading vs. age are plotted for the "truncation" (solid line) and "starburst" (dotted line) models described in section 4.2.1. Dashed horizontal lines represent the B-band TFR of spirals from Tully & Pierce (2000). The error bar in the upper left corner of each panel shows the median error. Dots with arrows indicate upper limits in ΔM_B. For ESO 358-G059 (dot with arrow of smaller shift) the results at $1\,R_e$ were re-plotted in the columns corresponding to $2\,R_e$.
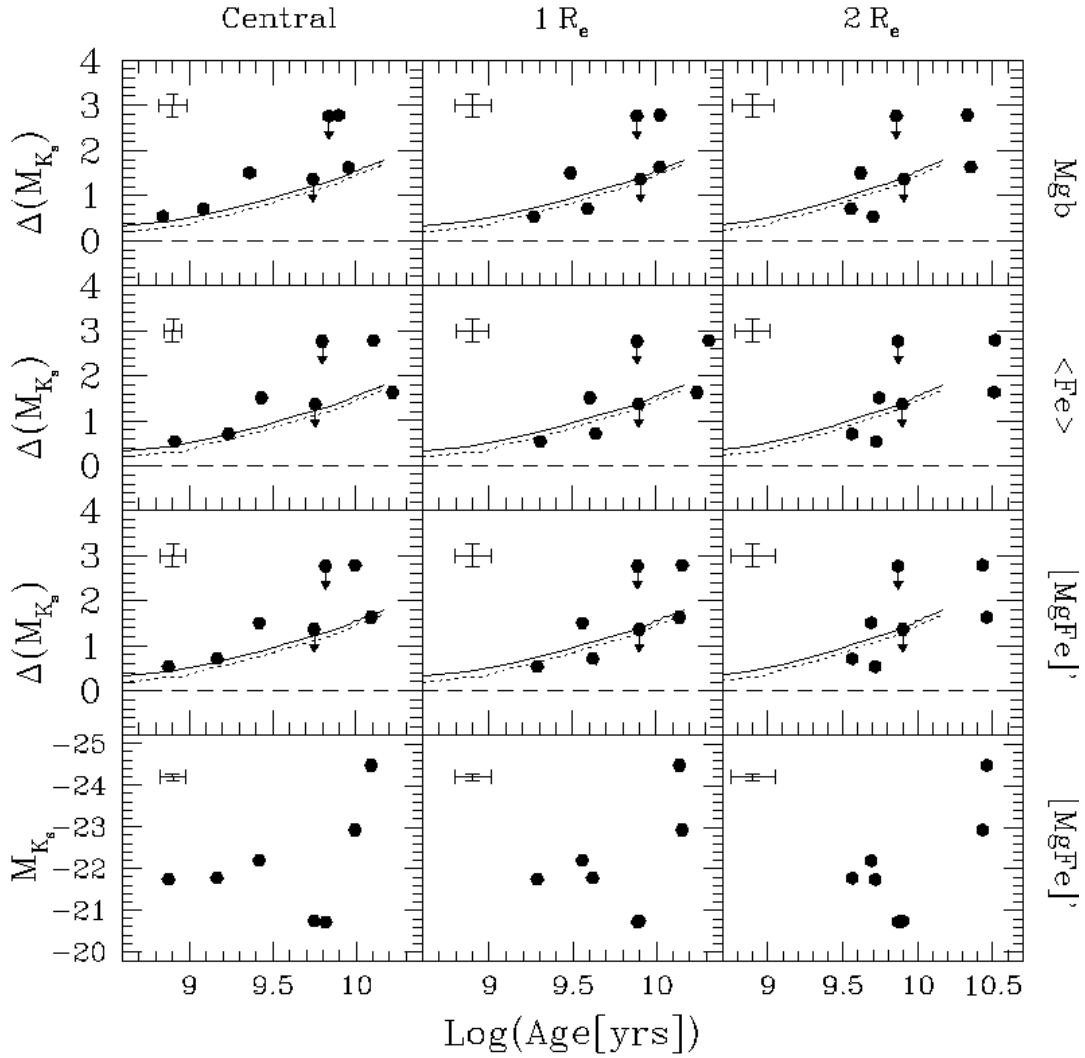
Figure 4.14. ΔM_{K_s} and M_{K_s} versus ages in the center, at $1\,R_e$ and at $2\,R_e$ of the bulge, using different metallicity indicators (Mgb, $\langle$Fe$\rangle$ and [MgFe]$'$). BC03 predictions of fading vs. age are plotted for the "truncation" (solid line) and "starburst" (dotted line) models described in section 4.2.1. Dashed horizontal lines represent the K_s-band TFR of spirals from Tully & Pierce (2000). The error bar in the upper left corner of each panel shows the median error. Dots with arrows indicate upper limits in ΔM_{K_s}. For ESO 358-G059 (dot with arrow of smaller shift) the results at $1\,R_e$ were re-plotted in the columns corresponding to $2\,R_e$.

similar data at $1\,R_e$ and $2\,R_e$. The correlations are stronger for central values than at larger galactocentric distances: a Spearman ranking correlation coefficient test shows that the correlations between central age and $\Delta M_{B,K_s}$ are significant at between the 90% to 97.5% level, while at larger radii the confidence levels decrease to a range between 85% to 90% level only. Apart from the obvious increase in age uncertainties at lower S/N ratios (so with increasing radius), there is another plausible explanation for the apparent radial dependence of the relation. If high redshift spirals simply switch-off their star formation in order to become local S0s, the age versus $\Delta M_{B,K_s}$ relation would be sensitive to the relative differences in luminosity-weighted age at the moment the passive fading starts. The importance of these differences will depend, among other factors, on the relative SFRs of the progenitor spirals and their radial SFR profile before truncation. This would introduce additional scatter to the discussed result. However, there is a possible mechanism which would diminish this effect in the inner regions: a central starburst. If a central starburst precedes the truncation of the star formation, the central ages would be "set to zero" just before passive fading starts. In consequence, relative differences in central age are minimised and the age versus $\Delta M_{B,K_s}$ relation becomes tighter. A central starburst has been proposed in the past as a possible (even as a necessary) step in the morphological transformation of a spiral into a S0 galaxy (Shioya et al. 2004; Christlein & Zabludoff 2004) and there is observational evidence in favour of this scenario (Poggianti et al. 2001; Mehlert et al. 2000, 2003; Moss & Whittle 2000). The youngest galaxies of the Fornax sample seem to have clear radial gradients in age, in agreement with this hypothesis. It is possible that a centrally-concentrated burst of star formation introduces scatter in the bulge properties of these galaxies, and therefore is responsible for the lack of correlation between the bulge properties and the galaxies' luminosities.

Also worthy of note in Figures 4.13 and 4.14 is the absence of a similar correlation between age and M_{B,K_s} at all radii. First, this lack of correlation rules out the possibility that the correlation with $\Delta M_{B,K_s}$ could be spuriously driven by a correlation with M_{B,K_s}, as discussed above. Second, it implies that there is no compelling evidence for the "downsizing scenario" (Gavazzi 1993; Boselli et al. 2001; Scodeggio et al. 2002) in this small sample of S0s, which would predict that the faintest galaxies should have the youngest stellar populations.

Although suggestive, these results are not yet definitive. The significance level of the age versus $\Delta M_{B,K_s}$ relations is not strong enough to totally discard the null hypothesis, and in case of a positive correlation, many questions remain open: does this relation depends on local environment; do all S0s follow this trend or must other properties, like luminosity, be taken into account? Clearly, what is needed is a larger set of high-quality data across a wide range of luminosities and environments to finally disentangle the life histories of these surprisingly complex objects.

Chapter 5

Conclusions and Future Work

In this thesis, a detailed study of the central stellar populations of S0s in the Fornax Cluster is presented. Also, using new and archival results for a sample of 60 galaxies in different environments, the largest study to date of the Tully–Fisher relation of nearby S0 galaxies in both the B- and K_{s}-bands is carried out. The main aim is to obtain new clues on the formation and evolution of these objects.

5.1   Conclusions

The main conclusions of this thesis are:

- The stellar kinematics of a sample of 9 S0 galaxies in the Fornax Cluster reveal a large amount of complexity in these systems. The presence of kinematically-distinctive components (such as bars) in NGC 1380, NGC 1381 and NGC 1375, suggests that their evolutionary histories may be relatively complex.

- By careful measurement of their maximum rotational speeds, it was found that 7 of these 9 S0s are rotationally-supported systems.

- Central absorption line indices correlate with central velocity dispersions in a way similar to what previous studies found for elliptical galaxies. However, a study of the stellar population properties of the Fornax S0s reveals that the trends shown by their line indices seem to be produced by relative differences in age and α-element abundances, contrary to what is found in ellipticals where the overall metallicities are the main drivers of the correlations.

- The scatter in the Index*–$\log(\sigma)$ relations can be partially explained by the rotationally-supported nature of many of our S0s. The tighter correlations found between Index* and $\log(V_{\mathrm{MAX}})$ support this statement.

- The dynamical mass is the physical property governing these correlations and in our Fornax S0s we need to study it by considering their rotationally-supported nature. For these systems, V_{MAX} is a better tracer of dynamical mass than σ.

- The local TFR of S0 galaxies presents an offset with respect to the local TFR of spirals. Interpreted as a shift in luminosity, it amounts to between -1.3 ± 0.1

and -1.7 ± 0.4 in the B-band and between -0.8 ± 0.4 and -1.2 ± 0.4 in K_s-band, with the exact values depending on the calibration adopted for the spiral galaxy TFR.

- The observed offsets between the spiral and S0 TFRs are consistent with an scenario where spirals have faded in order to become S0s.

- In a scenario where present-day S0s are the descendants of higher redshift spirals which have simply passively faded, the mean offsets for our sample constrains the average time since these galaxies started fading in both the B- and K_s-bands to a range between 1 and 6 Gyr. Although consistent within the relatively large uncertainties, the values derived from the B- and K_s-bands are uncomfortably different from each other. If a starburst is assumed before the truncation of the star formation, the upper end of the estimated fading timescales since transformation increase somewhat.

- Interestingly, however, if the parent population of high redshift spirals was ~ 1 mag brighter in B at z ~ 1, as some TFR studies suggest, the fading timescales derived in B and K_s become much more consistent (5.5–7.5 Gyr). However, the large scatter in the TFR means that such simple models with a single epoch of formation cannot provide the whole story.

- The total scatter in the TFR of S0s is found to be 0.88 ± 0.06 mag in the B-band and 0.98 ± 0.06 in the K_s-band. Only $\sim 10\%$ of this scatter can be attributed to the observational errors, with $\sim 90\%$ arising from the intrinsic astrophysical spread in the TFR. Such a scatter could be explained by a combination of effects. First, it could arise from the larger scatter observed in the spiral TFR at high redshift. Second, it could be a consequence of the different times when individual spirals have started their transformation. It could also be a product of the individual star formation histories of these galaxies.

- To explore other possible scenarios, correlations between the offset from the TFR and other properties of these systems have been studied. However, no structural property of the galaxies seems to correlate strongly with this offset.

- By investigating absorption line indices of Fornax S0s, it was found that the offset from the TFR correlates with the estimated age of the central stellar population of the individual galaxies, in the sense and of the magnitude expected if S0s had passively faded since being converted from spirals. A central starburst before the truncation of star formation would explain why the correlation is stronger with central age than at larger galactocentric distances.

- The overall results presented here warn about the potential danger in studying S0s and elliptical galaxies as one type of objects under the label of "early-type galaxies". Their physical properties may be mis-estimated or wrongly interpreted if both types of objects are assumed to have a common origin.

Indulging in a certain amount of speculation, the general properties observed in the Fornax S0s suggest that they could have followed different evolutionary paths.

The faint objects are good candidates for gas-stripped spirals who have fallen into the cluster potential from the field, having a final burst of star formation before truncation. In particular, the galaxies ESO 358-G006, ESO 358-G059 and ESO 359-G002 seem to be good candidates for a "harassment" scenario (Moore, Lake & Katz 1998). Their faint magnitudes, relatively weak rotational support and rounder isophotal shapes agree with the expected properties of a harassed remnant. Ram-pressure gas stripping (Gunn & Gott 1972) seems to be a plausible scenario for NGC 1380A and IC 1963. Their observed rotational support and disky isophotal shapes could be preserved from their past as spirals, while the gas was removed via interactions with the hot ICM. The case of NGC 1375 is more puzzling given the presence of a kinematically-distinct component in the central region, a strong rotational support but rater boxy isophotes. In consequence, it is hard to suggest one particular scenario for the evolution of this object On the other hand, bright rotationally-supported S0s seem to have suffered short and violent burst of star formation in the past, being closer to what is observed in mergers. Nevertheless, a study of population gradients may confirm if these interpretations hold.

The results found for local S0s and their TFR are compatible with the idea of an evolutionary link between spirals and these galaxies via fading of their stellar populations. However, the large scatter in some of the observed properties suggest that the overall evolutionary paths are more complicated.

The results of both the axes of work described in this thesis, the TFR and Fornax stellar population studies, are complementary. However, we should keep in mind that the former is weighted towards bright S0s in a variety of environments while the latter includes mainly faint objects in one particular cluster. This must be taken into account when trying to find a joint interpretation of the results. The new data from the Fornax Cluster show that we are finally in a position to use observations of nearby S0 galaxies to obtain important archaeological clues as to the mechanisms by which these systems form.

5.2 Future Work

The aim of this thesis was to shed new light on the formation and evolution of S0 galaxies. Although some important clues have been found in this study, there is still a long way to go if we want to finally understand the origin of these systems. Some initiatives to continue this research line are listed bellow:

- A small number of S0s in a single cluster will always limit the significance of the resulting measurements. Clearly, we need a larger homogeneous dataset of the quality now attainable with telescopes like the VLT to finish off the work begun here. This larger sample would permit a study of their TFR in greater detail with a totally homogeneous dataset. By having a complete sample of objects in few clusters, it would be possible to fit the TFR of local S0s (zero-point *and slope*) and compare it to the spiral counterpart as a function of luminosity. It would be also possible to confirm the existence of a trend between age and the shifts between spiral and S0 TFRs as is observed for Fornax S0s.

- Extend the stellar populations study presented here by analysing gradients of line indices, ages, metallicities and element abundances. This will probably place new constraints on the possible evolutionary scenarios considered for these objects.

- The use of population models based on higher resolution stellar libraries will be fundamental for the study of the stellar populations of many of these galaxies. Unfortunately the gap between current data quality and simple stellar population modelling is still large. Even the most popular models (e.g. TMB03; BC03; Vazdekis et al. 2003) are far from being able to exploit the full potential of data like those used in this thesis. However, the situation is changing. Dr. A. Vazdekis and collaborators are planning the prompt release of their models with new fitting functions based on the high resolution (2.3 Å) stellar library MILES (Sánchez-Blázquez et al. 2006). It is planned to take advantage of this new tool in our study of S0 galaxies, as well as exploring other models with non-solar abundance ratios (e.g. Maraston 2005; Schiavon 2006).

- A spectral bulge-disk decomposition of the Fornax S0 sample will permit the study of the stellar populations of these systems as a function of the structural component where they reside. This could give new clues as to how these galaxies form.

There is still much work to be done, however this thesis shows how much can be learned with the quality of data now attainable. More and new results seem to be within reach.

Bibliography

Andreon S., 1998, ApJ, 501, 533

Baes M., Buyle P., Hau G.K.T., Dejonghe H., 2003, MNRAS, 341, L44

Bamford S. P., Aragón-Salamanca A., Milvang-Jensen B., 2006, MNRAS, 366, 308B

Barr J., Jorgensen I., Chiboucas K., Davies R.L., Bergmann M., 2006, ApJ,649, 1

Bekki K., 1998, ApJ, 502, L133

Bekki K., 1999, ApJ, 510, L15

Bekki K., Shioya Y., Couch W.J, 2002, ApJ, 577, 651

Bell E.F., et al., 2004, ApJ, 608, 883

Bender R., Burstein D., Faber S.M., 1993, ApJ, 411, 153

Bender R., Saglia R.P., Ziegler B., Belloni P., Greggio L., Hopp U., Bruzual G., 1998, ApJ, 493, 529

Bernardi M., Alonso M.V., Da Costa L.M., Willmer C.N.A., Wegner G., Pellegrini P.S., Reté C., Maia M.A.G., 2002, AJ, 123, 2990B

Bernardi M., et al., 2003, AJ, 125, 1866

Bernardi M., Sheth R.K., Nichol R.C., Schneider D.P., Brinkmann J., 2005, AJ, 129, 61

Bertola F., 2005, ApJ, 631, 785

Bertola F., Buson L. M., Zeilinger W. W., 1992, ApJ, 401L, 79B

Binney J., Tremaine S., 1987, "Galactic Dynamics", Princeton Series in Astrophysics

Blakeslee J.P., et al., 2003, ApJL, 596, 143

Böhm A., et al., 2004, A&A, 420, 97

Boselli A., Gavazzi G., Scodeggio, M., 2001, AJ, 121, 753

Boselli A., Gavazzi G., 2006, PASP, 118, 517B

Bower R.G., Lucey J.R., Ellis R.S., 1992, MNRAS, 254, 589

Bravo-Alfaro H., Cayate V., van Gorkom J.H., Balkowski C., 2000, AJ, 119, 580

Brown T., 2001, Instrument Science Report STIS 2001-005

Bruzual G, Charlot S., 2003, MNRAS, 244, 1000B

Bureau M., Athanassoula E., 2005, ApJ, 626, 159

Bureau M.& Chung A., 2006, MNRAS, 366, 182B

Burstein D., Davies R.L., Dressler A., Faber S.M., Lynden-Bell A., Terlevich R.J., Wegner G., 1988, in *Towards Understanding Galaxies at Large Redshifts*, Ed: R.G. Kron and A. Renzini, (Kluwer, Dordrecht), 17

Byrd G.& Valtonen M., 1990, ApJ, 350, 89

Caon N., Capaccioli M., D'Onofrio M., 1994, A&AS, 106, 199

Cappellari M., Emsellem E., 2004, PASP, 116, 138

Cappelleri M., et al., 2006, MNRAS, 366, 1126

Carrasco L., 2001, ApJ, 563, L23

Chabrier G., 2003, PASP, 115, 763

Christlein D., Zabludoff A.I., 2004, ApJ, 616, 192C

Colless M., Burstein D., Davies R.L., McMahan R.K., Saglia R.P., Wegner G., 1999, MN-RAS, 303, 813

Conselice C. J., Bundy K., Ellis R. S., Brichmann J., Vogt N. P., Phillips A. C., 2005, ApJ, 628, 160

Courteau S., McDonald M., Widrow, L.M., 2006, ApJL, in press (astro-ph/0610721)

De Lucia G., et al., 2004, ApJL, 610, 77

Denicoló G., Terlevich R., Terlevich E., Forbes D.A., Terlevich A., Carrasco L., 2005, MN-RAS, 356, 1440D

Desay V., 2004, PhDT, 223D

Desai et al., 2006, submitted.

De Vaucouleurs, G., de Vaucouleurs A., Corwin H. G., Buta R. J., Paturel G., Fouque, P. 1991, Volume 1-3, XII, Springer-Verlag Berlin Heidelberg New York,

Dickey J.M., Gavazzi G., 1991, ApJ, 373, 347

Di Nella H., Garcia A.M., Garnier R., Paturel G., 1995, A&AS, 113, 151D

Djorgovski S., Davis M., 1987, ApJ, 313, 59

D'Onofrio M., Zaggia S.R., Longo G., Caon N., Capaccioli M., 1995, A&A, 296, 319

Dressler A., 1980, ApJ, 236, 351

Dressler A., Lynden-Bell D., Burstein D., Davies R.L., Faber S.M., Terlevich R., Wegner G., 1987, ApJ, 313, 42

Dressler A., Sangade A., 1983, ApJ, 265, 664

Dressler A., et al., 1997, ApJ, 490, 577

Ebeling H., Edge A.C., Bohringer H., Allen S.W., Crawford C.S., Fabian A.C., Voges W., Huchra J.P., 1998, MNRAS, 301, 881

Ellis R.S., Smail I., Dressler A., Couch W.J., Oemler A.Jr., Butcher H., Sharples, R.M., 1997, ApJ, 483, 582

Emsellem E., Cappellari M., Peletier R.F., et al., 2004, MNRAS, 352, 721

Faber S.M., 1973, ApJ, 179, 731

Fasano G., Poggianti B.M., Couch W.J., Bettoni D., Kjaergaard P.& Moles M., 2000, ApJ, 542, 673

Ferrarese L., 2002, ApJ, 578, 90

Ferrari C., Benoist C., Maurogordato S., Cappi A., Slezak E., 2005, A&A, 430, 19

Fisher D., Franx M., Illingworth G.D., 1995, ApJ, 448, 119

Fisher D., Franx M., Illingworth G., 1996, ApJ, 459, 110F

Flores H., Hammer F., Puech M. Amram P., Balkowski C., 2006, submitted to A&A, astro-ph/0603563

Freeman K.C., 1970, ApJ, 160, 811F

Fritz A., Ziegler B., Bower R.G., Smail I., Davies R.L., 2005, MNRAS, 358, 233

Fujita Y., 1998, ApJ, 509, 587

Gavazzi G., 1989, ApJ, 346, 59

Gavazzi G., Boselli A., Mayer L., Iglesias-Paramo J., Vílchez J.M.,

Gavazzi G., Contursi A., Carrasco L., Boselli A., Kennicutt R., Scodeggio M., Jaffe W., 1995, A&A 304, 325

Giovanelli R., Haynes M.P., da Costa L.N., Freudling W., Salzer J.J., Wegner G., 1997, ApJ, 477L, 1G

Gnedin O.Y., 2003a, ApJ, 582, 141

Gnedin O.Y., 2003b, ApJ, 589, 752

González J.J., 1993, PhD Thesis, University of California, Santa Cruz

Gorgas J., Efstathiou G., Aragón-Salamanca A., 1990, MNRAS, 245, 217

Goto T., et al., 2003, PASJ, 55, 757

Graham A.W., Colless M.M., Busarello G., Zaggia S., Longo G., 1998, A&AS, 133, 325

Gunn J.E., Gott J.R., 1972, ApJ, 176, 1

Guzman R., Lucey J.R., Carter D., Terlevich R.J., 1992, MNRAS, 257, 187

Henriksen M., Byrd G., 1996, ApJ, 459, 82

Hernquist L., 1990, ApJ, 356, 359

Hinz J.L., Rix H.,-W., Bernstein G.M., 2001, AJ, 121, 683

Hinz J.L., Rieke G.H., Caldwell N., 2003, AJ, 126, 2622

Hogg D.W., et al., 2004, ApJL, 601, 29

Holden B.P., et al., 2004, AJ, 127, 248

Jarret T.H., 2000, PASP, 112, 1008J

Jarret T.H., Chester T., Cutri R., Schneider S.E., Huchra J.P., 2003, AJ, 125, 525J

Jorgensen I., Franx M., 1994, ApJ, 433, 553

Jorgensen I., Franx M., Kjaergaard P., 1996, MNRAS, 280, 167

Jorgensen I., Franx M., Hjorth J., van Dokkum P.G., 1999, MNRAS, 308, 833

Kelson D.D., Illingworth G.D., van Dokkum P.G., Franx M., 2000, ApJ, 531, 184

Kenney J.D.P., Koopmann R.A., 1999, AJ, 117, 181

Kenney J.D.P., van Gorkom J.H., Vollmer B., 2004, AJ, 127, 3361

Kenney J.D.P., Young J.S., 1989, ApJ, 344, 171

Kissler-Patig M., 1997, A&A, 319, 83

Kuijken K., Fisher D., Merrifield M.R., 1996, MNRAS, 283, 543

Kuijken K., Merrifield M.R., 1995, ApJ, 443, L13

Kuntschner H., 2000, MNRAS, 315, 184K

Larson R.B., Tinsley B.M., Caldwell C.N., 1980, ApJ, 237, 692L

Longhetti M., Rampazzo R., Bressan A., Chiosi C., 1998, A&AS, 130, 267L

López-Cruz O., Barkhouse W.A., Yee H.K.C., 2004, ApJ, 614, 679

Lorenz H., Böhm P., Capaccioli M., Richter G.M., Longo G., 1993, A&AS, 277, L15

Madore B.F., Freedman W.C., Silbermann, N., et al., 1999, ApJ, 515, 29

Mao S., Mo H. J., White S.D.M., 1998, MNRAS, 297, L71

Maraston C., 2005, MNRAS, 362, 799

Mathieu A., Merrifield M., Kuijken K., 2002, MNRAS, 330, 251

McIntosh D.H., Zabludoff A.I., Rix H.-W., Caldwell N., 2005, ApJ, 619, 193

Mehlert D., Saglia R.P., Bender R., Wegner G., 2000, A&AS, 141, 449

Mehlert D., Thomas D., Saglia R.P., Bender R., Wegner G., 2003, A&A, 407, 423

Mei S., et al., 2006a, ApJ, 639, 81

Mei S., et al., 2006b, ApJ, 644, 759

Merrett H.R., Merrifield M.R., Douglas N.G., et al., 2006, astro-ph/0603125

Merritt D., 1984, ApJ, 276, 26

Mihos J.C., Hernquist L., 1994, ApJ, 425, L13

Miller R.H., 1986, A&A, 167, 41

Moore B., Lake G., Katz N., 1998, ApJ, 495, 139

Moss C., Whittle M., 2000, MNRAS, 317 667

Mould J.R. et al., 2000, ApJ, 529, 786

Mullis C.R., Rosati P., Lamer G., Bohringer H., Schwope A., Schuecker P., Fassbender R.,
    2005, ApJ, 623, L85

Nagashima M., Lacey C.G., Okamoto T., Carlton M.B., Frenk C.S., Cole S., 2005, MNRAS, 363, L31

Neistein E., Maoz D., Rix H.-W., Tonry J.L., 1999, AJ, 117, 2666

Nieto J.-L., Bender R., Surma P., 1991, A&A, 244, 37N

Oosterloo T., van Gorkom J., A&A, 437, L19

Owen F.N., Ledlow M.J., Keel W.C., Wang Q.D., Morrison G.E., 2005, AJ, 129, 31

Pizzella A., Corsini E.M., Dalla Bontà E., Sarzi M., Coccato L.,

Poggianti B. M., 1997, A&AS, 122, 399P

Poggianti B. M., Smail I., Dressler A., Couch W. J., Barger A. J., Butcher H., Ellis R. S., Oemler A., 1999, ApJ, 518, 576

Poggianti B., Bridges T.J., Carter D. et al. 2001, ApJ 563, 118

Postman M., et al., 2005, ApJ, 623, 721

Prugniel Ph., Simien F., 1995, ASPC, 86, 151P

Rengarajan T.N., Iyengar K.V.K., 1992, MNRAS, 259, 559

Rix H-W, Guhathakurta P., Colless M., Ing K., 1997, MNRAS, 285, 779R

Rubin V., Graham J.A., Kenney, J.D.P., 1992, ApJ, 394, L9

Sakai S., Mould J.R., Hughes S.M.G., et al., 2000, ApJ, 529, 698

Sánchez-Blázquez P., et al., 2006, MNRAS, 371, 703

Sandage A., Tammann G.A., 1987, A Revised Catalog of Shapley-Ames Galaxies (2d ed.; Washington:Carnegie Institution)

Schiavon R.P., 2006, to appear in ApJSS (astro-ph/0611464)

Schlegel D.J., Finkbeiner D.P., Davis M., 1998, ApJ, 500, 525S

Schweizer F., 1986, Sci, 231, 227S

Scodeggio M., Gavazzi G., Franzetti P., Boselli A., Zibetti S., Pierini D., 2002, A&A, 384, 812

Sharples R.M., 1997, ApJ, 483, 582

Shi Y., Rieke G.H., Papovich C., Pérez-González P.G., Le Floch E., 2006, Accepted in ApJ (astro-ph/0603453)

Shioya Y., Bekki K., Couch W.J., 2004, ApJ, 601, 654

Simard L., Willmer C.N.A., Vogt N.P. et al., 2002, ApJS, 142, 1S

Smail I., et al., 2001, MNRAS, 323, 839 217, 493

Stanford S.A., Eisenhardt P.R., Dickinson M., 1998, ApJ, 492, 461

Stanford S.A., Elston R., Eisenhardt P.R., Spinrad H., Stern D., Dey A., 1997, AJ, 114, 223

Terlevich A.I., Forbes D.A., 2002, MNRAS, 330, 547

Terlevich R., Davies R.L., Faber S.M., Burstein D., 1981, MNRAS, 196, 381

Thomas D., Maraston C., Bender R., 2002, Ap&SS, 281, 371

Thomas D., Maraston C., Bender R., 2003, MNRAS, 339, 897

Tody D., 1986, "The IRAF Data Reduction and Analysis System", in proc. SPIE Instrumentation in Astronomy VI, ed. D. L. Crawford, 627, 733

Tody D., 1993, "IRAF in the Nineties", in Astronomical Data Analysis Software and Systems II, A.S.P. Conference Ser., Vol 52, eds. R.J. Hanisch, R.J.V. Brissenden, J. Barnes, 173

Tonry J.L., Dressler A., Blakeslee J.P., et al., 2001, ApJ, 546, 681T

Trager S.C., Faber S.M., Worthey G., González J.J., 2000a, AJ, 119, 1645

Trager S.C., Faber S.M., Worthey G., González J.J., 2000b, AJ, 120, 165

Tully R.B., Fisher J.R., 1977, A&A, 54, 661T

Tully R.B., Pierce M.J., 2000, ApJ, 533, 744

van den Bergh S., 1990, ApJ, 348, 57

van den Bosch F.C., 2000, ApJ, 530, 177V

van Dokkum P.G., Franx M., Kelson D.D., Illingworth G.D., Fisher D., Fabricant D., 1998, ApJ, 500, 714

van Dokkum P.G., Franx M., Fabricant D., Illingworth G.D., Kelson D.D., 2000, ApJ, 541, 95

van Dokkum P.G., Stanford S.A., Holden B.P., Eisenhardt P.R., Dickinson M., Elston R., 2001, ApJL, 552, L101

Vazdekis A., Kuntschner H., Davies R.L., Arimoto N., Nakamura O., Peletier R., 2001, ApJ, 551L, 127

Veilleux S., Bland-Hawthorn J., Cecil G., Tully R.B., Miller S.T., 1999, ApJ, 520, 111

Verheijen M.A.W., 2001, ApJ, 563, 694

Visvanathan N., Sandage A., 1977, ApJ, 216, 214

Vogt N.P., et al., 1997, ApJ, 479, L121

Vollmer B., 2003, A&A, 398, 525

Vollmer B., Beck R., Kenney J.D.P., van Gorkom J.H., 2004, AJ, 127, 3375

Vollmer B., Braine J., Balkowski C., Cayatte V., Duschl W., 2001, A&A, 374, 824

Vollmer B., Cayatte V., Boselli A., Balkowski C., Duschl W., 1999, A&A, 349, 411

Vollmer B., Marcelin M., Amram P., Balkowski C., Cayatte V., Garrido O., 2000, A&A, 364, 532

Whitmore B.C., Schechter P.L., Kirshner R.P., 1979, ApJ, 234, 68

Willick J.A., 1994, ApJS, 92, 1

Yasuda N., Fukugita M., Okamura S., 1997, ApJS, 108, 417Y

Yoshida M., et al., 2004, AJ, 127, 90

Zwaan M.A., van der Hulst J.M., De Blok W.J.G., McGaygh S.S., 1995, MNRAS, 273L, 35Z

Appendix A

Line-of-sight Kinematics

This appendix shows plots of the major-axis kinematics for the sample of 9 Fornax S0 galaxies. The values of mean velocity, V_{LOS}, velocity dispersion, σ, and higher-moment coefficients, h_3 and h_4 are plotted as a function of radius. The location of the galaxy's bulge effective radius, R_{e}, is marked as a dashed line. The values of R_{e} and the position angle of the slit are annotated on the plot. The solid lines show the fit to the dispersion profile, $\sigma_{\mathrm{fit}}(R)$, adopted in Section 2.4.
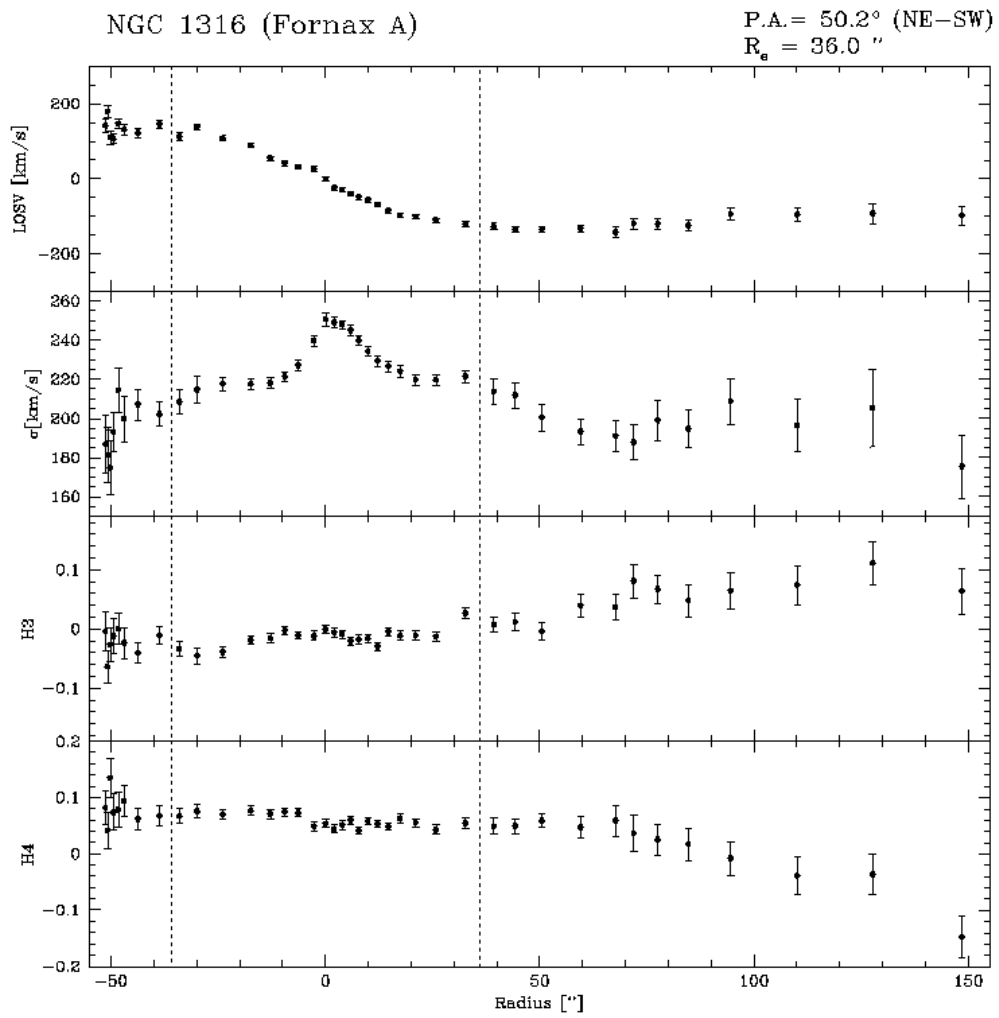
Figure A.1. The major-axis kinematics of NGC 1316.
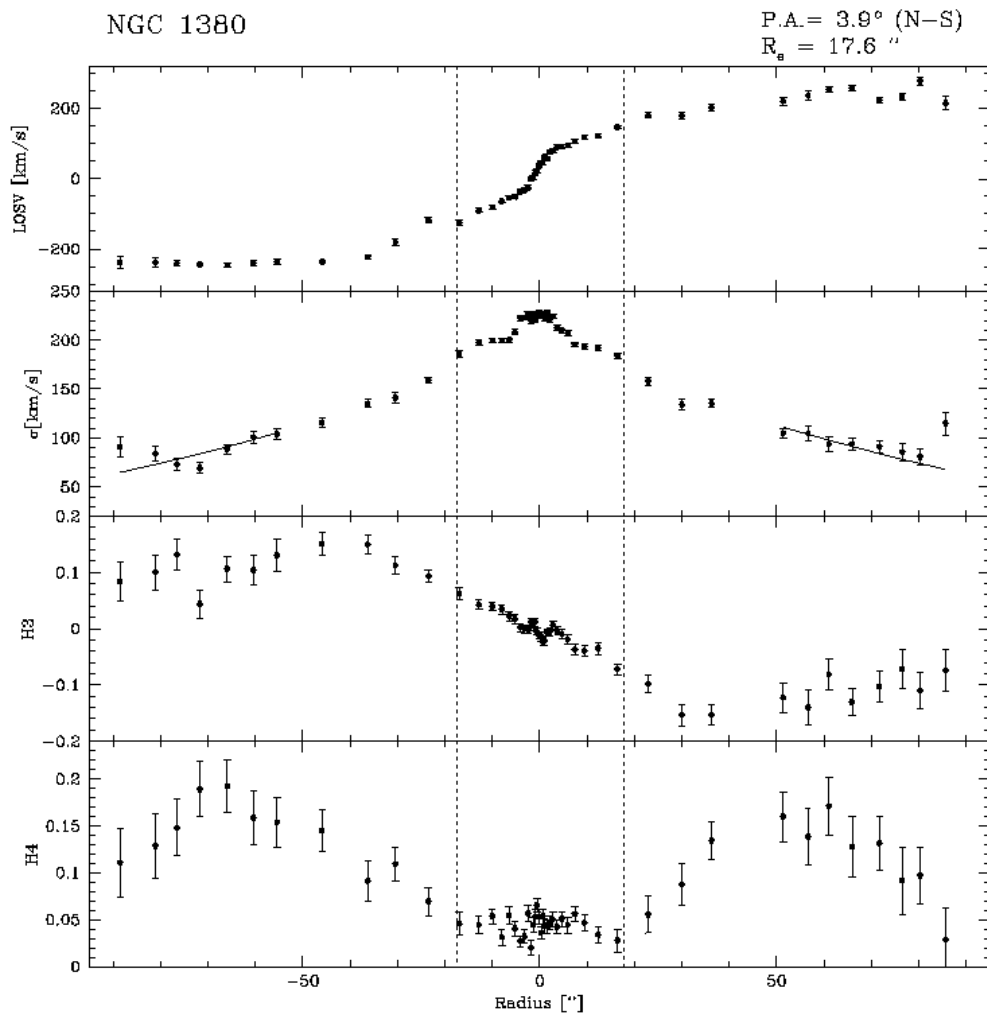
Figure A.2. The major-axis kinematics of NGC 1380.
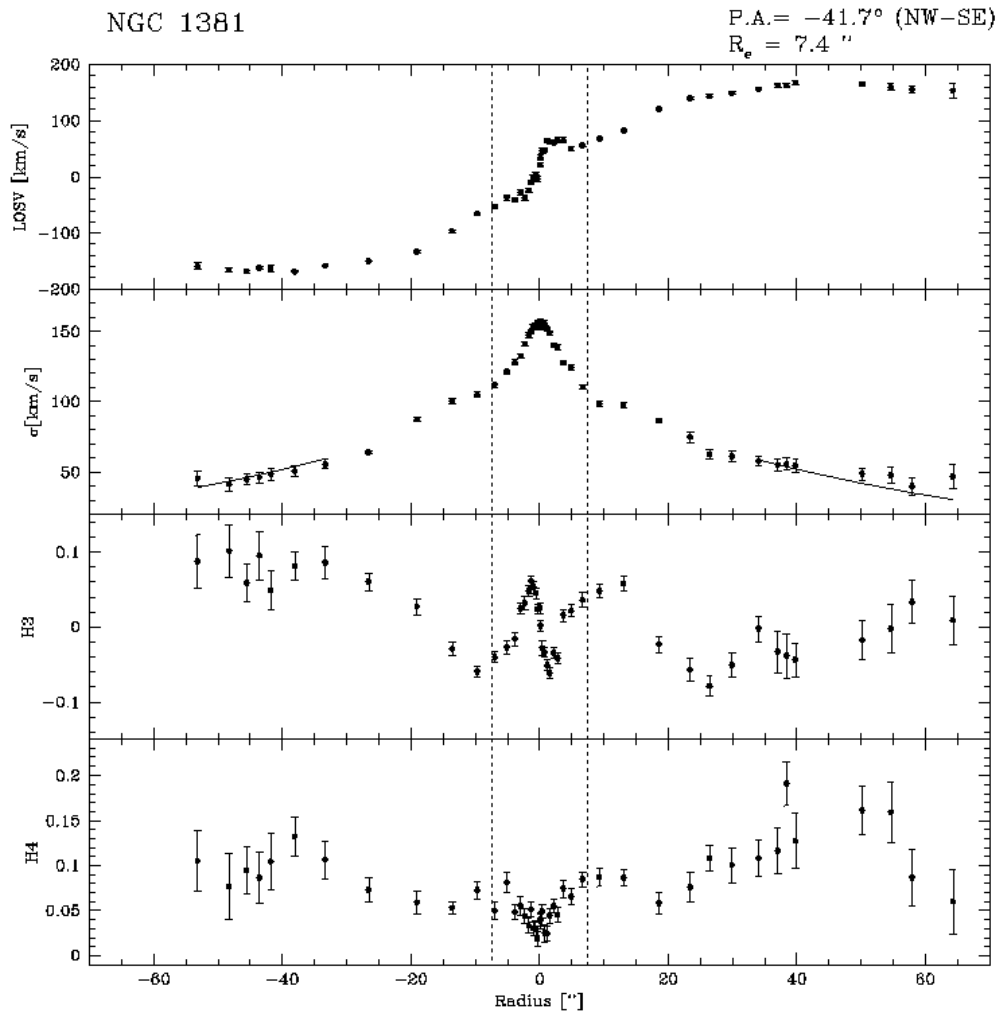
Figure A.3. The major-axis kinematics of NGC 1381.
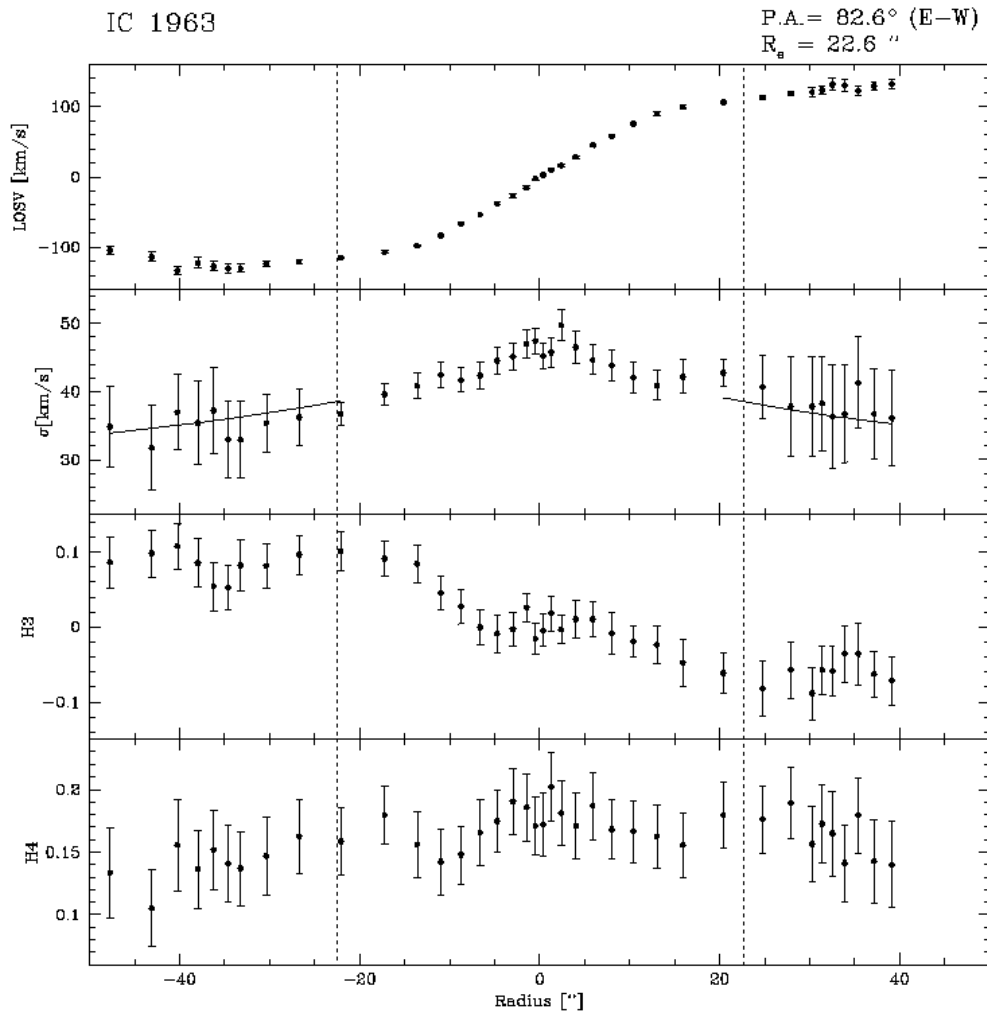
Figure A.4. The major-axis kinematics of IC 1963.
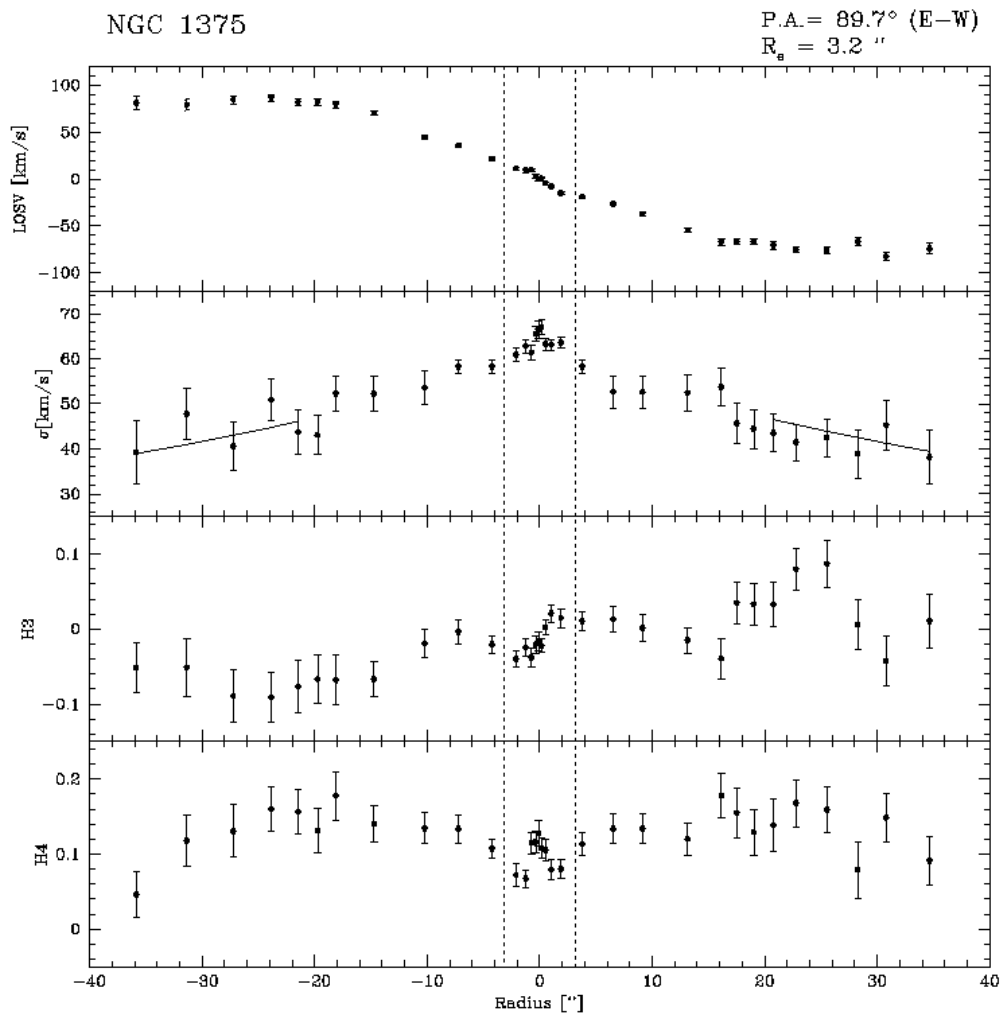
Figure A.5. The major-axis kinematics of NGC 1375.
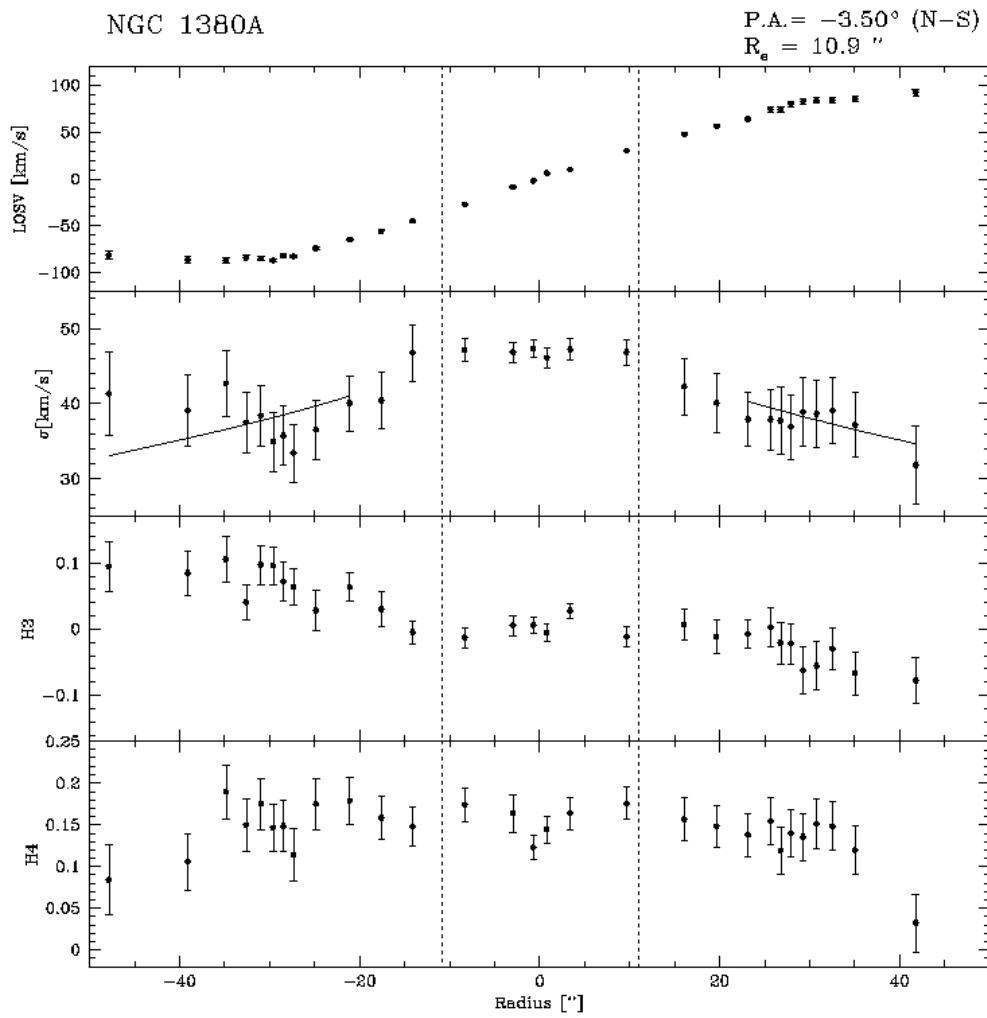
Figure A.6. The major-axis kinematics of NGC 1380A.
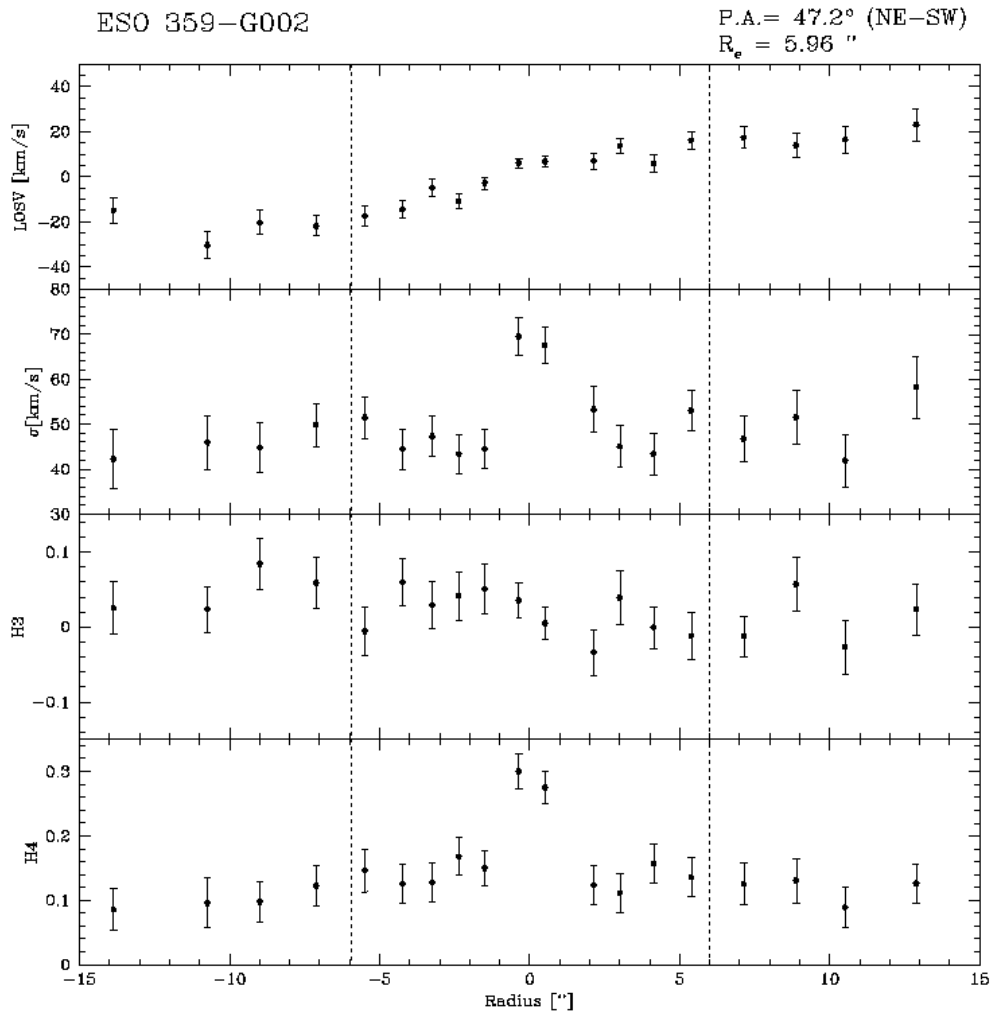
Figure A.7. The major-axis kinematics of ESO 359-G002.
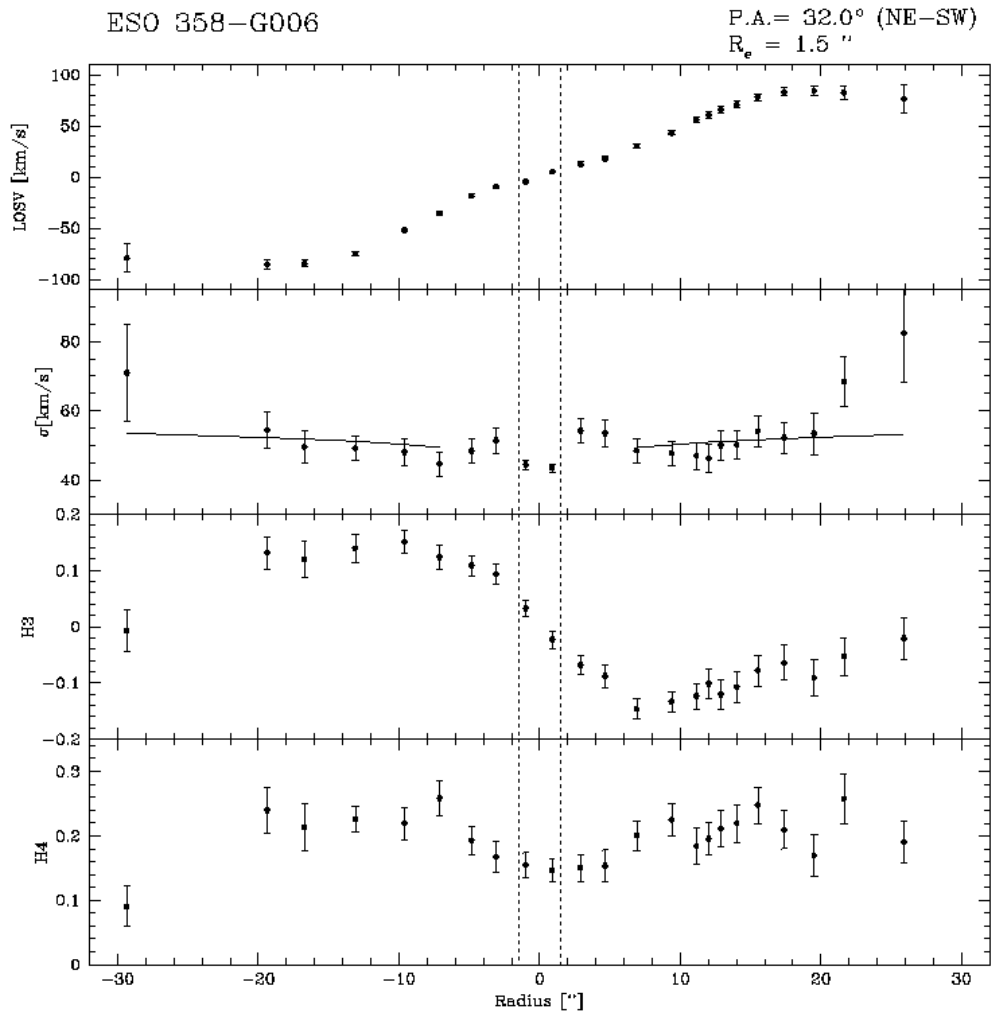
Figure A.8. The major-axis kinematics of ESO 358-G006.
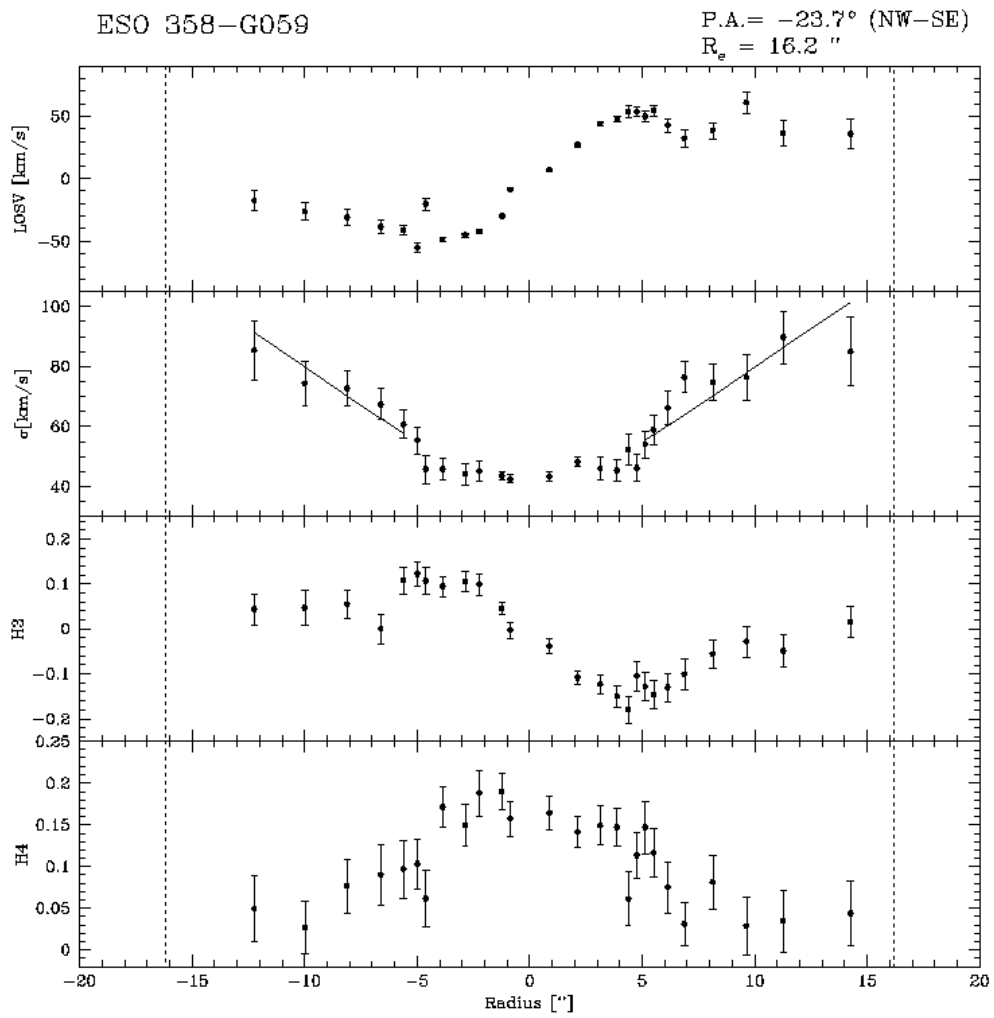
Figure A.9. The major-axis kinematics of ESO 358-G059.

Appendix B

Tables

In this appendix the tables with different parameters for the different S0 samples used in Chapters 3 and 4 are presented.

Table B.1 includes a compilation of absolute magnitudes (total $K_{\rm s}$-band from 2MASS) and shifts in magnitude from the $K_{\rm s}$-band TFR of spiral galaxies, $\log(V_{\rm MAX})$ and central velocity dispersions for ~ 60 S0 galaxies used in Chapter 4. Also, in the same table the different structural parameters estimated using $K_{\rm s}$-band photometry and GIM2D software (Simard et al. 2002) are included.

Tables B.2 and B.3 include different central absorption line indices for the Fornax sample, measured at 3 Å and Lick resolution, respectively. In Table B.4, central ages and metallicities are presented for the Fornax S0s by using different metallicity indicators at Lick resolution. Ages and metallicities were estimated using Bruzual & Charlot (2003) simple stellar population models. Also, B-band absolute magnitudes (from RC3) and shifts in magnitude from the B-band TFR of spiral galaxies are presented in the same table. Similar data for the rotationally-supported S0s at 1 and 2 $R_{\rm e}$ of the bulge are presented in Tables B.5 and B.6 respectively.

Table B.1. Tully-Fisher and Structural Parameters of S0 galaxies.

#	Name	$K_{\rm s,tot}$ [mag]	$M_{\rm K_s}$ [mag]	$\Delta(M_{\rm K_s})$ [mag]	$\log(V_{\rm MAX})$ [km s^{-1}]	σ_0 [km s^{-1}]	B/T	$R_{\rm e}$ [kpc]	$R_{\rm exp}$ [kpc]	i [^{o}]	Sérsic	$R_{\rm half}$ [kpc]
(1)	(2)	(3)	(4)	(5)	(6)	(7)	(8)	(9)	(10)	(11)	(12)	(13)
FIELD	(N99)[1]											
1	NGC 0584	7.30 (0.02)	-24.16 (0.10)	1.09 (0.26)	2.40 (0.09)	225 $(-)^a$	0.75 $^{+0.06}_{-0.02}$	1.50 $^{+0.22}_{-0.04}$	3.25 $^{+0.34}_{-0.34}$	57.5 $^{+4.4}_{-3.7}$	3.83 $^{+0.18}_{-0.08}$	2.27
2	NGC 0936	6.91 (0.02)	-24.92 (0.15)	1.42 (0.28)	2.52 (0.13)	193 $(-)^a$	0.38 $^{+0.00}_{-0.00}$	1.36 $^{+0.02}_{-0.02}$	4.36 $^{+0.01}_{-0.02}$	33.9 $^{+0.4}_{-0.2}$	2.92 $^{+0.03}_{-0.02}$	4.62
3	NGC 1023	6.24 (0.02)	-24.02 (0.16)	1.21 (0.29)	2.40 (0.03)	213 $(-)^a$	0.48 $^{+0.00}_{-0.00}$	0.86 $^{+0.01}_{-0.00}$	3.12 $^{+0.01}_{-0.02}$	74.3 $^{+0.1}_{-0.1}$	3.70 $^{+0.04}_{-0.02}$	2.69
4	NGC 1052	7.45 (0.01)	-23.78 (0.22)	0.41 (0.33)	2.28 (0.09)	204 $(-)^a$	0.73 $^{+0.01}_{-0.02}$	1.39 $^{+0.04}_{-0.05}$	1.53 $^{+0.04}_{-0.05}$	48.2 $^{+1.5}_{-2.7}$	4.29 $^{+0.05}_{-0.05}$	1.77
5	NGC 2549	8.05 (0.01)	-22.33 (0.23)	1.96 (0.34)	2.29 (0.07)	155 $(-)^a$	0.58 $^{+0.01}_{-0.01}$	0.48 $^{+0.01}_{-0.01}$	1.46 $^{+0.02}_{-0.01}$	75.7 $^{+0.2}_{-0.3}$	2.85 $^{+0.02}_{-0.03}$	1.05
6	NGC 2768	7.00 (0.03)	-24.88 (0.18)	0.35 (0.30)	2.40 (0.07)	193 $(-)^a$	0.52 $^{+0.00}_{-0.01}$	3.12 $^{+0.02}_{-0.05}$	5.23 $^{+0.04}_{-0.04}$	70.6 $^{+0.3}_{-0.3}$	3.98 $^{+0.05}_{-0.03}$	3.52
7	NGC 2787	7.26 (0.01)	-21.78 (0.34)	3.19 (0.41)	2.37 (0.06)	205 $(-)^a$	0.54 $^{+0.07}_{-0.08}$	0.34 $^{+0.05}_{-0.06}$	0.89 $^{+0.07}_{-0.07}$	54.1 $^{+2.4}_{-2.3}$	2.43 $^{+0.23}_{-0.31}$	0.72
8	NGC 3115	5.88 (0.02)	-23.95 (0.11)	2.76 (0.26)	2.57 (0.07)	220 $(-)^a$	0.59 $^{+0.00}_{-0.01}$	0.84 $^{+0.01}_{-0.02}$	2.22 $^{+0.00}_{-0.00}$	68.2 $^{+0.1}_{-0.1}$	2.98 $^{+0.01}_{-0.06}$	1.72
9	NGC 3384	6.75 (0.02)	-23.37 (0.15)	1.79 (0.28)	2.39 (0.06)	140 $(-)^a$	0.51 $^{+0.04}_{-0.05}$	0.42 $^{+0.06}_{-0.07}$	2.45 $^{+0.13}_{-0.20}$	63.7 $^{+1.7}_{-2.1}$	3.16 $^{+0.48}_{-0.52}$	1.53
10	NGC 3412	7.67 (0.01)	-22.54 (0.12)	1.84 (0.27)	2.30 (0.08)	105 $(-)^a$	0.43 $^{+0.01}_{-0.02}$	0.39 $^{+0.01}_{-0.02}$	1.72 $^{+0.04}_{-0.07}$	62.4 $^{+0.8}_{-0.7}$	3.60 $^{+0.14}_{-0.16}$	1.58
11	NGC 3489	7.37 (0.01)	-22.94 (0.15)	1.04 (0.28)	2.26 (0.12)	125 $(-)^a$	0.66 $^{+0.01}_{-0.02}$	0.55 $^{+0.02}_{-0.02}$	1.44 $^{+0.03}_{-0.04}$	65.8 $^{+0.6}_{-0.8}$	3.64 $^{+0.08}_{-0.10}$	1.01
12	NGC 4251	7.73 (0.01)	-23.65 (0.18)	1.01 (0.30)	2.33 (0.08)	120 $(-)^a$	0.77 $^{+0.01}_{-0.01}$	1.34 $^{+0.02}_{-0.03}$	1.58 $^{+0.06}_{-0.04}$	78.1 $^{+0.5}_{-0.4}$	3.64 $^{+0.06}_{-0.11}$	1.67
13	NGC 4382	6.14 (0.02)	-25.32 (0.14)	0.61 (0.28)	2.48 (0.06)	190 $(-)^a$	0.37 $^{+0.00}_{-0.00}$	2.10 $^{+0.03}_{-0.01}$	4.60 $^{+0.01}_{-0.01}$	46.5 $^{+0.1}_{-0.1}$	4.20 $^{+0.01}_{-0.02}$	5.65
14	NGC 4753	6.72 (0.02)	-24.98 (0.15)	-0.02 (0.28)	2.37 (0.04)	220 $(-)^a$	0.51 $^{+0.01}_{-0.00}$	1.90 $^{+0.03}_{-0.01}$	3.69 $^{+0.03}_{-0.03}$	59.6 $^{+0.3}_{-0.2}$	4.18 $^{+0.04}_{-0.02}$	4.00
15	NGC 4754	7.41 (0.03)	-23.60 (0.14)	1.93 (0.28)	2.43 (0.07)	171 $(-)^a$	—	—	—	—	—	—
16	NGC 5866	6.87 (0.02)	-23.95 (0.10)	1.50 (0.26)	2.42 (0.04)	140 $(-)^a$	0.88 $^{+0.01}_{-0.05}$	2.20 $^{+0.04}_{-0.28}$	1.66 $^{+0.22}_{-0.09}$	84.6 $^{+0.8}_{-1.3}$	2.75 $^{+0.02}_{-0.05}$	2.30
17	NGC 7332	8.01 (0.01)	-23.72 (0.17)	0.77 (0.30)	2.31 (0.03)	136 $(-)^a$	0.39 $^{+0.01}_{-0.01}$	0.46 $^{+0.02}_{-0.02}$	2.16 $^{+0.04}_{-0.03}$	77.7 $^{+0.3}_{-0.2}$	3.23 $^{+0.07}_{-0.04}$	2.05

Table B.1 *continued*

#	Name	$K_{\rm s,tot}$ [mag]	$M_{\rm K_s}$ [mag]	$\Delta(M_{\rm K_s})$ [mag]	$\log(V_{\rm MAX})$ [km s^{-1}]	σ_0 [km s^{-1}]	B/T	$R_{\rm e}$ [kpc]	$R_{\rm exp}$ [kpc]	i [^{o}]	Sérsic	$R_{\rm half}$ [kpc]
(1)	(2)	(3)	(4)	(5)	(6)	(7)	(8)	(9)	(10)	(11)	(12)	(13)
COMA^2												
18	DOI 215	11.12 (0.04)	-23.83 (0.05)	1.58 (0.24)	2.42 (0.05)	275.4 $(-)^b$	—	—	—	—	—	—
19	IC 3943	11.27 (0.04)	-23.68 (0.05)	1.00 (0.24)	2.33 (0.03)	281.8 $(-)^b$	—	—	—	—	—	—
20	IC 3990	10.50 (0.03)	-24.44 (0.04)	0.58 (0.24)	2.37 (0.04)	282.9 $(-)^b$	—	—	—	—	—	—
21	NGC 4787	11.40 (0.06)	-23.55 (0.06)	0.66 (0.25)	2.28 (0.03)	112.2 $(-)^b$	0.91 $^{+0.05}_{-0.07}$	6.53 $^{+2.13}_{-1.06}$	1.26 $^{+0.65}_{-0.40}$	64.7 $^{+5.1}_{-5.1}$	3.62 $^{+0.24}_{-0.16}$	5.60
22	NGC 4892	10.63 (0.03)	-24.32 (0.04)	1.02 (0.24)	2.41 (0.01)	186.1 $(-)^b$	0.14 $^{+0.05}_{-0.03}$	1.33 $^{+0.65}_{-0.37}$	4.56 $^{+0.19}_{-0.22}$	77.4 $^{+0.7}_{-0.8}$	3.21 $^{+0.09}_{-0.45}$	6.71
23	NGC 4931	10.31 (0.02)	-24.64 (0.04)	1.09 (0.24)	2.46 (0.02)	157.3 $(-)^b$	0.78 $^{+0.04}_{-0.16}$	3.41 $^{+0.29}_{-1.31}$	9.08 $^{+1.66}_{-2.79}$	47.0 $^{+13.5}_{-8.6}$	3.96 $^{+0.24}_{-0.60}$	5.12
24	NGC 4934	11.15 (0.04)	-23.80 (0.05)	-0.19 (0.24)	2.21 (0.03)	79.2 $(-)^b$	0.35 $^{+0.05}_{-0.06}$	1.88 $^{+0.34}_{-0.40}$	2.86 $^{+0.13}_{-0.14}$	81.7 $^{+0.8}_{-0.8}$	3.67 $^{+0.30}_{-0.32}$	3.84
25	NGC 4944	10.00 (0.03)	-24.95 (0.04)	-0.30 (0.24)	2.33 (0.02)	182.1 $(-)^b$	0.57 $^{+0.08}_{-0.07}$	2.95 $^{+0.49}_{-0.40}$	6.17 $^{+0.38}_{-0.49}$	75.9 $^{+1.5}_{-1.8}$	3.00 $^{+0.05}_{-0.06}$	5.59
26	NGC 4966	10.25 (0.03)	-24.70 (0.04)	0.12 (0.24)	2.35 (0.04)	159.0 $(-)^b$	0.39 $^{+0.02}_{-0.04}$	1.25 $^{+0.17}_{-0.23}$	4.20 $^{+0.15}_{-0.25}$	58.4 $^{+1.4}_{-1.9}$	3.66 $^{+0.10}_{-0.18}$	4.47
27	ZW 160$-$034	11.76 (0.05)	-23.18 (0.06)	-0.36 (0.25)	2.12 (0.04)	107.2 $(-)^b$	—	—	—	—	—	—
28	ZW 160$-$083	11.40 (0.05)	-23.55 (0.06)	0.35 (0.25)	2.25 (0.06)	140.2 $(-)^b$	—	—	—	—	—	—
29	ZW 160$-$101	11.20 (0.04)	-23.75 (0.05)	2.06 (0.24)	2.46 (0.02)	310.6 $(-)^b$	0.68 $^{+0.05}_{-0.04}$	1.29 $^{+0.15}_{-0.09}$	3.46 $^{+0.43}_{-0.52}$	80.2 $^{+1.8}_{-2.2}$	2.41 $^{+0.26}_{-0.21}$	2.11

Table B.1 *continued*

#	Name	$K_{\rm s,tot}$ [mag]	$M_{\rm K_s}$ [mag]	$\Delta(M_{\rm K_s})$ [mag]	$\log(V_{\rm MAX})$ [km s^{-1}]	σ_0 [km s^{-1}]	B/T	$R_{\rm e}$ [kpc]	$R_{\rm exp}$ [kpc]	i [^{o}]	Sérsic	$R_{\rm half}$ [kpc]
(1)	(2)	(3)	(4)	(5)	(6)	(7)	(8)	(9)	(10)	(11)	(12)	(13)
COMA[2]												
30	ZW 160−107	10.59 (0.03)	−24.36 (0.04)	0.94 (0.24)	2.40 (0.01)	267.2 (−)^b	0.41 $^{+0.02}_{-0.02}$	1.33 $^{+0.12}_{-0.13}$	2.82 $^{+0.09}_{-0.10}$	81.1 $^{+0.4}_{-0.6}$	3.35 $^{+0.19}_{-0.32}$	3.26
31	ZW 160−109	11.13 (0.05)	−23.82 (0.06)	1.50 (0.25)	2.41 (0.09)	− (−)	0.75 $^{+0.10}_{-0.20}$	2.26 $^{+0.38}_{-0.80}$	2.67 $^{+0.35}_{-0.46}$	47.9 $^{+7.9}_{-10.1}$	3.28 $^{+0.38}_{-0.19}$	2.84
32	ZW 160−119	11.38 (0.04)	−23.57 (0.05)	0.96 (0.24)	2.32 (0.04)	− (−)	—	—	—	—	—	—
33	ZW 160−214	11.04 (0.04)	−23.91 (0.05)	1.07 (0.24)	2.37 (0.06)	− (−)	0.71 $^{+0.07}_{-0.08}$	1.49 $^{+0.19}_{-0.21}$	4.07 $^{+0.34}_{-0.72}$	72.4 $^{+3.2}_{-3.9}$	2.38 $^{+0.28}_{-0.23}$	2.34
34	IC 3946	11.12 (0.04)	−23.83 (0.05)	1.66 (0.24)	2.43 (0.03)	− (−)	0.79 $^{+0.08}_{-0.09}$	1.59 $^{+0.36}_{-0.25}$	3.78 $^{+0.30}_{-0.72}$	76.9 $^{+3.8}_{-5.1}$	3.11 $^{+0.31}_{-0.24}$	2.21
35	IC 3955	11.38 (0.05)	−23.57 (0.06)	1.91 (0.25)	2.43 (0.07)	186.0 (9.0)^c	0.46 $^{+0.10}_{-0.13}$	1.40 $^{+0.48}_{-0.62}$	2.64 $^{+0.32}_{-0.22}$	61.4 $^{+4.4}_{-5.2}$	4.41 $^{+1.04}_{-0.61}$	3.07
36	IC 3976	11.50 (0.04)	−23.45 (0.05)	2.69 (0.24)	2.50 (0.04)	257.0 (6.0)^c	—	—	—	—	—	—
37	IC 4111	12.13 (0.09)	−22.82 (0.10)	−0.84 (0.26)	2.03 (0.04)	− (−)	0.57 $^{+0.10}_{-0.13}$	3.26 $^{+0.53}_{-0.60}$	2.75 $^{+0.50}_{-0.40}$	76.2 $^{+4.4}_{-4.3}$	3.27 $^{+0.39}_{-0.63}$	3.95
38	NGC 4873	11.25 (0.04)	−23.70 (0.06)	3.08 (0.25)	2.57 (0.06)	159.0 (11.0)^c	—	—	—	—	—	—
39	UGC 8122	11.45 (0.06)	−23.50 (0.07)	0.42 (0.25)	2.25 (0.15)	− (−)	0.34 $^{+0.11}_{-0.11}$	2.55 $^{+0.34}_{-0.56}$	3.32 $^{+0.41}_{-0.41}$	51.5 $^{+4.6}_{-7.9}$	3.20 $^{+0.72}_{-0.47}$	4.63

Table B.1 *continued*

#	Name	$K_{\rm s,tot}$ [mag]	$M_{\rm K_s}$ [mag]	$\Delta(M_{\rm K_s})$ [mag]	$\log(V_{\rm MAX})$ [km s^{-1}]	σ_0 [km s^{-1}]	B/T	$R_{\rm e}$ [kpc]	$R_{\rm exp}$ [kpc]	i [^{o}]	Sérsic	$R_{\rm half}$ [kpc]
(1)	(2)	(3)	(4)	(5)	(6)	(7)	(8)	(9)	(10)	(11)	(12)	(13)
FORNAX[3]												
40	NGC 1380	6.87 (0.02)	-24.49 (0.07)	1.56 (0.25)	2.49 (0.04)	227.8 (1.8)^d	0.58 $^{+0.01}_{-0.01}$	1.59 $^{+0.03}_{-0.03}$	3.28 $^{+0.09}_{-0.04}$	66.9 $^{+0.6}_{-0.4}$	3.34 $^{+0.03}_{-0.03}$	3.04
41	NGC 1381	8.42 (0.02)	-22.93 (0.07)	2.72 (0.25)	2.44 (0.05)	153.1 (1.8)^d	0.57 $^{+0.01}_{-0.01}$	0.67 $^{+0.02}_{-0.01}$	1.88 $^{+0.07}_{-0.05}$	82.5 $^{+0.4}_{-0.3}$	3.07 $^{+0.14}_{-0.10}$	1.48
42	NGC 1380A	9.57 (0.04)	-21.78 (0.08)	0.64 (0.25)	2.08 (0.01)	46.8 (0.9)^d	0.18 $^{+0.06}_{-0.03}$	0.98 $^{+0.32}_{-0.25}$	1.80 $^{+0.04}_{-0.06}$	78.1 $^{+0.6}_{-0.8}$	3.71 $^{+0.07}_{-0.10}$	2.69
43	NGC 1375	9.61 (0.03)	-21.75 (0.08)	0.47 (0.25)	2.06 (0.08)	66.8 (1.3)^d	0.19 $^{+0.01}_{-0.02}$	0.29 $^{+0.02}_{-0.03}$	1.33 $^{+0.04}_{-0.07}$	67.5 $^{+0.8}_{-1.2}$	2.22 $^{+0.07}_{-0.08}$	1.79
44	IC 1963	9.15 (0.02)	-22.20 (0.07)	1.44 (0.25)	2.22 (0.04)	46.3 (1.4)^d	0.39 $^{+0.03}_{-0.03}$	2.04 $^{+0.21}_{-0.12}$	1.42 $^{+0.03}_{-0.02}$	84.6 $^{+0.2}_{-0.2}$	3.61 $^{+0.10}_{-0.09}$	2.29
45	ESO 358−G006	10.62 (0.05)	-20.73 (0.09)	2.70 (0.26)	2.19 (0.07)	43.9 (0.9)^d	—	—	—	—	—	—
46	ESO 358−G059	10.60 (0.04)	-20.75 (0.08)	1.30 (0.25)	2.04 (0.22)	42.9 (1.0)^d	0.72 $^{+0.04}_{-0.07}$	1.46 $^{+0.20}_{-0.14}$	0.21 $^{+0.01}_{-0.02}$	61.9 $^{+2.0}_{-2.0}$	2.06 $^{+0.17}_{-0.40}$	0.91
VIRGO[4]												
47	NGC 4352	9.87 (0.04)	-21.08 (0.04)	2.91 (0.24)	2.26 (0.03)	85.0 (8.0)^c	0.76 $^{+0.07}_{-0.09}$	1.08 $^{+0.13}_{-0.17}$	2.02 $^{+0.23}_{-0.30}$	80.1 $^{+3.4}_{-5.4}$	3.40 $^{+0.24}_{-0.20}$	1.52
48	NGC 4417	8.17 (0.03)	-22.78 (0.03)	0.65 (0.24)	2.19 (0.05)	125.0 (4.0)^c	0.56 $^{+0.02}_{-0.02}$	0.62 $^{+0.03}_{-0.02}$	1.82 $^{+0.04}_{-0.05}$	78.2 $^{+0.4}_{-0.4}$	2.79 $^{+0.07}_{-0.06}$	1.37
49	NGC 4435	7.30 (0.02)	-23.66 (0.01)	0.72 (0.24)	2.30 (0.03)	174.0 (16.0)^c	0.53 $^{+0.10}_{-0.04}$	1.32 $^{+0.19}_{-0.15}$	4.20 $^{+0.00}_{-0.13}$	15.9 $^{+33.3}_{-11.1}$	4.18 $^{+0.17}_{-0.44}$	3.53
50	NGC 4442	7.29 (0.02)	-23.66 (0.02)	0.91 (0.24)	2.32 (0.02)	197.0 (15.0)^c	0.67 $^{+0.02}_{-0.01}$	0.92 $^{+0.04}_{-0.02}$	2.62 $^{+0.06}_{-0.05}$	73.5 $^{+0.8}_{-0.5}$	3.03 $^{+0.06}_{-0.03}$	1.63
51	NGC 4452	9.07 (0.03)	-21.88 (0.03)	-0.63 (0.24)	1.94 (0.02)	281.0 (15.0)^e	0.21 $^{+0.04}_{-0.07}$	1.37 $^{+0.24}_{-0.40}$	1.27 $^{+0.02}_{-0.03}$	85.2 $^{+0.2}_{-0.3}$	2.99 $^{+0.11}_{-0.10}$	2.00
52	NGC 4474	8.70 (0.02)	-22.26 (0.02)	-1.16 (0.24)	1.93 (0.04)	93.0 (7.0)^c	0.79 $^{+0.02}_{-0.01}$	1.21 $^{+0.07}_{-0.07}$	1.34 $^{+0.09}_{-0.05}$	81.2 $^{+1.0}_{-0.6}$	4.04 $^{+0.26}_{-0.41}$	1.47
53	NGC 4526	6.47 (0.02)	-24.48 (0.02)	1.96 (0.24)	2.54 (0.01)	316.0 (7.0)^c	0.61 $^{+0.01}_{-0.01}$	1.37 $^{+0.02}_{-0.02}$	4.25 $^{+0.04}_{-0.02}$	75.9 $^{+0.3}_{-0.3}$	2.96 $^{+0.05}_{-0.04}$	2.80
54	NGC 4638	8.21 (0.02)	-22.74 (0.02)	1.85 (0.24)	2.32 (0.02)	– (–)	0.74 $^{+0.01}_{-0.03}$	1.29 $^{+0.08}_{-0.22}$	0.50 $^{+0.04}_{-0.01}$	79.1 $^{+0.6}_{-0.5}$	3.74 $^{+0.15}_{-0.10}$	1.09

Table B.1 *continued*

#	Name	$K_{\rm s,tot}$ [mag]	$M_{\rm K_s}$ [mag]	$\Delta(M_{\rm K_s})$ [mag]	$\log(V_{\rm MAX})$ [km s^{-1}]	σ_0 [km s^{-1}]	B/T	$R_{\rm e}$ [kpc]	$R_{\rm exp}$ [kpc]	i [^{o}]	Sérsic	$R_{\rm half}$ [kpc]
(1)	(2)	(3)	(4)	(5)	(6)	(7)	(8)	(9)	(10)	(11)	(12)	(13)
FIELD	(M02)[5]											
55	NGC 1184	8.12 (0.02)	-24.59 (0.02)	0.95 (0.24)	2.43 (0.03)	229.0 (14.0)^f	0.31 $^{+0.01}_{-0.01}$	1.07 $^{+0.07}_{-2.43}$	3.80 $^{+0.06}_{-0.05}$	80.8 $^{+0.2}_{-0.2}$	3.58 $^{+0.07}_{-0.05}$	4.53
56	NGC 1611	9.41 (0.01)	-24.53 (0.01)	1.01 (0.24)	2.43 (0.02)	– (–)	—	—	—	—	—	—
57	NGC 2612	8.78 (0.02)	-23.06 (0.02)	2.20 (0.24)	2.40 (0.02)	– (–)	0.44 $^{+0.01}_{-0.01}$	0.71 $^{+0.02}_{-2.40}$	1.83 $^{+0.07}_{-0.06}$	75.0 $^{+0.8}_{-0.6}$	3.13 $^{+0.04}_{-0.06}$	1.88
58	NGC 3986	8.98 (0.02)	-24.37 (0.02)	1.41 (0.24)	2.46 (0.01)	206.0 (22.0)^f	0.53 $^{+0.02}_{-0.01}$	1.70 $^{+0.09}_{-2.46}$	5.67 $^{+0.15}_{-0.11}$	84.0 $^{+0.3}_{-0.2}$	2.48 $^{+0.09}_{-0.06}$	4.13
59	NGC 4179	7.92 (0.02)	-23.36 (0.04)	2.24 (0.24)	2.44 (0.01)	164.0 (15.0)^c	0.59 $^{+0.01}_{-0.01}$	0.83 $^{+0.02}_{-2.44}$	2.20 $^{+0.05}_{-0.04}$	80.5 $^{+0.3}_{-0.2}$	3.41 $^{+0.06}_{-0.07}$	1.73
60	NGC 5308	8.36 (0.03)	-23.97 (0.05)	2.22 (0.24)	2.51 (0.02)	260.0 (12.0)^f	0.39 $^{+0.04}_{-0.01}$	0.62 $^{+0.11}_{-2.51}$	2.68 $^{+0.12}_{-0.05}$	81.6 $^{+0.5}_{-0.2}$	2.99 $^{+0.04}_{-0.06}$	2.59

Notes: For all pertinent calculations, $H_0 = 70\,{\rm km\,s^{-1}\,Mpc^{-1}}$. All structural parameters derived from $K_{\rm s}$-band 2MASS photometry using GIM2D software (Simard et al. 2002). From (3) to (7), $1\,\sigma$ rms errors between "()"; from (8) to (12), 99% confidence intervals are presented; Col (1), number of each galaxy in the combined sample; Col (2), name; Col (3), total apparent magnitude in $K_{\rm s}$-band using 2MASS photometry; Col (4), absolute magnitude in $K_{\rm s}$-band, using redshifts/distance modulus described in main text; Col (5), shift in $K_{\rm s}$-band magnitude from Tully-Fisher relation of spiral galaxies from Tully & Pierce (2000); Col (6), logarithm (base 10) of the Maximum Rotational Velocity as published by the different authors of each subsample; Col (7), central velocity dispersion; Col (8), bulge to total fraction; Col (9), effective radius of the bulge component; Col (10), exponential disk scale length; Col (11), inclination angle; Col (12), Sérsic index; Col (13), half-light radius (computed by numerical integration of the best structural parameters).

References: (^{a}) Neistein et al. (1999); (^{b}) Hinz et al. (2001); (^{c}) Bernardi et al. (2002); (^{d}) Our own data; (^{e}) Prugniel & Simien (1995), unpublished measurements from OHP; (^{f}) di Nella et al. (1995).

(^{1}) Individual distance moduli from Tonry et al. (2001) were used.
(^{2}) Recessional velocity of $7269\,{\rm km\,s^{-1}}$ for Coma Cluster assumed (Struble & Rood 1999; Mould et al. 2000).
(^{3}) Distance modulus of 31.35 mag for Fornax Cluster assumed (Madore et al. 1999).
(^{4}) Recessional velocity of $1224\,{\rm km\,s^{-1}}$ for Virgo Cluster assumed (Ebeling et al. 1998; Mould et al. 2000).
(^{5}) Individual redshidts were used from NASA/IPAC Extragalactic Database (NED); for NGC 1611 and NGC 2612, redshifts were estimated from spectra by M02.

Table B.2. Central Line Indices measured at 3 Å resolution of S0 galaxies in Fornax.

Name	[MgFe]′ [Å]	⟨Fe⟩ [Å]	Hβ [Å]	Fe5015 [Å]	Mg₁ [mag]	Mg₂ [mag]	Mgb [Å]	Fe5270 [Å]	Fe5335 [Å]	Fe5406 [Å]	Fe5709 [Å]	Fe5782 [Å]
(1)	(2)	(3)	(4)	(5)	(6)	(7)	(8)	(9)	(10)	(11)	(12)	(13)
CENTRAL												
NGC 1380	4.14 (0.04)	3.53 (0.03)	1.48 (0.04)	6.10 (0.08)	0.149 (0.001)	0.305 (0.001)	4.92 (0.03)	3.43 (0.04)	3.64 (0.04)	2.29 (0.03)	1.11 (0.03)	1.02 (0.03)
NGC 1381	3.71 (0.04)	3.09 (0.03)	1.65 (0.04)	5.46 (0.08)	0.113 (0.001)	0.263 (0.001)	4.42 (0.03)	3.14 (0.04)	3.04 (0.04)	2.03 (0.03)	1.16 (0.03)	0.87 (0.03)
NGC 1380A	3.18 (0.09)	2.99 (0.06)	2.91 (0.08)	5.68 (0.16)	0.058 (0.001)	0.183 (0.002)	3.33 (0.08)	3.10 (0.08)	2.88 (0.10)	1.77 (0.07)	0.98 (0.07)	0.86 (0.07)
NGC 1375	2.71 (0.08)	3.06 (0.06)	3.89 (0.09)	6.76 (0.17)	0.053 (0.001)	0.161 (0.002)	2.43 (0.08)	2.98 (0.08)	3.15 (0.09)	1.78 (0.06)	1.10 (0.05)	0.76 (0.05)
IC 1963	3.54 (0.08)	3.31 (0.05)	2.45 (0.07)	6.40 (0.14)	0.072 (0.001)	0.212 (0.001)	3.76 (0.07)	3.38 (0.07)	3.24 (0.08)	1.97 (0.06)	1.16 (0.05)	0.79 (0.05)
ESO 358−G006	2.59 (0.16)	2.61 (0.11)	2.35 (0.15)	4.75 (0.29)	0.039 (0.003)	0.142 (0.003)	2.51 (0.14)	2.75 (0.15)	2.48 (0.17)	1.52 (0.13)	1.01 (0.11)	0.58 (0.12)
ESO 358−G059	2.82 (0.07)	2.56 (0.05)	2.25 (0.06)	4.71 (0.12)	0.048 (0.001)	0.155 (0.001)	3.03 (0.06)	2.70 (0.06)	2.42 (0.07)	1.69 (0.05)	0.94 (0.05)	0.46 (0.05)
NGC 1316	3.73 (0.08)	3.28 (0.05)	2.16 (0.07)	5.96 (0.14)	0.094 (0.014)	0.228 (0.001)	4.26 (0.07)	3.26 (0.07)	3.30 (0.08)	2.07 (0.06)	1.04 (0.05)	1.02 (0.05)
ESO 359−G002	1.95 (0.15)	1.92 (0.11)	3.54 (0.13)	3.99 (0.26)	0.025 (0.011)	0.107 (0.003)	2.01 (0.13)	1.87 (0.14)	1.97 (0.16)	1.12 (0.12)	0.57 (0.11)	0.63 (0.11)

Notes: From (2) to (13), 1σ rms errors between "( )"; Col (1), name; Col (2), [MgFe]′ combined index (González 1993; Thomas, Maraston & Bender 2003); Col (3), ⟨Fe⟩ combined index (Gorgas, Efstathiou & Aragón-Salamanca 1990); Col (4), Hβ index; Col (5), Fe5015 index; Col (6), Mg₁ index in magnitudes; Col (7), Mg₂ index in magnitudes; Col (8), Mgb index; Col (9), Fe5270 index; Col (10), Fe5335 index; Col (11), Fe5406 index; Col (12), Fe5709 index; Col (13), Fe5782 index.

Table B.3. Central Line Indices measured at Lick resolution of S0 galaxies in Fornax.

Name	[MgFe]′ [Å]	⟨Fe⟩ [Å]	Hβ [Å]	Fe5015 [Å]	Mg$_1$ [mag]	Mg$_2$ [mag]	Mgb [Å]	Fe5270 [Å]	Fe5335 [Å]	Fe5406 [Å]	Fe5709 [Å]	Fe5782 [Å]
(1)	(2)	(3)	(4)	(5)	(6)	(7)	(8)	(9)	(10)	(11)	(12)	(13)
CENTRAL												
NGC 1380	3.82 (0.04)	3.01 (0.03)	1.47 (0.04)	5.13 (0.08)	0.145 (0.004)	0.300 (0.001)	4.86 (0.04)	3.02 (0.04)	3.00 (0.04)	1.97 (0.03)	1.00 (0.03)	0.83 (0.03)
NGC 1381	3.40 (0.04)	2.70 (0.03)	1.65 (0.04)	4.83 (0.08)	0.111 (0.004)	0.261 (0.001)	4.20 (0.04)	2.81 (0.04)	2.60 (0.05)	1.75 (0.03)	1.05 (0.03)	0.75 (0.03)
NGC 1380A	2.88 (0.09)	2.65 (0.06)	2.78 (0.08)	4.69 (0.16)	0.058 (0.009)	0.182 (0.002)	3.07 (0.08)	2.79 (0.09)	2.51 (0.10)	1.53 (0.07)	0.90 (0.07)	0.66 (0.07)
NGC 1375	2.52 (0.07)	2.63 (0.05)	3.47 (0.07)	5.24 (0.14)	0.040 (0.009)	0.147 (0.001)	2.39 (0.07)	2.69 (0.07)	2.57 (0.08)	1.55 (0.06)	1.00 (0.05)	0.68 (0.05)
IC 1963	3.22 (0.08)	2.87 (0.05)	2.26 (0.07)	5.27 (0.14)	0.072 (0.014)	0.211 (0.001)	3.56 (0.07)	3.00 (0.07)	2.75 (0.08)	1.71 (0.06)	1.02 (0.05)	0.64 (0.05)
ESO 358−G006	2.41 (0.16)	2.23 (0.12)	2.11 (0.15)	3.97 (0.29)	0.037 (0.028)	0.139 (0.003)	2.51 (0.14)	2.44 (0.15)	2.03 (0.18)	1.35 (0.13)	0.89 (0.12)	0.50 (0.12)
ESO 358−G059	2.53 (0.07)	2.25 (0.05)	2.16 (0.06)	3.92 (0.13)	0.048 (0.005)	0.156 (0.001)	2.76 (0.06)	2.40 (0.06)	2.10 (0.07)	1.47 (0.05)	0.87 (0.05)	0.34 (0.05)
NGC 1316	3.22 (0.08)	2.76 (0.05)	2.11 (0.07)	5.15 (0.14)	0.094 (0.014)	0.228 (0.001)	3.74 (0.07)	2.77 (0.07)	2.75 (0.08)	1.66 (0.06)	0.93 (0.05)	0.77 (0.05)
ESO 359−G002	1.70 (0.14)	1.54 (0.10)	3.32 (0.13)	3.15 (0.25)	0.022 (0.011)	0.101 (0.003)	1.86 (0.13)	1.58 (0.14)	1.51 (0.16)	1.00 (0.12)	0.52 (0.11)	0.51 (0.11)

Notes: From (2) to (13), 1σ rms errors between "( )"; Col (1), name; Col (2), [MgFe]′ combined index (González 1993; Thomas, Maraston & Bender 2003); Col (3), ⟨Fe⟩ combined index (Gorgas, Efstathiou & Aragón-Salamanca 1990); Col (4), Hβ index; Col (5), Fe5015 index; Col (6), Mg$_1$ index in magnitudes; Col (7), Mg$_2$ index in magnitudes; Col (8), Mgb index; Col (9), Fe5270 index; Col (10), Fe5335 index; Col (11), Fe5406 index; Col (12), Fe5709 index; Col (13), Fe5782 index.

Table B.4. Central Ages and Metallicities using line indices at Lick resolution for S0 galaxies in Fornax. Also, B-band absolute magnitudes and $\Delta(M_{\rm B})$ from TFR.

Name	$M_{\rm B}$ [mag]	$\Delta(M_{\rm B})$ [mag]	$\log({\rm Age})_{\rm [MgFe]'}$ [yr]	$[{\rm Fe/H}]_{\rm [MgFe]'}$ [dex]	$\log({\rm Age})_{\langle {\rm Fe} \rangle}$ [yr]	$[{\rm Fe/H}]_{\langle {\rm Fe} \rangle}$ [dex]	$\log({\rm Age})_{\rm Mgb}$ [yr]	$[{\rm Fe/H}]_{\rm Mgb}$ [dex]	$\log({\rm Age})_{\rm Fe5709}$ [yr]	$[{\rm Fe/H}]_{\rm Fe5709}$ [dex]
(1)	(2)	(3)	(4)	(5)	(6)	(7)	(8)	(9)	(10)	(11)
CENTRAL										
NGC 1380	$-20.57\,(0.12)$	$1.87\,(0.27)$	$10.09\ ^{+0.06}_{-0.05}$	$0.23\ ^{+0.05}_{-0.05}$	$10.21\ ^{+0.06}_{-0.06}$	$-0.02\ ^{+0.03}_{-0.03}$	$9.95\ ^{+0.05}_{-0.05}$	$0.63\ ^{+0.06}_{-0.06}$	$10.23\ ^{+0.06}_{-0.05}$	$-0.05\ ^{+0.05}_{-0.05}$
NGC 1381	$-18.98\,(0.12)$	$3.13\,(0.27)$	$9.99\ ^{+0.05}_{-0.05}$	$0.06\ ^{+0.05}_{-0.05}$	$10.10\ ^{+0.06}_{-0.05}$	$-0.17\ ^{+0.03}_{-0.04}$	$9.89\ ^{+0.06}_{-0.06}$	$0.34\ ^{+0.07}_{-0.06}$	$9.99\ ^{+0.04}_{-0.04}$	$0.06\ ^{+0.06}_{-0.06}$
NGC 1380A	$-18.12\,(0.15)$	$1.32\,(0.28)$	$9.16\ ^{+0.06}_{-0.06}$	$0.53\ ^{+0.12}_{-0.11}$	$9.23\ ^{+0.04}_{-0.04}$	$0.33\ ^{+0.06}_{-0.06}$	$9.08\ ^{+0.08}_{-0.08}$	$0.77\ ^{+0.16}_{-0.15}$	$9.30\ ^{+0.04}_{-0.04}$	$0.07\ ^{+0.15}_{-0.17}$
NGC 1375	$-18.25\,(0.15)$	$1.02\,(0.28)$	$8.87\ ^{+0.05}_{-0.05}$	$0.67\ ^{+0.10}_{-0.10}$	$8.91\ ^{+0.04}_{-0.04}$	$0.56\ ^{+0.04}_{-0.04}$	$8.84\ ^{+0.06}_{-0.07}$	$0.78\ ^{+0.14}_{-0.13}$	$8.97\ ^{+0.04}_{-0.05}$	$0.36\ ^{+0.08}_{-0.09}$
IC 1963	$-18.53\,(0.12)$	$1.92\,(0.27)$	$9.41\ ^{+0.05}_{-0.06}$	$0.42\ ^{+0.10}_{-0.10}$	$9.43\ ^{+0.06}_{-0.05}$	$0.27\ ^{+0.05}_{-0.05}$	$9.36\ ^{+0.07}_{-0.07}$	$0.59\ ^{+0.14}_{-0.13}$	$9.47\ ^{+0.07}_{-0.06}$	$0.14\ ^{+0.11}_{-0.11}$
ESO 358−G006	$-17.49\,(0.16)$	$2.78\,(0.29)$	$9.81\ ^{+0.14}_{-0.13}$	$-0.37\ ^{+0.16}_{-0.15}$	$9.79\ ^{+0.13}_{-0.12}$	$-0.30\ ^{+0.12}_{-0.12}$	$9.83\ ^{+0.14}_{-0.13}$	$-0.43\ ^{+0.14}_{-0.13}$	$9.72\ ^{+0.15}_{-0.14}$	$-0.10\ ^{+0.25}_{-0.30}$
ESO 358−G059	$-17.41\,(0.15)$	$1.71\,(0.28)$	$9.74\ ^{+0.06}_{-0.07}$	$-0.25\ ^{+0.07}_{-0.07}$	$9.75\ ^{+0.06}_{-0.06}$	$-0.26\ ^{+0.05}_{-0.05}$	$9.74\ ^{+0.07}_{-0.08}$	$-0.23\ ^{+0.07}_{-0.06}$	$9.70\ ^{+0.06}_{-0.06}$	$-0.13\ ^{+0.11}_{-0.12}$
NGC 1316	$-\,(-)$	$-\,(-)$	$9.54\ ^{+0.09}_{-0.10}$	$0.28\ ^{+0.09}_{-0.09}$	$9.61\ ^{+0.07}_{-0.08}$	$0.12\ ^{+0.05}_{-0.05}$	$9.41\ ^{+0.09}_{-0.07}$	$0.57\ ^{+0.13}_{-0.13}$	$9.69\ ^{+0.08}_{-0.08}$	$-0.04\ ^{+0.11}_{-0.12}$
ESO 359−G002	$-\,(-)$	$-\,(-)$	$9.19\ ^{+0.05}_{-0.05}$	$-0.27\ ^{+0.16}_{-0.15}$	$9.23\ ^{+0.05}_{-0.05}$	$-0.45\ ^{+0.10}_{-0.10}$	$9.13\ ^{+0.06}_{-0.07}$	$-0.01\ ^{+0.17}_{-0.15}$	$9.37\ ^{+0.17}_{-0.13}$	$-0.89\ ^{+0.37}_{-0.42}$

Notes: From (2) to (3), $1\,\sigma$ rms errors between "( )"; from (4) to (11), 99% confidence intervals are presented. Col (1), name; Col (2), absolute total B-band magnitude from RC3 assuming distance modulus of 31.35 mag (Madore et al. 1999) for Fornax Cluster; Col (3), shift in B-band magnitude from Tully-Fisher relation of spiral galaxies from Tully & Pierce (2000); Col (4) (5), age and metallicity, estimated using Bruzual & Charlot (2003) simple stellar population models at Lick resolution and [MgFe]′ as metallicity indicator; Col (6) (7), age and metallicity, estimated using $\langle {\rm Fe} \rangle$ as metallicity indicator; Col (8) (9), age and metallicity, estimated using Mgb as metallicity indicator; Col (10) (11), age and metallicity, estimated using Fe5709 as metallicity indicator.

Table B.5. Line Indices, Ages and Metallicities at $1\,R_{\mathrm{e}}$ of 7 rotationally-supported S0 galaxies in Fornax.

Name	[MgFe]′ [Å]	⟨Fe⟩ [Å]	Hβ [Å]	Mgb [Å]	log(Age)$_{\mathrm{[MgFe]'}}$ [yr]	[Fe/H]$_{\mathrm{[MgFe]'}}$ [dex]	log(Age)$_{⟨\mathrm{Fe}⟩}$ [yr]	[Fe/H]$_{⟨\mathrm{Fe}⟩}$ [dex]	log(Age)$_{\mathrm{Mgb}}$ [yr]	[Fe/H]$_{\mathrm{Mgb}}$ [dex]
(1)	(2)	(3)	(4)	(5)	(6)	(7)	(8)	(9)	(10)	(11)
At $1\,R_{\mathrm{e}}$										
NGC 1380	2.98 (0.08)	2.47 (0.05)	1.56 (0.07)	3.58 (0.07)	$10.31\,^{+0.16}_{-0.14}$	$-0.34\,^{+0.08}_{-0.08}$	$10.39\,^{+0.16}_{-0.14}$	$-0.43\,^{+0.07}_{-0.07}$	$10.20\,^{+0.14}_{-0.12}$	$-0.19\,^{+0.08}_{-0.08}$
NGC 1381	3.11 (0.06)	2.46 (0.04)	1.57 (0.05)	3.85 (0.05)	$10.22\,^{+0.10}_{-0.09}$	$-0.23\,^{+0.06}_{-0.06}$	$10.37\,^{+0.12}_{-0.11}$	$-0.43\,^{+0.05}_{-0.05}$	$10.08\,^{+0.08}_{-0.07}$	$0.01\,^{+0.06}_{-0.06}$
NGC 1380A	2.69 (0.11)	2.39 (0.08)	2.15 (0.10)	2.97 (0.10)	$9.71\,^{+0.10}_{-0.09}$	$-0.13\,^{+0.12}_{-0.11}$	$9.71\,^{+0.09}_{-0.08}$	$-0.15\,^{+0.08}_{-0.08}$	$9.68\,^{+0.20}_{-0.16}$	$-0.09\,^{+0.15}_{-0.14}$
NGC 1375	2.59 (0.11)	2.36 (0.08)	2.29 (0.10)	2.80 (0.10)	$9.56\,^{+0.15}_{-0.12}$	$-0.11\,^{+0.12}_{-0.11}$	$9.58\,^{+0.12}_{-0.13}$	$-0.13\,^{+0.07}_{-0.08}$	$9.55\,^{+0.17}_{-0.12}$	$-0.07\,^{+0.14}_{-0.13}$
IC 1963	3.14 (0.08)	2.76 (0.05)	1.99 (0.07)	3.53 (0.07)	$9.71\,^{+0.09}_{-0.09}$	$0.12\,^{+0.09}_{-0.09}$	$9.73\,^{+0.08}_{-0.08}$	$0.07\,^{+0.05}_{-0.06}$	$9.67\,^{+0.10}_{-0.11}$	$0.21\,^{+0.11}_{-0.11}$
ESO 358−G006	2.35 (0.16)	2.04 (0.11)	1.97 (0.15)	2.70 (0.14)	$9.96\,^{+0.27}_{-0.17}$	$-0.50\,^{+0.16}_{-0.16}$	$9.98\,^{+0.26}_{-0.18}$	$-0.54\,^{+0.13}_{-0.14}$	$9.93\,^{+0.16}_{-0.15}$	$-0.41\,^{+0.14}_{-0.13}$
ESO 358−G059	2.37 (0.16)	2.13 (0.11)	2.03 (0.15)	2.53 (0.14)	$9.89\,^{+0.16}_{-0.14}$	$-0.45\,^{+0.15}_{-0.14}$	$9.89\,^{+0.15}_{-0.13}$	$-0.43\,^{+0.12}_{-0.12}$	$9.90\,^{+0.16}_{-0.14}$	$-0.47\,^{+0.14}_{-0.13}$

Notes: From (2) to (5), $1\,\sigma$ rms errors between "( )"; from (6) to (11), 99% confidence intervals are presented. Col (1), name; Col (2), [MgFe]′ combined index (González 1993; Thomas, Maraston & Bender 2003); Col (3), ⟨Fe⟩ combined index (Gorgas, Efstathiou & Aragón-Salamanca 1990); Col (4), Hβ index; Col (5), Mgb index, ; Col (6) (7), age and metallicity, estimated using Bruzual & Charlot (2003) simple stellar population models and [MgFe]′ as metallicity indicator; Col (8) (9), age and metallicity, estimated using ⟨Fe⟩ as metallicity indicator; Col (10) (11), age and metallicity, estimated using Mgb as metallicity indicator.

Table B.6. Line Indices, Ages and Metallicities at $2\,R_{\rm e}$ of 7 rotationally-supported S0 galaxies in Fornax.

Name	[MgFe]′ [Å]	⟨Fe⟩ [Å]	Hβ [Å]	Mgb [Å]	log(Age)$_{\rm [MgFe]'}$ [yr]	[Fe/H]$_{\rm [MgFe]'}$ [dex]	log(Age)$_{\langle Fe\rangle}$ [yr]	[Fe/H]$_{\langle Fe\rangle}$ [dex]	log(Age)$_{\rm Mgb}$ [yr]	[Fe/H]$_{\rm Mgb}$ [dex]
(1)	(2)	(3)	(4)	(5)	(6)	(7)	(8)	(9)	(10)	(11)
At $2\,R_{\rm e}$										
NGC 1380	2.89 (0.11)	2.44 (0.07)	1.52 (0.10)	3.45 (0.09)	$10.46\,^{+0.26}_{-0.22}$	$-0.44\,^{+0.11}_{-0.11}$	$10.50\,^{+0.25}_{-0.21}$	$-0.49\,^{+0.10}_{-0.10}$	$10.35\,^{+0.23}_{-0.19}$	$-0.31\,^{+0.11}_{-0.10}$
NGC 1381	2.81 (0.08)	2.33 (0.05)	1.56 (0.07)	3.34 (0.06)	$10.43\,^{+0.17}_{-0.15}$	$-0.47\,^{+0.08}_{-0.08}$	$10.51\,^{+0.17}_{-0.15}$	$-0.56\,^{+0.07}_{-0.07}$	$10.32\,^{+0.15}_{-0.13}$	$-0.35\,^{+0.07}_{-0.07}$
NGC 1380A	2.79 (0.09)	2.56 (0.06)	2.22 (0.08)	3.02 (0.08)	$9.56\,^{+0.12}_{-0.10}$	$0.00\,^{+0.10}_{-0.10}$	$9.55\,^{+0.10}_{-0.08}$	$0.01\,^{+0.06}_{-0.06}$	$9.55\,^{+0.13}_{-0.10}$	$0.03\,^{+0.12}_{-0.12}$
NGC 1375	2.49 (0.16)	2.23 (0.12)	2.20 (0.15)	2.73 (0.14)	$9.71\,^{+0.15}_{-0.20}$	$-0.25\,^{+0.17}_{-0.16}$	$9.72\,^{+0.14}_{-0.17}$	$-0.26\,^{+0.11}_{-0.12}$	$9.70\,^{+0.16}_{-0.22}$	$-0.22\,^{+0.18}_{-0.15}$
IC 1963	3.04 (0.16)	2.64 (0.11)	1.97 (0.15)	3.45 (0.14)	$9.77\,^{+0.18}_{-0.19}$	$0.02\,^{+0.18}_{-0.18}$	$9.80\,^{+0.16}_{-0.16}$	$-0.03\,^{+0.12}_{-0.13}$	$9.73\,^{+0.20}_{-0.23}$	$0.12\,^{+0.23}_{-0.20}$
ESO 358−G006	2.31 (0.16)	2.06 (0.12)	2.08 (0.14)	2.56 (0.14)	$9.86\,^{+0.14}_{-0.13}$	$-0.46\,^{+0.15}_{-0.14}$	$9.86\,^{+0.14}_{-0.12}$	$-0.47\,^{+0.12}_{-0.12}$	$9.85\,^{+0.14}_{-0.13}$	$-0.42\,^{+0.14}_{-0.13}$
ESO 358−G059	2.37 (0.16)	2.13 (0.11)	2.03 (0.15)	2.53 (0.14)	$9.89\,^{+0.16}_{-0.14}$	$-0.45\,^{+0.15}_{-0.14}$	$9.89\,^{+0.15}_{-0.13}$	$-0.43\,^{+0.12}_{-0.12}$	$9.90\,^{+0.16}_{-0.14}$	$-0.47\,^{+0.14}_{-0.13}$

Notes: From (2) to (5), $1\,\sigma$ rms errors between "( )"; from (6) to (11), 99% confidence intervals are presented. Col (1), name; Col (2), [MgFe]′ combined index (González 1993; Thomas, Maraston & Bender 2003); Col (3), ⟨Fe⟩ combined index (Gorgas, Efstathiou & Aragón-Salamanca 1990); Col (4), Hβ index; Col (5), Mgb index, ; Col (6) (7), age and metallicity, estimated using Bruzual & Charlot (2003) simple stellar population models and [MgFe]′ as metallicity indicator; Col (8) (9), age and metallicity, estimated using ⟨Fe⟩ as metallicity indicator; Col (10) (11), age and metallicity, estimated using Mgb as metallicity indicator.
[1] For ESO 358-G059 no data is available at $2\,R_{\rm e}$ of the bulge. In consequence, for this particular galaxy, we re-plot in Figure 4.13 the results at $1\,R_{\rm e}$ in the column corresponding to $2\,R_{\rm e}$.